AN ABSTRACT OF THE THESIS OF

Shannon K. Mayer for the degree of Doctor of Philosophy in Physics presented on January 22, 1997. Title: Low-Velocity Matter-Wave Source for Atom Interferometry Produced by Zeeman-Tuned Laser Cooling and Magneto-Optic Trapping.

Redacted for Privacy

Abstract Approved: _____
David H. McIntyre

A continuous, low-velocity, nearly monochromatic atomic beam is created using laser cooling and two-dimensional magneto-optic trapping. Rubidium atoms from an effusive oven are slowed and cooled using Zeeman-tuned slowing. The scattering force from a counter-propagating, frequency-stabilized diode laser beam is used to decelerate the thermal beam of atoms to a velocity of ~ 20 m/s. A spatially varying magnetic field is used to Zeeman shift the resonance frequency of the atom to compensate for the changing Doppler shift, thereby keeping the slowing atoms resonant with the fixed frequency laser. This slowing process also cools the beam of atoms to a temperature of a few Kelvin. The slow beam of atoms is loaded into a two-dimensional magneto-optic trap or atomic funnel. The atoms are trapped along the axis of the funnel and experience a molasses-type damping force in all three spatial dimensions. By frequency shifting the laser beams used to make the trap, the atoms are ejected at a controllable velocity. The continuous matter-wave source has a controllable beam velocity in the range of 2 to 15 m/s, longitudinal and transverse temperatures of approximately 500 μK, and a flux of 3.4×10^9 atoms/s. At 10 m/s, the de Broglie wavelength of the beam is 0.5 nm. The spatial profile of the atomic beam was characterized 30 cm from the exit of the atomic funnel using a surface ionization detector. The low-velocity atomic beam is an ideal source for atom interferometry and a variety of applications in the field of atom optics.

Low-Velocity Matter-Wave Source for Atom Interferometry Produced by Zeeman-Tuned Laser Cooling and Magneto-Optic Trapping

by

Shannon K. Mayer

A THESIS

submitted to

Oregon State University

in partial fulfillment of
the requirements for the
degree of

Doctor of Philosophy

Presented January 22, 1997
Commencement June 1997

Doctor of Philosophy thesis of Shannon K. Mayer presented on January 22, 1997

APPROVED:

Redacted for Privacy

Major Professor, Representing Physics

Redacted for Privacy

Chair of Department of Physics

Redacted for Privacy

Dean of Graduate School

I understand that my thesis will become part of the permanent collection of Oregon State University libraries. My signature below authorizes release of my thesis to any reader upon request.

Redacted for Privacy

Shannon K. Mayer, Author

Acknowledgments

I would like to thank my advisor, Dr. David McIntyre, for his guidance during this project. His knowledge, thoroughness, and resourcefulness have been a tremendous asset. He has taught me a great number of skills that helped me to become a better scientist. By his example, I have learned the importance of asking questions and have developed a healthy balance between thinking through a problem and simply getting in the lab and giving it a try. He has also modeled a number of attributes which will help me to become a better teacher. The patience he exhibits in working with students and his availability for questions are traits I hope to emulate. I am very grateful to have had the opportunity to learn from him.

I would also like to acknowledge the assistance of many people who contributed to the work in the laboratory during my time at OSU. Thanks to Nancy Silva and Tom Swanson for leading the way on the system; I benefited a great deal from our time working together on the project. Thanks to Mark Shroyer for building the solenoid for Zeeman-tuned slowing. Kerry Browne has been a great help in assisting with a variety of projects these last several months. John Archibald's fine machining skills were also a great asset to the group.

I would like to thank my husband, Steve, for his faithful encouragement as we have pursued this dream together. Thanks also to the friends who have come alongside in support of this endeavor. The friendship, encouragement, and impeccably timed humor have sustained me through this journey. Special thanks to Mike and Jennifer Jacobson, Bob and Beth Mumford, Bill Greenwood, Heidi Pattee, Corinne Manogue and the community at Logos House and Valley Christian Center. I would also like to thank my family for their support through the years.

Finally, I honor the Lord, Jesus Christ; the One who places in our hearts the desire to ask questions and allows us to discover, in some small measure, the working of the world He created.

Financial support has been provided by the Office of Naval Research and Oregon State University.

Table of Contents

	Page
Chapter 1. Introduction	1
1.1 Atom Interferometry: Historical Background and Applications	2
1.2 Overview of the Experiment	5
1.3 Thesis Outline	7
Chapter 2. Introduction to Atomic Physics: Relevant Properties of Rubidium	9
2.1 Overview	9
2.2 Atomic Energy Levels	9
2.3 Absorption and Emission Spectra	14
2.4 Zeeman Shifted Energy Levels	15
2.4.1 Zeeman Splitting in the Low Field Limit	18
2.4.2 Zeeman Splitting in the High Field Limit	19
2.4.3 Zeeman Splitting for General Fields	20
Chapter 3. Laser Manipulation of Atoms	26
3.1 Laser Cooling Theory	26
3.1.1 Momentum Transfer via Absorption and Spontaneous Emission of Photons	26
3.1.2 Laser Cooling Methods	29
3.1.3 Optical Pumping: Generating a Two-Level Cycling Transition	37
3.1.4 Transverse Heating	42
3.2 Optical Molasses and Magneto-optic Trapping Theory	42
3.2.1 Optical Molasses	42
3.2.2 The Magneto-Optic Trap	46
Chapter 4. Zeeman-Tuned Slowing: Implementation	50
4.1 Solenoid Design Criteria	50
4.2 The Solenoid for Zeeman-Tuned Slowing	53
4.2.1 Mechanical Design	54
4.2.2 Solenoid Coil Configuration	54
4.2.3 Solenoid Magnetic Field	56

Table of Contents (continued)

	Page
4.3 Theoretical Solenoid Performance	62
4.3.1 Analytical Model of Solenoid Performance	63
4.3.2 Theoretical Results from the Model	65
4.3.3 Spontaneous Emission and Transverse Heating	76
Chapter 5. System Description and Operation	78
5.1 System Overview	78
5.2 The Atomic Beam Machine	78
5.2.1 The Vacuum System	78
5.2.2 The Rubidium Oven	81
5.3 Lasers and Optics	87
5.3.1 Diode Laser Operation	87
5.3.2 Grating Feedback Stabilized Laser Diode	91
5.3.3 Frequency Calibration and Stabilization	93
5.3.4 Optical Layout and Laser Characteristics	99
5.4 The Atomic Funnel	102
5.5 The Surface Ionization Detector	104
5.5.1 Ionizing the Neutral Atomic Beam	105
5.5.2 Microchannel Plate Amplification	105
5.5.3 Detector Design and Operation	106
Chapter 6. Experimental Results: The Zeeman Slower	109
6.1 Optimizing System Parameters	111
6.2 State Preparation	112
6.2.1 The Function of the Cooling Laser in State Preparation	112
6.2.2 The Function of the Re-Pump Laser in State Preparation	114
6.3 Slowing Atoms Without Doppler Shift Compensation	115
6.4 Experimental Results: Zeeman Tuned Slowing	117
6.5 Comparison with Chirped Cooling	123
6.6 Isotope Comparison	124

Table of Contents (continued)

	Page
Chapter 7. Experimental Results: Characterization of the Low-Velocity Matter-Wave Source	126
7.1 Resonance Fluorescence: Estimating the Atomic Funnel Population	126
7.2 Time-of-Flight Analysis: Velocity and Temperature Measurements of the Atomic Beam	128
7.3 Surface Ionization Detection: Spatial Characteristics of the Atomic Beam	131
7.3.1 Detector Pulse Characteristics	132
7.3.2 Pulse Counting	133
7.3.3 Monitoring DC Current	135
7.3.4 Ionization Detector Efficiency	136
7.3.5 Predicted Spatial Distribution of the Atomic Beam	137
7.3.6 Measured Spatial Distribution of the Atomic Beam	141
7.4 Demonstration of Magneto-Optical Deflection of a Low-Velocity Atomic Beam	147
7.5 Feasibility Study: Diffraction of the Low-Velocity Atomic Beam by a Transmission Grating	153
Chapter 8: Conclusions and Future Research	156
Bibliography	158
Appendix: Maple Worksheet: Zeeman Shifted Energy Levels of the $5S_{1/2}$ and $5P_{3/2}$ States of Rubidium	167

List of Figures

Figure		Page
1.1	Three-grating Bonse-Hart interferometer for atom interferometry.	7
2.1	Fine structure and hyperfine structure splitting of the ground and first excited state energy levels of ^{85}Rb.	11
2.2	Energy level diagram for the ground and $5P_{3/2}$ state of ^{85}Rb and ^{87}Rb.	13
2.3	Measured Doppler-broadened absorption spectra for the $5S_{1/2}$ to $5P_{3/2}$ transition in rubidium.	16
2.4	Calculated Doppler-broadened absorption spectra for the $5S_{1/2}$ to $5P_{3/2}$ transition in rubidium.	16
2.5a	Zeeman shifted energy levels of the $5S_{1/2}$ and $5P_{3/2}$ states of ^{85}Rb.	22
2.5b	Zeeman shifted energy levels of the $5S_{1/2}$ and $5P_{3/2}$ states of ^{85}Rb (expanded view).	23
2.6a	Zeeman shifted energy levels of the $5S_{1/2}$ and $5P_{3/2}$ states of ^{87}Rb.	24
2.6b	Zeeman shifted energy levels of the $5S_{1/2}$ and $5P_{3/2}$ states of ^{87}Rb (expanded view).	25
3.1	Momentum transfer via photon absorption-emission.	27
3.2	Zeeman shift of ^{85}Rb energy levels relevant to Zeeman-tuned cooling.	32
3.3	Theoretical magnetic field profile for σ^- and σ^+ Zeeman-tuned cooling.	34
3.4	Zeeman shift in transition frequency for the π and σ^+ transitions relative to the σ^- cycling transition.	39
3.5	Relative scattering rate for optical pumping into the incorrect atomic sub-level during Zeeman tuned cooling.	41
3.6	Velocity damping of an atom in one dimension.	44
3.7	Force versus velocity curve for an atom in one-dimensional optical molasses.	44
3.8	A one-dimensional magneto-optic trap (MOT).	47
3.9	Two-dimensional magneto-optic trap or atomic funnel.	49
4.1	Water cooled solenoid support structure.	55
4.2	Designed solenoid field (solid line) compared with the theoretical profile (dashed line).	58

List of Figures (continued)

Figure		Page
4.3	Hall probe setup used to measure the axial magnetic field.	58
4.4	Measured solenoid axial magnetic field (solid line) compared with the theoretical profile (dashed line).	59
4.5	Radial component of the solenoid magnetic field for ρ = 0.2, 0.4, and 0.6 cm.	63
4.6	Ratio of radial to axial component of the magnetic field for ρ = 0.2, 0.4, and 0.6 cm.	63
4.7	An illustration of σ^- cooling for atoms slowed to 20 m/s.	66
4.8	An illustration of σ^- cooling for atoms slowed to 20 m/s.	66
4.9	An illustration of σ^+ cooling.	68
4.10	Final velocity as a function of laser detuning for σ^- cooling.	68
4.11	Final velocity as a function of laser detuning for σ^+ cooling.	69
4.12	Comparison between the ideal and designed magnetic field for σ^- and σ^+ cooling.	70
4.13	Final velocity versus detuning curve for both σ^- and σ^+ cooling for the ideal magnetic field profile.	71
4.14	Ideal magnetic field profiles for slowing atoms to different final velocities	72
4.15	Final velocity versus detuning curves for different solenoid profiles	72
4.16	Solenoid capture velocity as a function of cooling laser intensity.	75
4.17	Solenoid performance as a function of current shown for both constant bias solenoid current and constant taper solenoid current.	76
5.1	System schematic of the cooled-atom interferometer.	79
5.2	Vacuum system schematic.	80
5.3	The rubidium oven.	82
5.4	Spatial distribution of the thermal atomic beam.	84
5.5	Theoretical velocity distribution of the thermal rubidium beam.	86

List of Figures (continued)

Figure		Page
5.6	Absorption profile a "working" atomic beam.	88
5.7	Absorption profile a "non-working" atomic beam.	88
5.8	Diode laser with optical feedback from a diffraction grating.	92
5.9	Saturated absorption spectroscopy setup.	94
5.10	Saturated absorption spectra for the $F = 3 \rightarrow F' = 2, 3, 4$ transition in ^{85}Rb and the $F = 2 \rightarrow F' = 1, 2, 3$ transition in ^{87}Rb.	95
5.11	Polarization spectroscopy signal of the ^{85}Rb $F = 3 \rightarrow F' = 2, 3, 4$ transition.	97
5.12	Optical layout for the trapping lasers.	100
5.13	Optical layout for the cooling and diagnostic lasers.	101
5.14	The two-dimensional magneto-optic trap or atomic funnel.	103
5.15	The atomic funnel with the horizontal lasers detuned to eject atoms from the trap.	104
5.16	Schematic of the surface ionization detector.	107
5.17	Electrical configuration for the surface ionization detector.	107
6.1	Experimental setup for characterizing the velocity distribution of atoms emerging from the solenoid.	110
6.2	Fluorescence profile of the Zeeman slowed atomic beam.	110
6.3	Performance of the Zeeman slower bias solenoid field current.	114
6.4	Slowing atoms using a fixed frequency laser.	116
6.5	Fluorescence spectra for σ^- cooled ^{85}Rb atoms.	118
6.6	^{85}Rb, σ^- cooled beam final velocity as a function of laser detuning.	119
6.7	^{85}Rb cooled beam final velocity as a function of laser detuning for σ^+ and σ^- Zeeman tuned cooling.	120
6.8	Profile of the magnetic field used to compensate for the residual Zeeman solenoid field present in the atomic funnel region.	122
6.9	Comparison of cooling signals from chirped and Zeeman tuned cooling.	123

List of Figures (continued)

Figure		Page
6.10	Comparison of a ^{85}Rb and ^{87}Rb Zeeman slowed atomic beam.	125
7.1	Atomic velocity as a function of frequency offset for a funnel loaded using chirped cooling.	129
7.2	Atomic velocity as a function of frequency offset for a funnel loaded using Zeeman tuned cooling.	129
7.3	Experimental setup for characterizing the spatial profile of the atomic beam.	132
7.4	A single pulse from the surface ionization detector.	133
7.5	Ionization efficiency of the surface ionization detector as a function current through the rhenium ribbon.	137
7.6	Theoretical horizontal distribution of the atomic beam at the surface ionization detector.	139
7.7	Theoretical vertical distribution of the atomic beam at the surface ionization detector.	139
7.8	Spatial profile of the atomic beam 30 cm from the exit of the funnel for a horizontal trap laser detuning of ±7MHz.	143
7.9	Spatial profile of the atomic beam 30 cm from the exit of the funnel for a horizontal trap laser detuning of ±12MHz.	143
7.10	Spatial profile of the atomic beam 30 cm from the exit of the funnel with the vertical lasers and front horizontal laser pair blocked.	146
7.11	Controllable current source for modulating the magnetic field to deflect the low-velocity atomic beam.	149
7.12	Surface ionization signal for an atomic beam deflected using an applied magnetic field.	151

This thesis is dedicated to the memory of my father

Gerald William Ryan

Low-Velocity Matter-Wave Source for Atom Interferometry Produced by Zeeman-Tuned Laser Cooling and Magneto-Optic Trapping

Chapter 1: Introduction

In the traditional field of optics, light is manipulated through its interaction with matter. In recent years, a number of techniques have been developed in which the familiar roles are reversed; atoms are manipulated by interaction with light. Atom optics [Adams, 1994], as this field has been designated, allows for manipulation of the position and momentum of atoms and provides researchers with access to the wave properties of matter. Proposed applications are far reaching. Fundamental research pursuits include experiments in quantum mechanics, quantum optics, atomic collisions, and high resolution spectroscopy. Commercial interests include atom lithography, time standards, and gravitational and inertial measurements.

Control of atomic motion using light forces is realized in two ways: through the dipole force and the scattering force. A strong laser field will induce a dipole moment in an atom. Interaction between the induced dipole moment of the atom and the electric field gradient of a focused, intense laser produces a conservative force that attracts the atom toward the region of low potential energy. This technique is typically performed using far off-resonant light to avoid the scattering force associated with resonant photons. Many of the elements associated with conventional optics have been demonstrated using the dipole force. These include lenses [Bjorkholm, 1978], mirrors [Balykin, 1988], diffraction gratings [Martin, 1988] and cavities [Aminoff, 1993].

Since light carries momentum, a resonant or near resonant laser can be used to induce a force on an atom. During the absorption process, photons impart momentum to the atom in the direction of the laser beam. The scattering force exerted on the atom is proportional to the momentum and number of photons absorbed. The spontaneously re-emitted photons are symmetrically distributed. Thus, over the course of many

absorption-emission cycles, their contribution to the momentum of the atom averages to zero. This dissipative force has been used to slow and cool [Phillips, 1982; Blatt, 1984], trap [Raab, 1987], and funnel [Riis, 1990; Nellessen, 1990; Swanson, 1996] atoms. The ability to increase the de Broglie wavelength of the atoms ($\lambda = h/p$) makes experiments exploiting the wave nature of atoms more accessible. The state selectivity inherent in this resonant process also allows for novel beamsplitters that rely on absorption to coherently transfer population among atomic energy states [Lawall, 1994].

Micro-fabricated structures can also be used to manipulate atomic matter-waves. Recent advances in high-resolution electron beam lithography have made it possible to demonstrate diffraction gratings [Keith, 1988], lenses [Berkhout, 1989], and mirrors [Anderson, 1986] for atoms. In addition, computer-generated holograms have been used to diffract a cold atomic beam [Morinaga, 1996].

The focus of our experiment has been to create a continuous, low-velocity, nearly monochromatic atomic beam to be used as a source for an atom interferometer. Section 1.1 provides historical perspective on atom interferometers and discusses applications. An overview of our experiment is provided in section 1.2. Section 1.3 outlines the scope of this thesis.

1.1 Atom Interferometry: Historical Background and Applications

In 1802, Thomas Young's double-slit experiment demonstrated the wave nature of light. Though the proposition of light as a wave was not new, Young's papers on the subject introduced the idea of the *principle of interference*. At the time, the papers were criticized by the *Edinburgh Review* as being "destitute of every species of merit" [Hecht, 1987]. None-the-less, the wave theory of light continued to develop, and a number of interferometers were subsequently demonstrated as experimental manifestations of interference phenomena. A few classic designs include the Michelson [Michelson, 1882], Fabry-Perot [Fabry, 1899], Fizeau [Fizeau, 1862], and Sagnac [Sagnac, 1913]

interferometers. Optical interferometers have been a very powerful tool for precision measurements in both fundamental and commercial applications.

In 1924, de Broglie proposed that matter exhibits wave-like properties. Demonstration of an interferometer for matter-waves emerged as a logical extension of the wave nature of matter. Matter-wave interferometers have been demonstrated for electrons [Marton, 1953] and neutrons [Rauch, 1974]. The low velocities attainable with matter-wave sources have allowed for dramatic increases in the accuracy of some measurements. These devices have been used extensively for both precision measurements (e.g., measurement of the Sagnac effect using the rotation of the earth [Werner, 1979]) and tests of quantum mechanics (e.g., observation of the Aharonov-Casher effect [Cimmino, 1989] and the scalar Aharonov-Bohm effect [Allman, 1993]).

In recent years, atom interferometry has emerged as a promising new technique. Atoms offer many advantages over both neutron and electron matter-wave sources. Experiments using atoms are much more practical that those using neutrons. In addition, the internal structure inherent in atoms can be used to make the interferometer more sensitive to certain interactions.

The primary difficulty associated with constructing an interferometer for atoms has been lack of a suitable beam splitting technique. The techniques used in electron and neutron interferometry are not applicable, as atoms are charge neutral and cannot pass through matter. In addition, the small de Broglie wavelength of atoms results in a small diffraction angle even when using extremely small-scale physical structures. Recent developments in atom optics and micro-fabrication techniques have minimized many of these difficulties.

In 1991, four different atom interferometers were demonstrated. In two of the experiments [Keith, 1991a; Carnal, 1991], physical structures were used to spatially separate and recombine a beam of atoms. Keith *et al.* used a supersonic beam of sodium atoms and sub-micron transmission gratings in a Bonse-Hart three-grating geometry. Carnal and Mlynek used Young's double slit geometry and a supersonic metastable helium beam. In both experiments, the short de Broglie wavelength of the high-velocity

beam resulted in small diffraction angles, causing each of these interferometers to be over one meter in length.

The other two interferometers [Kasevich, 1991a; Riehle, 1991] did not rely on spatial separation and recombination of the beam, as is customary in a traditional interferometer. Instead, stimulated absorption and emission events caused the atom to travel through the interferometer in different energy states. Kasevich and Chu ejected atoms vertically from a magneto-optic trap and used stimulated Raman transitions to separate and recombine the atomic beams. Riehle *et al.* used a thermal beam of calcium atoms in an optical Ramsey geometry.

Following the initial atom interferometer experiments reported in 1991, additional techniques have been developed. Adiabatic population transfer between two hyperfine ground states was used to separate a cesium beam [Weitz, 1994]. Neon atoms were dropped from a magneto-optic trap through an interferometer in Young's double slit geometry [Shimizu, 1992]. Miniatura *et al.* [Miniatura,1992] created an atom interferometer based on the magnetic Stern-Gerlach effect. In addition, an interferometer for molecules was demonstrated [Chapman, 1995].

A number of potential applications have been proposed for atom interferometers including measurement of atomic properties, measurement of gravitational and inertial effects, and tests of fundamental aspects of quantum mechanics. The atom interferometers mentioned above are beginning to be viable tools for such experiments.

In the study of atomic properties, the system developed by Keith *et al.* [Keith, 1991a] was used to measure the index of refraction for sodium atoms [Schmiedmayer, 1995] and molecules [Chapman, 1995] traveling through various gases. In another experiment using the same system, Ekstrom *et al.* [Ekstrom, 1995] measured the electric polarizability of sodium. Interferometers have also been used to measure atomic properties such as Stark phase shifts [Shimizu, 1992; Rieger, 1993]. Weiss *et al.* [Weiss, 1993] used an atom interferometer to measure the ratio of Planck's constant to the mass of cesium h/m to one part in 10^7.

Atom interferometers also hold promise for precision measurement of inertial and gravitational effects [Clauser, 1988]. The system reported by Riehle *et al.* [Riehle, 1991],

was used to measure the Sagnac effect, demonstrating a sensitivity to the rate of rotation of 10^{-2} rad/s. The predicted sensitivity of a cold atom interferometer is 5 x 10^{-13} rad/s or 10^{-8} Ω_{Earth} [Adams, 1994]. In comparison, fiber optic gyroscopes (FOG) used in aircraft navigation have a demonstrated sensitivity of 2.5 x 10^{-8} rad/s. [Ezekiel, 1984]. Their predecessor, the ring laser gyroscope, is sensitive to 5 x 10^{-8} rad/s. [Chow, 1985].

The interferometer developed by Kasevich *et al.* demonstrated a sensitivity of 3 x $10^{-8}g$ [Kasevich, 1992]. The predicted achievable sensitivity of $<10^{-11}g$ for an atom interferometer will allow a wide range of gravimetric measurements to be performed with increased precision [Clauser, 1988]. Currently, the most precise absolute gravimeter is accurate to about $10^{-8}g$ [Faller, 1988]. It measures the acceleration of a falling cube using a laser interferometer. Proposed commercial applications for atom interferometers include earthquake prediction, geological surveying, monitoring seismic activity, and monitoring the mean level of oceans [Adams, 1994]. Gravimetric applications relevant to fundamental research include measurement of space-time curvature [Audretsch, 1994] and tests of local Lorentz invariance [Adams, 1994].

1.2 Overview of the Experiment

The focus of this experiment has been to create a continuous, low-velocity, nearly monochromatic atomic beam to be used as a source for an atom interferometer. The beam is generated in a two step process. A beam of rubidium atoms from an effusive oven is slowed and cooled using Zeeman-tuned slowing [Phillips, 1982; Barrett, 1991]. The scattering force from a counter-propagating diode laser is used to decelerate the thermal beam of atoms to a velocity of ~ 20 m/s. A spatially varying magnetic field is used to Zeeman shift the resonance frequency of the atom to compensate for the changing Doppler shift, thereby keeping the slowing atoms resonant with the fixed frequency laser. The slowing process also cools the beam of atoms to a temperature of a few Kelvin. In our previously employed technique of chirped cooling [Blatt, 1984], the cooling laser was swept in frequency to compensate for the changing Doppler shift of the atom, resulting in

a pulsed slow atomic beam. By avoiding the duty cycle limitations inherent in chirped cooling, the Zeeman slowing process increased the flux of atoms more than tenfold. The slow beam of atoms exiting the Zeeman solenoid is loaded into a two-dimensional magneto-optic trap or atomic funnel [Riis, 1990]. The atoms are trapped along the axis of the funnel and experience a molasses-type damping force in all three spatial dimensions [Chu, 1985]. By frequency shifting the laser beams used to make the trap, the atoms are ejected at a controllable velocity. The low-velocity atomic beam was characterized using a time-of-flight technique [Riis, 1990] and surface ionization detection [Ramsey, 1963; Scoles, 1992]. The continuous matter-wave source has a flux of 3.4×10^9 atoms/s, a controllable velocity in the range of 2 to 15 m/s, and longitudinal and transverse temperatures of approximately 500 μK. At 10 m/s, the de Broglie wavelength of the beam is 0.5 nm. In addition to its use in atom interferometry, it is also an ideal source for a variety of other applications in the field of atom optics.

The three-grating interferometer will be similar in design to the Bonse-Hart configuration used first for x-rays [Bonse, 1965] and later for neutrons [Bauspiess, 1974]. The interferometer, shown in Figure 1.1 consists of three gratings. The incident beam is diffracted by the first grating. The zero order and one of the first order diffracted beams are diffracted by the second grating. The two beams recombine to produce an interference pattern at the location of the third grating. Because the two interfering beams have intrinsically equal path lengths, the interference pattern is independent of the wavelength of the incident beam. In addition, the three-grating interferometer is relatively insensitive to misalignment [Chang, 1975; Mendlowitz, 1962].

The gratings that comprise the interferometer are free-standing silicon nitride transmission gratings similar to those used by Keith *et al.* for diffraction [Keith, 1988] and interference [Keith, 1991a] of a supersonic sodium beam. The gratings were fabricated by Tom Swanson at the National Nanofabrication Facility (NNF) at Cornell University using high-resolution electron beam lithography. A detailed description of the fabrication process is found in the work of Swanson [Swanson, 1995] and Keith *et al.* [Keith, 1991b]. The separation of the gratings for this experiment will be 5 cm, yielding

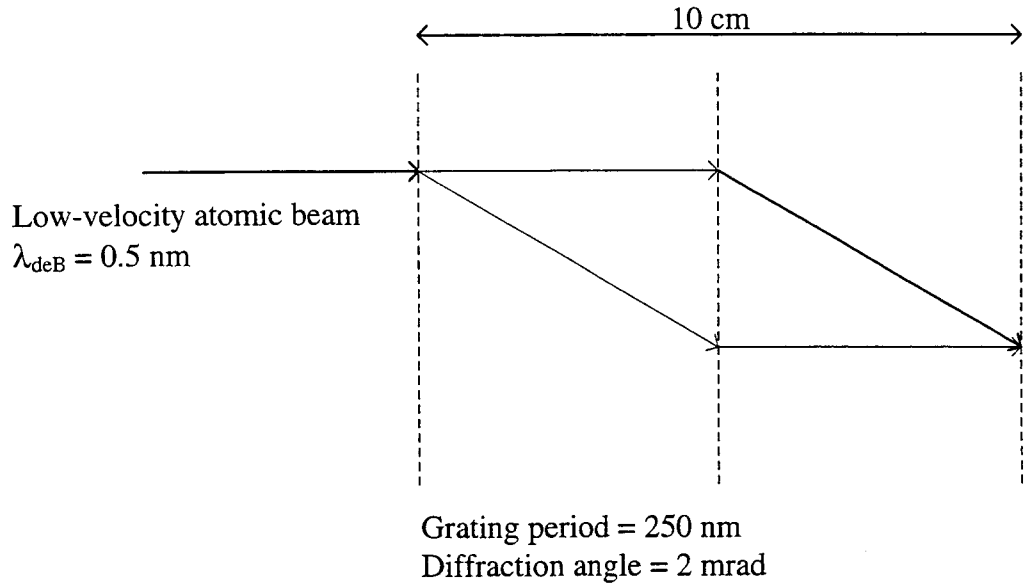

Figure 1.1 Three-grating Bonse-Hart interferometer for atom interferometry.

a much more compact system than the interferometer reported on by Keith *et al.* [Keith, 1991a].

The low-velocity atomic beam will also be used for other applications in atom optics. Many of the atom optical elements demonstrated previously can be simplified or enhanced using a low energy, long de Broglie wavelength source. Experiments proposed for the matter-wave source include beam diffraction, demonstration of magnetic lenses, deflection via magneto-optic forces, and atom holography.

1.3 Thesis Outline

This thesis describes the use of Zeeman-tuned laser cooling and two-dimensional magneto-optic trapping techniques to generate a low-velocity matter-wave source for experiments in atom interferometry and atom optics. Chapter 2 provides an introduction to the atomic physics relevant to the experiment. In Chapter 3, the theoretical basis for

laser cooling and magneto-optic trapping techniques is described. Chapter 4 details the design and fabrication of the magnet used for Zeeman-tuned slowing of the thermal atomic beam. It also describes the theoretical model used to make predictions about the performance of the Zeeman slower. Chapter 5 provides a description of the thermal beam source, electronically stabilized grating-feedback diode lasers, two-dimensional magneto-optic trap, and surface ionization detector that comprise the experimental system. Chapter 6 contains the experimental results obtained using Zeeman-tuned slowing to slow and cool a thermal rubidium beam. Chapter 7 describes the characterization of the low-velocity atomic beam ejected from the two-dimensional magneto-optic trap. The appendix contains the *Maple*[1] worksheet used to calculate the Zeeman shift in the energy levels of the $5S_{1/2}$ and $5P_{3/2}$ states of rubidium.

My primary contributions to this project include increasing the flux of atoms exiting the atomic funnel by implementing Zeeman-tuned slowing and characterizing the low-velocity matter wave source in preparation for its use in diffraction and interference experiments. I was the lead researcher involved in the design, numerical modeling, implementation, and testing of the Zeeman slower. The solenoid used to generate the magnetic field for Zeeman slowing was fabricated by Mark Shroyer.

Characterization of the low-velocity matter-wave source was accomplished by two independent techniques: Time-of-flight analysis and surface ionization detection. I worked with Tom Swanson and Nancy Silva during time-of-flight experiments on the trap loaded with atoms slowed by chirped cooling. This work, first reported in the Ph.D. thesis of Tom Swanson [Swanson, 1995], has since been published [Swanson, 1996]. I worked with Silva during similar time-of flight measurements on the trap loaded by Zeeman-tuned slowing [Silva, 1996]. The surface ionization detector used in characterization of the low-velocity atomic beam was designed by Silva [Silva, 1996]. I worked with her during installation and preliminary testing of the detector. Subsequently, I characterized the operation of the detector and used it to map out the spatial profile of the low-velocity beam. I also used the surface ionization detector to investigate the deflection of the atomic beam by magneto-optic forces.

---

[1] The computer algebra program *Maple* is a registered trademark of Waterloo Maple Software.

Chapter 2: Introduction to Atomic Physics: Relevant Properties of Rubidium

2.1 Overview

Laser cooling and trapping experiments involving atoms are typically performed using alkali metals. The atomic structure, consisting of a single valence electron outside a closed sub-shell, approximates a single electron atom. This allows for relatively simple theoretical analysis and provides an approximate two-level cycling transition. Strong resonance lines in the visible or near infrared region are accessible to available lasers and the relatively short radiative lifetime allows for rapid repeated excitation. The alkali atom used in this experiment is rubidium.

Rubidium occurs naturally in two isotopes: ^{85}Rb and ^{87}Rb. Rubidium 85, with a relative abundance of 72%, has nuclear spin I = 5/2. The nuclear spin of ^{87}Rb is I = 3/2. The brightest spectral line is the D_2 line, corresponding to a transition from the $5P_{3/2}$ excited state to the $5S_{1/2}$ ground state. It has a vacuum wavelength of 780.24 nm and a radiative lifetime of 26.5 ns. The atomic mass is 1.42×10^{-25} kg. The room temperature vapor pressure is 2×10^{-7} Torr and the melting point is 38.89° C.

A review of the atomic physics relevant to this experiment is provided below. Section 2.2 reviews the origin of the fine structure and hyperfine structure features in the atomic energy levels. Section 2.3 describes the observed spectral characteristics. In section 2.4 the theory for the Zeeman effect is detailed to provide a framework for the discussion of Zeeman-tuned slowing of atoms in Chapter 3.

2.2 Atomic Energy Levels

The ground and first excited states of the single electron in rubidium are $5S_{1/2}$ and $5P_{1/2,3/2}$ respectively. Atomic energy levels are split into different J sub-levels, where

$\mathbf{J} = \mathbf{L} + \mathbf{S}$ is the total electronic angular momentum of the state. This energy splitting, designated fine structure splitting, originates from relativistic effects such as spin-orbit coupling. For rubidium, the splitting of the 5P doublet is 14.32 nm. The splitting between the $5S_{1/2}$ ground state and the $5P_{3/2}$ excited state is 780.24 nm. The splitting between the $5S_{1/2}$ ground state and the $5P_{1/2}$ excited state is 794.6 nm. The spectral lines resulting from these transitions are labeled the D_2 and D_1 lines respectively.

In addition to fine structure splitting, narrow splitting (30 MHz to 7 GHz) of the J levels into F sub-levels occurs, where $\mathbf{F} = \mathbf{I} + \mathbf{J}$ and $\mathbf{I}$ is the nuclear spin. This phenomenon, designated hyperfine splitting, was first observed using optical interferometry by Michelson [Michelson, 1891], Fabry and Perot [Fabry, 1897] and Lummer and Gehrcke [Lummer, 1903]. Due to its relevance to the Zeeman effect, hyperfine splitting is examined in greater detail below. Figure 2.1 provides an illustration of the fine structure and hyperfine structure splitting for the ground and first excited states of ^{85}Rb.

Hyperfine splitting occurs as a result of the interaction between the electromagnetic multipole moments of the nucleus and the electromagnetic field produced by the electrons. The magnetic dipole moment of the nucleus interacts with the magnetic field of the valence electrons, providing the most significant contribution to the energy shift. A smaller contribution is provided by electrostatic interaction between the electric quadrupole moment of the nucleus and the atomic electrons. Though higher order multipole terms may be non-zero, their contributions are negligible and are generally ignored.

The complete hyperfine structure Hamiltonian for an atom is written [Corney, 1977, page 667],

$$H_{Hyperfine} = A_J \mathbf{I}\cdot\mathbf{J} + \frac{B_J}{2IJ(2I-1)(2J-1)}\left(3(\mathbf{I}\cdot\mathbf{J})^2 + \frac{3}{2}(\mathbf{I}\cdot\mathbf{J}) - I(I+1)J(J+1)\right), \quad (2.1)$$

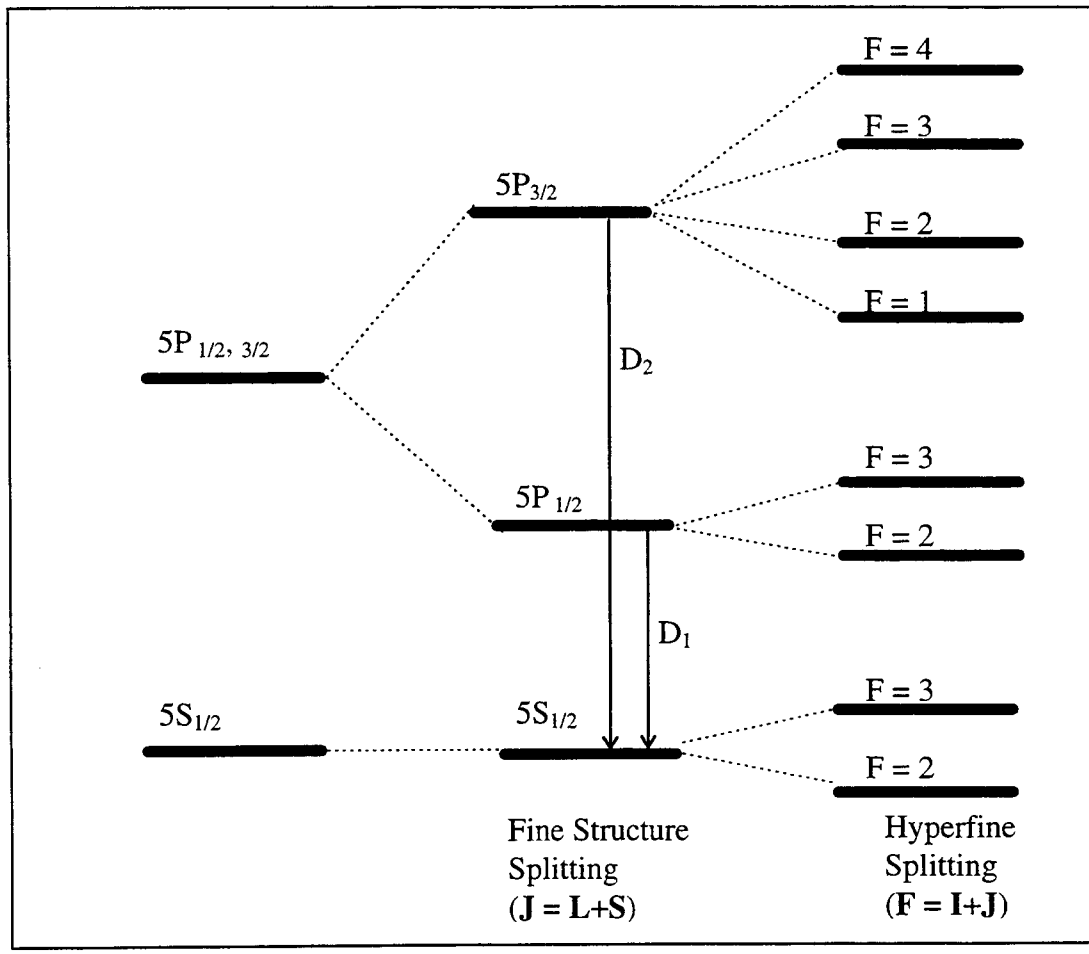

Figure 2.1 Fine structure and hyperfine structure splitting of the ground and first excited state energy levels of ^{85}Rb. (Not drawn to scale.)

where the first and second terms correspond to the magnetic dipole and electric quadrupole terms respectively. The magnetic hyperfine structure constant A_J and the electric quadrupole interaction constant B_J, are experimentally determined parameters.

Defining $\mathbf{F} = \mathbf{I} + \mathbf{J}$ to be the total angular momentum of the system, the matrix element $\langle \mathbf{I} \cdot \mathbf{J} \rangle$ is diagonal in the $| I\, J\, F\, M_F \rangle$ basis and reduces to

$$\left\langle IJFM_F \left| \mathbf{I}\cdot\mathbf{J} \right| IJFM_F \right\rangle = \left\langle \frac{1}{2}\left(F^2 - I^2 - J^2\right) \right\rangle$$

$$= \frac{1}{2}\left[F(F+1) - I(I+1) - J(J+1)\right]. \qquad (2.2)$$

By defining $K = F(F+1) - I(I+1) - J(J+1)$, the energy of a particular hyperfine level is given by

$$E_F = E_J + \left\langle IJFM_F \left| H_{\text{hyperfine}} \right| IJFM_F \right\rangle$$

$$= E_J + \frac{1}{2}A_J K + \frac{B_J}{8IJ(2I-1)(2J-1)}\left(3K(K+1) - 4I(I+1)J(J+1)\right), \qquad (2.3)$$

where E_J is the energy of the fine structure multiplet.

The relative energies of the F sub-levels for ^{85}Rb and ^{87}Rb were calculated using published values for A_J and B_J [Corney, 1977, page 718]. The ground state energy for ^{87}Rb is shifted down 80 MHz from the values calculated by equation 2.3. This shift, an experimentally determined parameter, is called the isotope shift, and results from the difference in nuclear volume between isotopes. Figure 2.2 shows the energy level diagram of the ground and $5^2P_{3/2}$ excited state of ^{85}Rb and ^{87}Rb. The quantities in parenthesis indicate the energy shift relative to energy E_J of the fine structure multiplet.

Allowed transitions among the atomic sub-levels are determined by calculating the appropriate transition rates. For electric dipole transitions, non-zero transitions rates result for transitions in which $\Delta F = 0, \pm 1$ ($F = 0$ to $F' = 0$ excluded) and $\Delta M_F = 0, \pm 1$.

For optical transitions, linearly polarized light (π) and circularly polarized light ($\sigma^{\pm}$) induce transitions where $\Delta M_F = 0$, $\Delta M_F = \pm 1$ respectively. One needs to be careful to define the direction of polarization relative to a defined quantization axis. In contrast with the notation of right-circular and left-circular polarization, which depends upon the direction of propagation of the light (i.e. for right-circular polarization, the electric field vector rotates clockwise as seen by an observer toward whom the wave is moving [Hecht, 1987]), $\sigma^{\pm}$ polarization is defined relative to the coordinate system. Circularly polarized

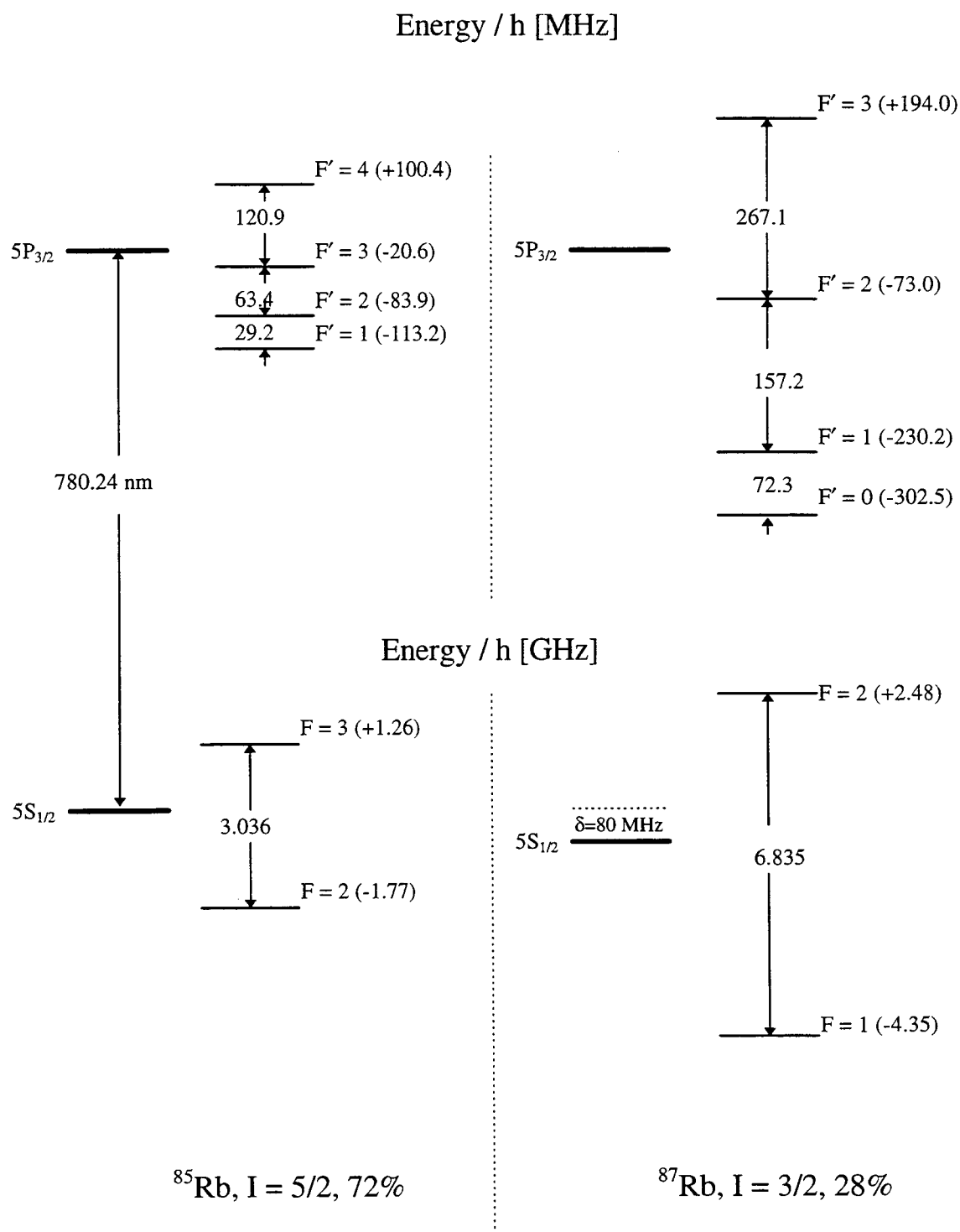

Figure 2.2 Energy level diagram for the ground and $5P_{3/2}$ excited state of ^{85}Rb and ^{87}Rb.

σ^+ [σ^-] light has a positive [negative] projection of angular momentum along the axis of quantization. Linearly polarized light is parallel to the quantization axis.

2.3 Absorption and Emission Spectra

Radiation emitted during a transition is not strictly monochromatic; spectral lines have observable width. Since the upper state of the transition has a finite radiative lifetime, the energy of the state is not infinitely sharp. As a result, the emitted radiation is distributed about the transition frequency. The normalized emission linewidth profile is a Lorentzian, given by

$$L(\omega) = \frac{\Gamma}{2\pi\left[\left(\omega - \omega_0\right)^2 + \frac{\Gamma^2}{4}\right]}. \qquad (2.4)$$

The full width at half maximum (FWHM) intensity Γ is defined to be the natural linewidth of the transition, where $\Gamma = 1 / \tau$. The radiative lifetime τ of the $5P_{3/2}$ state of rubidium is 26.5 ns. The natural linewidth, expressed as an angular frequency, is 2π x 6 MHz.

Additional broadening of spectral lines occurs due to atomic motion. The two types of broadening related to the atomic motion are designated collision broadening and Doppler broadening. Collision broadening results from dephasing collisions between atoms. A collision broadened spectral line exhibits a Lorentzian shape, with a width $\Gamma + 2/\tau_c$. Since the lifetime between collisions τ_c depends on the temperature and pressure of the sample of atoms this is alternatively referred to as pressure broadening. In a room temperature rubidium vapor the effect of collision broadening is insignificant since $2/\tau_c$ is much smaller than the natural linewidth of the transition.

Doppler broadening of spectral lines occurs due to the spread in atomic velocities of atoms in a sample. The profile of a spectral line dominated by Doppler broadening is Gaussian, expressed as

$$G(\omega) = \frac{2}{\sqrt{\pi}\Delta\omega_{Doppler}} e^{\left(-4\frac{(\omega-\omega_0)^2}{\Delta\omega_{Doppler}^2}\right)}. \quad (2.5)$$

In a room temperature rubidium vapor and a wavelength λ= 780.24 nm, the Doppler-broadened linewidth,

$$\Delta\omega_{Doppler} = \frac{2\omega_0}{c}\sqrt{\frac{2kT}{M}\ln 2}, \quad (2.6)$$

is ~ 2π x 510 MHz.

Experimentally measured absorption spectra, taken using a 5 cm long, glass, room temperature vapor cell, are shown in Figure 2.3. The two outside peaks originate from the ^{87}Rb transition, the two inner peaks from the ^{85}Rb transition. Two distinct peaks are evident for each isotope due to the large hyperfine splitting of the ground state. Hyperfine splitting of the upper states is sufficiently small that the individual peaks are not distinguishable. The relative height of the peaks is dictated by the difference in abundance of the two isotopes and the difference in transition probabilities of the distinct hyperfine transitions. The small dips evident in the absorption spectra result from saturation effects and are discussed in detail in section 5.3.3.1. For comparison, the calculated Doppler-broadened absorption spectra is illustrated in Figure 2.4.

2.4 Zeeman Shifted Energy Levels

In the presence of an external magnetic field the spectral lines of an atom split into closely spaced sub-levels. This phenomenon was first observed in 1897 by P. Zeeman [Zeeman, 1897] who used a grating with a radius of 10 feet and 14,938 lines per

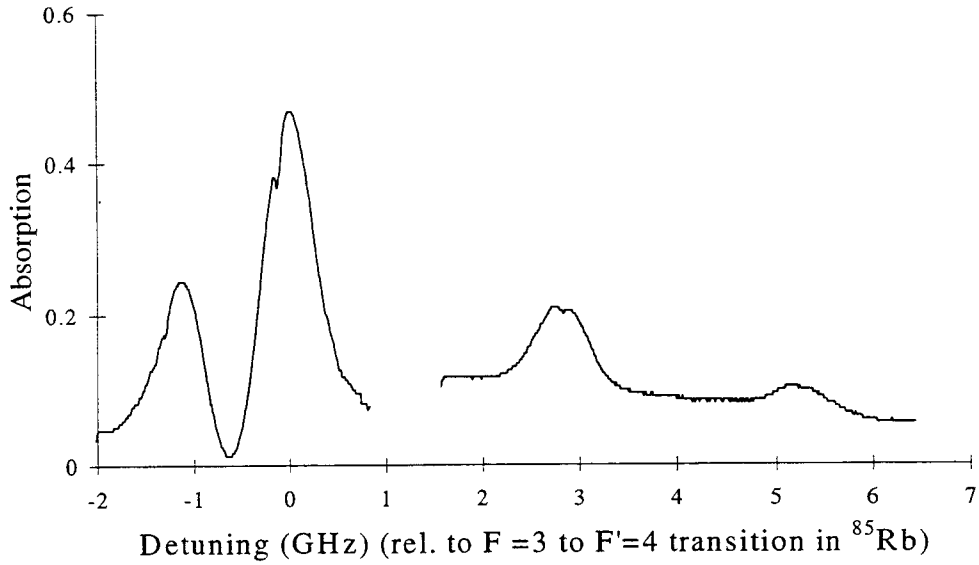

Figure 2.3 Measured Doppler-broadened absorption spectra for the $5S_{1/2}$ to $5P_{3/2}$ transition in rubidium. The peaks, from left to right, correspond to the transitions: ^{87}Rb F = 2 → F′ = 1, 2, 3; ^{85}Rb F = 3 → F′ = 2, 3, 4; ^{85}Rb F = 2 → F′ = 1, 2, 3; ^{87}Rb F = 1 → F′ = 0, 1, 2.

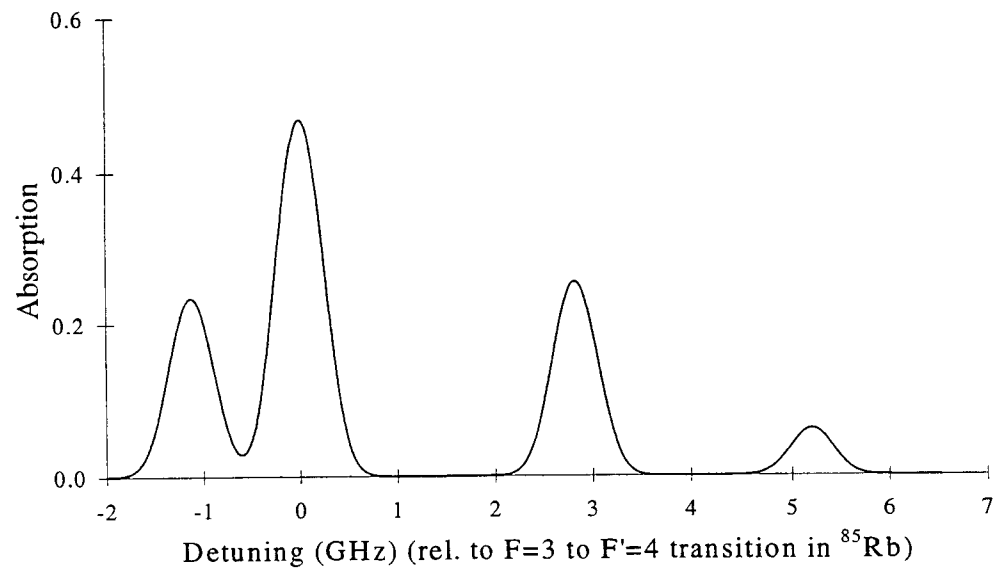

Figure 2.4 Calculated Doppler-broadened absorption spectra for the $5S_{1/2}$ to $5P_{3/2}$ cycling transitions in rubidium. The peaks, from left to right, correspond to the transitions: ^{87}Rb F = 2 → F′ = 3; ^{85}Rb F = 3 → F′ = 4; ^{85}Rb F = 2 → F′ = 1; ^{87}Rb F = 1 → F′ = 0.

inch to analyze the two D-lines of sodium. He observed broadening of the spectral lines in the presence of an applied magnetic field.

The Zeeman effect arises from the interaction between the atomic magnetic moments and the external magnetic field. Using conventional notation, the orbital and spin magnetic moments of an electron are given by

$$\vec{\mu}_l = -g_L\left(\frac{e}{2m_e}\right)\mathbf{l} = -\frac{1}{\hbar}g_L\mu_B\mathbf{l}, \tag{2.7}$$

$$\vec{\mu}_s = -g_s\left(\frac{e}{2m_e}\right)\mathbf{s} = -\frac{1}{\hbar}g_s\mu_B\mathbf{s}, \tag{2.8}$$

where **l**, **s**, g_L, and g_S are the orbital and spin angular momentum operators and the orbital and spin gyromagnetic ratios respectively. The orbital gyromagnetic ratio is equal to one. The spin gyromagnetic ratio is equal to two (2.00232). The Bohr magneton μ_B is $(h)(1.4\ \text{MHz/G}) = 9.27408 \times 10^{-28}$ J/G.

In a many-electron atom the magnetic moments of the individual electrons combine to produce a total contribution of

$$\vec{\mu}_L + \vec{\mu}_S = -\frac{1}{\hbar}g_L\mu_B\sum_i \mathbf{l}_i - \frac{1}{\hbar}g_s\mu_B\sum_i \mathbf{s}_i = -\frac{1}{\hbar}\mu_B\left(g_L\mathbf{L} + g_S\mathbf{S}\right). \tag{2.9}$$

The magnetic dipole moment resulting from the nuclear spin is

$$\vec{\mu}_I = g_I\left(\frac{e}{2m_p}\right)\mathbf{I} = \frac{1}{\hbar}g_I\mu_n\mathbf{I}, \tag{2.10}$$

where g_I is the nuclear g factor equal to 0.54108 for ^{85}Rb and 1.8337 for ^{87}Rb. The nuclear magneton $\mu_n = e\hbar/2m_P$ is 5.0508×10^{-31} J/G, and **I** is the nuclear spin angular momentum. Combining these terms yields a total atomic magnetic moment

$$\vec{\mu} = \frac{1}{\hbar}\left(-g_L\mu_B\mathbf{L} - g_S\mu_B\mathbf{S} + g_I\mu_n\mathbf{I}\right). \tag{2.11}$$

Interaction of the atomic magnetic moments with the external field **B** produces an additional energy term in the system Hamiltonian. It is expressed as

$$H_{zeeman} = -\vec{\mu} \cdot \mathbf{B}. \tag{2.12}$$

2.4.1 Zeeman Splitting in the Low-Field Limit

The Zeeman shift in the rubidium energy levels is determined by comparing the Zeeman shift term (2.12) to the hyperfine structure Hamiltonian (2.1). For a sufficiently weak magnetic field, the Zeeman splitting is small compared to the hyperfine structure splitting of the energy level. In this limit, the Zeeman energy shift can be treated as a perturbation to the hyperfine energy levels. The hyperfine structure Hamiltonian is diagonal in the $|I\,J\,F\,M_F\rangle$ basis. The Zeeman induced energy shift, calculated from perturbation theory, is

$$E_{\text{Zeeman low field}} = \langle IJFM_F | H_{zeeman} | IJFM_F \rangle. \tag{2.13}$$

By defining the magnetic field direction to be along the z-axis and expressing μ_n in terms of μ_B, the energy shift simplifies to

$$E_{\text{Zeeman low field}} = \frac{\mu_B B}{\hbar} \langle IJFM_F | (g_L L_z + g_S S_z) - g_I \frac{m_e}{m_p} I_z | IJFM_F \rangle. \tag{2.14}$$

From the Wigner-Eckart theorem [Cohen-Tannoudji, 1977, page 1050], the vector operators can be written as

$$L_Z = \frac{\mathbf{L} \cdot \mathbf{J}}{J(J+1)\hbar^2} J_Z \quad \text{and} \quad \mathbf{L} \cdot \mathbf{J} = \frac{1}{2}\left(J^2 + L^2 - S^2\right). \tag{2.15}$$

Computing the matrix elements, the energy shift reduces to

$$E_{\text{Zeeman low field}} = \mu_B B g_F M_F, \tag{2.16}$$

where g_F is given by

$$g_F = g_J\left(\frac{F(F+1)+J(J+1)-I(I+1)}{2F(F+1)}\right)-g_I\frac{m_e}{m_p}\left(\frac{F(F+1)+I(I+1)-J(J+1)}{2F(F+1)}\right), \quad (2.17)$$

and

$$g_J = g_L\left(\frac{J(J+1)+L(L+1)-S(S+1)}{2J(J+1)}\right)+g_S\left(\frac{J(J+1)+S(S+1)-L(L+1)}{2J(J+1)}\right). \quad (2.18)$$

The ratio of the masses m_e/m_p is 1/1836. For the $5P_{3/2}$, F′ = 4 state of ^{85}Rb, g_J is 4/3 and g_F is 1/2. For the $5S_{1/2}$, F = 3 state, g_J is 2 and g_F is 1/3. For the $5P_{3/2}$, F′ = 3 state of ^{87}Rb, g_J is 4/3 and g_F is 2/3. For the $5S_{1/2}$, F = 2 state, g_J is 2 and g_F is 1/2.

2.4.2 Zeeman Splitting in the High-Field Limit

In a strong magnetic field, where the contribution from the Zeeman shift term is large compared to the hyperfine splitting of the atom, we can first solve the Schrödinger equation for the Zeeman Hamiltonian and subsequently treat the hyperfine structure terms as a perturbation. The Zeeman Hamiltonian H_{Zeeman} is diagonal in the basis $|I\,J\,M_I\,M_J\rangle$ basis. The contribution from the Zeeman terms is then

$$E_{\text{Zeeman high field}} = \frac{\mu_B B}{\hbar}\left\langle IJM_I M_J\left|\left(g_L L_z + g_S S_z\right) - g_I\frac{m_e}{m_p}I_z\right|IJM_I M_J\right\rangle$$

$$= \mu_B B\left(g_J M_J - g_I\frac{m_e}{m_p}M_I\right). \quad (2.19)$$

The energy shift due to the hyperfine structure term, calculated from perturbation theory, is given by [Corney, 1977, page 671]

$$\Delta E_{\text{hyperfine}} = A_J M_J M_I + \frac{B_J}{4I(2I-1)J(2J-1)}\left(3M_J{}^2 - J(J+1)\right)\left(3M_I{}^2 - I(I+1)\right). \quad (2.20)$$

2.4.3 Zeeman Splitting for General Fields

Since the magnitude of the hyperfine structure splitting is distinct for different energy levels, the appropriateness of the low or high-field limit depends upon the energy level of interest. For example, for the $5S_{1/2}$ level of ^{85}Rb, the hyperfine-structure splitting is 3.0357 GHz. As such, the low-field limit corresponds to magnetic field strengths of much less than 1000 G. For the $5P_{3/2}$ level of ^{85}Rb, the hyperfine structure splitting is in the 30 to 120 MHz range. The low-field limit in this case is in the range of a few Gauss. For our experiment, the magnetic field ranges from approximately 30 to 600 Gauss depending on the configuration of the system. Thus, both the $5P_{3/2}$ excited state and $5S_{1/2}$ ground state are in the intermediate field range at some point.

At intermediate field strengths, the Hamiltonian is not diagonal in either the $|I\,J\,F\,M_F\rangle$ basis or the $|I\,J\,M_I\,M_J\rangle$ basis. In this region, the hyperfine structure Hamiltonian and Zeeman shift Hamiltonian must be diagonalized simultaneously to determine the energy levels. The general result will be consistent at the extremes with the results calculated by perturbation theory for the low and high field limits. A program was written in *Maple* to generate and diagonalize the complete hyperfine structure Hamiltonian. The Zeeman shifted energy levels for the atomic sub-levels of interest are shown in Figures 2.5 and 2.6. The appropriate quantum numbers for the low field limit (F, M_F) and high field limit (M_I, M_J) are indicated for reference. A copy of the *Maple* code is found in the appendix.

In our experiment, a laser is used to optically excite transitions between the $5S_{1/2}$ ground state and the $5P_{3/2}$ excited state. From the figures we observe that the Zeeman

energy shift is linear for the extreme angular momentum states (e.g. the $|F' = 4, M_F' = \pm 4\rangle$ states in ^{85}Rb). One would intuitively expect this result since the nuclear magnetic moment and the electron's orbital angular momentum and spin are all aligned for the extreme angular momentum states. Thus, for transitions between extreme angular momentum states, such as the $|F = 3, M_F = \pm 3\rangle \rightarrow |F' = 4, M_F' = \pm 4\rangle$ transition in ^{85}Rb and the $|F = 2, M_F = \pm 2\rangle \rightarrow |F' = 3, M_F' = \pm 3\rangle$ transition in ^{87}Rb, the shift in the transition frequency is proportional to the strength of the magnetic field. Expressed as an energy, the result is given by

$$\Delta E_{Zeeman} = \pm \mu_B B , \tag{2.21}$$

where the + [-] refers to σ^+ [σ^-] transitions respectively. For transitions between the other sub-levels the energy shift is a more complicated function of the magnetic field strength.

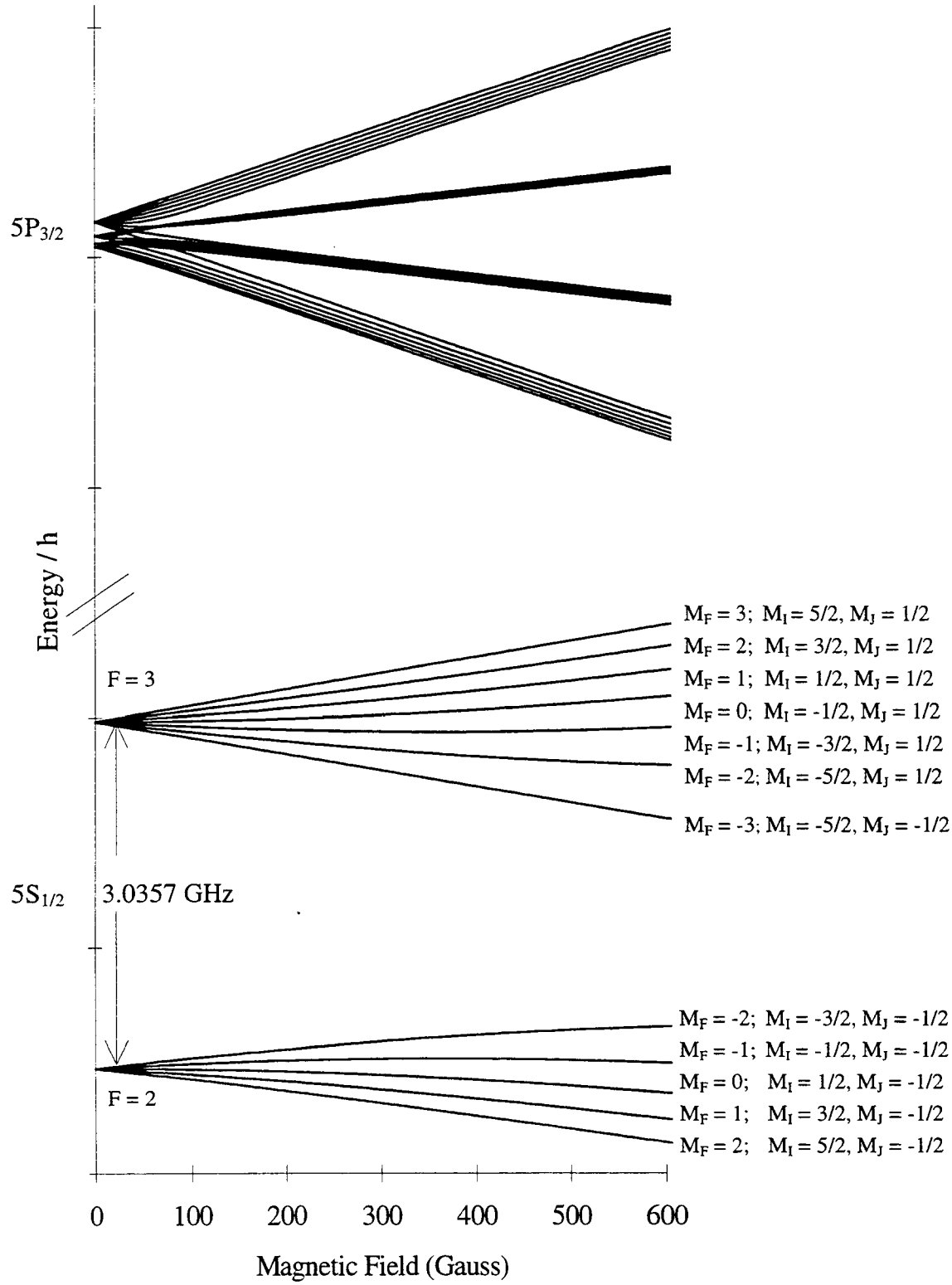

Figure 2.5a Zeeman shifted energy levels of the $5S_{1/2}$ and $5P_{3/2}$ states of ^{85}Rb.

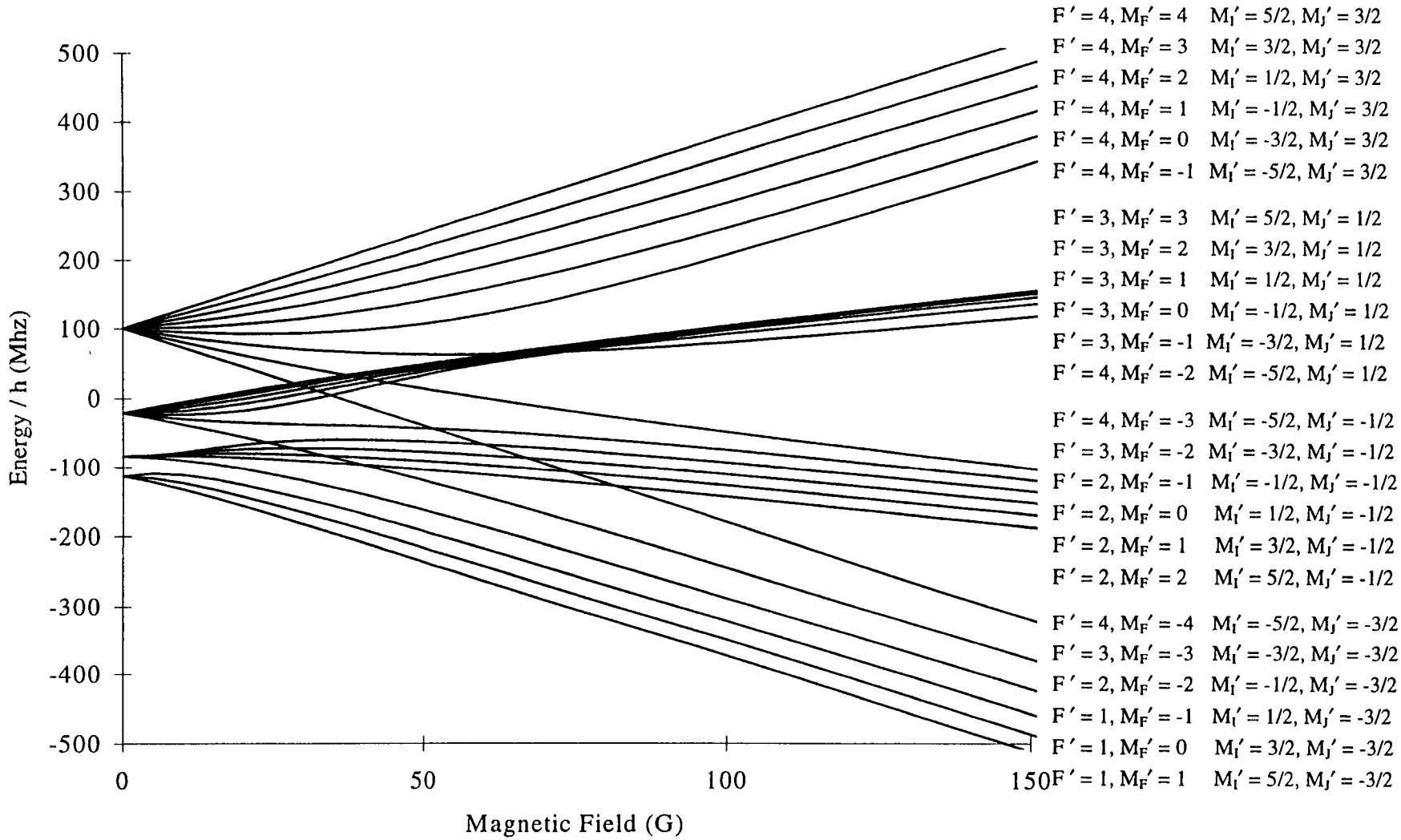

Figure 2.5b Zeeman shifted energy levels of the $5P_{3/2}$ state of ^{85}Rb (expanded view).

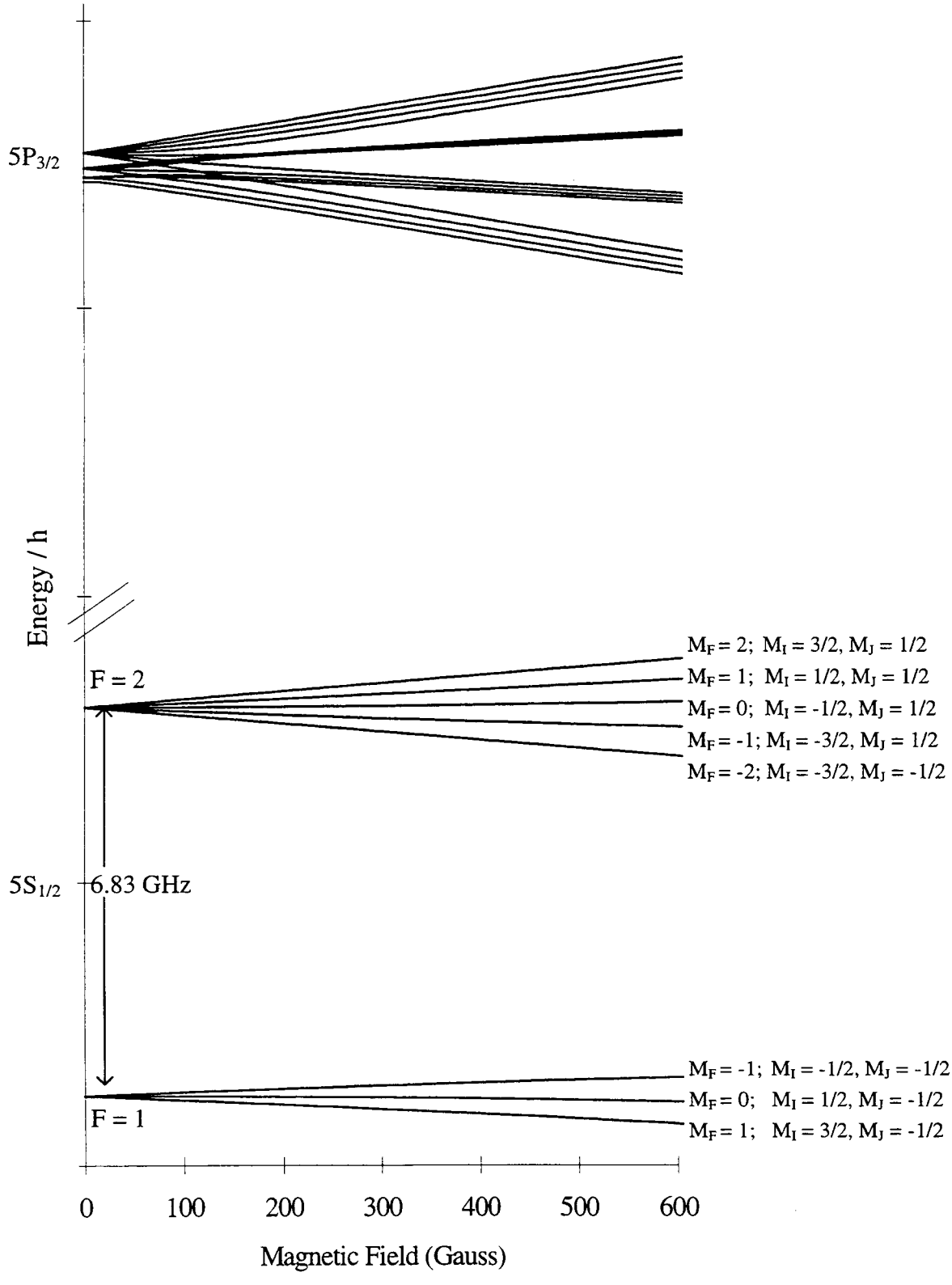

Figure 2.6a Zeeman shifted energy levels of the $5S_{1/2}$ and $5P_{3/2}$ states of ^{87}Rb.

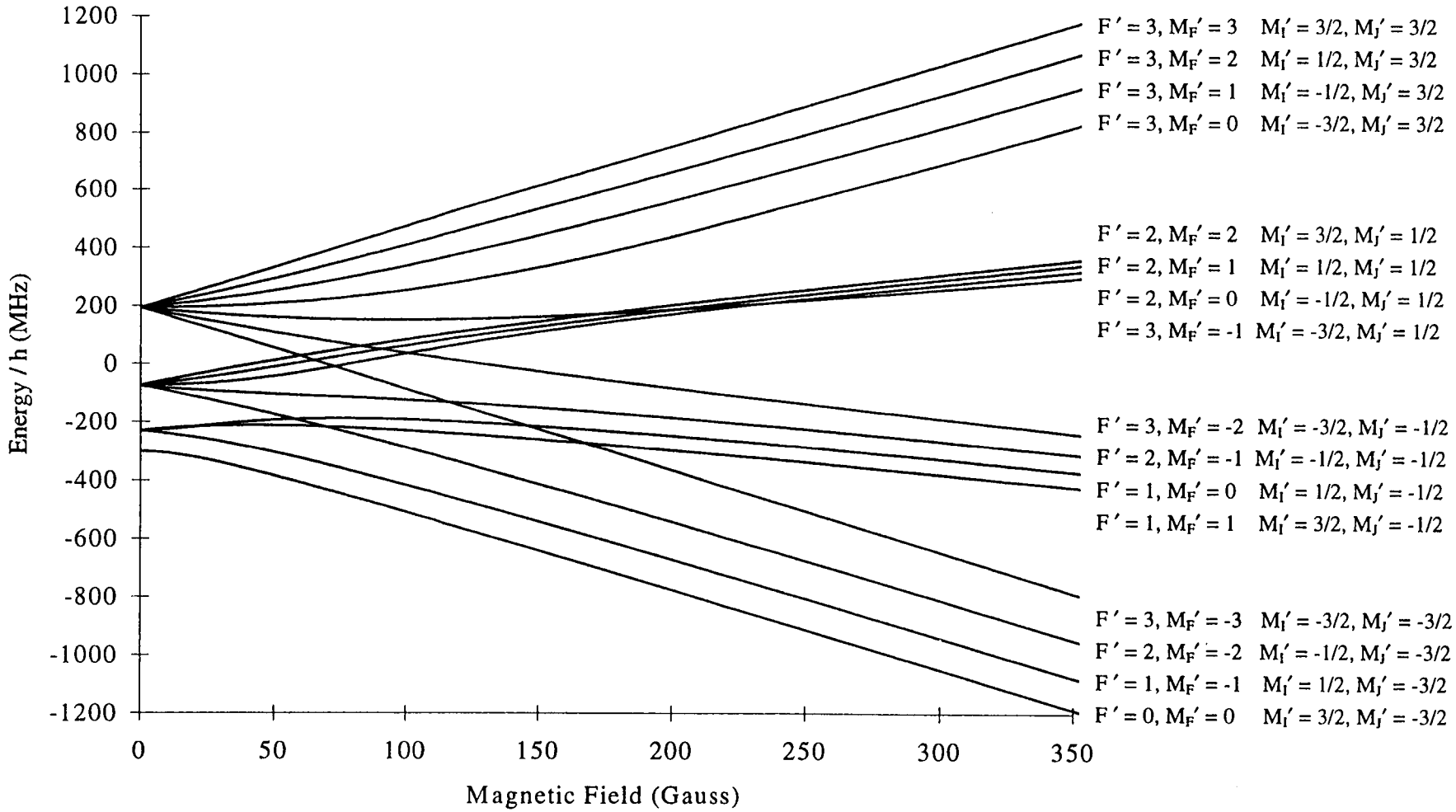

Figure 2.6b Zeeman shifted energy levels of the $5P_{3/2}$ state of ^{87}Rb (expanded view).

Chapter 3: Laser Manipulation of Atoms

3.1 Laser Cooling: Theory

3.1.1 Momentum Transfer via Absorption and Spontaneous Emission of Photons

It has long been established that radiation pressure is exerted on objects that reflect or scatter light. In 1933, Frisch [Frisch, 1933] used resonant light from a sodium-vapor lamp to deflect a beam of sodium atoms. In 1975, Hänsch and Schawlow [Hänsch, 1975] proposed using radiation pressure to cool neutral atoms. The novelty of their work was in illustrating that radiation pressure can be employed to cool a gaseous atomic sample. Slowing of atoms in the sample is accomplished by momentum transfer via absorption-spontaneous emission cycles. Since the force is velocity dependent, the spread in velocities of the slowed atomic sample can be reduced, thereby cooling the sample.

Consider the absorption-emission cycle depicted in Figure 3.1. Frame A illustrates an atom moving to the right with velocity v. It encounters a laser beam with frequency ω_L, tuned below the transition frequency ω_0 of the atom. Due to the velocity of the atom, the laser frequency, as seen in the rest frame of the atom (frame B), is Doppler shifted by an amount

$$\omega_L' = \omega_L \sqrt{\frac{1+v/c}{1-v/c}} = \omega_L - \mathbf{k}\cdot\mathbf{v} + \ldots, \tag{3.1}$$

where k is $2\pi/\lambda$. For a counter-propagating laser and an atom moving at non-relativistic speed, the Doppler shift reduces to $+kv$, thus shifting the laser frequency closer to resonance. In frame C, the resonant photon is absorbed, changing the momentum of the atom by an amount $\hbar k$. In frame D, the photon is re-radiated providing a momentum

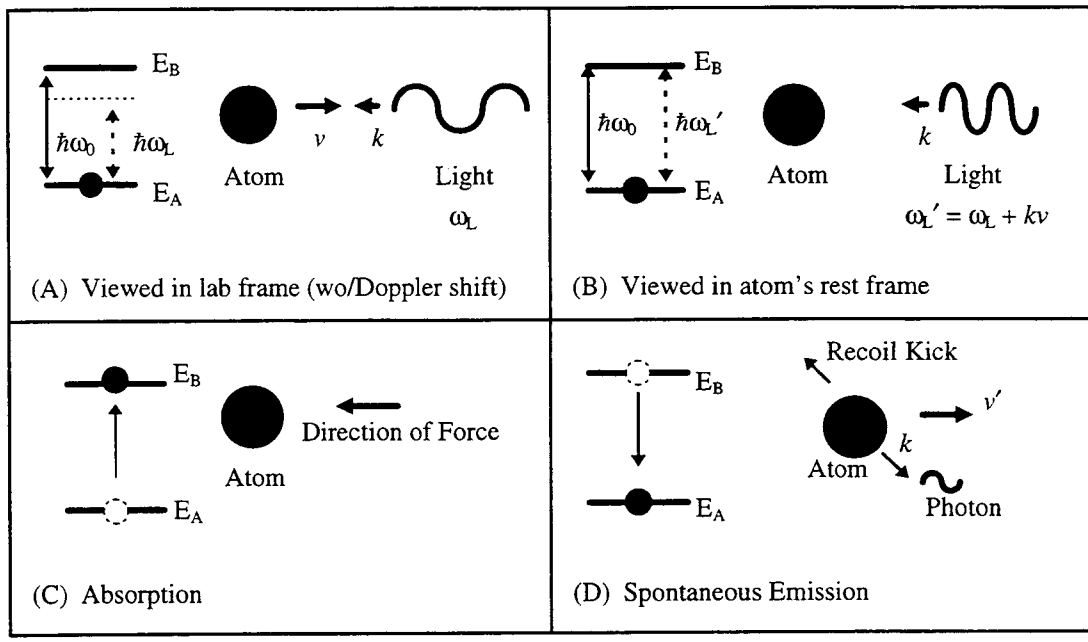

Figure 3.1 Momentum transfer via photon absorption-emission.

recoil kick to the atom, opposite the direction of the re-radiated photon. For N absorption-emission cycles, the change in velocity of the atom in the direction of the laser is $\hbar kN/M$. Because the spontaneously emitted photons are emitted in a symmetric, dipole radiation pattern, their average contribution to the momentum of the atom is zero.

To quantify the rate at which an atom is slowed, one must consider the photon scattering rate, the frequency and intensity of the laser light, and the spontaneous emission rate of the atom. For an atom at rest, the photon scattering rate R is

$$R = \frac{\Gamma}{2}\frac{p}{p+1}, \tag{3.2}$$

where Γ is the natural linewidth of the atomic transition and p is the saturation parameter given by

$$p = \frac{I}{I_{SAT}} \frac{\left(\frac{\Gamma}{2}\right)^2}{\left(\frac{\Gamma}{2}\right)^2 + \Delta^2}. \tag{3.3}$$

The detuning of the laser from resonance is $\Delta = \omega_L - \omega_0$. The laser intensity I and saturation intensity I_{SAT}, are related to the Rabi frequency Ω by the relationship

$$\frac{I}{I_{SAT}} = \frac{2\Omega^2}{\Gamma^2}. \tag{3.4}$$

The saturation intensity I_{SAT} is given by

$$I_{SAT} = \frac{\hbar\omega_0}{2\tau\sigma} = \frac{\hbar\omega_0}{2\tau(3\lambda^2/2\pi)} = 1.6 \text{ mW/cm}^2, \tag{3.5}$$

where σ is the absorption cross section.

For an atom moving with velocity $\mathbf{v}$, the laser detuning term must be replaced with $\Delta \rightarrow \Delta - \mathbf{k} \cdot \mathbf{v}$. Thus, the force on the moving atom, given by the change in momentum per absorbed photon multiplied by the scattering rate, is

$$\mathbf{F} = Ma = \hbar\mathbf{k}R = \hbar\mathbf{k}\left[\frac{\Gamma}{2} \frac{\frac{I}{I_{SAT}}}{\frac{4}{\Gamma^2}(\Delta - \mathbf{k}\cdot\mathbf{v})^2 + 1 + \frac{I}{I_{SAT}}}\right]. \tag{3.6}$$

For rubidium, the velocity change per absorbed photon is 0.6 cm/s and the atomic mass M is $1.42\text{x}10^{-25}$ kg, resulting in a maximum deceleration of $\hbar k\Gamma/2M = 1.1\text{x}10^7$ cm/s^2 for a fully saturated transition.

Clearly, to achieve an appreciable change in atomic velocity, a large number of photons must be scattered (e.g. 40,000 photons for a change of 240 m/s). A difficulty associated with achieving a large change in velocity is that the Doppler shift of the atom

changes as the velocity changes. Absorption of 1000 photons yields a change in velocity of 6 m/s, corresponding to a change of ~8 MHz in the Doppler shift. For a laser that is initially resonant, this change in Doppler shift reduces the scattering rate for a saturated transition by a factor of about 4. To achieve large changes in velocity, steps must be taken to maintain resonance between the slowing atom and the light source. The techniques that have emerged to address this issue are discussed in section 3.1.2.

The second difficulty associated with achieving a large change in velocity is that the atom must undergo numerous absorption-emission cycles without being optically pumped from the cycling transition. Alkali metals provide a favorable source for such experiments as they can be made to approximate a two-level system. In addition, the short radiative lifetime allows for rapid cycling. The method used to generate an approximate two-level cycling transition depends upon the scheme used for Doppler shift compensation. The techniques used are discussed in section 3.1.3.

3.1.2 Laser Cooling: Methods

A variety of experimental techniques have been demonstrated for slowing and cooling atoms. The two primary methods are chirped cooling and Zeeman-tuned cooling, first demonstrated by Ertmer *et al.* [Ertmer, 1985] and Phillips *et al.* [Phillips, 1982] respectively. In both methods, slowing of the atoms is accomplished by radiation pressure from resonant, counter-propagating laser light. The techniques differ in the method used to compensate for the changing Doppler shift of the decelerating atom. In chirped cooling, a counter-propagating laser beam is frequency tuned (i.e. 'chirped') to stay in resonance with the slowing atoms. Zeeman-tuned cooling uses the Zeeman shift provided by a spatially varying magnetic field to keep the slowing atom in resonance with a fixed frequency counter-propagating laser beam. Cooling of the atomic sample results because the velocity distribution of the slowed sample is narrowed, therefore reducing the temperature.

The theoretical basis and historical progress of chirped and Zeeman-tuned cooling are reviewed below. Readers interested in other methods for slowing and cooling atoms are referred to the following articles: saturation broadening with a high power laser [Balykin, 1984], stimulated emission [Aspect, 1986], intense optical standing-wave [Prentiss, 1989], broadband light, [Zhu, 1991], varying the angle of isotropic laser light [Ketterle, 1992], and the Stark effect [Gaggl, 1994] and [Yeh, 1995].

3.1.2.1 Chirped Cooling

In 1976, Letokhov *et al.* [Letokhov, 1976] proposed tuning the frequency of the laser to compensate for the changing Doppler shift of the slowing atom. The resonance condition is

$$\omega_0 = \omega_L + kv, \tag{3.7}$$

where the laser frequency ω_L is continuously increased as the Doppler contribution decreases. The velocity range over which atoms are slowed is limited by the range that the laser frequency is swept and the maximum rate the atom can be decelerated due its finite lifetime. The change in atomic velocity is related to the change in laser frequency by the relationship

$$\omega_{Lf} - \omega_{Li} = k(v_i - v_f). \tag{3.8}$$

The maximum rate at which the atom can be decelerated is given by

$$\left.\frac{\partial \omega_L}{\partial t}\right|_{MAX} = k a_{MAX} = k\left(\frac{\hbar k}{M}\frac{\Gamma}{2}\right). \tag{3.9}$$

For the D_2 transition in rubidium, the maximum chirp rate for a fully saturated transition is 142 MHz/ms (frequency expressed as $\omega/2\pi$). If the chirp rate of the cooling laser is

greater than the maximum value, the atom will not be decelerated sufficiently to remain resonant with the laser.

Chirped cooling was first implemented by a group of collaborators from the Joint Institute for Astrophysics, University of Colorado and the National Institute of Standards and Technology. In 1984, Blatt *et al.*[Blatt, 1984] published a detailed discussion of the technical requirements and computer-simulation results for chirped cooling. Thereafter, Ertmer *et al.* [Ertmer, 1985] slowed an atomic beam of sodium atoms using a frequency chirped counter-propagating laser beam. By using an electro-optic modulator to sweep the frequency of the laser light 1 GHz, they successfully achieved a velocity decrease of ~630 m/s in a time of 2 ms. The resulting cooled sample had a density of 10^6 atoms/cm^3 and a temperature below 50 mK. Subsequently Watts and Wieman [Watts, 1986] demonstrated a more simple and economical means of chirped cooling using a diode laser source. The diode laser frequency was chirped at a rate of 54 MHz/msec by applying a 20 msec ramp of amplitude 0.35 mA to the laser injection current. The frequency sweep produced a cooled beam of cesium atoms with a temperature of 1K. The efficiency of the cooling was about 10%; a beam of 10^{10} atoms/sec was obtained from a thermal beam containing ~ 10^{11} atoms/sec.

The chirped cooling technique has been used effectively in our laboratory to slow atoms with initial velocities of ~350 m/s or less to a final velocity of ~20 m/s. The diode laser used for cooling is frequency tuned at a rate of 60 MHz/ms by applying a voltage to a piezoelectric transducer (PZT) in the flexure of the extended cavity laser assembly in order to modify the cavity length. The laser frequency is tuned in a saw tooth fashion to produce a pulsed beam of slow atoms.

The total number of atoms available is duty cycle limited by the chirp method. To produce a continuous beam of cooled atoms for trapping, the technique of Zeeman-tuned cooling was explored.

3.1.2.2 Zeeman-Tuned Cooling

In Zeeman-tuned cooling, the laser frequency is kept constant and the frequency of the transition is changed by applying an external magnetic field to Zeeman shift the atomic sub-levels. Recall from section 2.4.3, the Zeeman shift in the transition frequency between extreme angular momentum states is a linear function of applied magnetic field. (see equation 2.21). The extreme angular momentum states for the $5S_{1/2}$ and $5P_{3/2}$ levels of ^{85}Rb, taken from Figure 2.5, are illustrated in Figure 3.2. Similar transitions with linear Zeeman shifts exist for ^{87}Rb, as well as for the other alkali atoms. The polarization of light used to excite the particular transition is indicated. To distinguish between the two possible transitions, slowing utilizing σ^+ [σ^-] polarized light is referred to as σ^+ [σ^-] Zeeman-tuned slowing.

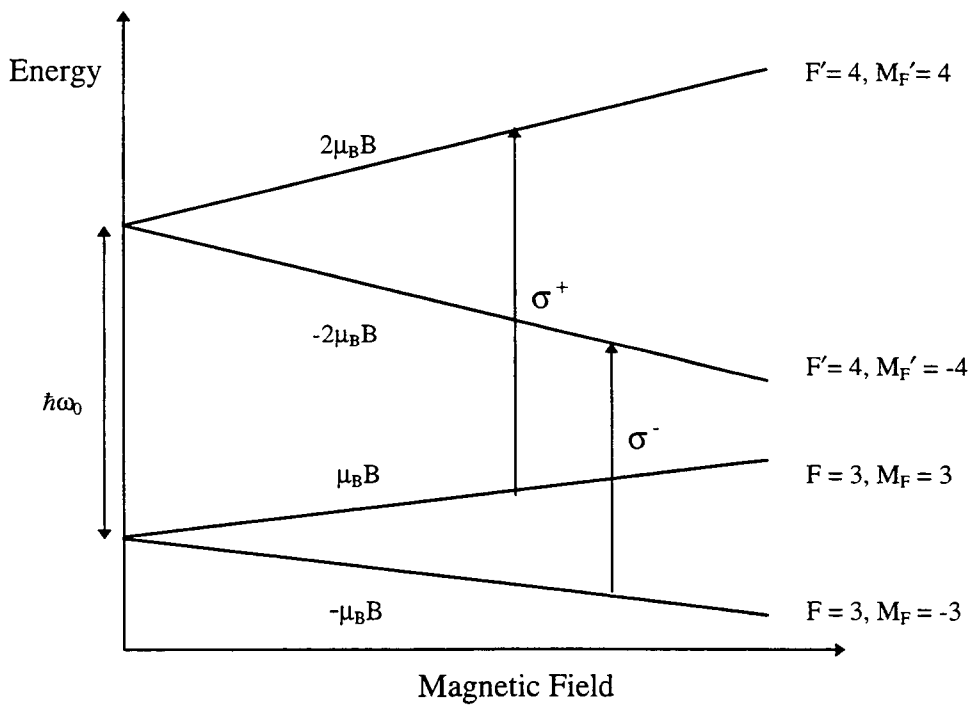

Figure 3.2 Zeeman shift of ^{85}Rb energy levels relevant to Zeeman-tuned cooling.

The resonance condition for Zeeman-tuned slowing is

$$\omega_0 \pm \frac{\mu_B}{\hbar} B = \omega_L + kv, \tag{3.10}$$

where the plus [minus] sign corresponds to σ^+ [σ^-] cooling respectively. Rewriting this expression in terms of the laser detuning $\Delta = \omega_L - \omega_0$ and solving for B, we find the required magnetic field profile for Zeeman-tuned slowing is

$$B = \pm \frac{\hbar}{\mu_B}(\Delta + kv). \tag{3.11}$$

For an atom decelerated at a constant rate, the velocity v as a function of position z is given by

$$v^2 = v_0^2 - 2az, \tag{3.12}$$

where v_o is the initial velocity and a is the deceleration.

Sample magnetic field profiles for the two orientations of Zeeman-tuned cooling are illustrated in Figure 3.3 (For this example $v = 0$ at $z = 60$ cm). For convention, we will define B to be positive and use the standard definitions for σ^- and σ^+ polarization (see section 2.2). (Defining B to be negative merely reverses the definition of σ^- and σ^+ polarization, leading to an identical expression for equation 3.11.) For both σ^- and σ^+ cooling, the field must decrease the atomic transition frequency to compensate for the reduction in Doppler shift as the atom slows. Thus, for σ^+ cooling, where the transition frequency increases with increasing magnetic field strength, the magnetic field must be decreasing in strength. The cooling laser frequency must be greater than or equal to the zero-field atomic resonance (i.e. zero or positive Δ) to achieve resonance. For σ^- cooling the situation is reversed; the transition frequency decreases with increasing field strength, so the laser frequency is below the zero-field atomic resonance (i.e. negative Δ) and the magnetic field increases in magnitude as the atom slows.

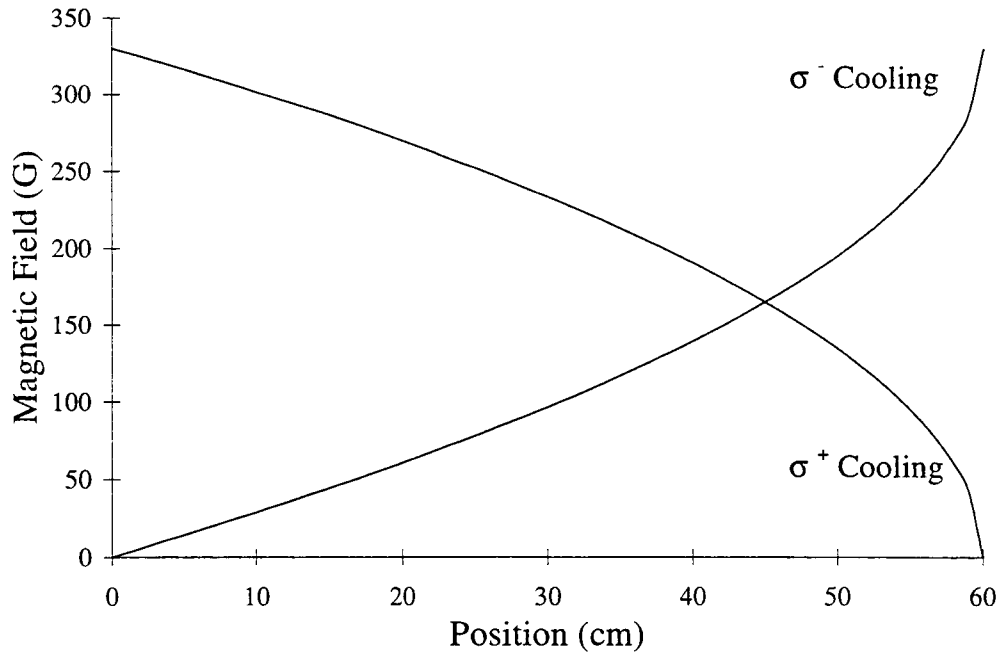

Figure 3.3 Theoretical magnetic field profile for σ^- and σ^+ Zeeman-tuned cooling. For this example, $\hbar k v_0 / \mu_B = 330$ G, $v = 0$ at $z = 60$ cm, and $\hbar \Delta / \mu_B = -330$ [0] for σ^- [σ^+] cooling.

Recall, the finite lifetime of the excited state imposes a fundamental limit on the rate at which an atom can be decelerated. For chirped cooling, this restriction is manifest by imposing a maximum rate on the chirped frequency of the slowing laser (see equation 3.9). In Zeeman-tuned slowing, a limit is imposed on the allowable magnetic field gradient. The maximum deceleration is related to the maximum field gradient by the relationship

$$a = \frac{\partial v}{\partial t} = \frac{\partial v}{\partial z}\frac{\partial z}{\partial t} = \frac{\partial v}{\partial z} v, \tag{3.13}$$

where, from equation 3.11 we have

$$v = -\frac{\mu_B B}{\hbar k} - \frac{\Delta}{k} \qquad \text{and} \qquad \frac{\partial v}{\partial z} = -\frac{\mu_B}{\hbar k}\frac{dB}{dz}. \tag{3.14}$$

Writing dB/dz in terms of the deceleration a, we find the magnetic field gradient is

$$\frac{dB}{dz} = -\frac{\hbar ka}{v\mu_B} = \frac{\hbar ka}{\left(\frac{\mu_B B}{\hbar k} + \frac{\Delta}{k}\right)\mu_B}. \tag{3.15}$$

Thus, since the maximum deceleration a_{MAX} is $\hbar k\Gamma/2M$, the maximum field gradient is given by

$$\left.\frac{dB}{dz}\right|_{MAX} = \frac{\hbar^2 k^3}{\mu_B M\left(\frac{\mu_B}{\hbar}B + \Delta\right)}\left(\frac{\Gamma}{2}\right). \tag{3.16}$$

If the magnetic field gradient is such that the required deceleration is larger than the maximum allowable value, the atom will not be decelerated sufficiently to follow the field. When this occurs, the atom will go out of resonance with the laser, and subsequently stop being decelerated.

Zeeman-tuned slowing was first demonstrated by Phillips *et al.* [Phillips, 1982]. They successfully slowed sodium atoms ($3S_{1/2}$ (F = 2) $\rightarrow$ $3P_{3/2}$ (F′ = 3) transition, λ = 589 nm) from 1180 m/s to ~700 m/s using σ^+ polarized light and the Zeeman shift from a decreasing strength magnetic field. Later, they successfully used this method to stop a thermal sodium beam [Prodan, 1985]. σ^+ Zeeman-tuned slowing was subsequently used to slow calcium atoms [Beverini, 1989b] and magnesium atoms [Beverini, 1989a].

Large changes in velocity were achieved using σ^+ Zeeman-tuned slowing. However, it was observed that atoms slowed to low velocities (less than ~100 m/s), never went out of resonance with the field, and were thus brought to rest or turned around within the solenoid. For applications requiring a slow atomic beam, extracting the slow beam from the solenoid posed a technical challenge. A few techniques were demonstrated to overcome this problem. Phillips *et al.* [Phillips, 1982] turned off the slowing laser and allowed the atoms to drift out of the solenoid. This solution is not favorable as it yields a pulse of atoms rather than a continuous beam. Bagnato *et al.* [Bagnato, 1991] utilized a special magnetic field design that allowed the atoms to be

optically pumped out of the cycling transition near the exit end of the solenoid. The atoms, no longer resonant with the cooling laser, drifted out of the solenoid. This technique yields a continuous beam of slow atoms. However, constraints on the magnetic field requirements are more cumbersome.

Barrett *et al.* [Barrett, 1991] overcame the difficulty associated with σ^+ Zeeman-tuned slowing more simply by demonstrating a modified version of the Zeeman slower. In contrast with earlier work, they employed σ^- polarized light and a magnetic field of increasing strength. This modification resulted in a significantly more accessible beam of slow atoms. Their beam of ^{87}Rb atoms ($5^2S_{1/2}$ (F = 2) $\rightarrow$ $5^2P_{3/2}$ (F′ = 3) transition, I = 3/2, λ = 780 nm), slowed to 40 m/s, had an intensity of 2 x 10^{10} atoms/cm^{2}s. Subsequently, σ^- Zeeman-tuned slowing was demonstrated using sodium atoms [Joffe, 1993] and Xenon atoms [Walhout, 1993].

At first glance, it would seem that σ^+ and σ^- slowing are essentially equivalent processes. However, the ability to use σ^- slowing to generate an accessible low-velocity beam indicates there are some basic differences between the two configurations. The difference in behavior between σ^+ and σ^- cooling has been attributed to the difference in the magnetic field profiles (i.e. the σ^- field increases and the σ^+ decreases as a function of distance along the solenoid) [Barrett, 1991]. Specifically, it is stated that the decreasing nature of the σ^+ field causes atoms slowed to low velocity to remain resonant with the cooling laser and get turned around within the solenoid. And in contrast, the increasing field of σ^- cooling, with its rapid drop to zero at the end of the solenoid, allows the slowing to be abruptly stopped. While this assessment is essentially correct, our theoretical modeling of the cooling process has allowed us to gain additional insight into the quantitative differences between σ^+ and σ^- cooling. The results are presented and discussed in Chapter 4.

Zeeman-tuned slowing was implemented in our laboratory using σ^- light and an increasing strength magnetic field, utilizing the $5^2S_{1/2}$ (F = 3) $\rightarrow$ $5^2P_{3/2}$ (F′ = 4) transition in ^{85}Rb. While the solenoid was designed and optimized for σ^- cooling, an appropriate

decreasing strength magnetic field can easily be generated by reversing the field direction in one of the magnets. This alternate configuration was used to study σ^+ cooling.

3.1.3 Optical Pumping: Generating a Two-Level Cycling Transition

During the laser cooling process a large number of photons must be scattered to achieve an appreciable change in atomic velocity. The techniques of chirped cooling and Zeeman-tuned cooling provide a means for compensating for the changing Doppler shift. However, these techniques are only effective if the atomic transition can be cycled many times. Because rubidium is not a two-level atom, atoms can be optically pumped from the designated cycling transition into an undesired sub-level, thereby inhibiting the cooling process. The steps required to generate an approximate two-level cycling transition differ between chirped cooling and Zeeman-tuned cooling. The methods are described below.

3.1.3.1 Optical Pumping in Chirped Cooling

In chirped cooling of ^{85}Rb, the desired cycling transition is $5S_{1/2}$ (F = 3) $\rightarrow$ $5P_{3/2}$ (F′ = 4) (reference Figure 2.2). If this were a closed two-level cycling transition, it could be repeatedly cycled without interruption. However, a laser tuned on resonance has some probability of exciting the F = 3 $\rightarrow$ F′ = 3 transition 120.7 MHz away. This state may decay into the F = 2 ground state. The 3 GHz ground state separation ensures that such atoms are not resonant with the cooling laser and thus, without intervention, the atoms are eliminated from further participation in the cooling process.

To compensate for optical pumping into the F = 2 ground state, a second laser is used during chirped cooling. This laser, designated the re-pump laser, is tuned to the F = 2 $\rightarrow$ F′ = 3 transition to pump atoms lost from the cooling transition back into the

F = 3 ground state. Because the cooling laser is scanned in frequency during chirped cooling, the re-pump must be synchronously scanned in frequency in order to maintain resonance.

3.1.3.2 Optical Pumping in Zeeman-Tuned Slowing

The optical pumping situation during Zeeman-tuned slowing is distinct from that of chirped cooling. The presence of an externally applied magnetic field during Zeeman slowing eliminates the degeneracy of the Zeeman sub-levels, thus allowing for transitions between specific Zeeman sub-levels. Through proper selection of the laser polarization, a true two-level cycling transition can be achieved. For ^{85}Rb, the cycling transition for σ^- Zeeman tuned slowing is $|F = 3, M_F = -3\rangle \rightarrow |F' = 4, M_F' = -4\rangle$. For pure σ^- polarization, all other transitions are forbidden by electric dipole selection rules.

In practice, optical pumping remains an issue during Zeeman slowing due to imperfect laser polarization and misalignment between the cooling laser and the axis of the magnetic field. To minimize optical pumping, a constant bias field can be applied to increase the energy separation between the neighboring atomic sub-levels, thereby frequency shifting the undesired transitions farther from resonance. The rate at which atoms are optically pumped from the cycling transition is related to the quality of polarization of the cooling laser, and the relative transition probability and detuning from resonance of the transitions involved. Since approximately 40,000 scattering events are required to slow an atom from 250 m/s down to 20 m/s, suppression of the scattering rate by a factor ~ 2×10^{-5} is desired to avoid optical pumping.

Figure 3.4 illustrates the separation of the Zeeman sub-levels in the presence of an externally applied magnetic field. The upper and lower states of the cycling transition for σ^- Zeeman slowing are designated by bold lines. The transitions allowed by electric dipole selection rules are indicated for σ^-, σ^+ and π polarized light. (Recall, in the high field limit (fields larger than a few Gauss for the $5P_{3/2}$ state), the electronic and nuclear

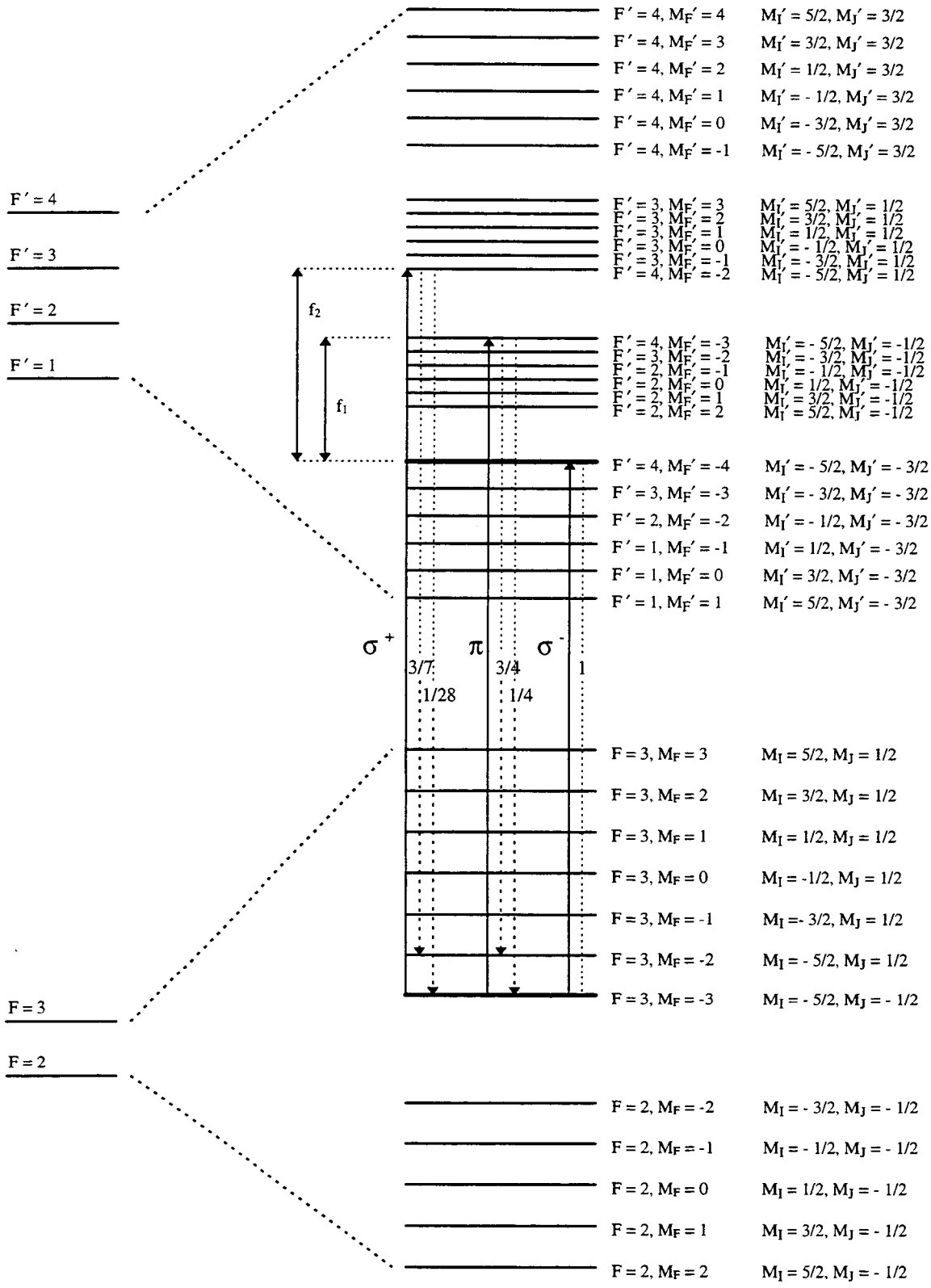

Figure 3.4 Zeeman shift in the transition frequency of the π and σ^+ transitions relative to the σ^- cycling transition.

spins are decoupled, so transitions involving a change in nuclear quantum number M_I are forbidden.) The fractional spontaneous emission rates, which mediate the decay to the ground state are indicated as well. The frequencies shown, f_1 and f_2, correspond to the detuning of the π and σ^+ transitions from resonance with the cooling laser. Equation 3.2 was used to calculated the scattering rate R for the transitions indicated in Figure 3.4 which decay to the wrong ground state. The scattering rate was scaled to account for the fractional transition probability and light polarization. Based on experimental observations, the calculations assumed that the nominally σ^- polarized beam contained approximately 3% each of π and σ^+ polarization. The results, summarized in Figure 3.5 are expressed as a ratio R/R_{MAX}. The cooling laser intensity is 7 mW/cm^2, thus the maximum value of the scattering rate $R_{MAX} = (0.81)\Gamma/2$. For comparison, transition rates were calculated for a 400 G, 200 G and 30 G minimum solenoid field. Since the numbers shown were calculated for the minimum solenoid field, they overestimate the scattering rate. Thus, for a cooling laser with well defined σ^- polarization, only a moderate bias field is required to eliminate unwanted optical pumping within the Zeeman slower.

Another important issue in Zeeman-tuned slowing that is related to optical pumping is state preparation. Atoms exiting the oven are distributed in the F = 2 and F = 3 ground states in a 5/7 ratio; the ratio of Zeeman sub-levels. The number of atoms available for slowing can be maximized by pre-pumping atoms into the desired $|F = 3, M_F = -3\rangle$ ground state. Two types of pre-pumping are relevant; hyperfine pumping can be used to pre-pump atoms from the F = 2 ground state into the F = 3 state and Zeeman pumping can be used to pre-pump atoms in the F = 3 state into the $M_F = -3$ sub-level.

Some Zeeman pumping will occur naturally in the region between the oven and the entrance to the solenoid due to the presence of the cooling laser in this region. The small residual Zeeman field defines a quantization axis for the system along the axis of the solenoid. The cooling laser, polarized σ^-, will optically pump resonant or near-resonant atoms into the Zeeman sub-level with the lowest projection of angular momentum (i.e. $M_F = -3$) [Ungar, 1989]. The pre-pumping efficiency is related to

Minimum Solenoid Field (G)	Transition	Frequency Detuning (MHz)	% of Light with Polarization Indicated	Relative Scattering Rate (R/R_{MAX})
400	π	$f_1 = 668$	3 %	2.5×10^{-6}
400	σ^+	$f_2 = 1360$	3 %	3.4×10^{-7}
200	π	$f_1 = 307$	3 %	1.2×10^{-5}
200	σ^+	$f_2 = 619$	3 %	1.6×10^{-6}
30	π	$f_1 = 28$	3 %	1.3×10^{-3}
30	σ^+	$f_2 = 53$	3 %	2.2×10^{-4}

Figure 3.5 Relative scattering rate for optical pumping into the incorrect atomic sub-level during Zeeman-tuned cooling.

the detuning of the cooling laser from resonance with the zero-field atoms, the laser intensity, and the distance between the oven and solenoid.

Ideally, one would like to pre-pump all the atoms in the velocity capture range of the solenoid into the desired Zeeman sub-level. Practically, this is difficult to do with a fixed frequency laser since all the atoms are not simultaneously resonant with the cooling laser. The situation is further complicated because the cooling laser is resonant with a different class of atoms prior to the solenoid than it is within the solenoid. (Recall the resonance condition for σ^- slowing is $\Delta + kv + \mu_B B / \hbar = 0$.) Because of these factors, off-resonant excitation is required for efficient pre-pumping. To maximize the probability of off-resonant excitation occurring, Phillips *et al.* [Phillips, 1985] used a very intense cooling laser (~50 times the saturation intensity) in a σ^+ slowing experiment on sodium. The high intensity laser provided sufficient power broadening to ensure an appreciable transition rate for off-resonant transitions. If laser power is limited, the Zeeman pre-pumping process will be less efficient since the range for accessible off-resonant velocities is reduced. With this constraint, the optimum approach is to use the minimum strength bias field necessary, thereby decreasing the zero-field detuning of the cooling laser.

Hyperfine pre-pumping of atoms from the F = 2 ground state into the F = 3 ground state can be accomplished by adding a second, fixed-frequency laser tuned to the zero-field F = 2→ F′ = 3 transition.

3.1.4 Transverse Heating

The longitudinal cooling accomplished by one-dimensional laser cooling is accompanied by transverse heating due to spontaneous emission. The recoil kick from spontaneously emitted photons imparts a transverse velocity to the atom and results in transverse spreading of the atomic beam. The transverse root mean squared (rms) velocity imparted to the atom, expressed using the notation of Joffe *et al.* [Joffe, 1993], is

$$(v_T)^2 = \alpha \frac{(\Delta v)^2}{3} N, \tag{3.17}$$

where α = 9/10 accounts for the dipole radiation pattern (α = 1 for isotropic radiation), Δv is the velocity change per scattered photon, and N, the number of scattered photons is $N = (v_i - v_f)/\Delta v$. For a rubidium atom slowed from 250 m/s down to 20 m/s, the transverse velocity acquired from recoil heating is approximately 0.43 m/s. Thus, the transverse spread of a 20 m/s atomic beam will be ±2 cm per meter of longitudinal travel.

3.2 Optical Molasses and Magneto-Optic Trapping: Theory

3.2.1 Optical Molasses

The description of Doppler cooling provided above focused on using the scattering force to decrease the forward velocity of an atomic beam. The original

proposal by Hänsch and Schawlow [Hänsch, 1975] proposed using radiation pressure from three orthogonal pairs of lasers to cool a sample of neutral atoms. In 1985, Chu *et al.* [Chu, 1985] succeeded in experimentally demonstrating such cooling. They used radiation pressure from six counter-propagating laser beams to viscously confine and cool a sample of sodium atoms to a temperature of 240 μK. Due to the viscous nature of this confining force, they gave this process the name "optical molasses." A thorough review of optical molasses is provided in the work of Lett *et al.* [Lett, 1988]. A summary is provided below.

The configuration for one-dimensional optical molasses is illustrated in Figure 3.6. The atom, placed between two laser beams each tuned to the low-frequency side of the atomic transition, experiences a net force opposing its velocity. An atom traveling with velocity $+v$ is Doppler shifted closer to resonance with the laser beam from the right ($-k$) and farther from resonance with the laser beam from the left ($+k$). The situation is reversed for an atom traveling with velocity $-v$. Since the atom has a higher probability of absorbing the photon that is closer to resonance, the net force opposes the velocity of the atom. For low intensity ($I << I_{SAT}$) the average force on the atom can be obtained by summing the scattering force from each laser. Thus, from equation 3.6, the net force is given by

$$F = \frac{\hbar k \Gamma}{2} \frac{I}{I_{SAT}} \frac{kv}{\Gamma} \frac{16\Delta/\Gamma}{1 + \frac{8}{\Gamma^2}\left(\Delta^2 + k^2 v^2\right) + \frac{16}{\Gamma^4}\left(\Delta^2 - k^2 v^2\right)^2}. \qquad (3.18)$$

This expression is plotted in Figure 3.7 for $\Delta = -\Gamma/2$ and $I / I_{SAT} = 1/4$. The dashed lines correspond to the individual force from each laser and the solid line is the sum of the two opposing forces. In the region where $|kv| < \Gamma$ and $|kv| << |\Delta|$, the force is approximately linear in velocity and can be written

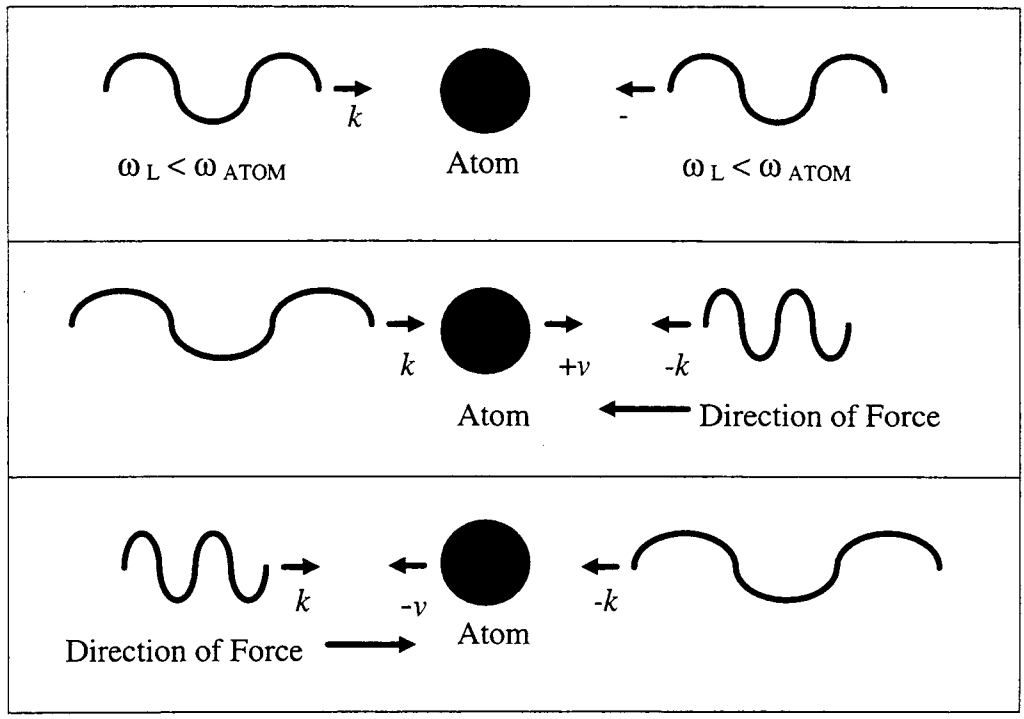

Figure 3.6 Velocity damping of an atom in one dimension.

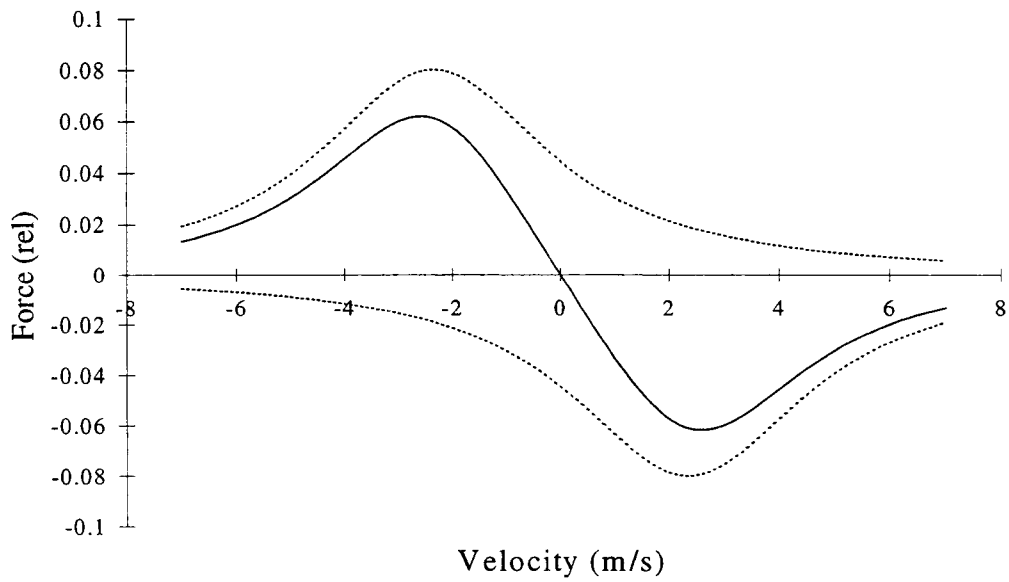

Figure 3.7 Force versus velocity curve for an atom in one-dimensional optical molasses. The detuning $\Delta = -\Gamma/2$ and $I / I_{SAT} = 1/4$. The dashed lines correspond to the individual force from each laser and the solid line is the net force.

$$F = \left[4\hbar k^2 \frac{I}{I_{SAT}} \frac{\frac{2\Delta}{\Gamma}}{\left(1+\left(\frac{2\Delta}{\Gamma}\right)^2\right)^2} \right] v . \tag{3.19}$$

For negative detuning Δ, this force is a damping or frictional force ($F = -\alpha v$). This non-conservative force opposes the velocity of the atom, thereby decreasing the energy of the system. The rate of energy dissipation is proportional to the power input of the damping force, thus

$$\left(\frac{dE}{dt}\right)_{cooling} = \mathbf{F} \cdot \mathbf{v} = -\alpha v^2 . \tag{3.20}$$

The minimum achievable temperature is limited due to heating from the spontaneously emitted photons. By balancing the rate of heating with the rate of cooling, a minimum temperature can be calculated. For one-dimensional optical molasses the minimum temperature for Doppler cooling is given by [Wineland, 1979]

$$T_{MIN} = \frac{\hbar\Gamma}{2k_B}, \tag{3.21}$$

and corresponds to a laser detuning of $\Delta = -\Gamma/2$. For rubidium, the Doppler cooling limit is 140 μK.

The temperature measured by Chu *et al.* [Chu, 1985] was consistent with the 240 μK Doppler cooling limit for sodium. However, subsequent experiments [Lett, 1988] yielded significantly colder temperatures than those predicted by Doppler cooling theory. Doppler cooling theory is based on the assumption of a simple two-level cycling transition. In 1989, Ungar *et al.* [Ungar, 1989] and Dalibard *et al.* [Dalibard, 1989] independently proposed a more complete theory for laser cooling that included effects related to the multilevel nature of the atom. The theory incorporates the effects of

polarization gradients, the AC stark shift, and optical pumping and predicts temperatures significantly below the Doppler cooling limit. A detailed discussion of sub-Doppler cooling is beyond the scope of this work. The interested reader is referred to an overview in *Physics Today* by Cohen-Tannoudji and Phillips [Cohen-Tannoudji, 1990], as well as the detailed discussions provided by Ungar *et al.* [Ungar, 1989] and Dalibard *et al.* [Dalibard, 1989].

3.2.2 The Magneto-Optic Trap

Three-dimensional optical molasses provides an effective means for viscously confining and cooling a sample of neutral atoms. However, no localization of position is inherent in this process, as atoms in optical molasses undergo a random walk in position space much like the Brownian motion of particles in a viscous fluid [Chu, 1985]. Spatial confinement can be provided using a weak magnetic field in conjunction with circularly polarized light. The basic scheme used for trapping neutral atoms is illustrated in Figure 3.8. This simplified one-dimensional configuration assumes an atom with a $J = 0$ ($M_J = 0$) ground state and $J' = 1$ ($M_J' = -1, 0, 1$) excited state. The applied magnetic field is zero at the origin and linearly increasing away from the origin. The presence of the magnetic field Zeeman shifts the atomic sub-levels of the atom by the amount $\Delta E = \mu_B g_J M_J B$ (see equation 2.16). The Zeeman shift, coupled with the laser polarization, provides a spatially dependent confining force. Since an atom to the right [left] of the origin will be closer to resonance with the σ^- [σ^+] polarized beam, the net scattering force will be directed toward the origin. Using lasers tuned below resonance, the velocity damping imposed by optical molasses is also present.

Magneto-optic trapping of neutral atoms was first demonstrated experimentally by Raab *et al.* [Raab, 1987] using a spherical quadrupole magnetic field and six mutually orthogonal laser beams of appropriate circular polarization. The magnetic field, generated using a pair of anti-Helmholtz coils, was zero at the origin and linearly

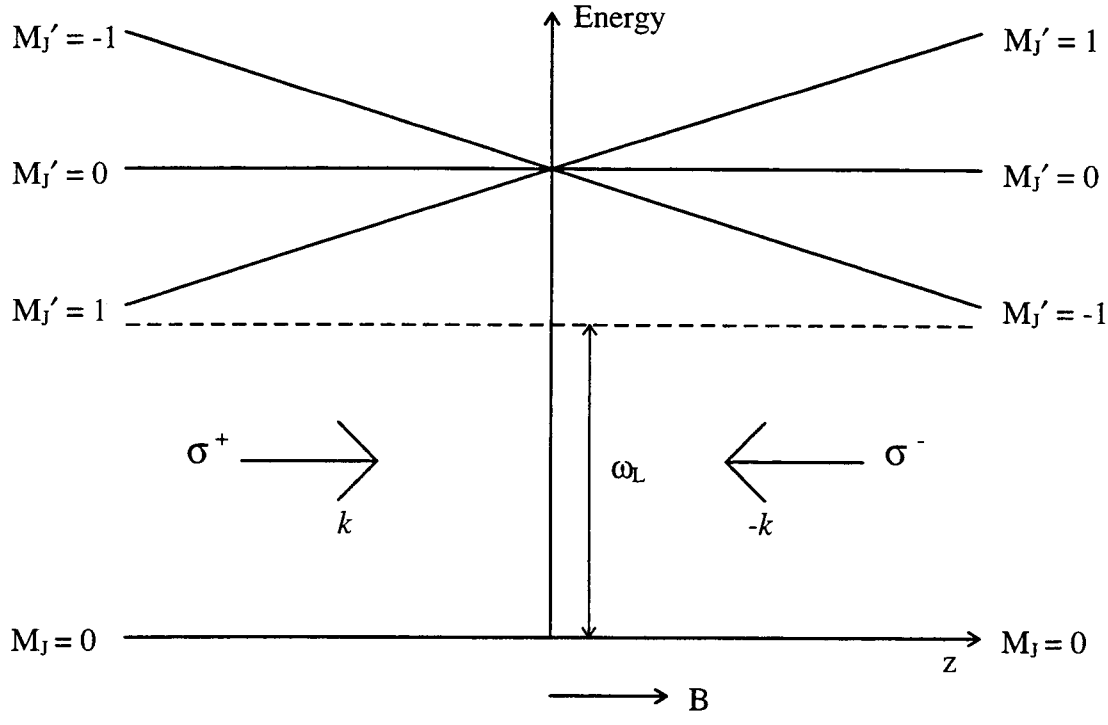

Figure 3.8 A one-dimensional magneto-optic trap (MOT). B > 0 for z > 0. B < 0 for z < 0. The J = 0 ground state in unaffected by the applied magnetic field. The magnetic sub-levels of the J′ = 1 excited state are Zeeman shifted by the amount $\Delta E = \mu_B g_J M_J B$.

increasing along any direction. This configuration, which has become the standard for the three-dimensional magneto-optic trap (MOT), was used by Raab to trap 10^7 sodium atoms and cool them to a temperature of less than 1 mK [Raab, 1987]. Magneto-optic traps have subsequently been a useful tool in a variety of atomic physics experiments requiring access to a cold, dense, atomic sample. Examples include the study of cold-atom collisions [Gould, 1988; Prentiss, 1988], trapping of radioactive isotopes [Gwinner, 1994; Lu, 1994], experiments in precision spectroscopy [Zhu, 1993; Oates, 1996], and use of a MOT to pre-cool atoms for Bose-Einstein condensation [Anderson, 1995].

In 1990, a two-dimensional version of the magneto-optic trap, or so-called atomic funnel, was demonstrated for sodium by Riis *et al.* [Riis, 1990]. In this experiment,

spatial confinement was provided in two-dimensions using a two-dimensional magnetic quadrupole field. Atoms were slowed from a thermal beam using chirped cooling and entered the atomic funnel at an angle of about 7° relative to the funnel axis. Two orthogonal pairs of appropriately polarized, counter-propagating laser beams directed perpendicular to the atomic funnel axis were used to trap the atoms in a line along the zero-field axis of the funnel. The laser pairs also provided molasses-type damping of the atoms. A third pair of counter-propagating laser beams, directed along the axis of the funnel, provided cooling along the axis of the funnel. Atoms were ejected from the atomic funnel with velocities in the range of 1 to 5 m/s using either a differential shift in frequency or an imbalance in intensity between the axial laser pair. Applications are somewhat limited in this configuration due to the presence of the molasses lasers along the axis of the funnel.

Two additional atomic funnels have been demonstrated; Nellessen *et al.* [Nellessen, 1990] reported on an atomic funnel for sodium and Yu *et al.* [Yu, 1994] demonstrated an atomic funnel for cesium. In contrast with the funnel by Riis [Riis, 1990], both of these experiments used molasses-type velocity damping in only the two transverse directions (no axial laser beams). Thus, while no laser beams are present along the atomic funnel axis to block the exit of atomic beam, maximum brightness is not achieved due to lack of axial cooling.

The atomic funnel developed for our experiment [Swanson, 1996] is most similar in design to the funnel of Riis [Riis, 1990]. (The mechanical details are described in section 5.4). However, our objective was to provide three-dimensional velocity compression and two-dimensional spatial compression, while simultaneously avoiding the presence of a laser beam along the axis of the funnel. To accomplish this, four horizontal trapping laser beams, located in the horizontal plane, enter the trap region at an angle of 45° relative to the funnel axis. A vertical laser beam pair is oriented perpendicular to the axis of the funnel. The configuration for the trap is illustrated in Figure 3.9. The six laser beams are aligned to overlap with the slowed atomic beam, which enters the atomic funnel at 90° relative to the funnel axis. With the lasers at the

same frequency, the scattering force from the six beams is balanced and the atoms experience zero net force. By shifting the frequency of the front horizontal lasers relative to the back lasers, atoms are ejected from the trap at the velocity that corresponds to zero net force. Thus, this moving molasses configuration [Kasevich, 1991b] imparts an axial drift velocity to the atom of $v = \sqrt{2}\,\lambda\Delta f$ [1.1 (m/s)/MHz for rubidium].

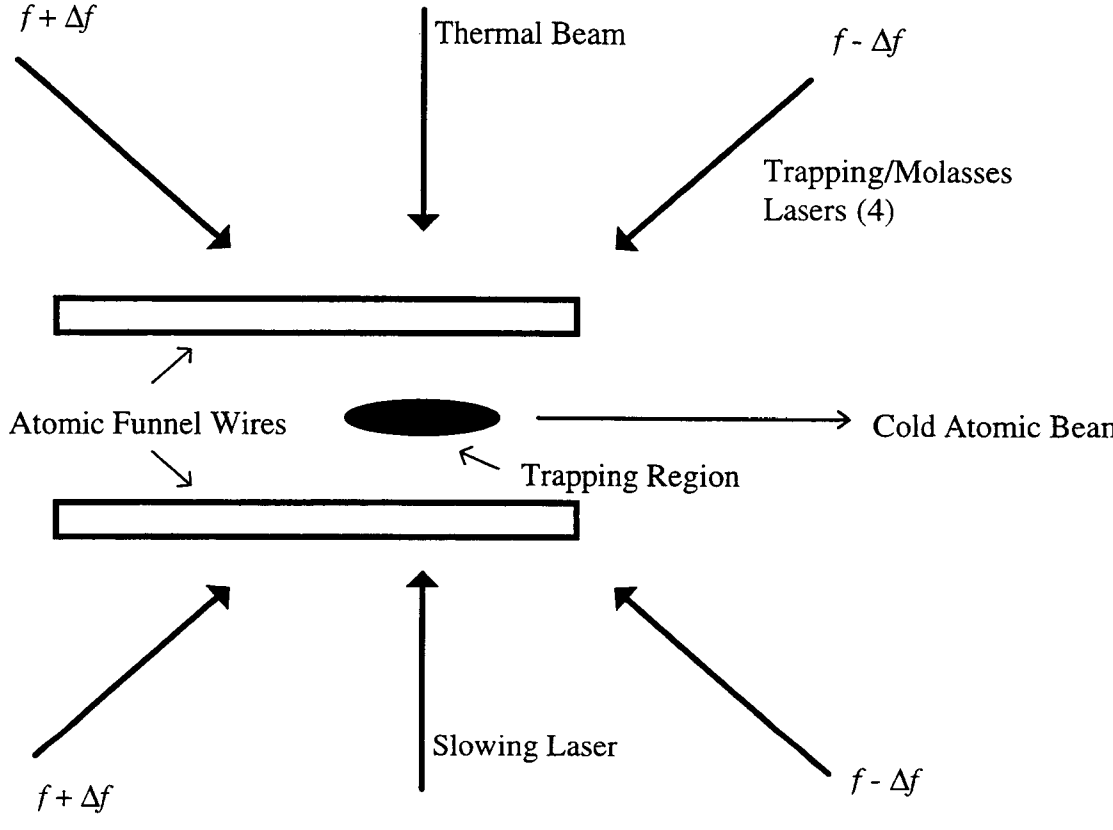

Figure 3.9 Two-dimensional magneto-optic trap or atomic funnel (vertical view). The third counter-propagating laser pair is perpendicular to the page (not shown).

Chapter 4: Zeeman-Tuned Slowing: Implementation

Zeeman-tuned slowing was implemented in our laboratory using a spatially varying magnetic field. The field was generated by sending current through wire wound at varying pitch around a constant diameter cylinder. Section 4.1 discusses the design criteria for the solenoid. The mechanical design, fabrication process, and characterization of the solenoid field are detailed in section 4.2. Section 4.3 describes the analytical model used to make predictions about the performance of the Zeeman slower.

4.1 Solenoid Design Criteria

The magnetic field profile required for Zeeman-tuned slowing was derived in section 3.1.2.2 to be

$$B = \pm\frac{\hbar}{\mu_B}(\Delta + kv), \tag{4.1}$$

where the velocity v, as a function of position z, is given by

$$v^2 = v_0^2 - 2az. \tag{4.2}$$

The deceleration a is assumed to be constant. For constant deceleration, and solenoid length z_0, the exit velocity v_f of the atom is given by $v_f^2 = v_0^2 - 2az_0$. Thus, equation 4.1 can be rewritten

$$B = \pm\frac{\hbar}{\mu_B}\left(\Delta + kv_o\sqrt{1 - \frac{z}{z_0} + \left(\frac{v_f^2}{v_o^2}\right)\frac{z}{z_0}}\right) \tag{4.3}$$

For a small final velocity (i.e. $v_f^2 / v_0^2 << 1$), this expression reduces to

$$B = \pm\frac{\hbar}{\mu_B}\left(\Delta + kv_o\sqrt{1-\frac{z}{z_0}}\right). \tag{4.4}$$

For σ^- cooling and $v_f / v_0 << 1$, the field profile can be written in simplified form as

$$B = B_0 - B'\sqrt{1-\frac{z}{z_0}}, \tag{4.5}$$

where

$$B_0 = -\frac{\hbar\Delta}{\mu_B} \quad \text{and} \quad B' = \frac{\hbar k v_0}{\mu_B}. \tag{4.6}$$

The requirements outlined above apply in general to Zeeman-tuned slowing. In our experiment, the slowed atoms will be loaded into a two-dimensional magneto-optic trap (atomic funnel). The characteristics of the funnel impose additional design constraints. The capture velocity of the atomic funnel was predicted theoretically [Swanson, 1995; Steane, 1992] and verified experimentally [Swanson, 1995] to be 20-25 m/s. If the cooled-beam velocity is larger than the capture velocity, atoms will not be efficiently captured by the trap. For slower beam velocities, transverse expansion of the beam limits the number of atoms that can be captured within the trap, since the coils that generate the magnetic field are spaced a distance of one inch apart. Transverse expansion of the atomic beam results from geometric expansion between the oven and the atomic funnel and the transverse heating that accompanies longitudinal cooling. The geometric expansion of the beam is dictated by the distance between the oven and funnel (see section 5.2.1.1). The transverse velocity from recoil heating depends on the number of photons scattered (see section 3.1.4). Combining these factors, along with fundamental constraints imposed by the configuration of our vacuum system, the solenoid magnetic field length z_0 is limited to about 60 cm.

The maximum initial velocity that can be slowed in a 60 cm long solenoid (hereafter referred to as the solenoid capture velocity) depends upon the deceleration of the atom. Assuming the atom is decelerated at the constant maximum rate, the capture

velocity v_c is given by $v_c^2 = v_f^2 + 2 a_{MAX} z_0$. The maximum deceleration of rubidium for a fully saturated transition is 1.1 x 10^5 m/s (see equation 3.6). However, the available cooling laser intensity of I = 7 mW/cm^2 limits the deceleration in this case to a'_{MAX} = 9 x 10^4 m/s. The corresponding maximum solenoid capture velocity is 330 m/s. In practice, the capture velocity will be somewhat less due to the non-ideal nature of the solenoid. Using these design parameters we find that even for a somewhat reduced capture velocity the relationship $v_f^2 / v_0^2 << 1$ is satisfied. Thus, designing the field to satisfy the profile defined by equation 4.5 is acceptable.

In order to assure maximum flexibility in operating and optimizing the Zeeman slower, a few additional design constraints were imposed on the magnetic field. First, a separate, independently controllable bias field was added to the solenoid to provide a constant magnetic field offset to the field defined by equation 4.5. The bias field is current adjustable and ranges in magnitude from zero to 370 Gauss. The bias field is used to increase the energy separation of the Zeeman sub-levels and minimize optical pumping (see section 3.1.3.2). In addition, it can also be used in conjunction with the spatially varying field to generate the decreasing strength magnetic field required for studying σ^+ cooling.

The second self-imposed magnetic field requirement was to design the solenoid such that the maximum required deceleration of the atom not exceed 75% of a_{MAX} (90% of a'_{MAX}). The field was designed for nominal operation at slightly less that the maximum value to provide allowance for irregularities in the constructed solenoid field. Without such allowance, a bump in the constructed field could result in too steep a magnetic field gradient and cause the atom to prematurely go out of resonance with the cooling laser. Some post-fabrication control of the field gradient is possible by adjusting the taper solenoid current.

The final values of parameters B_0 and B' were arrived at by modeling the magnetic field and theoretically characterizing the solenoid performance. The parameters will be summarized below, along with some justification. Further clarification will be provided during the discussion of the magnetic field model in section 4.2 and the performance model in section 4.3.

Parameter B_0 is essentially an offset term, similar in function to the bias field mentioned above. It defines the maximum value of the taper field and dictates the required laser detuning, but is not an integral part of the decelerating process. Since we are including a separate bias field, this term could be set equal to B'. However, it is difficult to build a tapered field that starts at zero. In addition, preliminary estimates indicated that a large bias field (~700 Gauss) might be required to avoid optical pumping. Since power supply constraints limited the constant bias field to a maximum of 360 G, B_0 was selected to be ~360 Gauss. The parameter B' was then selected such that the full range of available pitch values on the lathe was utilized (see discussion in section 4.2.2). The analytical model described in section 4.3 was used to model the performance of the Zeeman slower. Adjustments to the solenoid coil configuration were made in order to simultaneously maximize the capture velocity of the solenoid and assure that the maximum required deceleration and final velocity fall within the design constraints.

The bias and taper solenoid fields were built to match the magnetic field profiles given by

$$B_{\text{bias}} = 14.8\, I_{\text{B}} \text{ (Gauss)} \tag{4.7}$$

$$\text{and} \qquad B_{\text{taper}} = \left(13.8 - 12.7\sqrt{1 - \frac{z}{60\text{ cm}}} \right) I_{\text{T}} \text{ (Gauss)}, \tag{4.8}$$

where the bias and taper solenoid field currents were nominally designed to be $I_B = 24.25$ amps and $I_T = 26$ amps.

4.2. The Solenoid for Zeeman-Tuned Slowing

A magnetic field was fabricated to match the profiles defined by equations 4.7 and 4.8. The solenoid was fabricated by winding wire, at the appropriate pitch, around a constant diameter cylinder. Water cooling for the solenoid is provided by feeding water through the channel between two concentric cylinders, with the outermost cylinder

forming the base of the solenoid. The mechanical design is described in section 4.2.1. The coil configuration is provided in section 4.2.2. Characterization of the solenoid field is provided in section 4.2.3.

4.2.1 Mechanical Design

The solenoid is composed of wire wound around a constant diameter cylindrical support structure. The support structure consists of two concentric brass cylinders with outer diameters of 1.5 and 2.0 inches and wall thicknesses of 0.042 and 0.049 inches respectively. Two brass end caps, machined to accommodate adapters for water feed through, were soldered to the ends of the cylindrical tubes. Water flow through the concentric cylinders of approximately 2 gallons per minute cools the solenoid, which generates approximately 550 watts of power during standard operation. An illustration of the solenoid base is provided in Figure 4.1.

To construct the solenoid, the support structure was mounted in a lathe and the wire for the bias and taper fields was wrapped on the outer cylinder. Due to power supply limitations, multiple layers of each type were required. The ten bias field layers were wound using gauge 20, insulated, square wire with 0.0331 inch diameter. The six taper field layers were wound using gauge 20, insulated, cylindrical wire with 0.0334 inch diameter. The outermost layer of wire was lacquered in place.

4.2.2 Solenoid Coil Configuration

To determine the appropriate coil spacing, the field of an ideal (infinite) solenoid was considered. The on-axis magnetic field of an ideal solenoid is $B = \mu_o In$, where pitch n is the number of turns per unit length and μ_o is the permeability of free space equal to

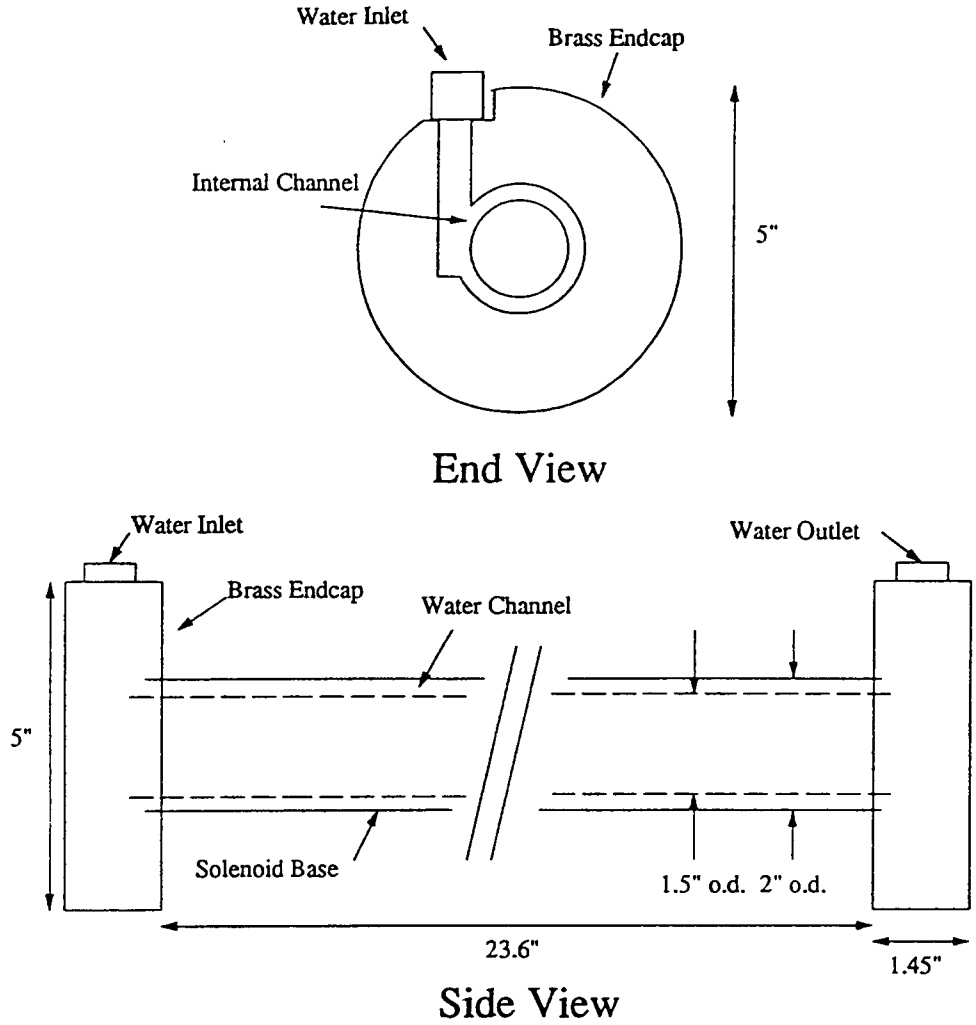

Figure 4.1 Water Cooled Solenoid Support Structure.

$4\pi/10$ G cm/A. Away from the ends, the field of a finite length solenoid approaches that of the ideal solenoid. Thus, the approximate coil spacing was determined from the expression

$$spacing = \frac{1}{n} = \frac{\mu_0 I}{B}. \tag{4.9}$$

The bias field was wound at the maximum pitch of 30 turns per inch, resulting in 709 windings. To provide a field of approximately 360 Gauss, 10 layers were wound carrying a total current of 24.25 amps.

The coil spacing for the taper field was nominally determined from equation 4.9. However, refinements to the pitch were required in order to compensate for the non-ideal nature of the tapered solenoid. Specifically, the pitch was increased at both ends to compensate for the decrease in field strength at these points due to the finite solenoid length. Optimization of the taper solenoid pitch was accomplished through an iterative process that consisted of defining the pitch, calculating the resulting field (see section 4.2.3.1), and comparing the result with the design requirements of equation 4.8.

The coil spacing also deviated from the ideal values due to the discrete nature of the pitch values available on the lathe. The taper field was wound at a variable pitch ranging from 4 to 28 turns per inch. During preliminary modeling of the solenoid it was determined that the discrete nature of the available pitches on the lathe resulted in a bumpy (stair step) magnetic field. This problem was more pronounced the smaller the diameter of the solenoid. In order to minimize this effect, the solenoid diameter was selected to be two inches and the maximum range of pitch values available on the lathe was used. By changing the pitch more frequently, discrete fluctuations in the field were effectively minimized. Six taper layers were wound, consisting of 268 windings each. A total current of 26 amps yielded a field which matched approximately to the theoretical profile 361 G - 330 G $(1\text{-}z/60\text{cm})^2$.

4.2.3 Solenoid Magnetic Field

4.2.3.1 Calculated Axial Field

The axial field of the solenoid was calculated for comparison with the desired profile. The magnetic field on the axis of a single circular current loop is given by

$$B_z(z) = \frac{1}{2}\frac{a^2 I\mu_0}{\left(a^2 + (z-d)^2\right)^{3/2}}, \tag{4.10}$$

where a is the radius of the loop, I is the current, d is the position of the coil. The magnetic field for multiple coaxial coils is calculated by summing up the contribution from the individual loops. For a solenoid consisting of N coils, where the position of each of the coils is defined by an array of points $d(n)$, the designed field is calculated from

$$B_{z\,solenoid-on-axis}(z) = \sum_{n=1}^{N} \frac{1}{2}\frac{a^2 I\mu_0}{\left(a^2 + (z-d(n))^2\right)^{3/2}}. \tag{4.11}$$

Theorist[2] was used to perform the summations of equation 4.11 as a function of position z, where z ranged from -10 to 70 cm in increments of 0.25 cm. A plot comparing the designed on-axis field with the theoretical curve is shown in Figure 4.2 for I_B = 24.25 amps and I_T = 26 amps. As expected, the field at the ends of the solenoid is still somewhat reduced from the desired values. In addition, the field tapers off to zero, rather than dropping abruptly, resulting in a field of about 1.7 Gauss in the funnel region.

4.2.3.2 Measured Axial Field

Following completion of the solenoid, the axial magnetic field was measured using a Hall probe. A linear output Hall effect transducer was used, in conjunction with a simple differential amplifier circuit and x-y plotter, to map the field inside the solenoid. A diagram of the Hall probe setup is provided in Figure 4.3.

A Hall effect transducer is a semiconductor device that produces a voltage linearly proportional to the local magnetic field. This device output a voltage of 7.5 mV/G. The full scale operating range of ± 400 G was referenced to a zero field offset of 6 V. For a positive magnetic field the differential amplifier circuit, which amplifies the difference

[2] The computer algebra program Theorist is a registered trademark of Prescience Corporation.

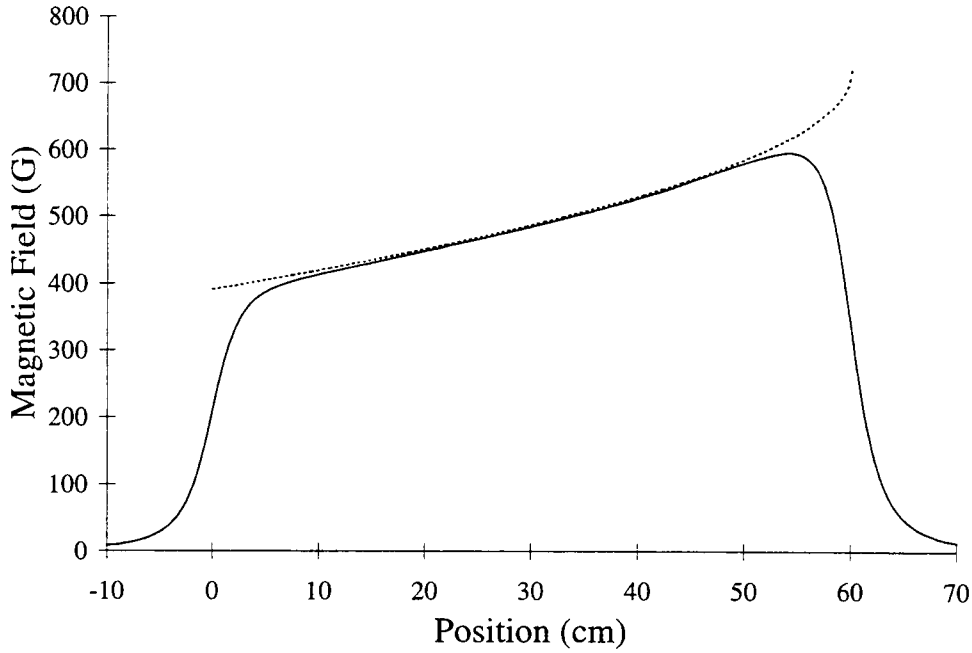

Figure 4.2 Designed solenoid field (solid line) compared with the theoretical profile (dashed line).

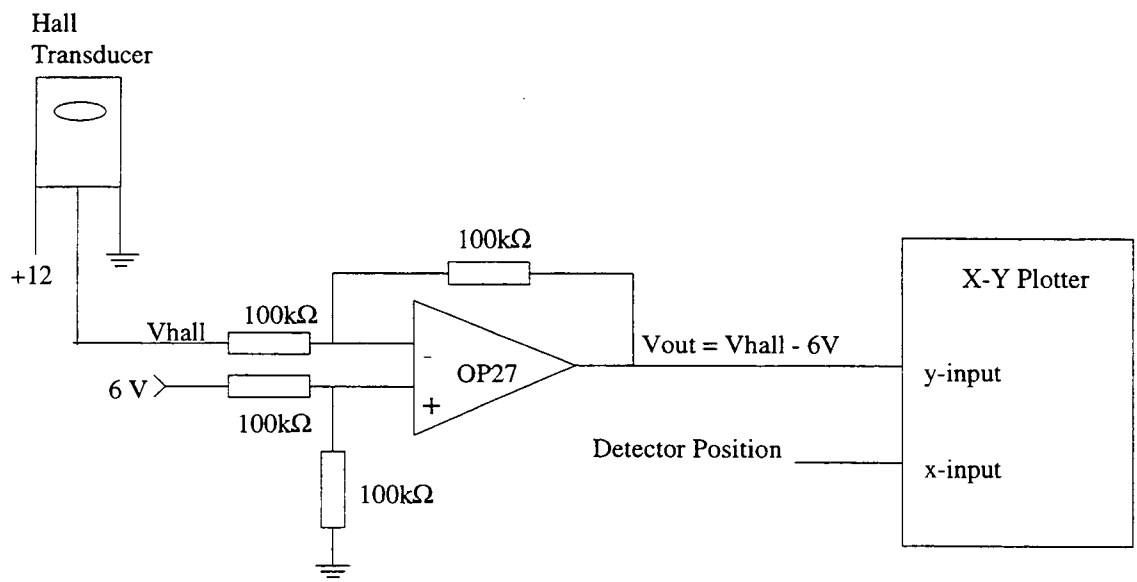

Figure 4.3 Hall probe setup used to measure the axial magnetic field.

voltage between the two input signals, produced a positive output voltage referenced to zero. The output from the circuit was used to drive the y-axis of the x-y plotter. The x-axis value was correlated with the position of the Hall probe within the solenoid. A plot of the measured field is shown in Figure 4.4. When winding the field, some minor bunching of the wire occurred near the high field end of the solenoid, resulting in some deviation from the design.

4.2.3.3 Calculated Radial Field

The magnetic field inside an infinite solenoid consists of only a longitudinal component (B_z). For a non-infinite solenoid, the radial component is non-zero near the ends. The magnitude and extent of the radial component is significant since the total magnetic field defines the quantization axis of the system.

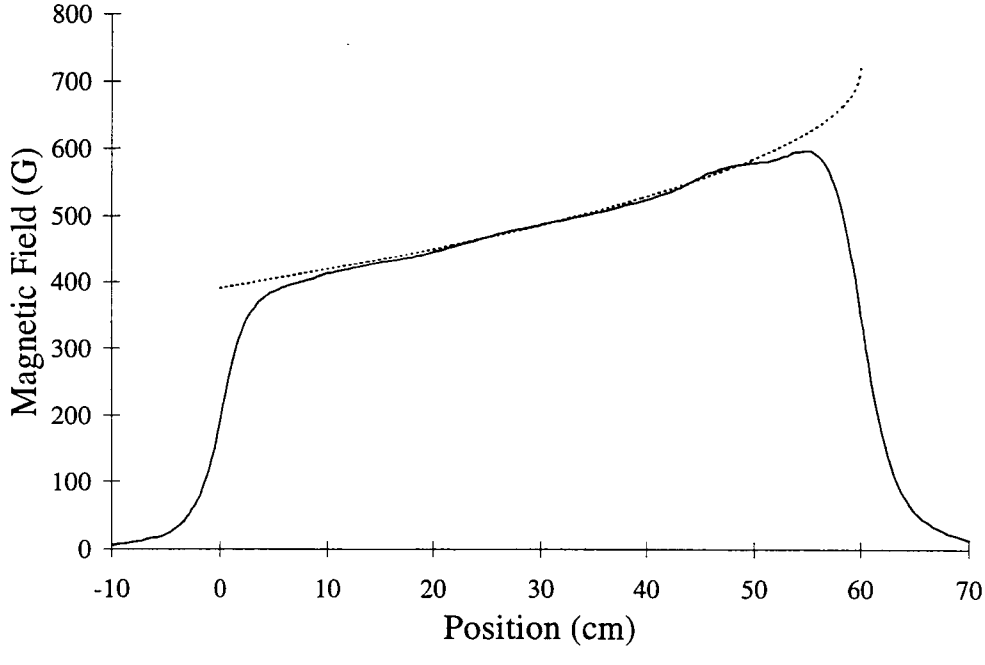

Figure 4.4 Measured solenoid axial magnetic field (solid line) compared with the theoretical profile (dashed line).

From classical electromagnetic theory it can be shown [Jackson, 1975] that the only non-vanishing component of the vector potential for a circular current loop (radius a,current I, oriented in the x-y plane a distance d from the origin) is

$$A_\phi = \frac{\left(\left(2-k^2\right)K(k)-2E(k)\right)Ia\mu_0}{(\pi)k^2\sqrt{(a+\rho)^2+(z-d)^2}}, \tag{4.12}$$

where

$$k = \frac{\sqrt{4a\rho}}{\sqrt{(a+\rho)^2+(z-d)^2}}. \tag{4.13}$$

The elliptic integrals K and E, expressed in terms of series expansions [Abramowitz, 1972], are written

$$K(k) = \frac{\pi}{2}\left(1+\sum_{n=1}^{\infty}\frac{\left((2n)!\right)^2 k^{2n}}{(n!)^4\left(2^n\right)^4}\right) \tag{4.14}$$

and

$$E(k) = \frac{\pi}{2}\left(1-\sum_{n=1}^{\infty}\frac{\left((2n)!\right)^2 k^{2n}}{(n!)^4\left(2^n\right)^4(2n-1)}\right). \tag{4.15}$$

The components of the magnetic field, calculated from the vector potential using

$$\mathbf{B} = \vec{\nabla}\times\mathbf{A}_\phi, \tag{4.16}$$

are given by

$$B_\rho = -\frac{\partial A_\phi}{\partial z}, \tag{4.17}$$

$$B_\phi = 0, \tag{4.18}$$

$$B_z = \frac{1}{\rho}\frac{\partial}{\partial\rho}\left(\rho A_\phi\right). \tag{4.19}$$

Substituting in the series expansions and calculating the necessary derivatives one finds that

$$B_\rho = -\frac{(z-d)\left(K(k)k+\left(k^2-2\right)\frac{\partial K}{\partial k}\right)Ia\mu_0}{k\pi\left((a+\rho)^2+(z-d)^2\right)^{3/2}}, \tag{4.20}$$

where

$$\frac{\partial K}{\partial k} = \frac{\pi}{2}\left(\sum_{n=1}^{\infty}\frac{2\Gamma(2n+1)^2 n16^{(-n)}k^{(2n-1)}}{\Gamma(n+1)^4}\right) \tag{4.21}$$

and

$$B_z = \frac{-\mu I\sqrt{a}\left(K(k)k+\left(k^2-2\right)\frac{\partial K}{\partial k}\right)\left(a^2-\rho^2+(z-d)^2\right)}{2k\pi\rho\left((a+\rho)^2+(z-d)^2\right)^{3/2}}+\frac{1}{2\rho}A_\phi. \tag{4.22}$$

For the case where $\rho = 0$, equations (4.20) and (4.22) reduce to the familiar expressions for the magnetic field on the axis of a circular current loop. Namely

$$B_\rho = 0 \tag{4.23}$$

and

$$B_z = \frac{1}{2}\frac{a^2 I\mu_0}{\left(a^2+(z-d)^2\right)^{3/2}}. \tag{4.24}$$

The expressions above provide the magnetic field for a single current loop. For a solenoid comprised of many loops, the total magnetic field can be calculated by summing up the contributions from the individual loops. For the on-axis case, the total solenoid field was calculated in section 4.2.3.1 using equation 4.11. For the off-axis case, the total solenoid field was calculated by summing equations (4.20) and (4.22) in a similar manner. For the off-axis calculations sufficient terms were kept in the series expansions of the elliptic integrals to ensure accuracy greater than 99.8 %. The radial component of

the field is plotted in Figure 4.5 for ρ values of 0.2, 0.4 and 0.6 cm. Figure 4.6 shows the ratio of the radial and axial components.

During slowing, the atom is resonant with the cooling laser in the region from approximately 5 to 55 cm. From the results above, we find that the radial component of the field, though fairly significant in magnitude, extends over a range where the atom is not resonant with the laser. As such, optical pumping should not be a problem in this region. Thus, the desired orientation of the quantization axis is maintained and optical pumping should not be significantly enhanced due to a radial field component.

4.3 Theoretical Solenoid Performance

Performance of the solenoid is modeled using the analytical model described in section 4.3.1. The predicted performance of the solenoid is presented section 4.3.2 Modeling of transverse heating effects are discussed in section 4.3.3.

4.3.1 Analytical Model of Solenoid Performance

The performance of the Zeeman solenoid is predicted using a simple analytical model developed in *Excel*[3]. By numerically integrating the equation of motion, the position and velocity of the atom is determined as it traverses the solenoid. To perform the numerical integration, the deceleration is assumed to be constant for a small time interval Δt and the new velocity (v_i+1) and position (z_i+1) are calculated from

$$v_{i+1} = v_i - a_i \Delta t \tag{4.25}$$

and

$$z_{i+1} = z_i + v_i \Delta t \,. \tag{4.26}$$

[3] Excel is a registered trademark of Microsoft.

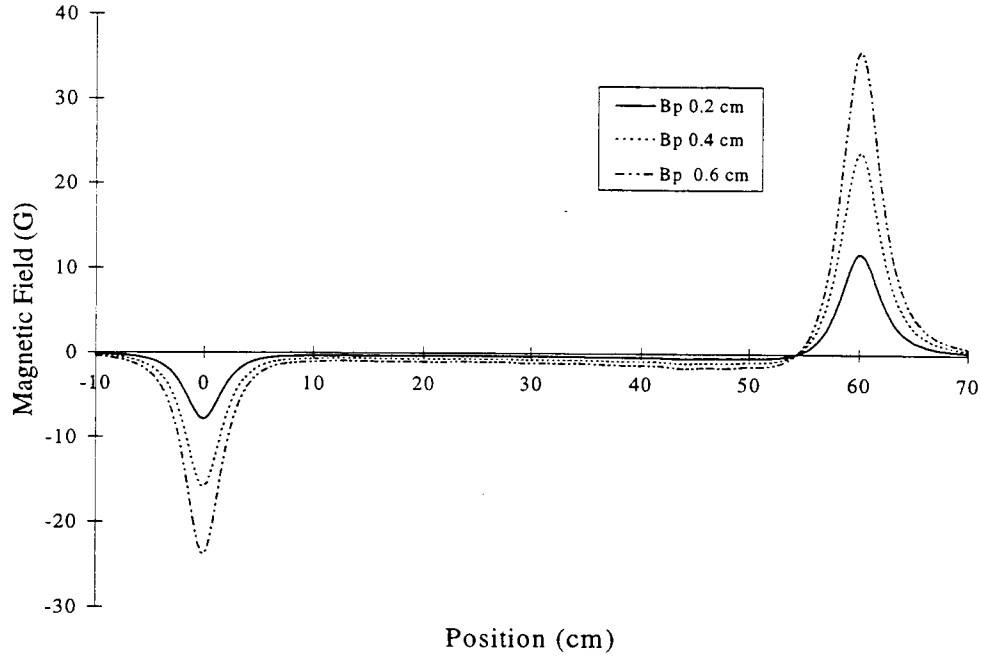

Figure 4.5 Radial component of the magnetic field for ρ = 0.2, 0.4, and 0.6 cm.

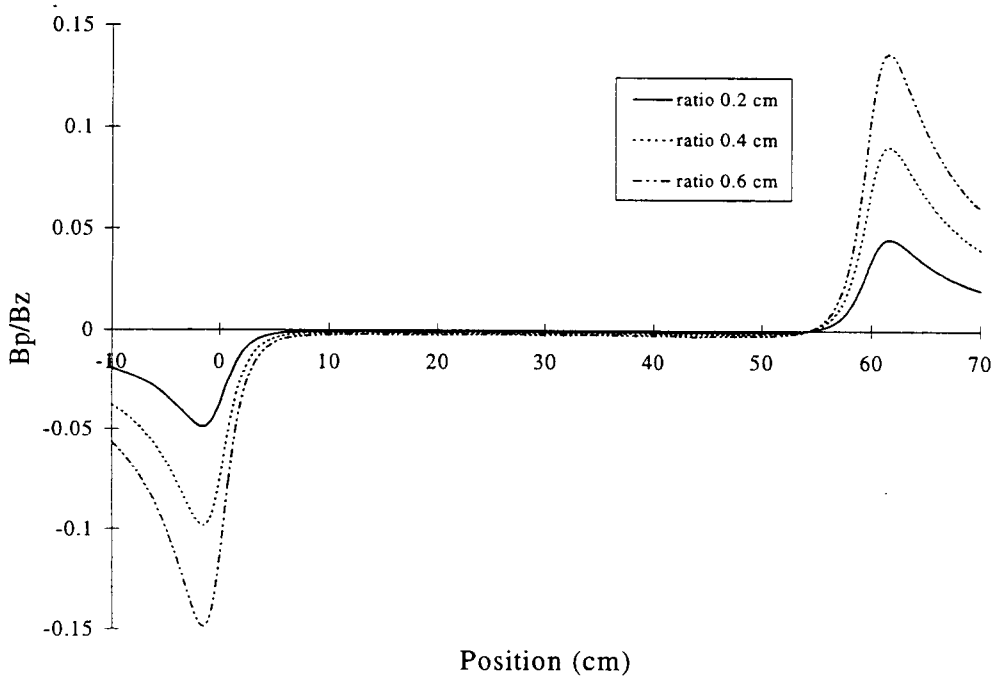

Figure 4.6 Ratio of radial to axial component of the magnetic field for ρ = 0.2, 0.4, and 0.6 cm.

The deceleration a is given by the expression

$$\mathbf{a} = \frac{\hbar \mathbf{k}}{M}\left[\frac{\Gamma}{2}\frac{\frac{I}{I_{SAT}}}{\frac{4}{\Gamma^2}\left(\Delta + kv \mp \frac{\mu_B}{\hbar}B\right)^2 + 1 + \frac{I}{I_{SAT}}}\right], \tag{4.27}$$

where - [+] corresponds to σ^+ [σ^-] cooling.

For theoretical analysis prior to fabrication of the solenoid, the magnetic field values used in equation 4.27 are derived from the table of values generated in section 4.2.3.1 for quarter centimeter increments of z. The magnetic field strength is assumed to follow a linear relationship between the quarter centimeter increments. Theoretical analysis of the real solenoid is performed using measured magnetic field values. Performance of the designed and measured magnetic fields are very similar. Thus, unless otherwise noted, the results presented are for the measured field.

The performance model does not take into account optical pumping effects or spatial variations in the laser intensity. The transition is assumed to be a two-level cycling transition in which photons are scattered at the rate dictated by equation 4.27. Optical pumping effects, which result in atoms being lost from the slowing process, are primarily related to the bias field strength and laser polarization and are addressed independently. The laser intensity value used in the calculation was measured on axis at the entrance into the vacuum chamber. Since the actual beam is slightly focused, the intensity increases as the beam approaches the oven. In contrast, the spatial profile of the laser beam is Gaussian, resulting in a decrease in intensity as a function of radial distance off-axis. Since the laser intensity is well above saturation and the two intensity variations mentioned have opposite effects, the impact of this simplification to the model is considered to be slight.

4.3.2 Theoretical Results from the Model

Theoretical performance of the solenoid was evaluated as a function of current, cooling laser intensity, cooling laser detuning, and initial atomic velocity using the model described above. Sample output from the model is illustrated in Figure 4.7. The resonance condition $\Delta + kv = \pm\ \mu_B B / \hbar$ is examined for atoms with different initial velocities by comparing $\Delta + kv$ to $\pm\ \mu_B B / \hbar$. Atoms moving fast enough that they are never brought into resonance by the magnetic field are not slowed within the solenoid. Those that remain resonant throughout the solenoid emerge bunched at the desired final velocity. In cases where the atom only satisfies the resonance condition in a particular region, the atom is partially slowed and ceases being slowed when the deceleration becomes negligible (i.e. $\Delta + kv \mp\ \mu_B B / \hbar >> \Gamma$).

The selected laser detuning, laser intensity, and magnetic field current dictate the final velocity. The solenoid was designed for optimum performance at bias and taper field currents of 24.25 and 26 amps respectively. The results that follow utilize these design values. The impact of modifying the bias and taper field currents is quantitatively discussed below.

Figure 4.7 illustrates the performance when the normal operating parameters are used. The model predicts that atoms with initial velocities less than ~250 m/s remain resonant throughout the solenoid and emerge bunched at the final velocity of 20 ± 1 m/s.

In Figure 4.8, the laser detuning is selected to yield a larger final velocity. Thus, a faster velocity class of atoms (120 m/s to 350 m/s atoms) is involved in the slowing process compared to the example in Figure 4.7 (20 m/s to 250 m/s atoms). In this configuration, atoms with initial velocities less than ~ 200 m/s are slowed to a final velocity of 120 ± 1 m/s. The atoms traveling faster than ~ 250 m/s cannot scatter photons quickly enough to remain resonant with the slowing laser and are therefore slowed very little within the solenoid. (Recall the maximum allowable field gradient is inversely proportional to the atomic velocity, so slower atoms tolerate a steeper field.) Atoms in the 200 - 250 m/s velocity class remain resonant until they encounter the bump in the

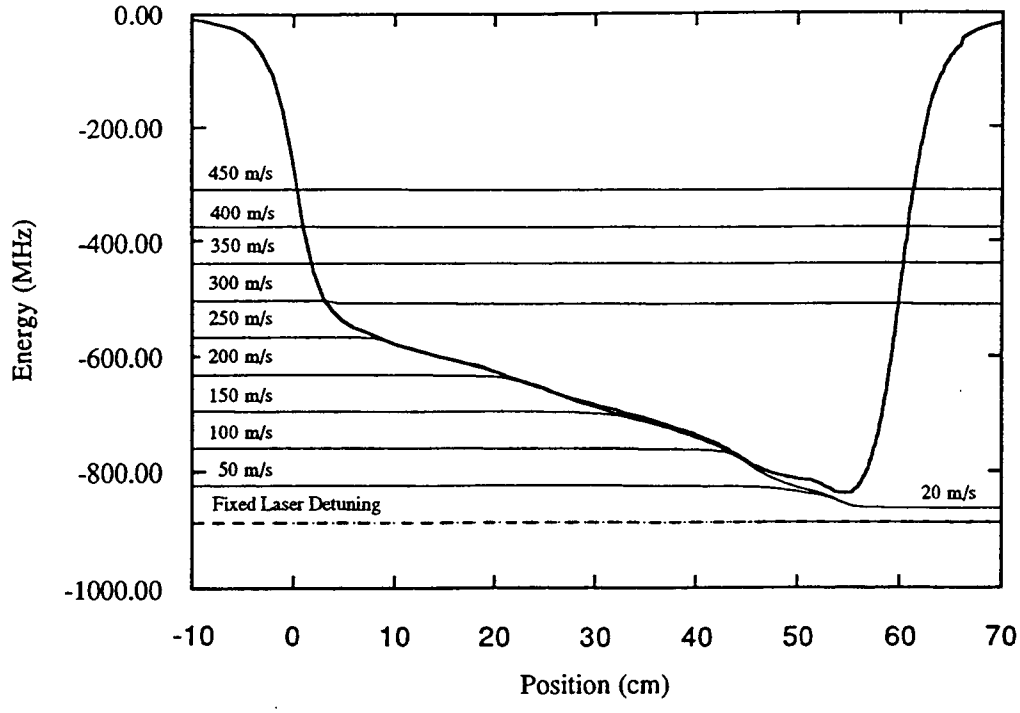

Figure 4.7 An illustration of σ^- cooling for atoms slowed to 20 m/s.

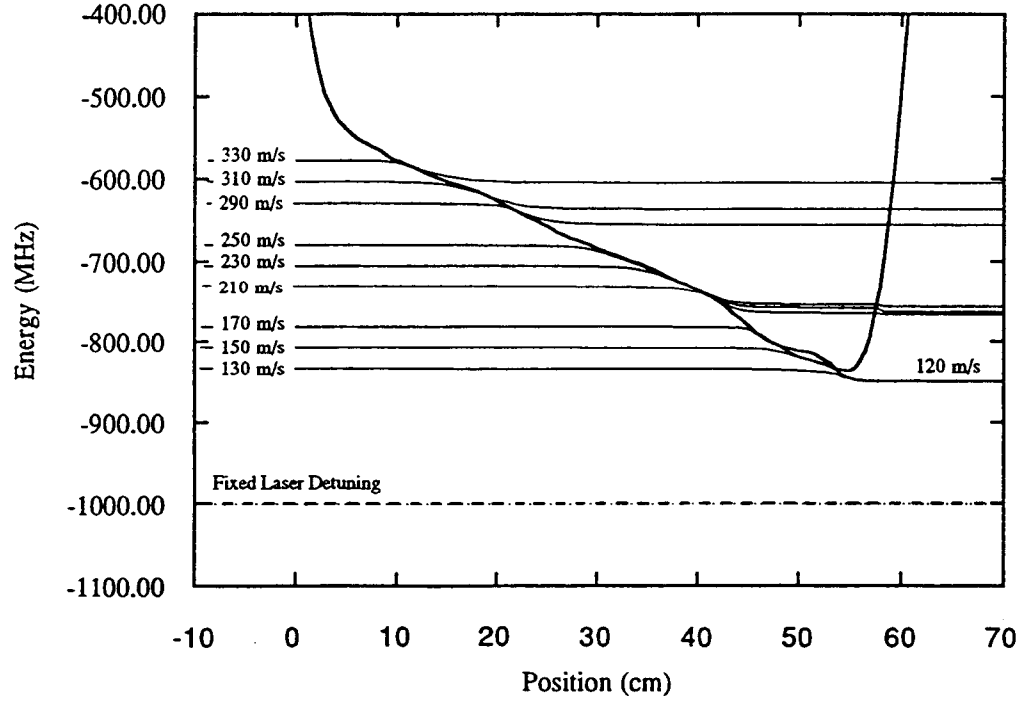

Figure 4.8 An illustration of σ^- cooling for atoms slowed to 120 m/s.

solenoid field at ~ 45 cm. Because of the bump, the field gradient is significantly steeper in this region. From the model it was determined that atoms can follow the bump in the field if they are traveling at a speed of less than approximately 130 m/s when they encounter it. For the 20 m/s final velocity configuration, the slowed atoms are traveling at less than this velocity at the location of the bump. Thus, the slowing process is not perturbed. For the 120 m/s final velocity case, the atoms encounter the bump in the field at a large enough velocity that the field gradient is too steep. Thus, the atoms emerge bunched at the velocity attained at that point, namely 185 ± 5 m/s. A wider spread in final velocity is evident because different velocity atoms go out of resonance at slightly different locations (i.e., the three curves illustrated never overlap.). Atoms traveling slower than ~200 m/s begin being slowed after the steepest region of the field is encountered, and thus are able to remain resonant throughout. The deviations evident in the field in the ~ 50 cm region produce a gradient that is more shallow than the designed field. Thus, the atoms simply follow the deviations in the field.

Figure 4.9 illustrates the resonance condition for σ^+ cooling using the designed solenoid field with bias and taper field subtracted rather than added. In this case, atoms in the velocity range 230 to 290 m/s emerge at a final velocity of ~ 90 ± 10 m/s. Atoms with initial velocities less than about 200 m/s are turned around inside the solenoid. The cause for this is discussed below.

Since optimum loading of the atomic funnel occurs at approximately 20 m/s, both the spread in final velocity and fluctuation in final velocity are important. The primary cause of fluctuation in the final velocity is frequency drift of the cooling laser. To quantify the required laser stability, the slope of the final velocity versus laser detuning curve was analyzed. If the slope is too steep at the desired final velocity, small changes in laser frequency will result in significant changes in final velocity, and thus adversely impact the efficiency of trap loading. Figure 4.10 shows a plot of the final atomic velocity as a function of the cooling laser detuning for σ^- cooling. Two different initial velocity classes are illustrated corresponding to the two velocity classes present at laser detunings larger than -930 MHz. Atoms with velocities less than ~ 200 m/s follow the lower curve. Atoms with velocities between ~ 200-250 m/s follow the upper curve for

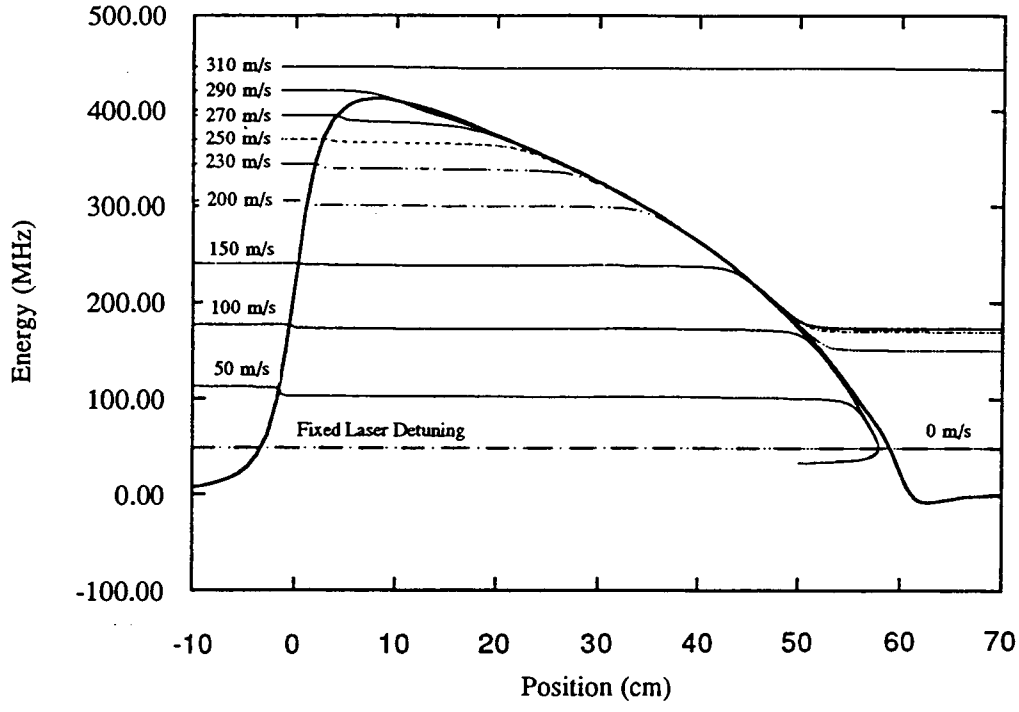

Figure 4.9 An illustration of σ^+ cooling.

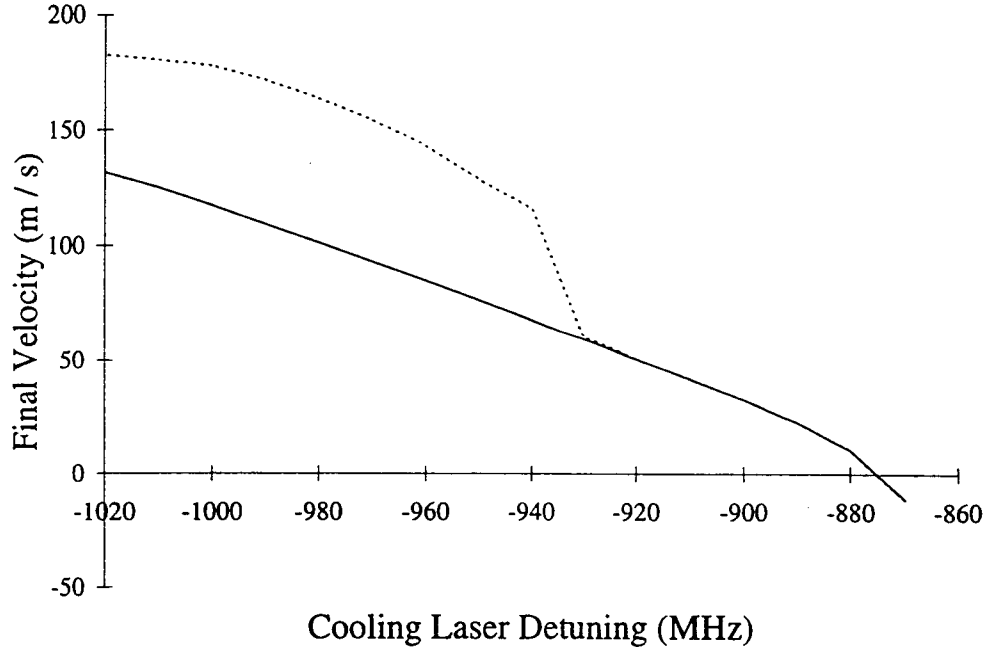

Figure 4.10 Final velocity as a function of laser detuning for σ^- cooling. The taper and bias currents are 26 amps and 24.25 amps respectively. The laser intensity is 7 mW/cm^2. The solid [dashed] curve corresponds to atoms with initial velocities less than [greater than] ~200 m/s.

detunings larger than -930 MHz. Fundamentally, we are interested in atoms slowed to a final velocity of ~ 20 m/s. Thus, the discontinuity in the detuning curve that occurs at -930 MHz does not impact the solenoid performance in the velocity range of interest. For σ^- cooling, the slope of the velocity versus detuning curve at 20 m/s is -1.12 (m/s)/MHz, resulting in a required laser stability on the order of a few MHz.

Figure 4.11 illustrates the velocity versus detuning characteristics for σ^+ cooling for atoms with initial velocity less than ~ 200 m/s. Since the slope is effectively infinite for velocities below ~150 m/s, it is difficult to create a very slow atomic beam using σ^+ cooling. This is consistent with the experimental results reported previously by groups using σ^+ cooling [Phillips, 1982]. For initial velocities greater than 200 m/s there is a discontinuity in the velocity versus detuning curve similar to that found in σ^- cooling.

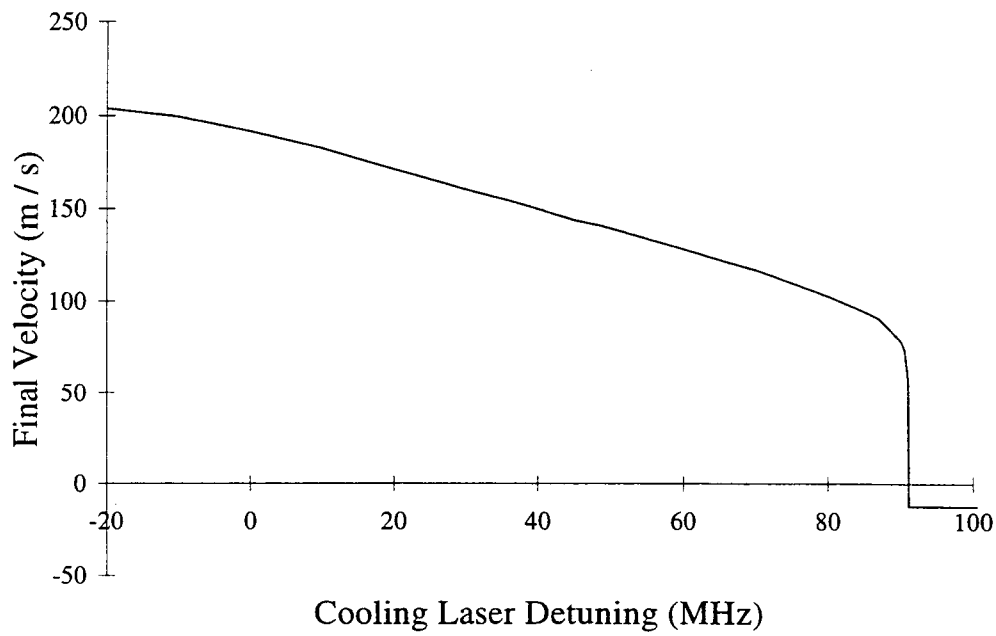

Figure 4.11 Final velocity as a function of laser detuning for σ^+ cooling. The taper and bias currents are 26 amps and 24.25 amps respectively. The laser intensity is 7 mW/cm^2.

To gain insight into the difference between σ^- and σ^+ cooling, the designed and ideal solenoid fields for both σ^- and σ^+ cooling were compared. From the comparison shown in Figure 4.12, we find that for σ^+ cooling it is possible to design a field that closely matches the ideal field. For σ^- cooling, the designed field is less well matched to the ideal profile, particularly at the exit end of the solenoid. This occurs because it is difficult to wind the solenoid coils tightly enough to create the steep increase at the high field end.

If just the ideal solenoid profile is considered (dashed line curves in Figure 4.12), σ^- and σ^+ cooling are essentially identical processes. This is illustrated in Figure 4.13, where the final velocity versus detuning characteristics of the ideal solenoid field are illustrated for both σ^- and σ^+ cooling. (The σ^+ curve is shifted in frequency 910 MHz to facilitate plotting on the same graph.) From this comparison we find that the steep curve at low final velocity is inherent, in theory, to both σ^- and σ^+ cooling for the ideal magnetic field profiles shown.

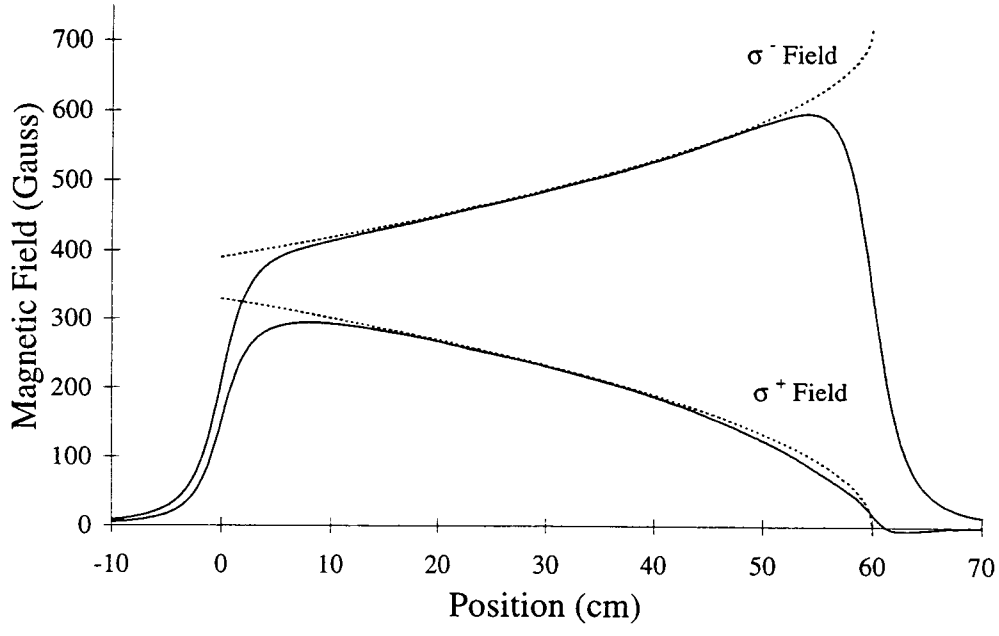

Figure 4.12 Comparison between the ideal (dashes) and designed (solid) magnetic field for σ^- and σ^+ cooling.

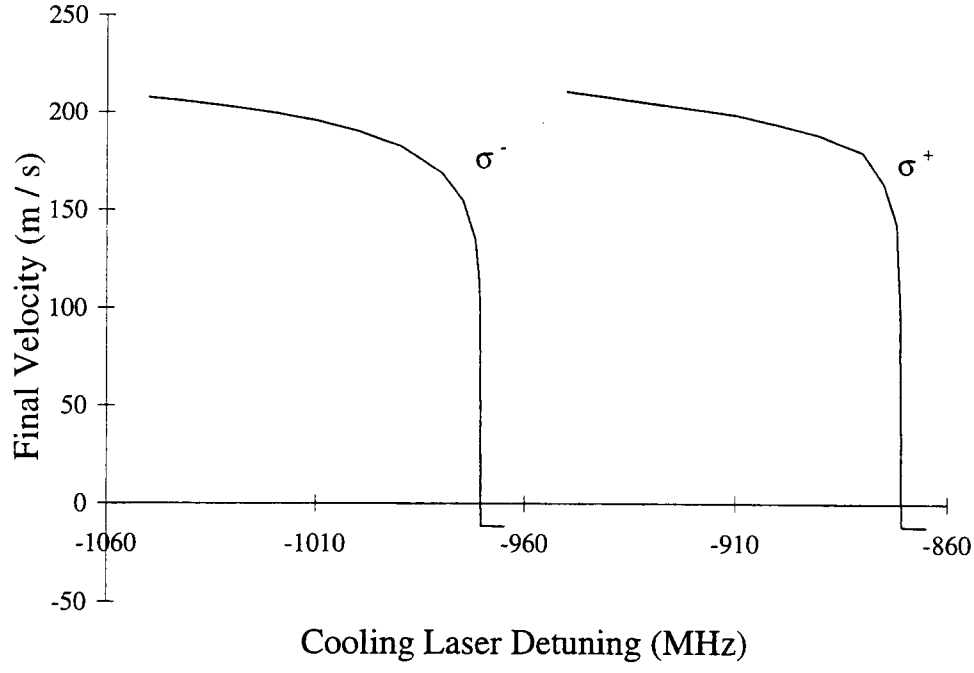

Figure 4.13 Final velocity versus detuning curve for both σ^- and σ^+ cooling for the ideal magnetic field profile.

The ideal magnetic field profiles shown in Figure 4.12 will slow atoms to zero velocity (i.e. the v_f^2 / v_0^2 term in equation 4.3 is zero.) In contrast, the required field profiles to slow atoms to a faster velocity are illustrated in Figure 4.14 (for constant $v_0^2 - v_f^2$). The most significant difference occurs at the exit end of the solenoid, where the non-negligible v_f^2 / v_0^2 term produces a more gradual field profile for faster final velocities. An interesting feature of these different magnetic field profiles is the impact on the characteristics of the final velocity versus laser detuning curve. Figure 4.15 shows the final velocity versus detuning curves for the four different profiles depicted in Figure 4.14. (The results shown are for the σ^+ cooling configuration. However, the σ^+ and σ^- results are identical except for an overall shift in laser detuning). For comparison, the σ^- final velocity versus detuning curve for the measured field (see Figure 4.10) was plotted on the same chart (with a shift in frequency).

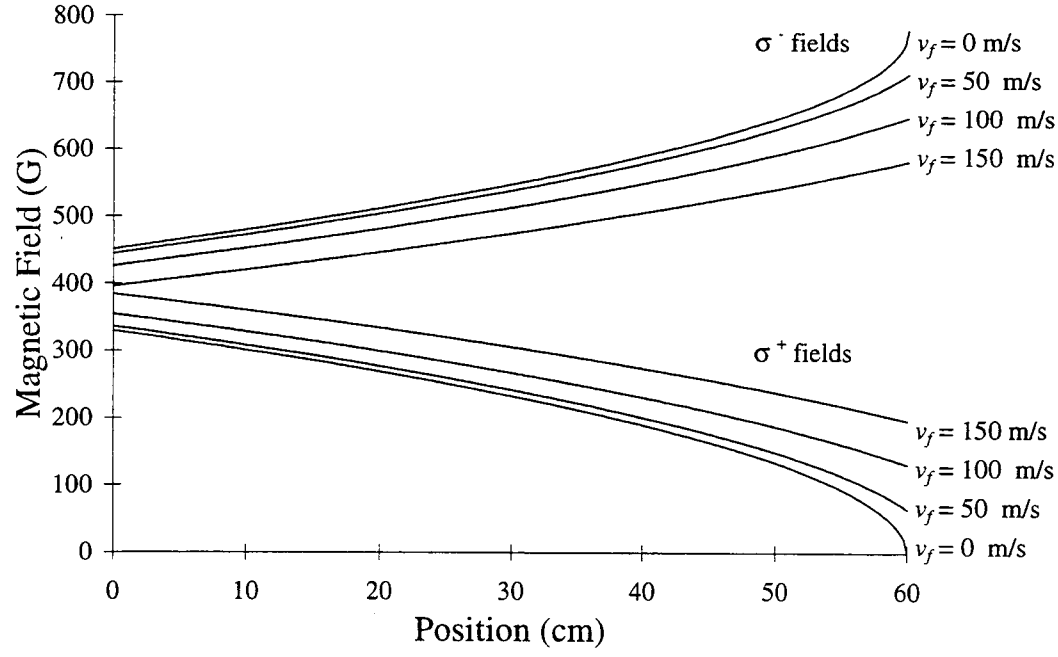

Figure 4.14 Ideal magnetic field profiles for slowing atoms to different final velocities (v_0^2 - v_f^2 = constant).

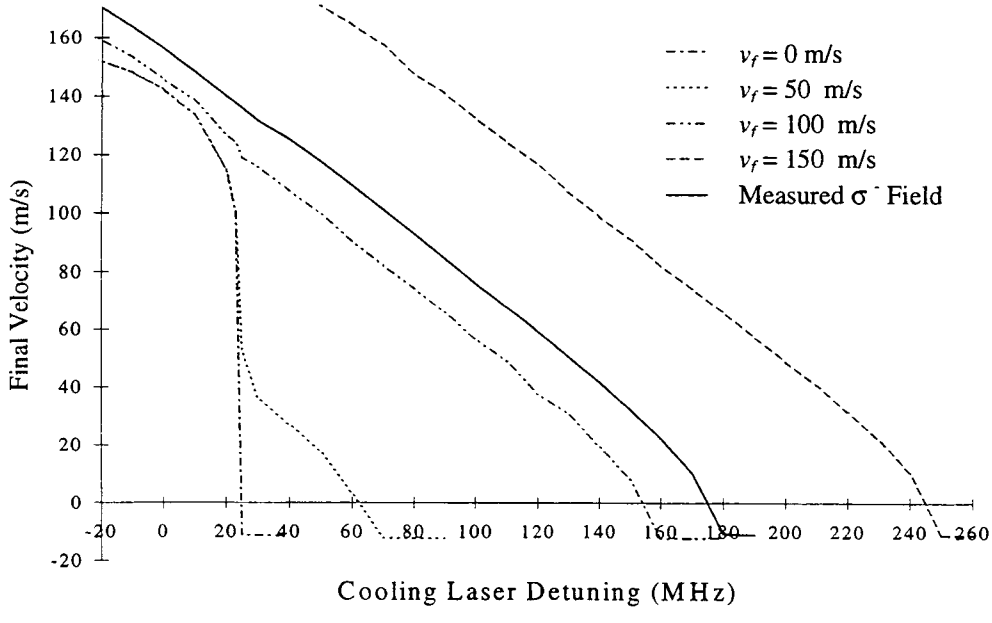

Figure 4.15 Final velocity versus detuning curves for different solenoid profiles. The results shown are for the four ideal profiles illustrated in Figure 4.14 for σ^+ cooling. For comparison, the σ^- velocity versus detuning curve for the measured solenoid field was plotted on the same chart (with a shift in frequency).

From the results shown in Figures 4.15 we find that the velocity versus detuning curve for the measured σ^- field essentially matches that of the ideal field designed to slow atoms to 100 or 150 m/s. In addition, the designed magnetic field profile for σ^- slowing shown in Figure 4.12 appears to more closely match those of the ideal solenoid profiles in Figure 4.14 corresponding to a 100 or 150 m/s final velocity. Thus, σ^- slowing to controllable low velocities is possible because the rapid decrease in the field at the exit end of the solenoid modifies the magnetic field profile from the ideal case. The resulting field profile and corresponding performance characteristics match those of a solenoid designed to slow atoms to a final velocity in the range of 100 to 150 m/s.

In contrast, the designed magnetic field profile shown in Figure 4.12 for a σ^+ slowing most closely matches the ideal field corresponding to zero final velocity. In order to design a field for σ^+ slowing to match any of the profiles shown in Figure 4.14 with non-zero final velocity, a steep decrease in the magnetic field is required from the end of the solenoid to zero field. (The detuning characteristics shown in Figure 4.15 were generated assuming a discontinuous jump from the non-zero magnetic field value at the end of the solenoid to zero field). This steep gradient is required in order for the atom to go out of resonance with the slowing laser. If, instead of a rapid drop to zero, the magnetic field gradually decreases to zero, the profile essentially mimics that designed for zero final velocity; the atom will remain resonant with the laser and eventually be turned around within the solenoid. Thus, while σ^+ cooling can be used in theory to produce atoms with controllable low velocities, an appropriate decreasing strength magnetic field cannot be built to implement such a process.

A remaining issue to address is why the field profiles corresponding to non-zero final velocity can be used to produce controllable low-velocity atoms and the profile for zero final velocity cannot. Insight can be gained by examining the detuning curve illustrated in Figure 4.15 for the solenoid designed to slow atoms to a 50 m/s final velocity. In this curve, the steep slope that is characteristic of the detuning curve for zero final velocity separates two regions of more gradual slopes. The region to the left of the discontinuity corresponds to atoms being slowed to velocities faster than 50 m/s and the region to the right to velocities slower than 50 m/s.

To slow atoms to a different velocity than the designed final velocity, the detuning of the cooling laser must be changed. For a velocity less than the designed final velocity, the detuning is increased [decreased] for σ^+ [σ^-] slowing. In this situation, the atom comes into resonance with the solenoid sooner and is therefore traveling more slowly than the designed resonant value at that point in the solenoid. As a result, the atom has to decelerate less than the designed deceleration to remain resonant and thus, is able to remain resonant with the cooling laser throughout the solenoid. In contrast, to slow atoms to a velocity faster than the designed final velocity, the detuning situation is reversed. Now, the atom comes into resonance later in the solenoid, traveling at a velocity faster than the designed resonant velocity at that point. To remain resonant requires a greater deceleration than the designed deceleration. For a field designed for less than the maximum allowable deceleration, the atom can be decelerated over some length of the solenoid. However, when the field gradient gets too steep, the atom goes out of resonance and the deceleration stops. For the field profiles in Figure 4.14, the field gradient is much steeper for the slower final velocity curves. Thus, only in the earlier segment of the solenoid can atoms remain resonant. This results in a larger exit velocity and is responsible for the large discontinuity in the detuning curves in Figure 4.15.

To further characterize σ^- cooling with the measured solenoid field, the analytical model was also used to examine the performance of the solenoid as a function of laser intensity and solenoid field current. The solenoid capture velocity is plotted as a function of laser intensity in Figure 4.16. The results are provided for both the designed and measured solenoid field. The discontinuities in the measured field result arise from the bumps in the magnetic field profile. As expected, significant increases in capture velocity are observed as the laser intensity increases in the region near the saturation intensity. The impact of laser intensity is not as significant for intensities much greater than saturation.

The capture velocity of the solenoid was also examined as a function of current. Since the model does not incorporate the effect of optical pumping, the result merely

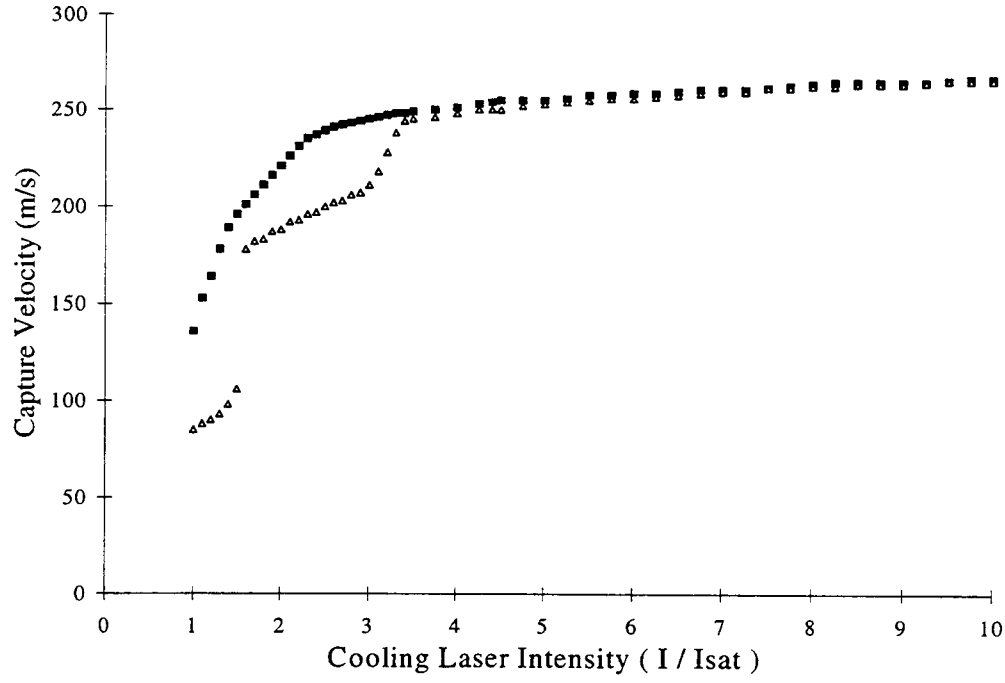

Figure 4.16 Solenoid Capture Velocity as a Function of Cooling Laser Intensity. The triangle [square] markers correspond to the measured [designed] solenoid field.

provides insight into the effect of the solenoid field on the slowing process. The two curves illustrated in Figure 4.17 correspond to varying the current for one field while holding the other constant at its designed value. As anticipated, solenoid performance is closely correlated with the taper field current, since the slope of the field determines the deceleration rate of the atoms. Above the designed operating current of ~26 amps, the capture velocity is decreased because the slope of the field is too steep for the faster atoms to follow. Modifying the bias current does not affect solenoid performance as significantly. For a perfectly constant bias field, the bias field current should only impact the required laser detuning and affect optical pumping by dictating the energy separation of neighboring hyperfine levels. Since the real bias field tapers off at the ends of the solenoid, rather than discontinuously returning to zero field, the bias current has a slight impact on performance.

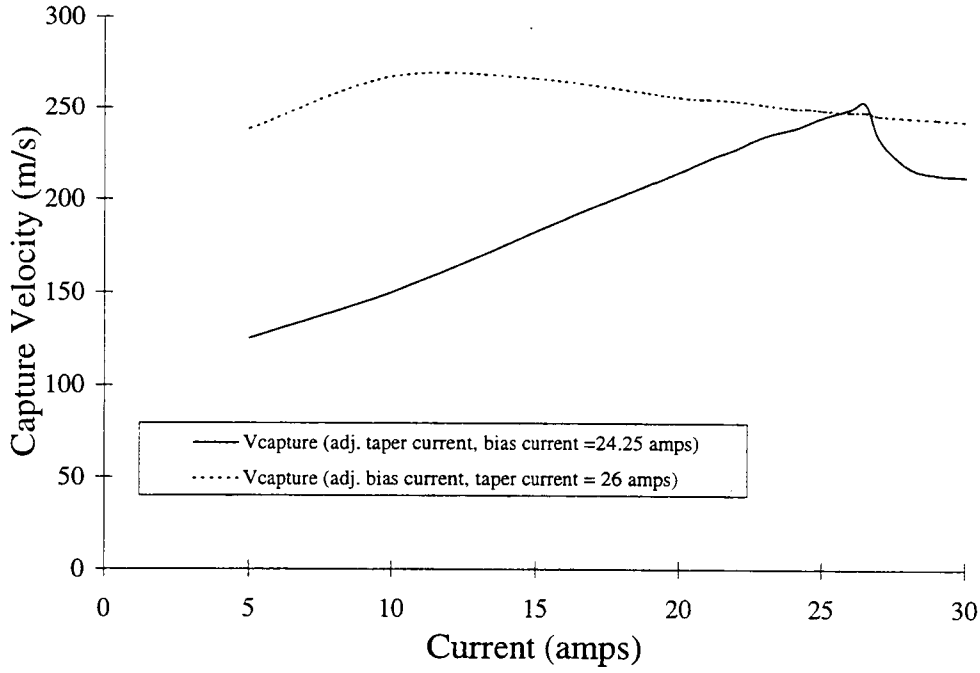

Figure 4.17 Solenoid performance as a function of current shown for both constant bias solenoid current and constant taper solenoid current. The laser intensity is 7 mW/cm^2.

From the model, the operating parameters of the system were clarified and performance predictions were made. In summary, the nominal operating taper current was established to be 26 amps. The bias current was nominally designed to be a maximum of 24.25 amps. The laser intensity, which is limited by the available laser to 7 mW/cm^2, corresponds to I/I_{sat} of 4.4. Using these parameters, a laser detuning of -887 MHz is required for a final velocity of ~20 m/s. The capture velocity of this configuration is predicted to be 250 m/s.

4.3.3 Spontaneous Emission and Transverse Heating

The model described above does not included the recoil kick associated with spontaneous emission. To examine the effect of spontaneous emission, randomly directed velocity kicks were added to the model. For each 0.6 cm/s change in forward

velocity a random number generator was used to select the direction for a velocity kick of magnitude 0.6 cm/s. Inclusion of such spontaneous emission events had no significant impact on performance. To further confirm the robustness of the model, all of the spontaneous emission events in one time interval (approximately 770 photons) were directed in the direction of motion of the atom. Even by nulling the effect of slowing for one integration step, no significant impact on performance was observed.

Spontaneous emission results in transverse spread of the beam. In practice, the majority of the expansion occurs between the output of the Zeeman slower and the trap region, since the velocity of the atom is significantly slower in this region. Assuming a 230 m/s change in velocity, the transverse velocity at the output of the slower is 0.64 m/s. Thus, for a travel distance of 25.5 cm from the solenoid to the trap, the spread due to transverse heating is 0.9 cm (measured from the center line to the outside edge). An additional spread of 0.5 cm occurs due to the geometric expansion of the thermal beam from the oven to the funnel region. The spreading within the solenoid due to transverse heating is 2.6×10^{-6} cm. Thus, the beam diameter at the entrance to the magneto-optic trap is 2x(1.5 cm) or approximately 1.2 inches.

Transverse spreading is a more significant problem for lighter atoms since v_{transv} scales as $M^{-3/4}$ [Joffe, 1993], so techniques have been developed to minimize the effect. Joffe *et al.* [Joffe, 1993] introduce a narrow gap in the windings near the end of their increasing field Zeeman slower and utilize two-dimensional optical molasses in this region to minimize the transverse spreading of a slowed sodium beam. While this technique is effective, it is somewhat awkward to implement, and the degree of spreading predicted for the slowed rubidium beam is approximately accommodated by our magneto-optic trap.

Chapter 5: System Description and Operation

5.1 System Overview

The experimental system is illustrated in Figure 5.1. The rubidium oven, atomic funnel, and surface ionization detector (not shown) are currently housed within the vacuum system. The gratings that will comprise the Bonse-Hart interferometer are indicated for reference. The Zeeman slower magnet, which is built on a cylindrical base tube, fits over the vacuum pipe. There are six trapping lasers; the four shown and a pair of counterpropagating beams perpendicular to the page. The lasers are located on a separate optical bench and directed into the chamber via mirrors mounted to the vacuum system. Except for the Zeeman solenoid, which was described in detail in Chapter 4, the sub-system components are described below.

5.2 The Atomic Beam Machine

5.2.1 The Vacuum System

The rubidium oven, atomic funnel, and surface ionization detector are located within a differentially pumped dual chamber vacuum system. Figure 5.2 [Swanson, 1995] shows a schematic of the vacuum system. The oven chamber, pumped by a Varian Turbo-V80 turbomolecular pump, exhibits a nominal pressure of ~1 x10^{-7} Torr. The backing pump is a Varian mechanical pump. The oven chamber is isolated from the high vacuum chamber by a electro-pneumatic gate valve that is open during operation of the system. The oven chamber can be isolated from the turbo pump by the oven isolation gate valve. Initial pumping down of the oven chamber is done, with the turbo pump off, using the mechanical pump.

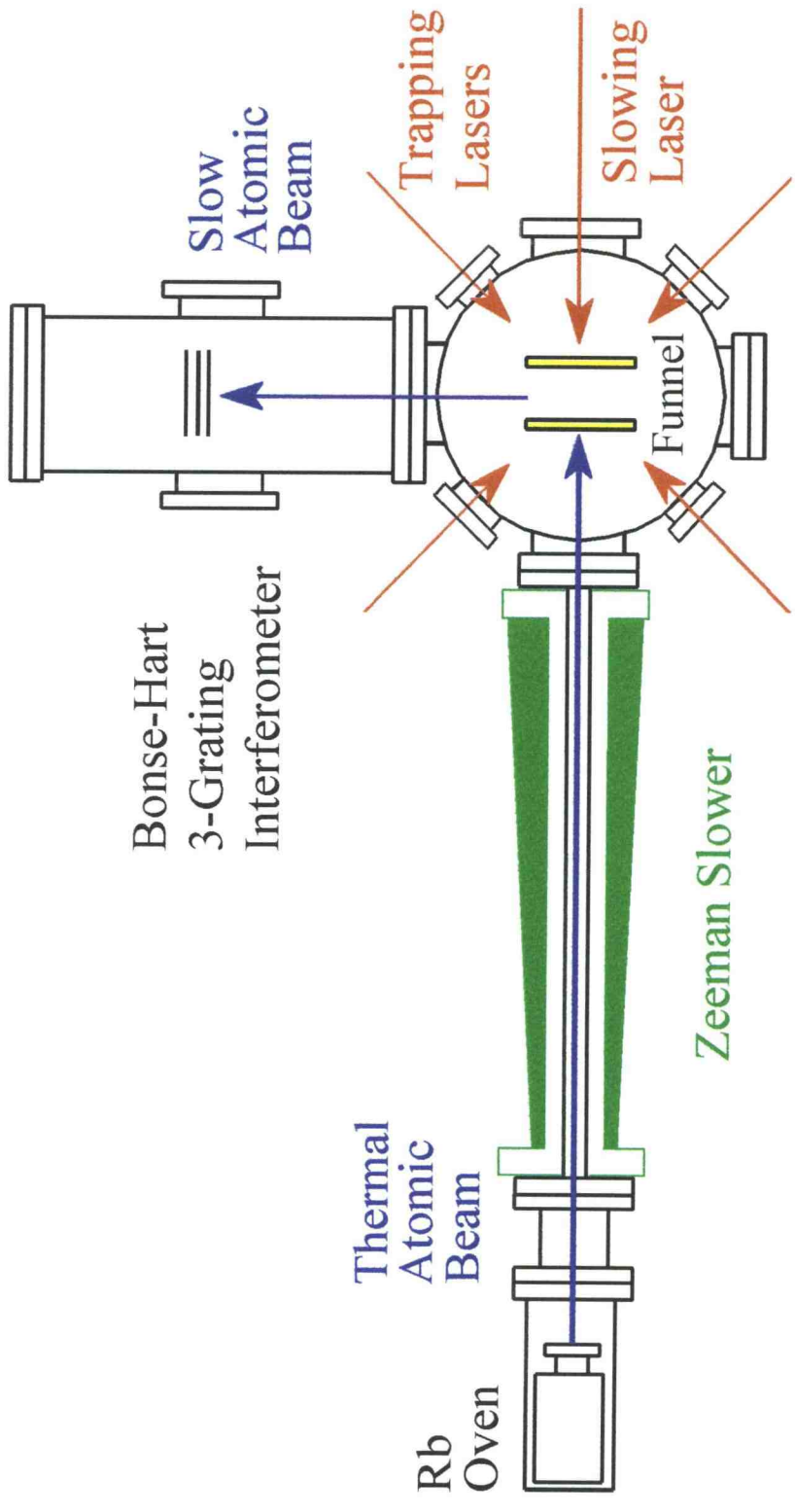

Figure 5.1 System schematic of the cooled-atom interferometer.

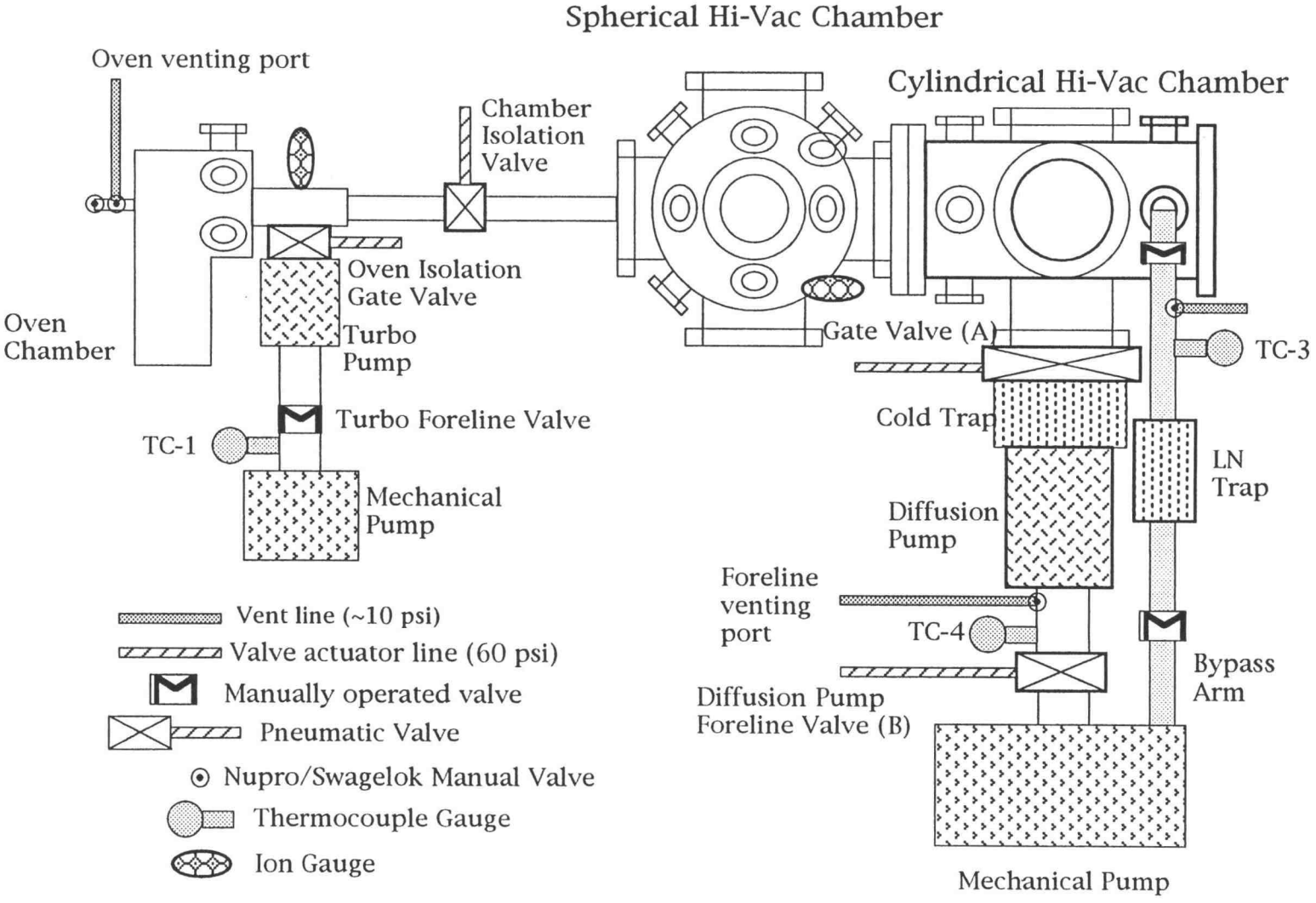

Figure 5.2 Vacuum System Schematic.

The high vacuum chamber consists of two compartments; a spherical chamber that houses the atomic funnel, and a cylindrical chamber that contains the surface ionization detector and will house the interferometer. The high vacuum compartments are pumped through a methanol filled, -20° C cryo-trap, by a Varian VHS-6 diffusion pump. A Varian mechanical pump serves as the foreline pump for the diffusion pump. The diffusion pump fluid, polyphenyl ether (Santovac 5), has a room temperature vapor pressure of 4×10^{-10} Torr. The nominal pressure in the high vacuum chamber is $\sim 1 \times 10^{-9}$ Torr. The electro-pneumatic gate valve (A) and foreline valve (B) allow for isolation of the diffusion pump. The high vacuum chamber is roughed out through the bypass arm using the mechanical pump. The liquid nitrogen trap (LN), filled when roughing out the chamber, ensures that mechanical pump oil does not backstream into the high vacuum chamber.

Both the oven chamber and high vacuum chamber are equipped with a Varian 571 Bayard-Alpert ionization gauge to measure pressure. In addition, thermocouple gauges (TC - #) are used for pressure measurements in the $> 1 \times 10^{-3}$ Torr range. The vent lines shown allow for venting the oven chamber, turbo pump, bypass arm, and diffusion pump to nitrogen. Venting to nitrogen, rather than air, is done to prevent oxygen and water from degrading or damaging the pump fluids or reacting with rubidium.

5.2.2 The Rubidium Oven

The thermal atomic beam used in this experiment originates from an effusive oven. The design of the oven was motivated by the work of Lambropoulos *et al.* [Lambropoulos, 1977] and Carter *et al.* [Carter, 1978]. A detailed description of the design and operation of the oven used in this experiment is provided in the work of Swanson [Swanson, 1995]. A brief description follows.

The three-stage oven, illustrated in Figure 5.3, consists of a cylindrical sample reservoir, nozzle assembly, and recirculation system. The oven body is made of stainless steel and has the capacity to hold a 5 gram ampule of rubidium. The ampule is placed in

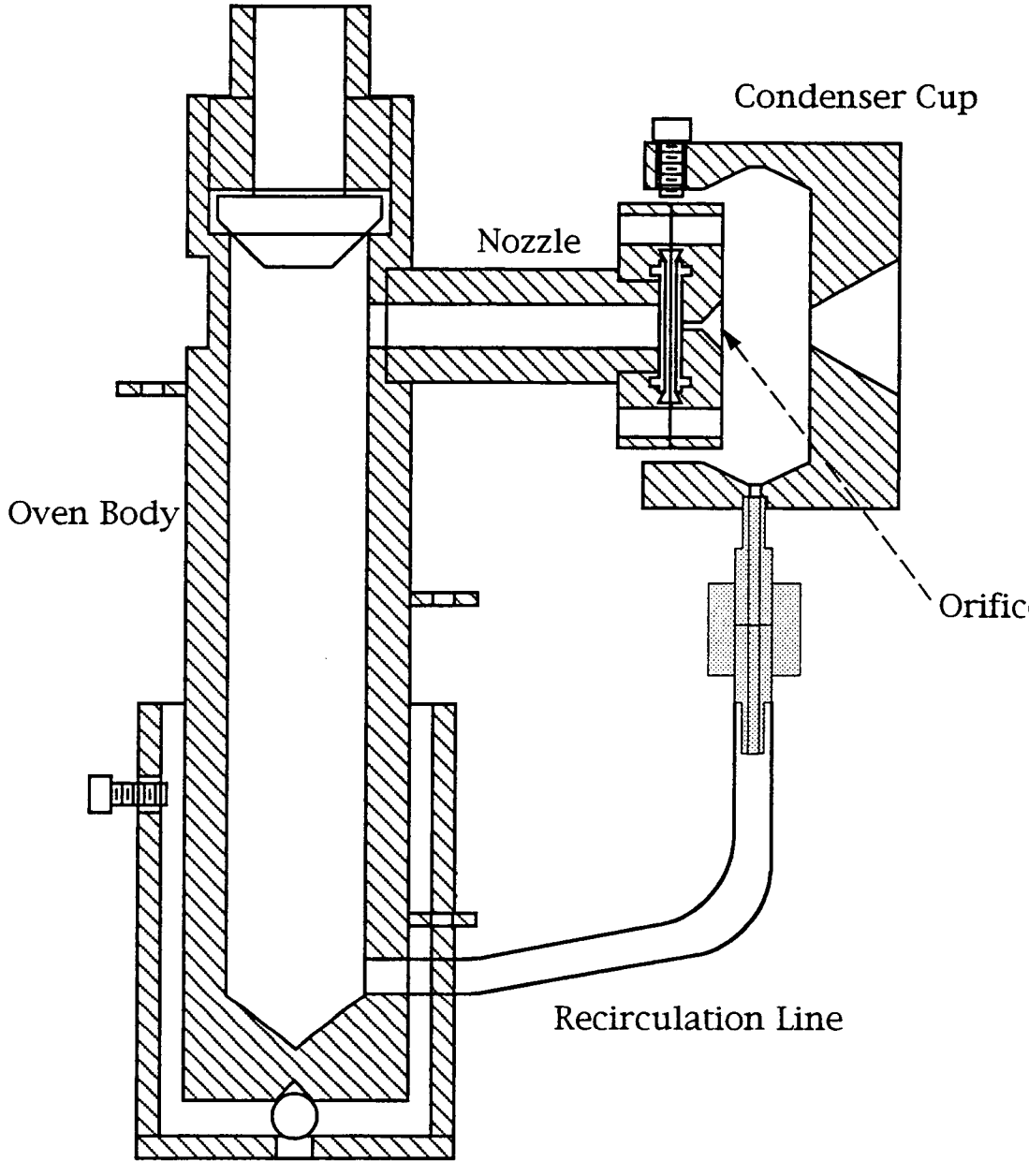

Figure 5.3 The Rubidium Oven.

the oven, open side down. When heated, the melted rubidium flows into the bottom of the oven chamber and blocks the recirculation line. The nozzle, also made of stainless steel, has a 0.1 cm orifice which provides the exit path for the rubidium vapor when the oven is heated. The output end of the orifice is tapered to minimize the length through which the atoms travel to 0.38 cm. Since the angular distribution of atoms exiting the oven is broad, much of the vapor is not directed along the beam axis. To recapture and reuse much of the excess rubidium, a recirculation system is employed. The condenser cup which surrounds the nozzle is gold plated copper and has a 0.5 cm hole in it. It is water cooled, via an internal channel, to a temperature of ~ 15° C so that the rubidium that strikes it solidifies on the surface. To minimize thermal conduction between the oven body and the condenser cup, the recirculation line is made of thin-walled stainless steel tubing.

The oven is inserted into a larger housing that rests on kinematic support posts that provide for positioning and leveling of the oven. The entire assembly is mounted on the flange on the bottom of the oven chamber. To minimize thermal contact between the oven body and the rest of the assembly, the oven rests on a single ball bearing and is held in place via three screws in contact with the oven body.

Independent heating of the oven body, nozzle, and recirculation line is achieved by sending current through heater wire wound around each element. During typical operation, a current of 4.0 amps and 0.8 amps pass through the nozzle heater wire, and oven heater wire, respectively, resulting in an oven temperature of ~ 235° C and a nozzle temperature of ~ 245° C. This temperature difference is maintained in order to avoid condensation of liquid in the orifice. The recirculation line heater is not used during beam operation.

Following beam operation, recycling of the system is achieved by heating the recirculation line with the nozzle current reduced and the water cooling to the condenser cup removed. During this process, the condensed rubidium melts and drains through the recirculation tube into the oven. During operation the beam density near the output of the oven is ~ 6 x 10^{10} atoms/cm^3. Refilling of the oven is required after about ~50 cycles of beam operation/recycling.

5.2.2.1 Spatial Distribution of the Thermal Beam

The geometry of the system restricts the amount of the thermal beam that is available for cooling and trapping. Initially, collimation of the beam was provided by a 0.95 cm (3/8 inch) circular aperture located 48 cm downstream from the nozzle. Following implementation of Zeeman tuned slowing, the limiting aperture became the 1.6 cm (5/8 inch) inner diameter of the vacuum tube at the exit end of the solenoid. Based on this geometry, depicted in Figure 5.4, only atoms in the ± ~0.4° cone exiting the oven contribute to atoms in the trap. The calculated diameter of the thermal beam at the entrance of the funnel is 1.9 cm. The funnel coils are separated by 2.54 cm.

5.2.2.2 Velocity Distribution of the Thermal Beam

The velocity distribution of the thermal beam was modeled following the work of Ramsey [Ramsey, 1956]. Atoms exiting the effusive oven are distributed in a Maxwell

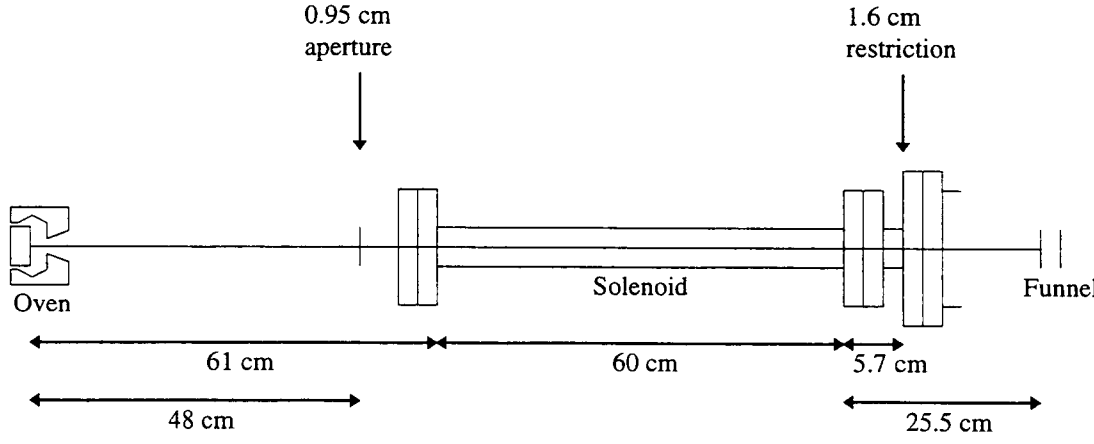

Figure 5.4 Spatial distribution of the thermal atomic beam (not drawn to scale). Atoms in the ± ~ 0.4° cone exiting the oven contribute to the trap. The diameter of the thermal beam at the entrance of the funnel is 1.9 cm. The funnel coils are separated by 2.54 cm.

speed distribution multiplied by a factor of velocity, since the exit probability is proportional to velocity. The number of atoms per second with velocities between v and $v + dv$ is given by $I(v)\,dv$ where

$$I(v) = \frac{2I_0}{\alpha^4} v^3 \exp\left(\frac{-v^2}{\alpha^2}\right). \tag{5.1}$$

The full beam intensity (I_0) is related to the detector area (A_d), the area of the source (A_s), the distance (L) from the source to the detector, the density (n) in the oven, oven factor K, and the mean velocity ($v_m = \left(2/\sqrt{\pi}\right)\alpha$) by the relationship

$$I_0 = \frac{1}{4\pi} \frac{A_d}{KL^2} n v_m A_s . \tag{5.2}$$

The source area, calculated from the orifice diameter, is $A_s = 7.85\text{x}10^{-7}\,\text{m}^2$. Length L is 1.46 m. The detector area is determined from the overlap between the probe laser used to induce fluorescence and the thermal atomic beam. For a laser with rectangular cross section measuring 2 cm x 1 cm, and a thermal beam 1.9 cm in diameter, the fluorescence area is approximately $A_d = 1.9\text{x}10^{-4}\,\text{m}^2$. The density is given by $n = P/kT$, where the vapor pressure is $P = 10^{4.312-4040/T}$ (atm) [Weast, 1978]. The most probable atomic velocity (α) inside the source is expressed as

$$\alpha = \sqrt{2\text{kT}/\text{M}}, \tag{5.3}$$

where k is Boltzmann's constant, T is the temperature, and M is the atomic mass. The factor K corrects for the shape of the oven aperture. For a cylindrical orifice of length l and radius r, K is $3l/8r$ [Ramsey, 1956].

The theoretical velocity distribution is depicted in Figure 5.5 for an oven temperature of 235° C. At this temperature, the total flux of ^{85}Rb atoms in the thermal beam is $I_0(0.72) = 1.0\text{x}10^{12}$ atoms/s. From the velocity distribution, we can estimate the number of ^{85}Rb atoms available as a function of the velocity capture range of the Zeeman

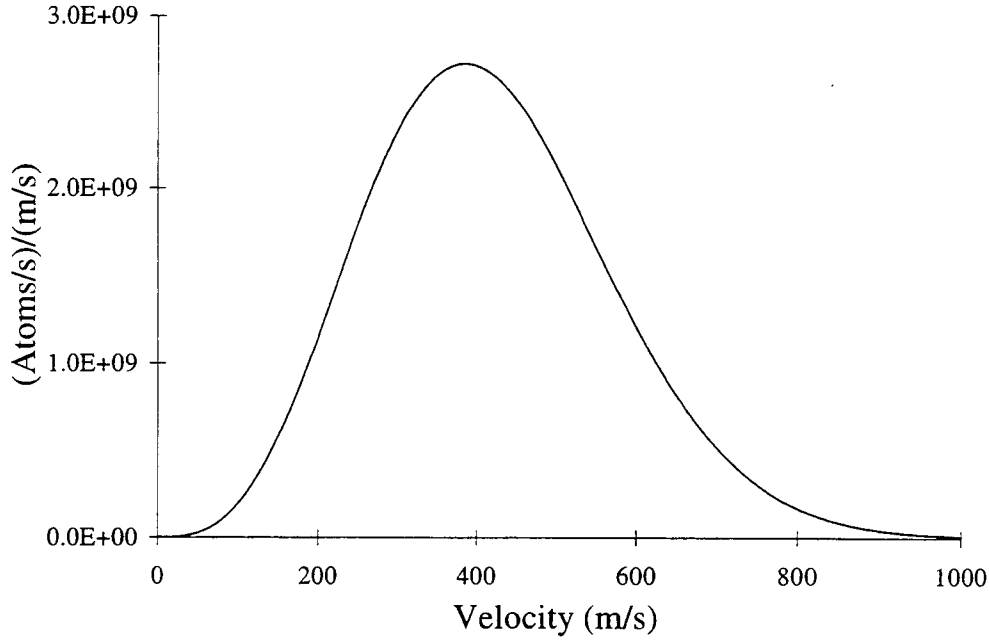

Figure 5.5 Theoretical velocity distribution of the thermal rubidium beam. The oven temperature is 235° C. The total flux is ~1.0×10^{12} atoms/s in the ^{85}Rb thermal beam.

slower. A 250 m/s capture velocity corresponds to 1.4×10^{11} atoms/s, approximately 14% of the thermal beam. A 300 m/s capture velocity increases this number to 2.4×10^{11} atoms/s.

5.2.2.3 Oven Diagnostics

As the oven runs out of atoms or problems arise, it is useful to analyze the quality and intensity of the thermal beam near the oven. To do this, a laser is directed in the window by the oven and aligned to intersect the atomic beam axis at 90°. A photodetector, located at the opposite window, monitors absorption as the laser is scanned in frequency. Since the probe laser is perpendicular to the atomic beam axis, atoms traveling along the atomic beam axis are resonant with an on-resonance probe independent of their velocity. Comparing the photodetector signal to the absorption

signal of the laser beam through a rubidium vapor cell yields information about beam quality. Figure 5.6 shows the absorption profile of the perpendicular probe laser through a working atomic beam. The narrowness of the distribution, relative to that through the vapor cell, indicates the presence of a beam. The beam density, calculated from the absorption signal, is 6 x 10^{10} atoms/cm^3. In contrast, the distribution shown in Figure 5.7 was taken when the condenser cup was clogged. The broad absorption signal indicates the presence of rubidium vapor rather than a beam. A similar "vapor cell" type absorption signal results, but with less absorption, when the oven runs out of atoms.

5.3 Lasers and Optics

The laser system consists of nine tunable diode lasers: the cooling laser, cooling re-pump laser, three trapping lasers, trap re-pump, trap master laser, gate laser, and molasses laser. An introduction to the physics of diode lasers, discussion of the extended cavity configuration, and description of the servo-locking techniques employed are provided in Section 5.3.1 through 5.3.3. The description of the optical layout used in the experiment follows in Section 5.3.4.

5.3.1 Diode Laser Operation

The traditional laser source for atomic physics research has been the tunable dye laser, and in more recent years, the titanium-sapphire laser. Diode lasers provide a simple, inexpensive alternative to such traditional sources. The lasers used in this experiment are AlGaAs double heterostructure semiconductor devices with nominal room temperature emission in the 780-790 nm wavelength range. The typical operating output power is 20 - 50 mW. The three commercially available laser sources used in this experiment are: Sharp model numbers LT024 and LT025 and Hitachi model number 7851G.

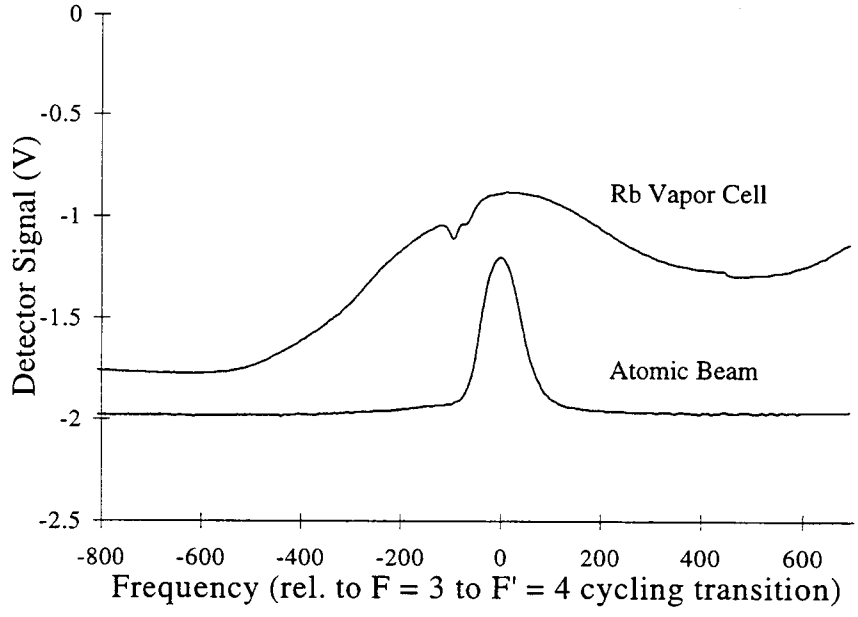

Figure 5.6 Absorption profile of a "working" atomic beam. The profile was taken near the exit of the rubidium oven using a perpendicular 13 mm x 8 mm laser with 8 mW/cm^2 intensity.

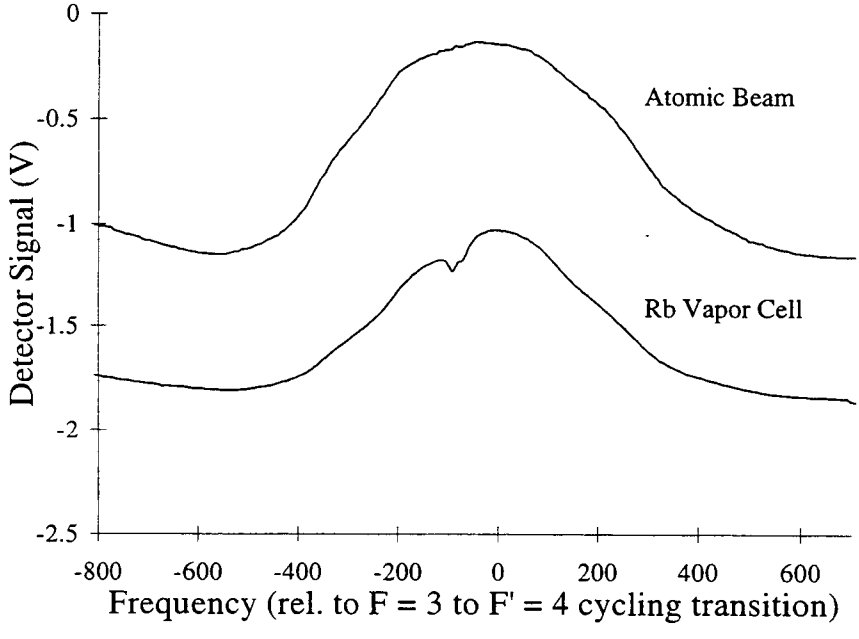

Figure 5.7 Absorption profile of a "non-working" atomic beam. The profile was taken near the exit of the rubidium oven using a perpendicular 13 mm x 8 mm laser with 8 mW/cm^2 intensity.

In a diode laser, the lasing medium is the semiconductor. Double heterostructure devices consist of an undoped active region ($Al_yGa_{1-y}As$) surrounded by an n doped and p doped region ($Al_xGa_{1-x}As$, x>y). When a current is applied to the device, electrons are injected from the n-type layer into the active region. Simultaneously, a comparable density of holes is injected from the p-type region. The radiative recombination of the electrons and holes produces photons with an energy corresponding to the bandgap of the semiconductor. The laser "cavity" is created by cleaving the semiconductor along natural crystal planes. The difference in index of refraction between the active region (n ~ 3.5) and the surrounding air provides for approximately 30% reflection. The lasers used in this experiment are index guided devices; confinement of the transverse spatial mode is achieved due to the index of refraction of the active region being higher than that of the surrounding cladding.

Since the emission region of the semiconductor laser is small (0.1 μm x 0.3 μm), the output beam is divergent. Typical angles of divergence are 30 degrees for the major axis and 10 degrees for the minor axis. In addition, the beam exhibits astigmatism due to different beam waists for the major and minor axes. Using a small focal length (6 - 8 mm) collimating lens, a collimated elliptical output beam can be achieved. An anamorphic prism can be used to produce a circular output beam. Spatial irregularities can be compensated for through spatial filtering. In the far field, the polarization of the output beam is along the direction of the minor axis.

Spacing of the laser cavity modes is dictated by the free spectral range (FSR) of the cavity, which is given by c/2nL. The Sharp lasers have a free spectral range of ~ 150 GHz, corresponding to a cavity mode spacing of about 0.3 nm at the operating wavelength of 780 nm. The Hitachi diodes exhibit a cavity mode spacing of 0.12 nm. A free running diode laser will lase on the cavity mode with the highest gain. Injection current and temperature impact the gain curve, and thereby influence the output wavelength of the laser. The injection current changes the carrier density which modifies both the index of refraction and the bandgap energy of the device. The resulting current tuning of the laser wavelength is approximately 0.01 nm/mA. The temperature affects the

cavity length and the gain curve, resulting in variations in wavelength of approximately 0.3 nm/K.

Diode lasers exhibit a typical linewidth of about 20-50 MHz. If left unmodified, their usefulness is limited in applications requiring narrowband radiation. Initial measurements of AlGaAs laser linewidths in the early 1980's revealed a Lorentzian shape linewidth, with a full width at half maximum intensity Δf that varied inversely with laser output power [Fleming, 1981b]. While these features were anticipated based on the modified Schawlow-Townes relation [Eastham, 1986], the measured linewidths were about 50 times greater than the predicted values. The linewidth broadening was subsequently attributed to variations of the refractive index of the laser cavity with instantaneous carrier density [Henry, 1982].

Several methods have been employed to reduce the laser linewidth; the most widely used method being optical feedback, which consists of directing part of the laser light back into the cavity. Optical feedback reduces the linewidth primarily by increasing the optical cavity length. The extended cavity decouples the resonant laser frequency from strong dependence on the index of refraction of the semiconductor [Fleming, 1981a]. As a result, linewidth broadening due to index of refraction fluctuations is reduced. Optical feedback narrowing of diode laser linewidths has been achieved using a variety of reflecting elements including a mirror [Chinone, 1978], Fabry-Perot cavity [Dahmani, 1987; Hemmerich, 1990], optical fiber cavity [Figueroa, 1980], and grating [Wieman, 1991; Maki, 1993].

Optical feedback is also used to influence the laser's frequency. A diode laser cavity has very low finesse and the gain curve is fairly flat as a function of wavelength [Wieman, 1991]. As a result, the gain of the system only weakly depends upon wavelength and the lasing wavelength is easily perturbed. By using a wavelength selective cavity to externally impose the desired wavelength, wavelength selection can be achieved. Tunability of such systems is achieved by appropriate modulation of the external reflecting element.

5.3.2 Grating Feedback Stabilized Laser Diode

In this experiment, optical feedback from a diffraction grating [Maki, 1993] is used to select the wavelength and narrow the linewidth of the diode laser. A schematic of the laser assembly is shown in Figure 5.8 [Swanson, 1995].

The collimated laser beam is incident on a holographic diffraction grating mounted in the Littrow configuration [Yariv, 1985]. In this configuration, the zero order (undiffracted) beam is reflected off the grating and serves as the output beam. The first order diffracted beam provides optical feedback to the laser. A diffraction grating will reflect a given order of the incident beam back along the direction of incidence provided the grating equation $2d\cos\theta = m\lambda$ is satisfied, where m is the diffraction order, d is the ruling distance, and θ is the angle between the propagation direction and the normal to the grating surface. Using an 1800 line/mm grating and a wavelength of 780 nm, an angle θ of approximately 45° is required to reflect the first order diffracted beam back into the laser. In this configuration the laser cavity is defined primarily by the rear laser facet and the diffraction grating. The resulting grating-controlled wavelength is that which satisfies the grating equation since other wavelengths are not reflected back along the axis of the laser cavity. Tuning of the laser wavelength is accomplished by rotating the grating. Approximately 75 % of the light is reflected into the zero order mode. Ten percent is diffracted into the first order beam.

While the output wavelength is determined by the grating orientation, not all wavelengths are accessible at a given injection current and temperature due to the longitudinal cavity mode spacing. To achieve the desired wavelength, the proper combination of temperature and injection current is found. These parameters are then carefully maintained to provide a stable, resonant source. Temperature is controlled and stabilized to several mK using a Peltier element and a control circuit [Bradley, 1990]. The circuit employs a thermistor, located near the diode laser, in a Wheatstone bridge configuration. Changes in temperature modify the resistance of the thermistor in the bridge, which produces an error current. This signal is amplified and used as feedback to regulate the power to the Peltier element. In addition, the laser assembly is housed in a

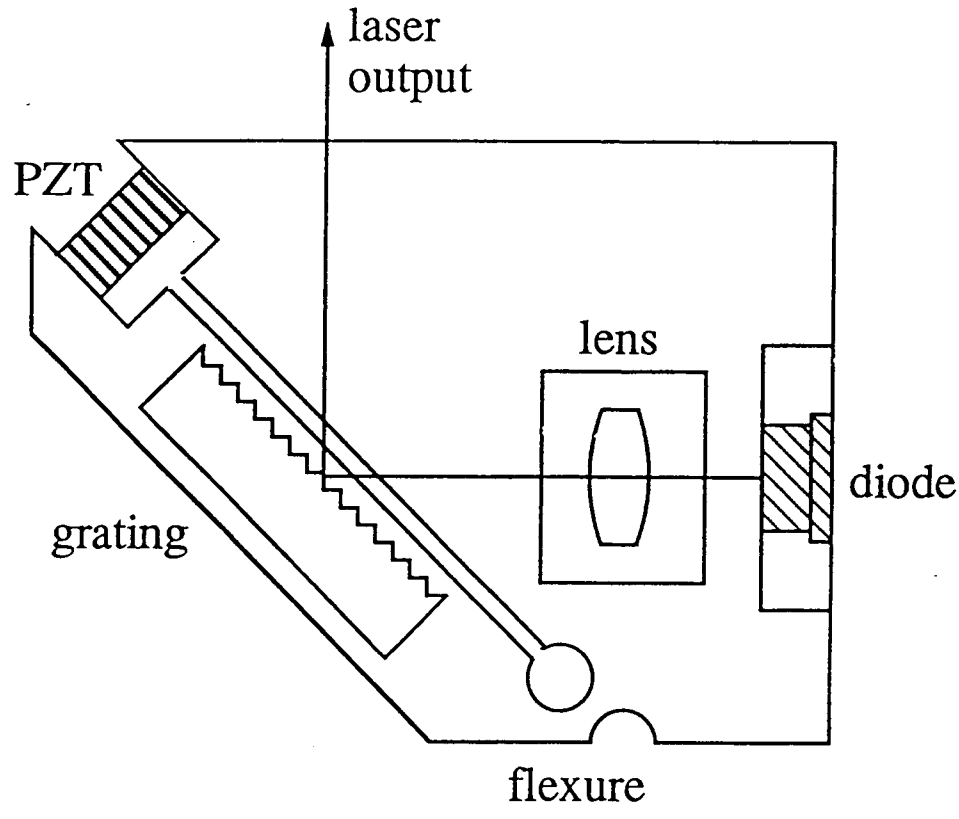

Figure 5.8 Diode laser with optical feedback from a diffraction grating.

Plexiglas enclosure to reduce thermal drifts. The injection current is provided by a battery driven low-noise current source stable to 1 μA [Hemmerich, 1990].

Fine tuning of the laser wavelength is achieved by applying a voltage to the piezo-electric-transducer (PZT) located in the flexure shown in Figure 5.8. Application of ± 15 V provides ±1 μm of PZT extension, which allows for a tuning range of 5 - 10 GHz.

The linewidth of the laser system is limited by mechanical vibrations and thermal fluctuations of the extended cavity. Correction for small frequency fluctuation is provided by electronic stabilization of the laser injection current. The resulting linewidth of the laser system is approximately 150 kHz.

5.3.3 Frequency Stabilization and Calibration

The temperature and drive current stabilization circuits discussed in section 5.3.2 help to minimize frequency drift of the lasers. However, additional stabilization is required to achieve long term stability at a calibrated frequency. Frequency calibration is accomplished using a Doppler-free saturated absorption spectrum. Frequency stabilization is achieved using one of several laser frequency stabilization techniques such as polarization spectroscopy locking [Wieman, 1976], frequency-offset locking [Maki, 1993], and etalon locking [Hemmerich, 1990]. In each of the stabilization techniques an electronic servo-control circuit is used to lock the laser frequency to the appropriate dispersive signal.

5.3.3.1 Saturated Absorption Spectroscopy

Saturation effects in absorption spectra, first observed after the advent of the gas laser in 1961 [Levenson, 1988], result from nonlinear optical effects. Such spectra are commonly used for frequency calibration. A typical saturated absorption spectroscopy setup is shown in Figure 5.9 [Smith, 1971].

Two counter-propagating laser beams of the same frequency are directed through an evacuated cylindrical glass cell containing a small amount of room temperature rubidium. The beam traveling directly through the sample is designated the probe beam. A second beam, referred to as the pump beam, is directed around the cell and enters from the opposite direction. The pump beam is aligned to intersect the probe beam at a small angle, and thus overlap over the length of the cylinder. The transmitted light intensity of the probe beam is measured using a photodetector. When the pump and probe beams are sufficiently overlapped, small saturated absorption dips are visible in the absorption lines. In practice, the saturated absorption dips can be viewed using a single beam, due to reflections off the windows of a well aligned vapor cell. A sample absorption spectrum of the $5S_{1/2}$ to $5P_{3/2}$ transition of rubidium was shown in Chapter 2 (see Figure 2.3.) An

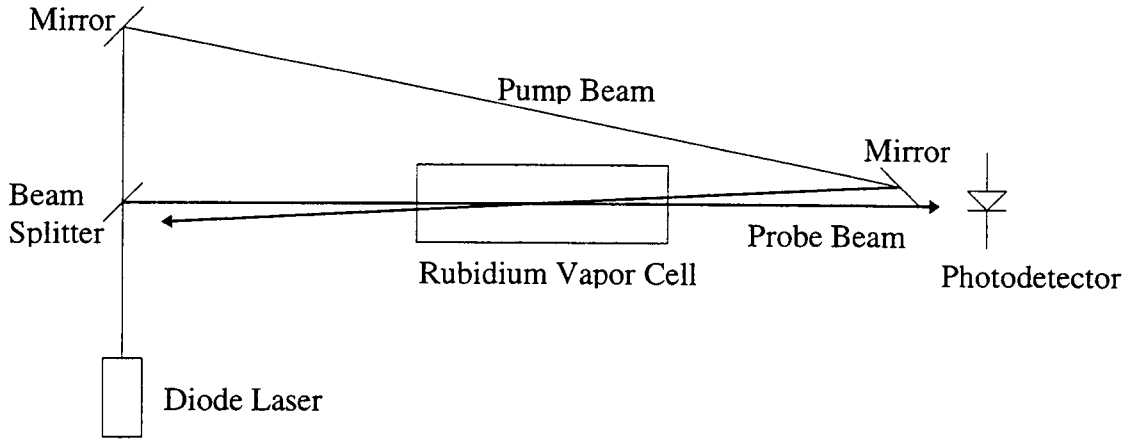

Figure 5.9 Saturated absorption spectroscopy setup.

expanded view of the ^{85}Rb F = 3 → F′ = 2, 3, 4 and ^{87}Rb F = 2 → F′ = 1, 2, 3 absorption peaks are illustrated in Figure 5.10. The saturated absorption features are discussed below.

The dip at the center of the ^{85}Rb F = 3 → F′ = 2, 3, 4 absorption peak is called the Lamb dip. It results from atoms with $v = 0$ axial velocity that are simultaneously resonant with both lasers. The atoms absorb less light from the probe beam because the pump beam has already partially depleted the ground state. The Lamb dip visible in the spectra corresponds to the zero-velocity resonance of the F = 3 → F′ = 4 transition. Similar Lamb dips occur for the zero-velocity resonances of the F = 3 → F′ = 3 and F = 3 → F′ = 2 transitions. However, they are not visible in this spectra (see discussion below).

The off-center dips, called crossover peaks, occur at a frequency halfway between zero-velocity resonances. They can occur if two transitions that share a common ground state differ in frequency by an amount that is smaller than the Doppler width of the transition. Because of the Doppler shift, an atom traveling with axial velocity v encounters one laser at a frequency $\omega_L + kv$ and the other at a frequency $\omega_L - kv$. When one laser is shifted up in frequency to one atomic transition and the other is shifted down in frequency to the other atomic transition, a saturated absorption dip occurs as a result of

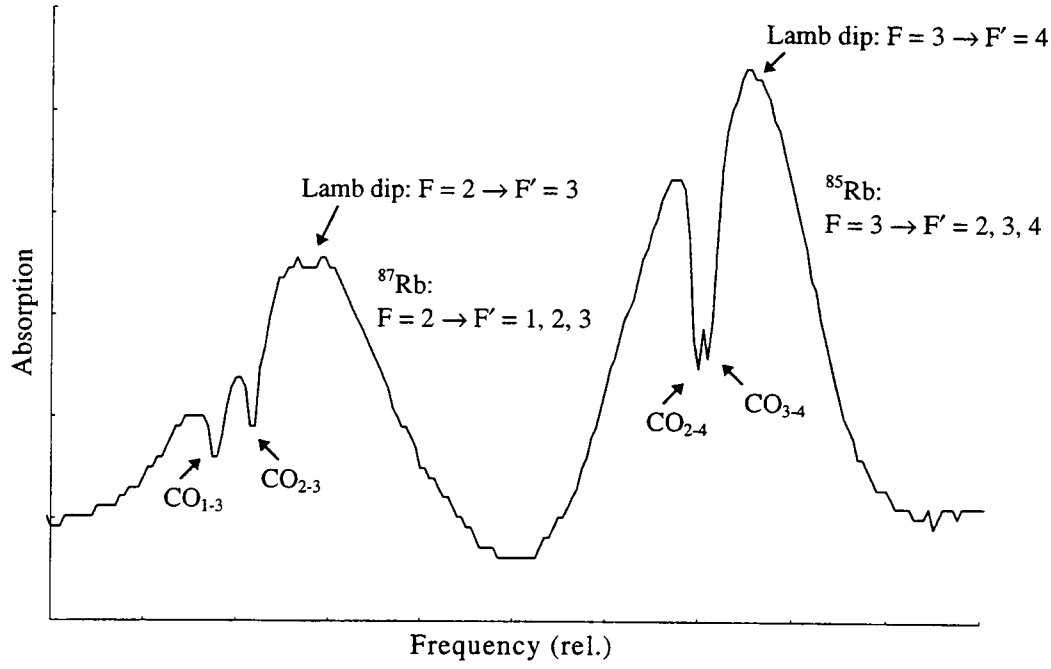

Figure 5.10 Saturation absorption spectra for the F = 3 → F′ = 2, 3, 4 transitions in ^{85}Rb and F = 2 → F′ = 1, 2, 3 transitions in ^{87}Rb.

depletion of the ground state. The two crossover (CO) resonances visible in the ^{85}Rb F = 3 → F′ = 2, 3, 4 absorption peak occur at frequencies, relative to the Lamb dip, of 60.35 MHz (CO_{3-4}) and 92.05 MHz (CO_{2-4}). The 31.7 MHz frequency splitting between the two crossover peaks is used for calibration purposes. The Lamb dip and crossover peaks visible in the ^{87}Rb peak are labeled.

For the spectra of the ^{85}Rb F = 3 → F' = 2, 3, 4 transition, only the dips associated with the F′ = 4 upper state are visible. This is related to both the experimental configuration used to take the spectra and optical pumping effects. Because of constraints imposed by electric dipole selection rules, the F′ = 4 upper state can only decay to the F = 3 ground state (ΔF = -1). In contrast, the F′ = 2 and 3 upper states have an allowable decay route to the non-resonant F = 2 ground state. The F = 3 → F′ = 4 transition is therefore referred to as the "cycling transition." For a cycling transition, more absorption of the pump laser is possible and the saturation features are therefore larger. With less laser intensity and better overlap between the counter-propagating pump

and probe lasers the saturation features corresponding to the non-cycling transitions can also be observed.

5.3.3.2 Polarization Spectroscopy Locking

One method of frequency stabilization is to electronically servo-lock the laser to a feature on the saturated absorption spectra. Polarization spectroscopy [Wieman, 1976], is used to create a dispersive saturation feature for more effective servo-locking. The spectroscopy setup illustrated in Figure 5.9 is modified for polarization spectroscopy; a quarter wave plate is added into the pump beam path and a linear polarizer is inserted in the probe beam path before the photodetector. Since the laser output is nominally linearly polarized, the quarter wave plate provides a nearly circularly polarized pump beam. The linearly polarized probe beam passes through the rubidium cell and then through a nearly crossed linear polarizer before entering the photodetector. Because of optical pumping among the magnetic sub-levels, varying the orientation of the linear polarizer or the amount of circular polarization in the pump beam impacts the saturation features and therefore the shape of the absorption spectra [Schmidt, 1994]. A polarization spectroscopy signal is shown in Figure 5.11. The master laser for the trap is servo-locked to the high frequency side of the $v = 0$ resonance shown in Figure 5.11. The frequency range over which the master laser could be servo-locked was measured to be ± 30 MHz from the $F = 3 \rightarrow F' = 4$, $v = 0$ resonance. The trap re-pump, tuned to the $F = 2 \rightarrow F' = 3$ transition, is locked in a similar manner.

For applications where the desired laser frequency is farther than a few linewidths from a particular hyperfine transition (i.e., beyond the locking range of the saturated absorption feature), an acousto-optic modulator (AOM) can be used to frequency shift the location of the Lamb dip. To accomplish this, an AOM is placed in the pump beam path at an orientation such that the acoustically modulated output beam, with frequency $\omega_L + \omega_{AOM}$, is transmitted through the vapor cell. The RF frequency driving the AOM controls

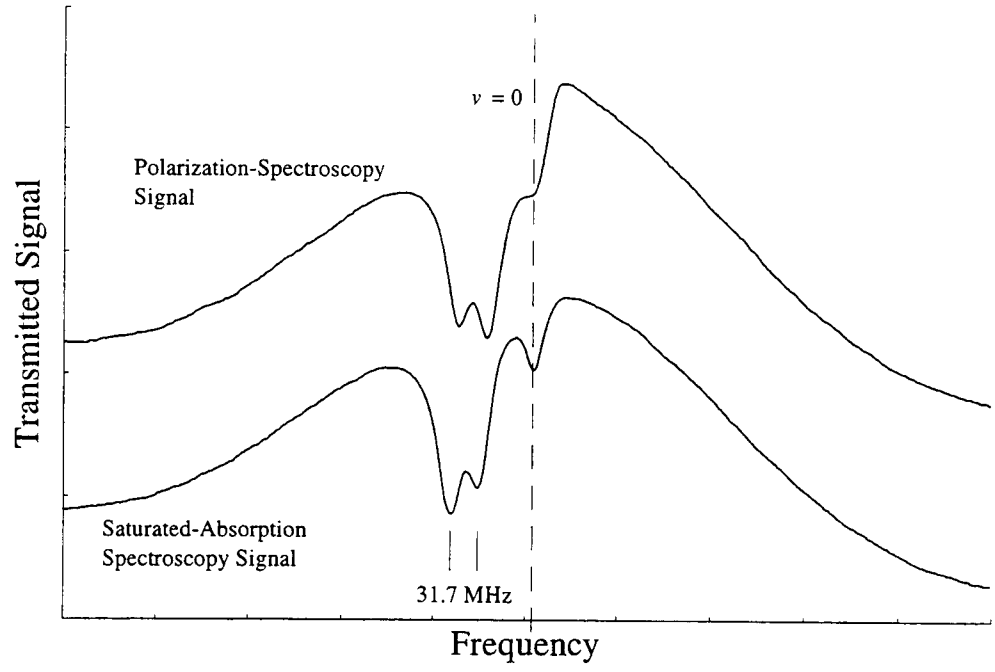

Figure 5.11 Polarization spectroscopy signal of the ^{85}Rb F = 3 → F ' = 2, 3, 4 transition.

the frequency shift and ranges in value from 50 to 110 MHz. In this configuration, an atom in the vapor cell is resonant with a counter-propagating pump beam provided $\omega_{ATOM} = \omega_L - kv + \omega_{AOM}$. The probe beam is simultaneously resonant provided $\omega_{ATOM} = \omega_L + kv$. Thus, the laser must be shifted up in frequency from the hyperfine transition by an amount ½ ω_{AOM} to be simultaneously resonant and produce the Lamb dip. Using the AOM at ~100 MHz and polarization spectroscopy set-up, the downstream molasses laser can be servo-locked ~ 20-50 MHz from the F = 3 → F ' = 4 hyperfine transition.

5.3.3.3 Frequency-Offset Locking

During operation of the two-dimensional magneto-optical trap, the three trapping lasers, designated front, back and vertical, are operated at relative frequencies of $(f + \Delta f)$, (f), and $(f - \Delta f)$ respectively. To stabilize the frequency differences among the three

lasers, they are each independently locked to a master laser using a frequency-offset locking system described in detail in the paper by Maki *et al.* [Maki, 1993]. The master laser is first servo-locked to a polarization spectroscopy signal as discussed in section 5.3.3.2. Each trapping laser is then frequency-offset locked to the master laser using an electronic frequency discriminator circuit. A portion of both the master laser and trap laser beams is heterodyned in a fast photodiode with flat frequency response to 100 MHz. The heterodyned signal is amplified by 30 dB and fed into the frequency discriminator that produces an output voltage proportional to $\frac{1}{2} - f T$, where f is the beat note difference frequency and T is the electronic delay of the discriminator circuit. The output signal is sent to the integrating servo-control circuit that controls the trap laser's frequency. Using this scheme, the trap laser is frequency-offset locked to the master laser with an offset range of 2 to 30 MHz. Adjustment of the offset voltage in the servo-control circuit or the electronic delay in the frequency discriminator controls the offset frequency. Since the stability of the master laser is passed on to the trap laser, the resulting long term stability is on the order of the laser linewidth.

5.3.3.4 Etalon Locking

During chirped cooling, the cooling laser must be scanned in frequency to provide continuous Doppler shift compensation. Frequency stabilization was achieved by servo-locking the laser to a Fabry-Perot etalon. The etalon consists of two curved mirrors of high reflectivity, separated by a distance of $L = 5$ cm. The cavity finesse is approximately 80. The incident beam is transmitted provided the wavelength satisfies $L = n \lambda / 2$, where n is an integer. Applying a voltage to a piezoelectric element at the output mirror changes the mirror spacing. To lock the laser to the cavity at a set wavelength, the length of the etalon cavity is electronically adjusted such that the desired wavelength is transmitted. The laser frequency is then stabilized to the side of the resulting Airy transmission curve using a servo-control circuit. To continuously tune the laser frequency the etalon cavity

length and laser PZT are scanned synchronously while the laser remains servo-locked to the cavity.

The laser used in Zeeman-tuned cooling is too far from a hyperfine transition to be servo-locked using either polarization spectroscopy or frequency-offset locking. The detuning, which depends on solenoid current, ranges from -234 MHz (0 amp bias field) to -875 MHz (24.25 amp bias field) from the zero-field atomic resonance. The laser could be locked to an etalon of fixed cavity length. However, it was found to be sufficiently stable without supplementary stabilization.

5.3.4 Optical Layout and Laser Characteristics

A layout of the lasers and optics used in the experiment is provided in Figures 5.12 and 5.13. Figure 5.12 shows the optical layout of the trapping lasers. The master laser is locked to a polarization spectroscopy signal. The three trapping lasers are each frequency-offset locked to the master laser. Each of the trapping lasers is split into two beams prior to entering the trap region; the pairs are designated front, back, and vertical. A telescope is used in the optical path of each of the trapping lasers to produce an expanded, collimated beam. The front and back trapping lasers have dimensions 2 cm x 1 cm and an intensity of 4.5 mW/cm^2 each at the entrance windows to the chamber. The vertical beam, which has a circular cross section of diameter 1.5 cm, has an input intensity of 7.5 mW/cm^2. To improve the spatial quality of the beams, spatial filtering is provided by a 30 micron pinhole placed at the focus of the first lens in each beam-expanding telescope. The vertical beam also has an optical isolator in the beam path prior to the beam splitter to minimize optical feedback to the laser from the counter-propagating beams. A quarter wave plate is placed in the beam path of each of the trapping lasers just prior to entry into the chamber. The counter-propagating pairs are configured $\sigma^+ - \sigma^-$.

Figure 5.13 depicts the lasers involved in cooling and diagnostics. Both the cooling laser and cooling re-pump laser are operated without electronic stabilization for

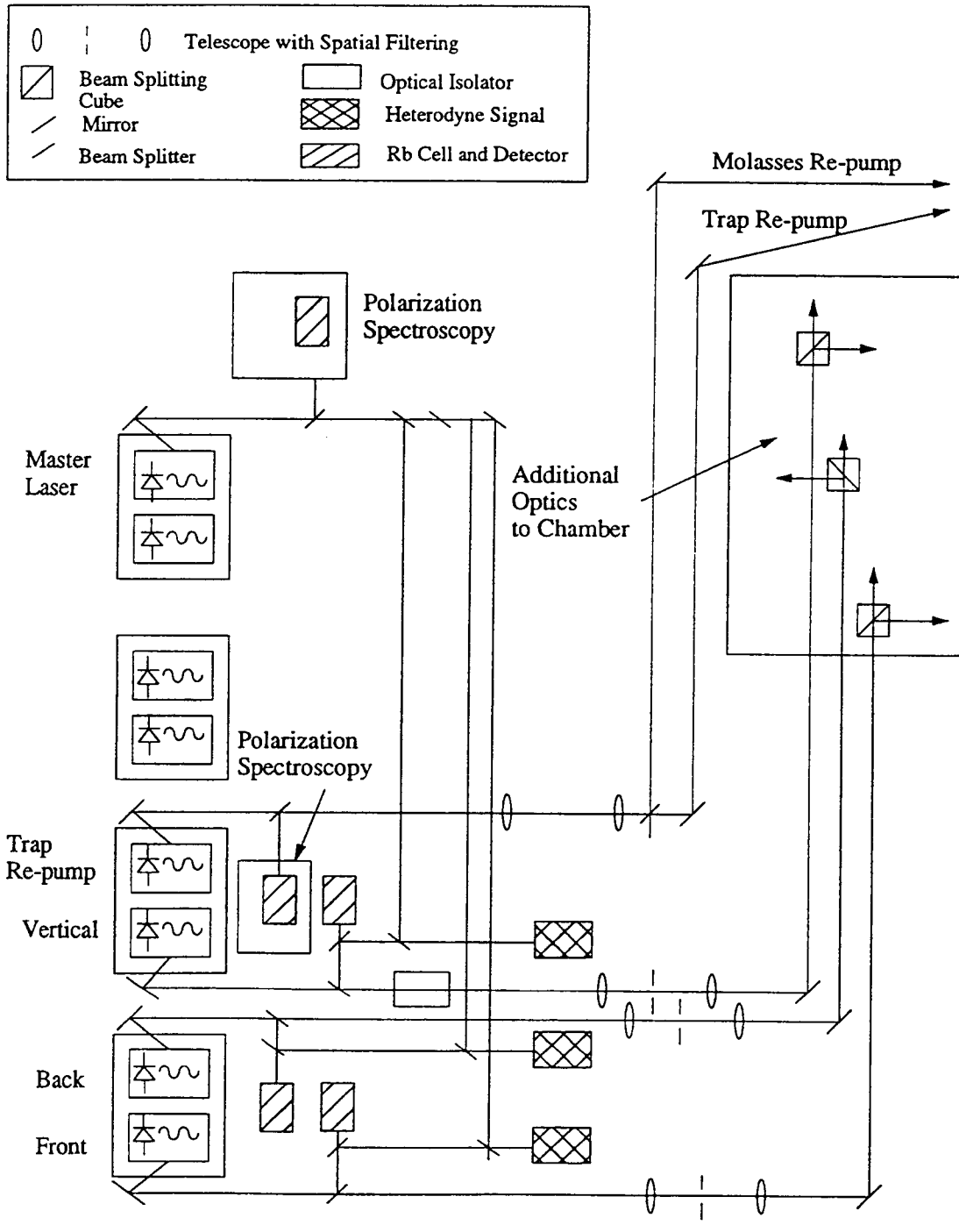

Figure 5.12 Optical layout for the trapping lasers.

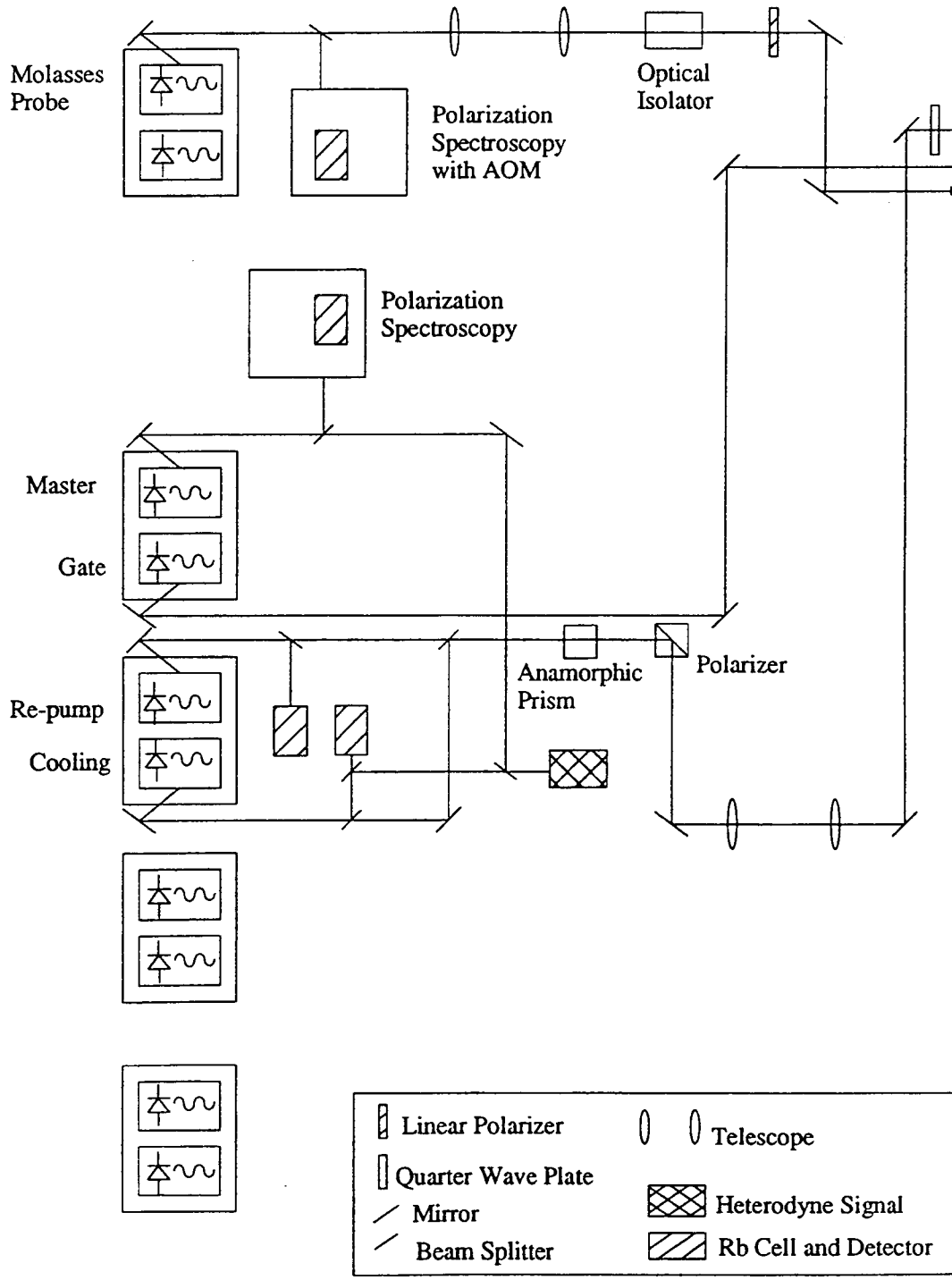

Figure 5.13 Optical layout for the cooling and diagnostic lasers.

Zeeman slowing. The frequency of the cooling laser is monitored by observing a heterodyne beat-note between the cooling laser and the polarization spectroscopy locked master laser using a fast photo-diode and radio-frequency spectrum analyzer. The cooling laser and re-pump laser beams are each expanded using a telescope in the beam path. An anamorphic prism is used to generate a circular beam shape. The cooling laser is 1.4 cm in diameter at the entrance to the chamber. At this location, the intensity is 7 mW/cm^2. The re-pump laser has a diameter of 1.4 cm and an intensity of 0.1 mW/cm^2. Both lasers are focused on the oven in order to maximize efficient overlap between the laser and the atomic beam. Circular polarization of the cooling and re-pump beams is provided by a linear polarizer and quarter wave plate. Due to optical constraints, the linear polarizer is located early in the optical path. To maximum the quality of circular polarization for Zeeman slowing, the quarter wave plate is located just prior to the entrance of the chamber.

The gate laser is operated without supplemental electronic stabilization. The beam size is limited by a circular aperture to 2 mm in diameter. It has an intensity of 35 mW/cm^2. The molasses laser is locked to a polarization spectroscopy signal with an AOM in the pump beam to shift the locking frequency. This 1 cm x 0.25 cm beam can be limited by a circular aperture and has intensity of 25 mW/cm^2. The laser is linearly polarized entering the chamber and is transmitted through a quarter wave plate and retro-reflected off a mirror located inside the vacuum chamber. This configuration yields lin $\perp$ lin molasses. To change to $\sigma^+ - \sigma^-$ molasses, a quarter wave plate is added to the molasses laser beam path prior to entry into the chamber.

5.4 The Atomic Funnel

The magnetic quadrupole field for the 2-dimensional magneto-optic trap is generated by sending current through copper tubing bent into a hairpin geometry [Riis, 1990]. A schematic of the funnel is shown in Figure 5.14. The 3/16 inch diameter copper tubing is configured to approximate four infinite straight wires located at the

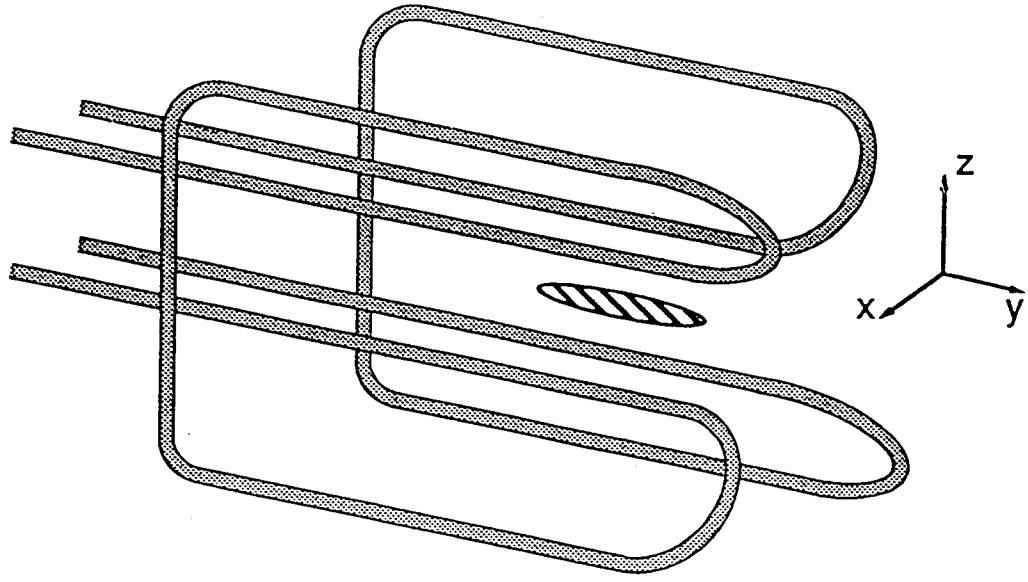

Figure 5.14 The two-dimensional magneto-optic trap or atomic funnel.

corners of a 1 inch square. The return paths, located at the corners of a 2.5 inch square, diminish the field strength by approximately 20 %. With a current of 70 amps, the radial magnetic field gradient is approximately 13 G/cm in the trapping region. Cooling of the coils is provided by running water through the copper tubing.

The configuration for operation of the atomic funnel is illustrated in Figure 5.15. The four horizontal trapping lasers are in the *xy*-plane and enter the trap region at 45° relative to the funnel axis. To eject atoms from the trap, the front [back] horizontal laser pairs are shifted down [up] in frequency by an amount Δf. The vertical pair counter-propagate along the *z*-axis tuned to a frequency *f*. This moving molasses configuration [Kasevich, 1991] imparts a drift velocity to the atom of $\mathbf{v} = \sqrt{2}\,\lambda\Delta f\,\hat{j}$ [1.1 (m/s)/MHz for rubidium]. The gate laser and molasses laser included in the picture are used for diagnostic purposes and beam characterization. The molasses laser is also used to provide a one-dimensional downstream molasses region for transverse cooling of the atomic beam.

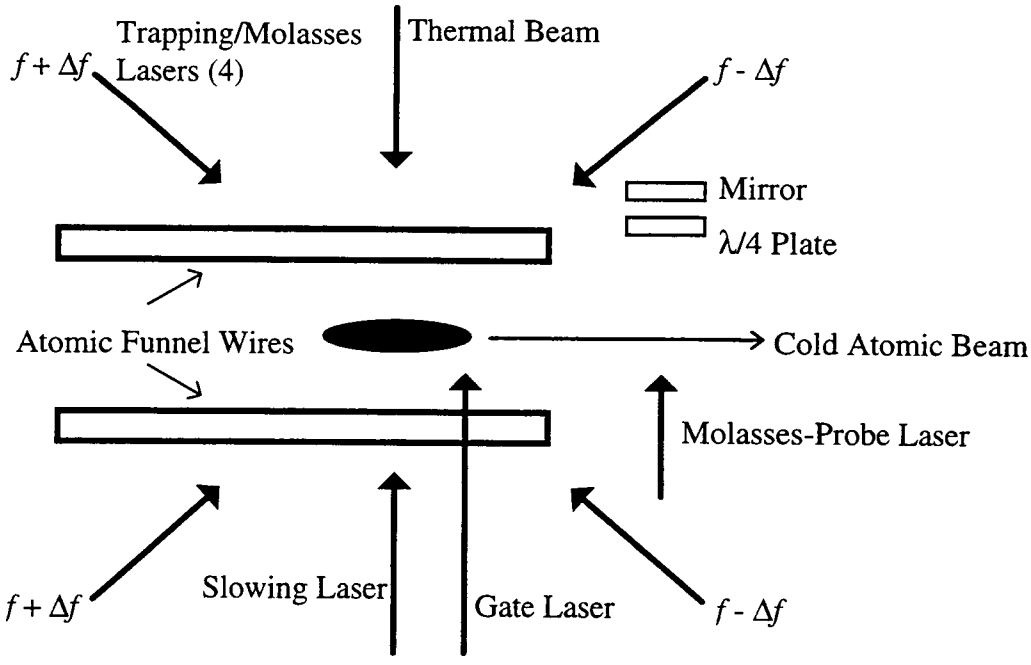

Figure 5.15 The atomic funnel with the horizontal lasers detuned to eject atoms from the trap.

5.5 The Surface Ionization Detector

Detection of the low-velocity atomic beam ejected from the funnel is accomplished using a surface ionization detector. Detection occurs in two steps: beam ionization and ion detection. Ionization of the neutral atomic beam is accomplished using a heated metal surface. Detection of the ions can be performed a number of ways. In this experiment, a microchannel plate amplifier is used to amplify the signal to a detector anode. The amplified pulses can then be counted via a particle counter or, for a sufficiently large count rate, the DC current can be monitored. The theory of surface ionization is reviewed in section 5.5.1. Microchannel plate amplification is discussed in section 5.5.2. The design and operating parameters of the surface ionization detector used in this experiment are discussed in section 5.5.3.

5.5.1 Ionizing the Neutral Atomic Beam

When a neutral atom strikes a hot surface an electron may be transferred from the atom to the surface, thus ionizing the atom. Atoms can be efficiently ionized provided the ionization energy of the atom I is less than the work function ϕ of the hot surface. For a surface at temperature T, the ratio of positive ions to neutral atoms is given by [Ramsey, 1956]

$$\frac{n_+}{n_0} = \exp\frac{-e(I-\phi)}{kT}. \tag{5.4}$$

Thus, the percent of atoms ionized can be written

$$\frac{n_+}{n_+ + n_0} = \left[1+\exp\frac{e(I-\phi)}{kT}\right]^{-1}. \tag{5.5}$$

The ionization energy of rubidium is 4.18 eV. Suitable hot wire materials include rhenium or tungsten, with work functions of 5.00 eV and 4.55 eV respectively. At a temperature of 1200 K, rhenium ionizes 99.9% of the rubidium atoms that strike it. Tungsten will ionize 97% of the atoms.

5.5.2 Microchannel Plate Amplification

Microchannel plates (MCP)[4] are used to amplify the ion current generated by the hot wire. Originally developed for military night vision goggles, MCP assemblies can detect ions, electrons, soft x-rays and ultraviolet light. A microchannel plate consists of an array of small holes or microchannels. Each microchannel functions as a channel electron multiplier (CEM). The operation of a CEM is similar in principle to the electron cascade process in a photomultiplier tube. The microchannel walls are coated with a

4 The device description and performance specifications detailed herein are based on microchannel plate product literature provided by Galileo Electro-Optics Corporation.

layer of material which emits secondary electrons when struck by energetic photons or charged particles. A single MCP contains ~10^5 independent channels, which are connected in parallel via metal electrodes deposited on the front and back surfaces of the MCP assembly. A bias voltage of 800 to 1000 volts applied to the MCP accelerates the emitted electrons toward the output end of the channel. As emitted electrons travel down the channel, additional secondary electrons are generated. The avalanche process can yield 10^4 electrons per input pulse. Employing two microchannel plates in series, a gain of 10^7 or more can be obtained.

The detection efficiency of the MCP depends on both the type and kinetic energy of the incoming particle. The detection efficiency ranges from 5 to 40% for 0.5 to 3 KeV ions.

5.5.3 Detector Design and Operation

The surface ionization detector is illustrated in Figure 5.16 [Silva, 1996]. It consists of a rhenium ribbon, a pair of microchannel plates, an accelerating grid, a repelling plate and a detector anode. A detailed description of the mechanical design of the detector is found in the work of Silva [Silva, 1996]. The electrical configuration for operation of the detector is illustrated in Figure 5.17.

The ionizing surface in the detector is a rhenium ribbon of rectangular cross section measuring 760 μm x 25 μm. The height of the ribbon installed in the detector is 2.54 cm. The purity of the material is 99.99% with no trace alkalis. The typical contaminants (< 1 ppm) are Al, Cu, Ca, Mg, Fe and P. Rhenium is commercially available in ribbon or wire in a variety of sizes[5]. In the present configuration, the ribbon is installed with the wide edge toward the incoming atomic beam to maximizing overlap between the beam and the ionizing surface, thereby providing the largest signal. Ribbon was chosen over wire to maximize the front surface area while minimizing the cross sectional area. Spatial resolution, which is limited by the width of the ribbon, can be

5 The rhenium ribbon used in this experiment was purchased from ESPI.

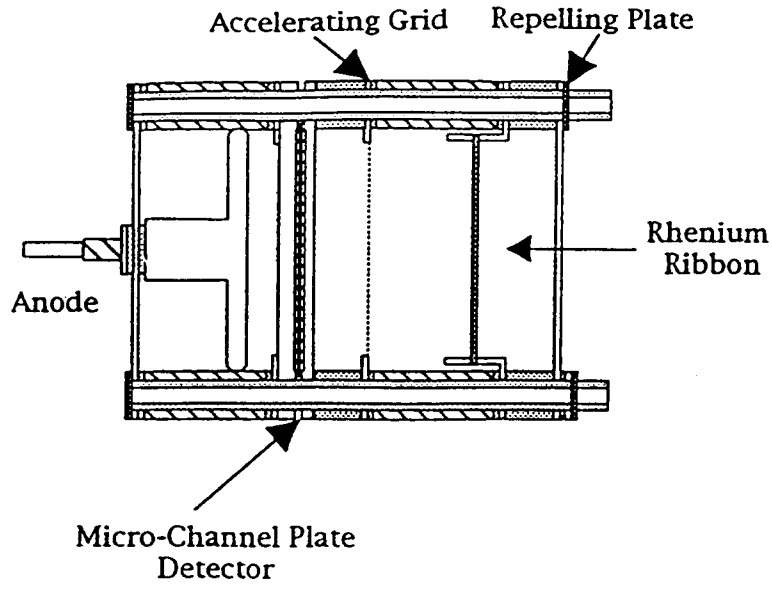

Figure 5.16 Schematic of the surface ionization detector.

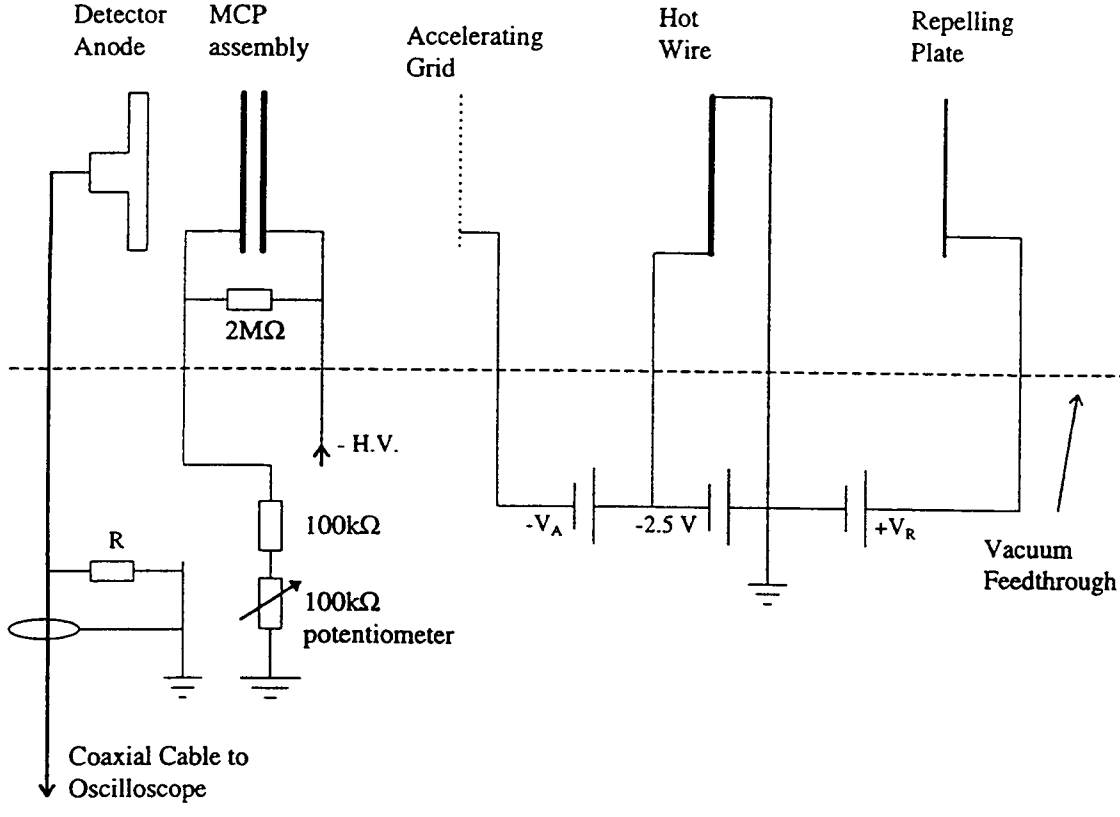

Figure 5.17 Electrical configuration for the surface ionization detector.

enhanced for future work by turning the ribbon on edge or using a smaller diameter wire. A current of 1.25 amps (~2.5 V) is used to heat the rhenium ribbon to an estimated temperature of 1200 K.

The MCP assembly consists of a pair of 25 mm microchannel plates held in a stainless steel assembly at a separation of 0.008 inches. The front surface of the MCP assembly is held at -1800 V. The potential on the back plate can be varied from -75 to -150 V depending on the resistance of the external 100 kΩ potentiometer. The back plate bias voltage provides an electrical potential to accelerate the electrons emitted in each microchannel toward the anode. The stainless steel anode is electrically isolated from the rest of the detector by a nylon washer and the detected signal is carried on a shielded coaxial cable to a floating shield vacuum feedthrough. Outside the vacuum chamber, the anode is connected through a resistor to ground. The value of the resistor is selected based on the desired detection method. For pulse counting a resistance of 50 Ω is used. To monitor the DC current, a 1 MΩ resistor or larger is employed.

The accelerating grid and repelling plate were designed to generate an electric field to increase the flux of ions reaching the MCP's. To date, gains achieved using the field have been insignificant.

Chapter 6: Experimental Results: The Zeeman Slower

The performance of the Zeeman slower was characterized as the controllable system parameters such as solenoid current, laser intensity, frequency, and polarization were modified. The primary performance criterion is the number of ~20 m/s slow atoms available for loading the atomic funnel. Comparison is made between Zeeman cooling and the previously employed method of chirped cooling. In addition, σ^- and σ^+ cooling are compared to provide insight into differences between the two methods. Results for ^{87}Rb are included to compare the efficiency of the Zeeman slowing process for each isotope.

To characterize the performance of the Zeeman slower, the velocity distribution of the atoms emerging from the solenoid was recorded as system parameters were modified. The experimental configuration used to characterize the velocity profile of the atomic beam exiting the Zeeman slower is illustrated in Figure 6.1. For each velocity profile the cooling laser was tuned to the desired frequency. A probe laser beam was aligned to intersect the atomic beam in the funnel region at an angle of 45 degrees. The probe laser was scanned in frequency through the rubidium resonance. A photomultiplier (PMT) tube measured fluorescence from the atomic beam while a photodetector monitored the rubidium absorption spectrum through a vapor cell. The PMT and photodetector signals were recorded using a computer and commercially available data acquisition software. A sample fluorescence signal and the corresponding rubidium absorption profile are illustrated in Figure 6.2. The relationship between velocity and frequency is determined using the crossover peaks in the rubidium absorption spectrum as a frequency scale along with the relation $f = (k/2\pi)\, v \cos(45°)$. When a sinusoidal, rather than saw tooth, voltage ramp is applied to the PZT to scan the frequency of the laser, the frequency scale is not a linear function of time (elapsed time t is $t = nr$, where r is the sample rate and n is the data point number). In such cases, the frequency scale is first calibrated using the relationship $f = f_0 + A \sin[(2\pi/T)\, t]$, where T is the sine wave period, and the amplitude A and offset f_0 terms are determined using the crossover peaks for frequency calibration.

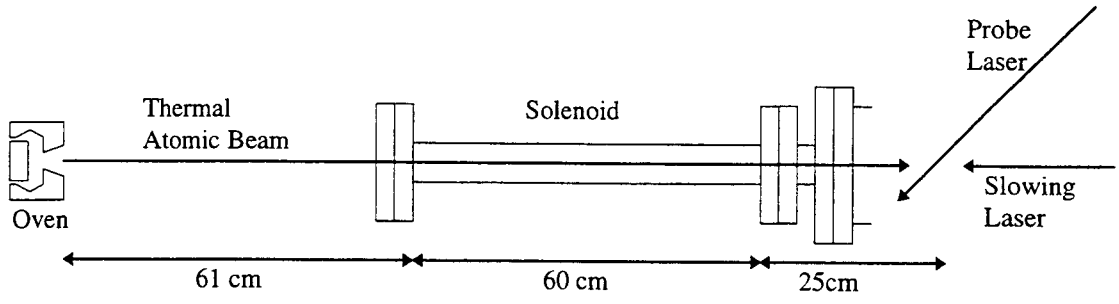

Figure 6.1 Experimental setup for characterizing the velocity distribution of atoms emerging from the solenoid.

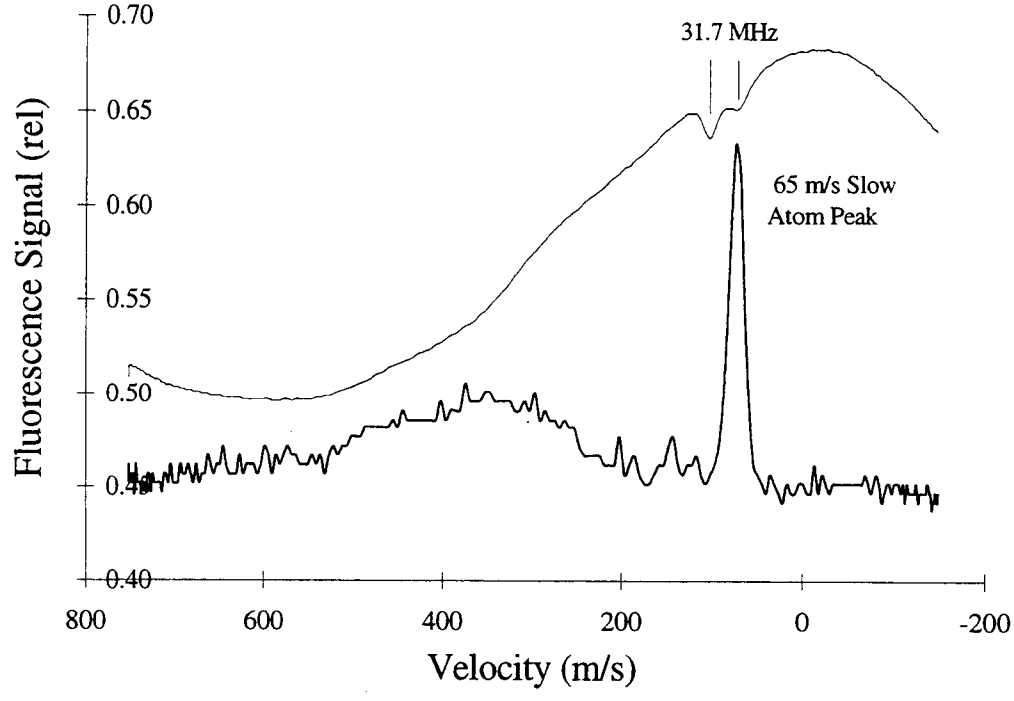

Figure 6.2 Fluorescence profile of the Zeeman slowed atomic beam. The cross-over peaks in the rubidium profile are separated by 31.7 MHz and are used to calibrate the velocity scale.

6.1 Optimizing System Parameters

Several parameters impact the performance of the Zeeman slower. The theoretical model was used to establish preliminary guidelines for these parameters. The optimal values, clarified experimentally, are summarized below.

Small variations in the taper solenoid current from the designed operating value of 26 amps did not significantly impact the performance of the solenoid. For a taper current of 28 amps, the number of slowed atoms decreased about 10% due to a decrease in capture velocity as the slope of the field became too steep for the faster atoms. Taper current less than ~24 amps produced significantly fewer slow atoms since the slope of the taper field dictates the rate of deceleration. The bias solenoid field was designed to operate at 24.25 amps. However, the signal was found to increase with decreasing bias field current. The relationship between bias field current and performance is discussed in detail in Section 6.2.1.

Decreasing the intensity of the cooling laser below the typical value of 7 mW/cm^2 had a significant impact on the number of atoms in the slow beam. For a laser intensity of 3.4 mW/cm^2, the number of atoms in a 30 m/s cooled beam decreased by approximately 50%. The model predicted a 60% decrease. In contrast, the model predicts only a 10% increase in the number of atoms for a laser intensity of 10 mW/cm^2. Thus, minimal advantage is gained once the transition is sufficiently saturated. As a result, no effort was taken to increase the cooling laser power beyond its typical operating value.

As expected, the quality of circular polarization of the cooling beam had a very significant impact on solenoid performance. The two components that impact circular polarization quality are the linear polarizer and the quarter wave plate. Without the linear polarizer in the beam path some cooling is still achievable due to the nominally linearly polarized laser output. However, by improving the polarization using a linear polarizer, the signal is enhanced. Due to optical constraints, the quarter wave plate was initially located in the cooling laser beam path immediately following the polarizing beam splitter (ref. Figure 5.12). Subsequent reflection off optical elements distorted the quality of

circular polarization, thus degrading the slowing efficiency. Subsequent relocation of the quarter wave plate to after the last optical element enhanced the signal by ~ 40 %. In this configuration, the percentage of light not polarized σ^- is limited to a few percent. Without the quarter wave plate, no Zeeman slowing is evident.

6.2 State Preparation

The cycling transition for σ^- Zeeman slowing is $|F = 3, M_F = -3\rangle \rightarrow |F' = 4, M_F' = -4\rangle$. As mentioned in Chapter 3, optical pre-pumping, or state preparation, can be used in the region between the oven and the solenoid to maximize the number of atoms in the $|F = 3, M_F = -3\rangle$ ground state. Two lasers were involved in the state preparation process; the cooling laser and the re-pump laser. The cooling laser, tuned to the $|F = 3, M_F = -3\rangle \rightarrow |F' = 4, M_F' = -4\rangle$ transition, pre-pumped atoms into the $M_F = -3$ sub-level (Zeeman pumping). The re-pump laser, tuned to the $|F = 2\rangle \rightarrow |F' = 3\rangle$ transition, pre-pumped atoms into the F = 3 ground state (hyperfine pumping). The experimental arrangement of the cooling and re-pump lasers is described below.

6.2.1 The Function of the Cooling Laser in State Preparation

The role of the cooling laser in state preparation is to pre-pump atoms that are within the capture velocity range of the Zeeman slower (20-250 m/s) into the $|F = 3, M_F = -3\rangle$ ground state. The cooling laser serves this function simultaneously with its role in slowing atoms within the Zeeman slower. Thus, the velocity class of atoms resonant with the cooling laser prior to entry into the solenoid is dictated by the laser detuning required for Zeeman slowing. Some control of this parameter is possible, because the laser detuning can be adjusted by changing the strength of the solenoid bias field. At a particular frequency, the velocity range of atoms impacted is determined by the laser intensity. For this experiment, this parameter is fixed.

To optimize the pre-pumping process, the efficiency of the Zeeman slower was analyzed as a function of bias solenoid field current. Minimizing the bias field brings the frequency of the cooling laser closer to resonance with atoms in the solenoid velocity capture range in the zero field region. This should enhance off-resonant Zeeman optical pumping of these atoms into the $|F = 3, M_F = -3\rangle$ ground state, thereby increasing the number of atoms available for Zeeman slowing. However, since minimizing the bias field increases the probability of hyperfine optical pumping of atoms out of the cycling transition during Zeeman slowing process, there is some question about where the optimum balance is found. The theoretical calculations of section 3.1.3.2 suggest that optical pumping within the Zeeman slower may begin to negatively impact the cooling process at low bias field strengths (zero bias field corresponds to a 30 Gauss minimum solenoid field).

To analyze the situation experimentally, the performance of the Zeeman slower was characterized as a function of bias field current. The results are summarized in Figure 6.3. The square markers corresponds to the relative number of ~20 m/s atoms entering the funnel, determined from the velocity profile of the atomic beam. The triangle markers corresponds to the relative number of atoms in the atomic funnel as determined from trap fluorescence. The data are normalized to the same maximum value for ease of comparison.

Clearly, the number of atoms increases as the bias field is decreased. Thus, it appears that the gains achieved by pre-pumping atoms into the desired $M_F = -3$ ground state more than compensate for any increase in hyperfine optical pumping within the Zeeman solenoid at zero bias field. From the experimental data we also find that the bias current does not impact the loading of the atomic funnel; i.e. the number of atoms loaded is proportional to the number slowed.

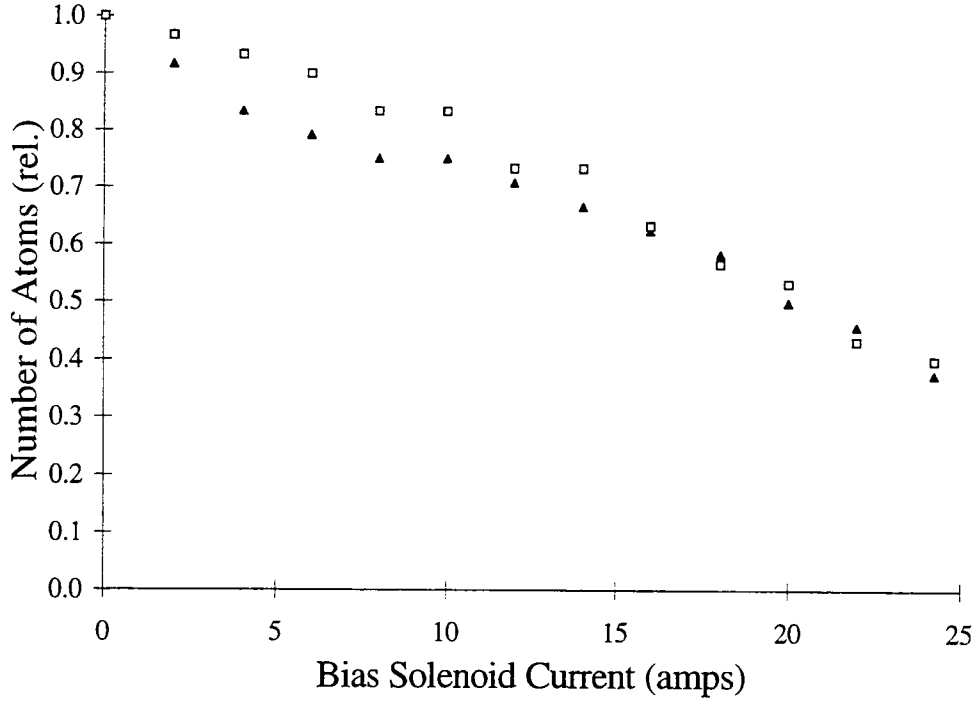

Figure 6.3 Performance of the Zeeman slower as a function of bias solenoid field current. The square markers corresponds to the relative number of ~20 m/s atoms entering the funnel. The triangle markers corresponds to the relative number of atoms in the atomic funnel.

6.2.2 The Function of the Re-pump Laser in State Preparation

A re-pump laser was used in state preparation to hyperfine pump atoms into the F = 3 ground state. Since state preparation occurs in the region between the oven and the Zeeman slower, two configurations for hyperfine pumping were investigated. In the first configuration, the re-pump laser was aligned co-propagating with the cooling laser. In the second, the re-pump laser was aligned perpendicular to the atomic beam. Due to optical constraints, different lasers were used.

The re-pump laser, co-propagating with the cooling laser, was polarized σ^- and had an intensity of 0.1 mW/cm^2 at the entrance to the chamber. By adjusting the frequency of the laser relative to the zero-velocity re-pump transition, it became resonant with different velocity classes of atoms. The laser was found to enhance the number of

Zeeman slowed atoms over a ~250 MHz range of laser frequencies. Improvement over this wide a range of frequencies was not surprising since hyperfine pumping of atoms anywhere in the 20 - 250 m/s velocity capture range would enhance the signal. The maximum improvement of ~ 40% occurs with the re-pump laser detuned ~ -125 MHz from the $F = 2 \rightarrow F' = 1$ cycling transition. At this detuning and a small (~zero) magnetic field, the laser is resonant with the $F = 2 \rightarrow F' = 3$ transition for atoms traveling at ~170 m/s. Because of the small residual Zeeman field preceding the solenoid, the quantization axis is defined along the atomic beam axis. Thus, the σ^- polarized re-pump laser should also simultaneously provide some optical pumping into the desired $M_F = -3$ sub-level. Additional improvement could be obtained using either a broadband re-pump laser or a fixed frequency laser with greater intensity. In either case the accessible velocity range of atoms would be enhanced.

For the perpendicular configuration, a laser tuned to the re-pump transition was directed in the window on the oven chamber to intersect the atomic beam about 3 cm outside the condenser cup. The 13 mm x 8 mm beam was linearly polarized and had an intensity of 8 mW/cm^2. Due to the absence of a Doppler shift at 90° interception, the laser tuned to the $F = 2 \rightarrow F' = 3$ transition is resonant with all the atoms in the $F = 2$ state, regardless of their velocity. In this configuration, Zeeman sub-level specificity is not possible, so the atoms pumped into the $F = 3$ ground state are distributed among the Zeeman sub-levels. This method of state preparation only enhanced the number of slow atoms a few percent.

6.3 Slowing Atoms without Doppler Shift Compensation

Limited slowing of the thermal beam can be accomplished using a fixed frequency laser and no Doppler shift compensation. If no steps are taken to compensate for the changing Doppler shift of a slowing atom, the cooling laser will slow an initially resonant or near resonant atom until the Doppler shift changes sufficiently to cause the scattering rate to become negligible. This type of laser slowing, illustrated in Figure 6.4, is

demonstrated for both pedagogical reasons and because such a peak is evident in some of the experimental spectra. The velocity profiles shown were measured for different fixed cooling laser frequencies using the experimental configuration of Figure 6.1. The spectra look nearly identical with the Zeeman solenoid field on or off, indicating that the majority of the slowing occurs in the 60 cm region between the oven and the entrance to the solenoid. The intensity of the cooling laser was 7 mW/cm^2. In each case, a fixed frequency re-pump laser was used to reduce optical pumping into the F = 2 ground state. The change in velocity of 30-50 m/s is consistent with theoretical predictions.

It is evident from the figure that uncompensated slowing using a laser of moderate intensity is not a feasible method for producing an intense, 20 m/s atomic beam. For a fixed laser intensity, the size of the peak is dictated by the number of atoms in the thermal beam in the affected velocity class. Thus, the small number of atoms in the low velocity tail limits the number of atoms that can be slowed to very low velocity. Using a very intense laser [Prentiss, 1989] or broadband source [Zhu, 1991] appreciable slowing to low velocity can be achieved.

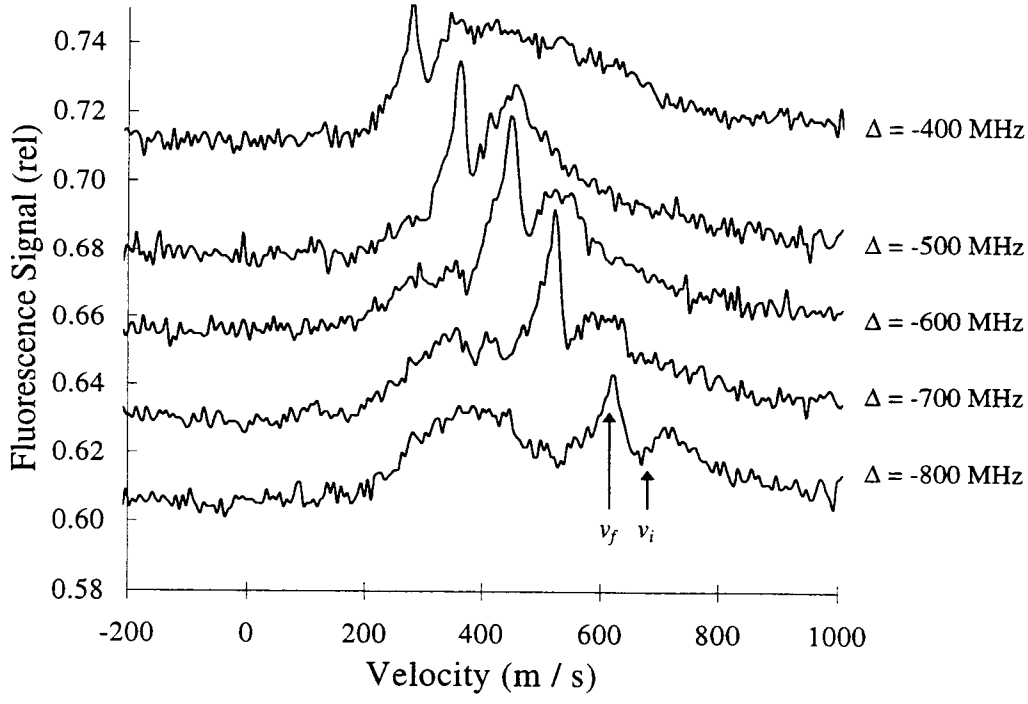

Figure 6.4 Slowing atoms using a fixed frequency laser.

In our experiment, the Zeeman solenoid is located 60 cm from the rubidium oven. In the region between the oven and entrance to the solenoid, the cooling laser is resonant with the velocity class of atoms satisfying the relationship $\Delta = kv$, where the cooling laser detuning Δ is dictated by the solenoid current. In cases where the resonant velocity falls within the velocity range of atoms recorded in the experimental spectra, the peak from uncompensated slowing is evident along with the low-velocity Zeeman slowed peak.

It would be possible, by adding an appropriately tuned independent laser, to use uncompensated slowing in the region between the oven and solenoid to pre-slow additional atoms into the velocity capture range of the Zeeman slower. A 7 mW/cm^2 laser, with a detuning of ~ -375 MHz from the zero velocity cooling transition, would extend the capture range from 250 to 300 m/s. This pre-slowing configuration was tried by tuning the existing re-pump laser as the desired pre-slowing frequency. In this configuration, the pre-slowing laser was found to enhanced the number of Zeeman slowed atoms. However, the absence of a laser tuned to the re-pump transition, coupled with the low laser power, resulted in fewer total slow atoms compared to the normal configuration in which the re-pump laser was tuned to the re-pump transition.

6.4 Experimental Results: Zeeman Tuned Slowing

Sample velocity profiles for σ^- Zeeman slowed ^{85}Rb atoms are shown in Figure 6.5. From such data, the cooled atom velocity was determined and plotted as a function of cooling laser detuning. The results are shown in Figure 6.6. From these data, we find the experimental results are well matched to the predictions of the theoretical model. As expected, σ^- Zeeman slowing produces a slow beam of atoms at a controllable velocity.

Multiple velocity classes are clearly evident in the spectra in Figures 6.5 with a detuning Δ of -960 MHz. Similar results are found in the spectra for larger detuning. This confirms the theoretical prediction that the irregularity in the measured solenoid field creates a magnetic field gradient that the faster atoms cannot follow. As predicted, turning the taper field current down decreases the gradient and eliminates the multiple

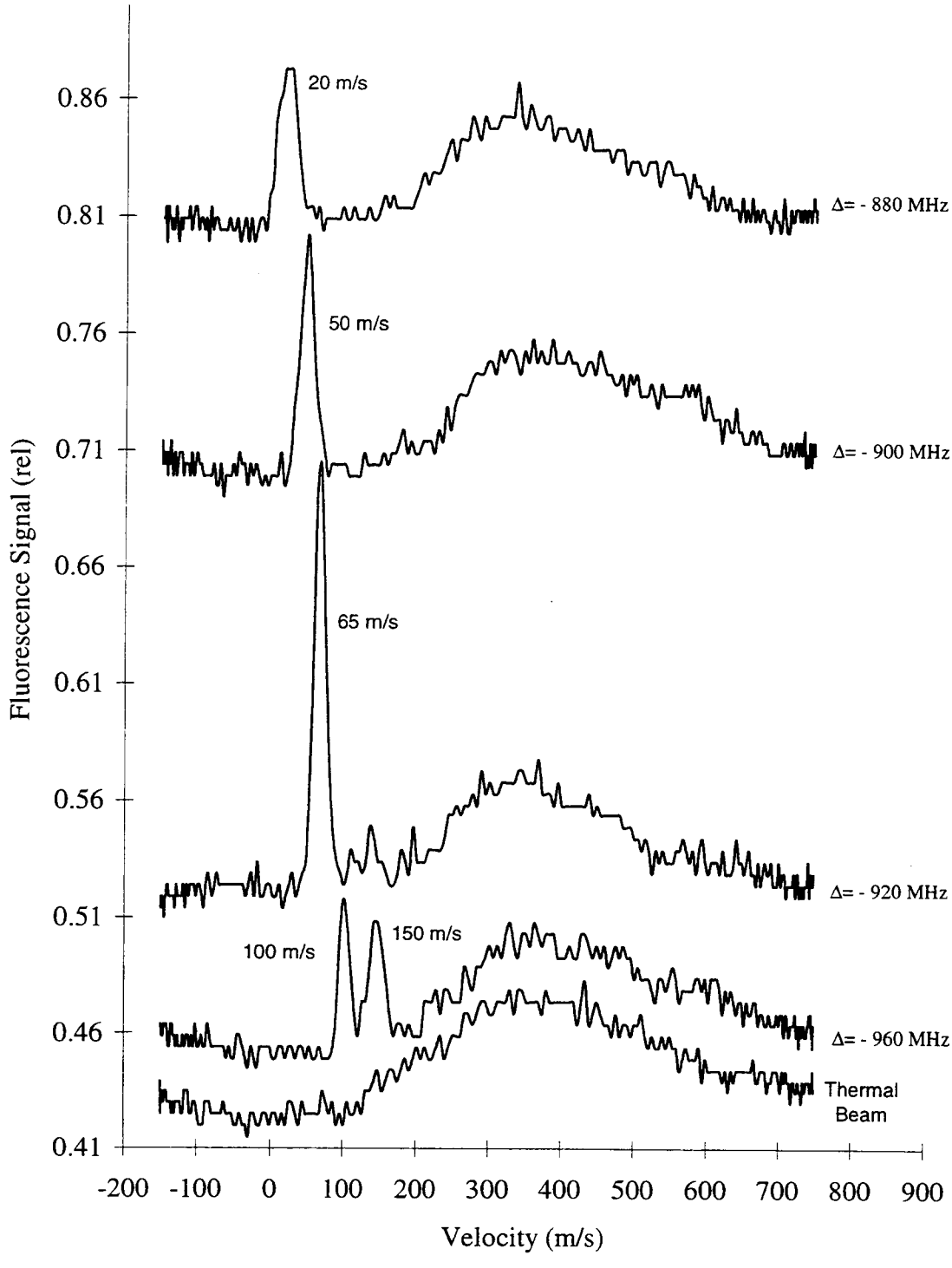

Figure 6.5 Fluorescence spectra for σ^- cooled ^{85}Rb atoms. The taper current is 26 amps. The bias current is 24.25 amps. The laser intensity is 7 mW/cm^2. The detuning of the cooling laser is indicated for each velocity profile.

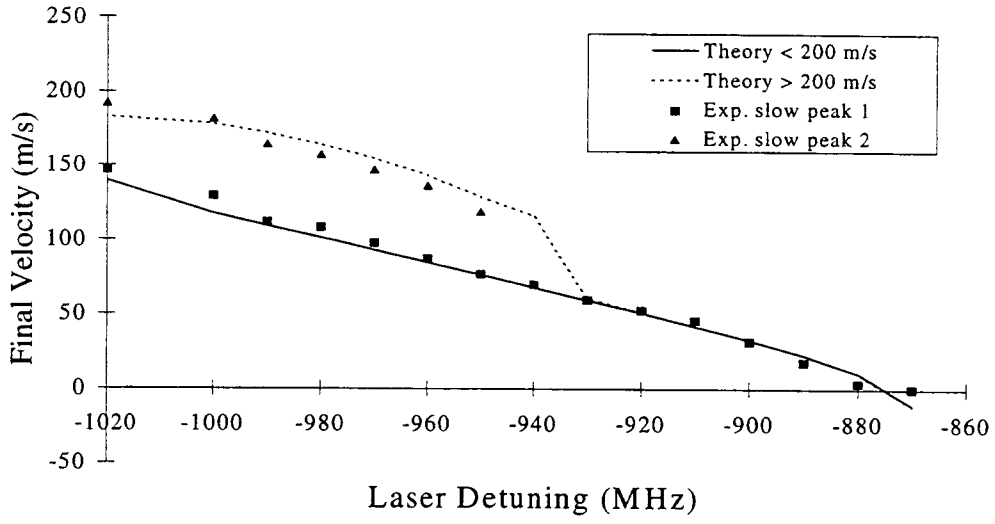

Figure 6.6 ^{85}Rb, σ^- cooled beam final velocity as a function of laser detuning. The theoretical curves (solid line) were calculated from the numerical model using the measured solenoid field. The two curves correspond to atoms with initial velocities of 140m/s and 200 m/s respectively. The taper and bias field currents are 26 amps and 24.25 amps respectively. The laser intensity is 7 mW/cm^2.

velocity classes. These experimental results are useful in demonstrating the accuracy of the theoretical model in predicting the experimental performance of the solenoid. However, it should be kept in mind that the multiple velocity classes have no practical impact on the operation of the Zeeman slower since it was designed to generate a ~20 m/s atomic beam.

Similar velocity profiles were obtained for σ^+ cooled atoms. The two velocity classes present at large detuning in σ^- slowing are also evident in σ^+ slowing. Figure 6.7 compares the final velocity versus detuning behavior for σ^+ and σ^- Zeeman slowing. The σ^+ curve was shifted -960 MHz to make the curves coincide at zero velocity. As predicted, for final velocities less than ~ 120 m/s, the slow atom peak is not appreciable for σ^+ slowing. Thus, no data points were obtained in that region. The results demonstrate that σ^+ slowing is not a satisfactory method for producing slow atoms to load the atomic funnel.

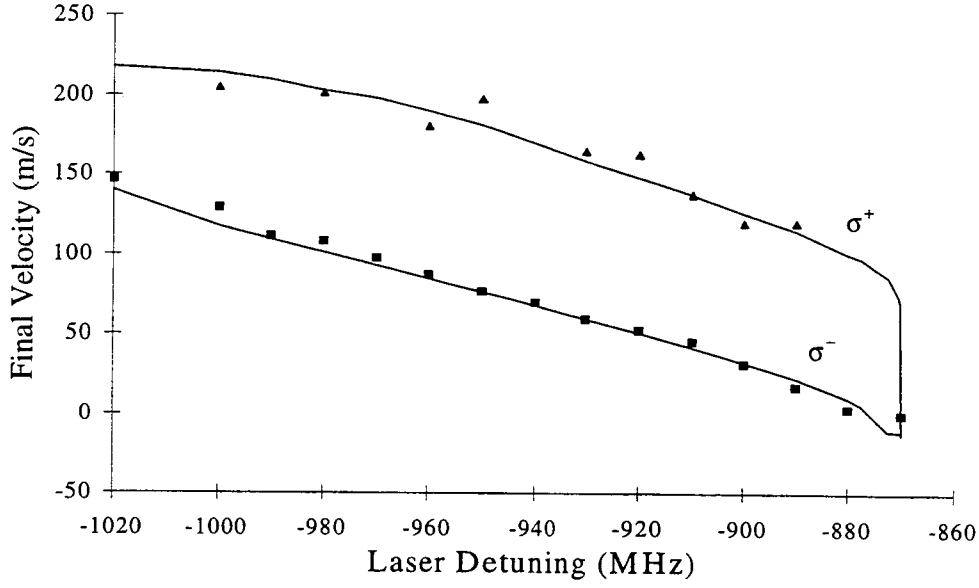

Figure 6.7 ^{85}Rb cooled beam final velocity as a function of laser detuning for σ^+ and σ^- Zeeman tuned cooling. The theoretical curves (solid line) were calculated from the numerical model using the measured solenoid field. The σ^+ curve was shifted -960 MHz to make the curves coincide at zero velocity. The taper and bias field currents are 26 amps and 24.25 amps respectively. The laser intensity is 7 mW/cm^2.

The number of atoms per second in the thermal atomic beam was determined by comparing the measured thermal beam profile with the expected fluorescence signal. The measured signal was converted to a power distribution using the PMT calibration factor 0.13 nW/mV (825 V PMT voltage). The theoretical distribution of atoms per second per velocity interval $I(v)$ (equation 5.1) was converted to a fluorescence distribution using the relationship

$$\text{Signal}(\Delta) = \left[\frac{hc}{\lambda}\int_0^\infty I(v)\,P(v,\Delta)\,dv\right][\%\ \text{collected}], \qquad (6.1)$$

where $P(v, \Delta)$ is the number of photons each atom emits at is travels through the laser beam. The time the atom spends in the probe laser beam is given by l/v, where the

interaction length l is 2.8 cm and v is the velocity of the atom. Thus, for a scattering rate R (equation 3.2), $P(v, \Delta)$ is given by the expression

$$P(v,\Delta) = \frac{l}{v} R . \tag{6.2}$$

To enhance the light collection efficiency, a one inch lens was positioned two inches from the center of the trap to focus light from one-half the probe region onto the PMT. In this configuration, the lens subtended 0.016 of the total solid angle. The resulting fluorescence profile is given by the expression

$$\text{Signal}(\Delta) = (0.008)(0.72)\left(\frac{hc}{\lambda}\right)\left(\frac{\pi l I_0 \Gamma^2}{2k^3\alpha^4}\right)\frac{\frac{I}{I'_{SAT}}}{\sqrt{1+\frac{I}{I'_{SAT}}}}\Delta^2 \exp\left[-\left(\frac{\Delta}{k\alpha}\right)^2\right]. \tag{6.3}$$

For this measurement, the saturation intensity $I'_{SAT} = (7/3)I_{SAT}$ is scaled to account for the average over M_F levels and the intensity I of the probe laser is 4.5 mW/cm^2. The total flux of ^{85}Rb atoms in the measured thermal beam is $(0.72)I_0 = 2.7\text{x}10^{12}$ atoms/s. The estimated flux of ^{85}Rb atoms in the thermal beam was $(0.72)I_0 = 1.0\text{x}10^{12}$ atoms/s (equation 5.2). The difference is reasonable due to the uncertainty in estimating the parameters in equation 5.2.

The temperature and flux of atoms in the slow atom peak was determined by fitting equation 6.3 to the measured low-velocity fluorescence peak. The adjustable parameters were the temperature (contained in α) and the full beam intensity I_0. For typical operating parameters, the flux of atoms in the 20 m/s beam was determined to be $2.7\text{x}10^{10}$ atoms/s; 1% of the atoms in the thermal beam. Theoretical calculations, which assumed all of the atoms were in the desired hyperfine level for slowing, predicted slowing 14% of the thermal beam; $3.8\ \text{x}10^{11}$ atoms/s. The approximate temperature of the 20 m/s velocity peak was determined to be 2.4 K. The actual temperature may be lower since measurement resolution is limited by the 5 m/s separation in experimental data points and the 6 MHz natural linewidth of the transition.

From the fluorescence signal captured on the CCD camera, it was observed that both the trap and the downstream molasses region were shifted off-axis for the trap loaded using Zeeman-tuned slowing. The cause of the shift was determined to be the residual Zeeman field present in the funnel region which changed the location of the zero field line of the 2-dimensional magneto-optic trap. Reducing the bias field minimized the lateral offset. By reversing the direction of the Zeeman field and making the required change to the cooling laser polarization, the direction of the shift could be reversed. To counter this residual field, a small magnetic field was generated (coaxial with the Zeeman field) by sending current through a pair of 70 turn coils wound around the vacuum chamber portholes. Due to space limitations, a true Helmholtz configuration was not possible. The profile used, shown in Figure 6.8 for a current of one amp, provides a nearly constant field in the funnel region. The field outside this region does not impact Zeeman slowing or loading of the trap. The magnitude of the compensation field at the center of the atomic funnel is $B_C = 0.93I$ (G/Amp). For a 24.25 amp solenoid bias field, a

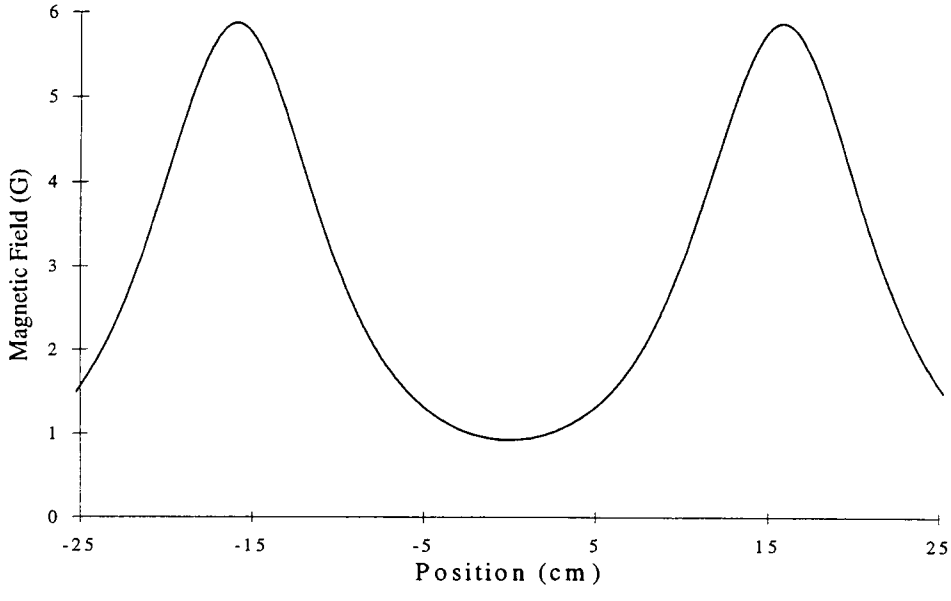

Figure 6.8 Profile of the magnetic field used to compensate for the residual Zeeman solenoid field present in the atomic funnel region. The magnitude of the compensation field at the center of the atomic funnel is $B_C = 0.93I$ (G/amp).

current of one amp successfully aligned the trap and molasses regions along the funnel axis. For a smaller bias field, less current is required.

6.5 Comparison with Chirped Cooling

Characterization of the chirped beam was accomplished with a slight modification of the system described in Figure 6.1. Because chirped cooling produces a pulsed beam of atoms, the complete velocity distribution could not be acquired by a single scan of the probe beam. Instead, while the 45° probe laser was slowly scanned, a sample and hold circuit was used to sample the fluorescence signal at the end of each chirp cycle. In this fashion, about 100 consecutive chirped atom packets were probed to map out the fluorescence signal. Results obtained using the sample and hold method on Zeeman slowed atoms were consistent with those taken in a continuous fashion. Figure 6.9 compares the velocity distribution obtained using chirped and Zeeman slowing. The flux

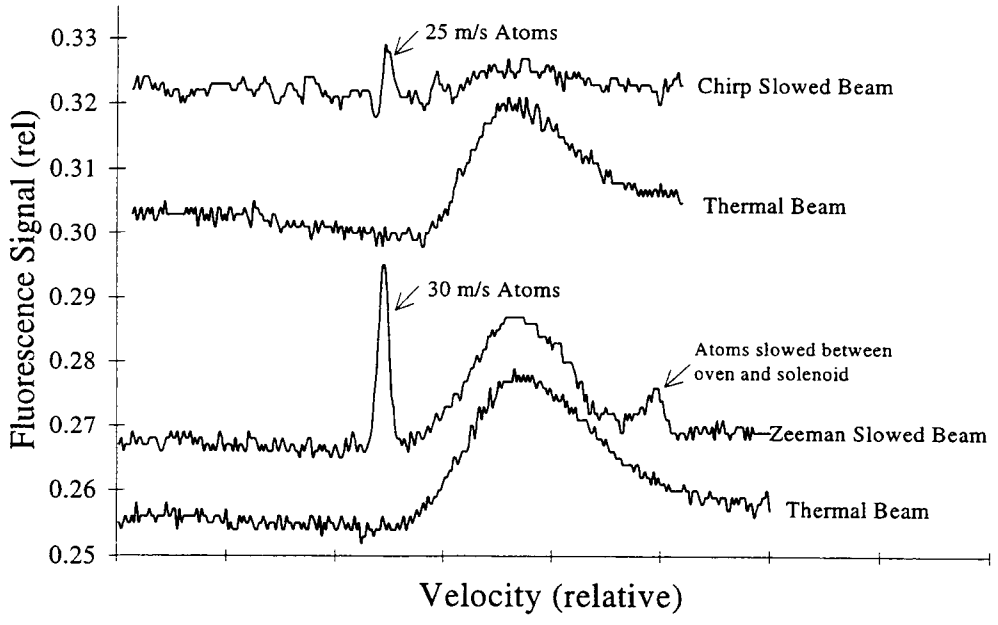

Figure 6.9 Comparison of cooling signals from chirped and Zeeman slowing.

of atoms in the chirp cooled peak is about $1.6x10^{10}$ atoms/s, approximately 60% of the number in the Zeeman cooled peak.

6.6 Isotope Comparison

In order to examine the difference in Zeeman slowing between the isotopes, experimental data was gathered on ^{87}Rb. The sample velocity profiles shown in Figure 6.12 provide a comparison between Zeeman slowed ^{85}Rb and ^{87}Rb atoms. The data were taken on the same day using a 26 amp taper field, 24.25 amp bias field, and 7 mW/cm^2 intensity cooling laser. The difference in natural abundance between isotopes is reflected in the size of the thermal beam distributions; the measured thermal beam flux for ^{87}Rb is (28/72) that of the ^{85}Rb thermal beam. Despite the large difference in natural abundance, the flux in the slow atom peak for ^{87}Rb is approximately 90% that of ^{85}Rb. Thus, the Zeeman slowing process is more efficient for ^{87}Rb atoms.

The difference in hyperfine and Zeeman structure of ^{85}Rb and ^{87}Rb is the most likely reason for the contrast in Zeeman slowing efficiency between the isotopes. For a given magnetic field strength, the energy splitting of ^{87}Rb is much larger than that of ^{85}Rb (see Figures 2.5 and 2.6). Thus, the solenoid bias field will provide better suppression of unwanted optical pumping in ^{87}Rb. As a result, fewer ^{87}Rb atoms should be lost from the cycling transition, resulting in a greater percentage of slow atoms.

Zeeman-tuned slowing with σ^- light has been demonstrated previously using ^{87}Rb [Barrett, 1991]. In their experiment, atoms are slowed from ~ 200 m/s to 40 m/s in a 60 cm solenoid. The cooling laser intensity was 5 mW/cm^2 and a bias field of 800 G was employed to discriminate against optical pumping within the Zeeman slower. They estimate the intensity of their 40 m/s peak to be 2 x 10^{10} atoms/cm^{2}s. Their data indicate approximately 20% that number, or ~ 4 x 10^9 atoms/cm^{2}s, in the 20 m/s peak. The number of atoms in the thermal beam is not indicated. In comparison, using ^{87}Rb, we achieved ~ 8.1 x 10^9 atoms/cm^{2}s in a 20 m/s slow beam.

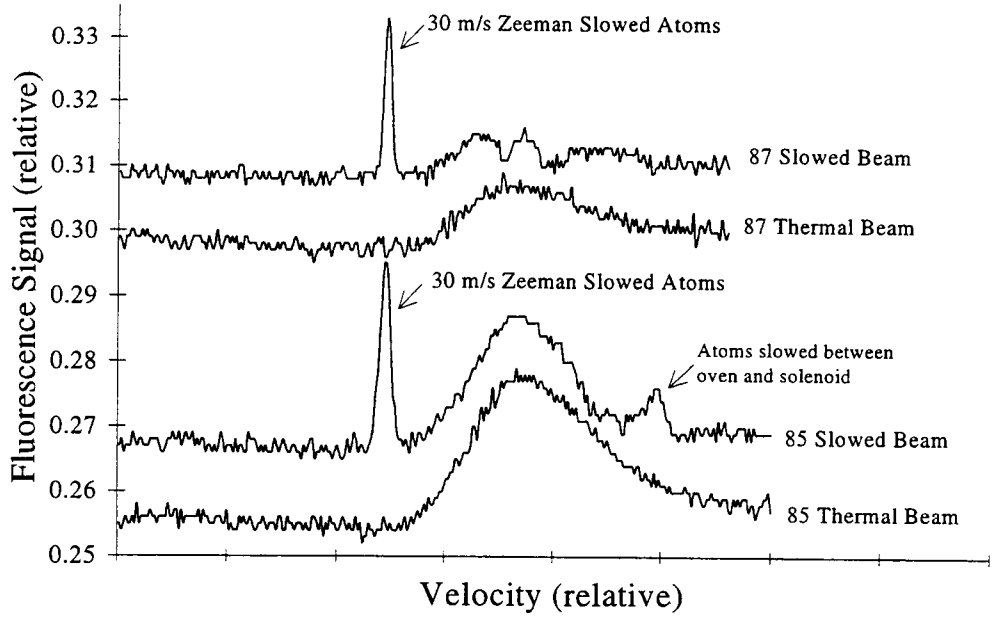

Figure 6.10 Comparison of ^{85}Rb and ^{87}Rb Zeeman slowed atomic beam. The taper field is 26 amps. The bias field is 24.25 amps. The cooling laser intensity is 7 mW/cm^2 beam.

Chapter 7: Experimental Results: Characterization of the Low Velocity Matter-Wave Source

The low velocity matter-wave source exiting the atomic funnel was characterized using a number of techniques. Resonance fluorescence was used to estimate the number of atoms exiting the funnel. A time-of-flight experiment was performed to determine the exit velocity of the atoms as a function of the frequency offsets of the horizontal trapping lasers. The surface ionization detector was used to map out the spatial profile of the beam and estimate the transverse temperature and number of atoms. Deflection of the atomic beam was studied in the presence of an applied magnetic field. The results are described in sections 7.1 through 7.4. Section 7.5 discusses the characteristics of the beam relative to its use in diffraction experiments.

7.1 Resonance Fluorescence: Estimating the Atomic Funnel Population

To estimate the population of atoms in the atomic funnel a resonance fluorescence technique was used. Fluorescence of atoms in the trap was collected using a photomultiplier tube (PMT) and an estimate of the number of atoms was obtained. The location of the PMT was the same as that used to measure fluorescence of the Zeeman slowed thermal beam in Section 6.5. Thus, the collection efficiency factor (0.016)(1/2) is the same. For this measurement, a probe laser was not required since the lasers used in trapping induce fluorescence. The instantaneous PMT power (in Watts) is related to the number of atoms in the trap by the equation

$$PMT_{POWER} = N_{ATOMS}\left(\frac{hc}{\lambda}\right)\left(\frac{\Gamma}{2}\frac{\frac{I}{I'_{SAT}}}{1+\frac{I}{I'_{SAT}}+\frac{4}{\Gamma^2}\Delta^2}\right)\left[(0.016)\left(\frac{1}{2}\right)\right]. \qquad (7.1)$$

For this measurement, the total intensity I of the six trapping lasers is 33 mW/cm^2 and their detuning from resonance Δ is 15 MHz. Thus, the relationship between PMT power and number of atoms is $PMT_{POWER} = N_{ATOMS}(1.31 \times 10^{-14}$ W/atom).

To estimate the number of atoms in the trap, the atomic beam was ejected from the funnel loaded with Zeeman slowed atoms at a velocity of ~ 5 m/s. The change in PMT fluorescence was measured with the slowing laser on and off resonance. The PMT registered a continuous 170 mV offset signal with the trap on. The measured signal was converted to power using the PMT calibration factor of 0.395 nW/mV (750 V PMT voltage). Using the conversion factor above, a PMT signal of 170 mV corresponds to 5.1 x10^6 atoms. The 5 m/s atom will spend 1.5 ms traversing the 7.5 mm imaged region of the trap. (The trap is 15 mm long, however, only one half the trap is imaged). Thus, the flux of atoms exiting the funnel is 3.4x10^9 atoms/s. This corresponds to ~12% of the atoms slowed by the Zeeman slower.

The number of atoms in the funnel loaded using chirped cooling was calculated from the PMT fluorescence signal in essentially the same manner as described for the Zeeman loaded funnel. However, because chirped cooling loads the funnel in a pulsed fashion, not all the atoms contribute to the peak of the PMT pulse. The loading time is 6 ms. Thus, for an ejection velocity of 5 m/s, only ¼ of the atoms per chirp contribute to the instantaneous PMT signal (1.5 ms/6ms = 0.25) [Swanson, 1995]. The total laser intensity for this measurement was 48 mW/cm^2. The resulting conversion factor from equation 7.1 is thus $PMT_{POWER} = N_{ATOMS}(2.5 \times 10^{-14}$ W/atom). The pulsed PMT fluorescence signal had an amplitude of 60 nW, corresponding to 2.4x10^6 atoms. A pulse duration of 6 ms and chirp rate of 25 Hz yield a duty cycle of 0.15. Thus, the fluorescence signal corresponds to 2.4 x10^8 atoms/s. Therefore, about 15 times more atoms per second are available with Zeeman slowing.

7.2 Time-of-Flight Analysis: Velocity and Temperature Measurements of the Atomic Beam

A time-of-flight experiment was performed to characterize the exit velocity and temperature of atoms leaving the atomic funnel. The experiment was patterned after that of Riis *et at.* [Riis, 1990] who used a similar technique to characterize the temperature and velocity of a slow atomic beam of sodium. For this experiment, the lasers were configured as illustrated in Figure 5.14. The horizontal trapping lasers were offset in frequency $\pm \Delta f$ relative to the vertical laser to eject atoms from the funnel with a controllable mean velocity. The gate laser, tuned to resonance with the cycling transition, deflected the low-velocity atomic beam out of the molasses region. By shifting the laser off resonance for a short duration (3 - 5 ms), a pulse of atoms traveled the 15 - 20 mm distance to the horizontal molasses-probe region. Fluorescence from the probe region was detected using a PMT. The arrival time of the pulse and width of the distribution were used to determined the mean velocity and longitudinal temperature of the atomic beam. A detailed description of the method used to analyze the time-of-flight results is provided in the work of Swanson [Swanson, 1995].

Previously, time-of-flight analysis was performed on the atomic funnel loaded with chirped cooled atoms. Data was taken for a range of values of the frequency offset of the horizontal trapping lasers. The beam velocity as a function of frequency offset is presented for reference in Figure 7.1 [Swanson, 1996]. The dashed line corresponds to the result expected from simple theory $v = \sqrt{2}\,\lambda\Delta f$. The solid lines, shown for nominal detuning of -2Γ [upper] and -3Γ [lower], take into account an axial magnetic field and a finite damping time in the funnel [Swanson,1996]. The time-of-flight results yield controllable mean velocities in the range of 3 - 10 m/s and a longitudinal temperature[6] of $500^{+500}_{-250}\,\mu$K.

Subsequently, time-of-flight data was taken on the funnel loaded with Zeeman slowed atoms. The results, summarized in Figure 7.2, correspond to four different data

[6] Temperature is not a vector quantity. However, the dynamics of the cooling and trapping process allow for generation of a beam with a different velocity distribution in the different spatial dimensions.

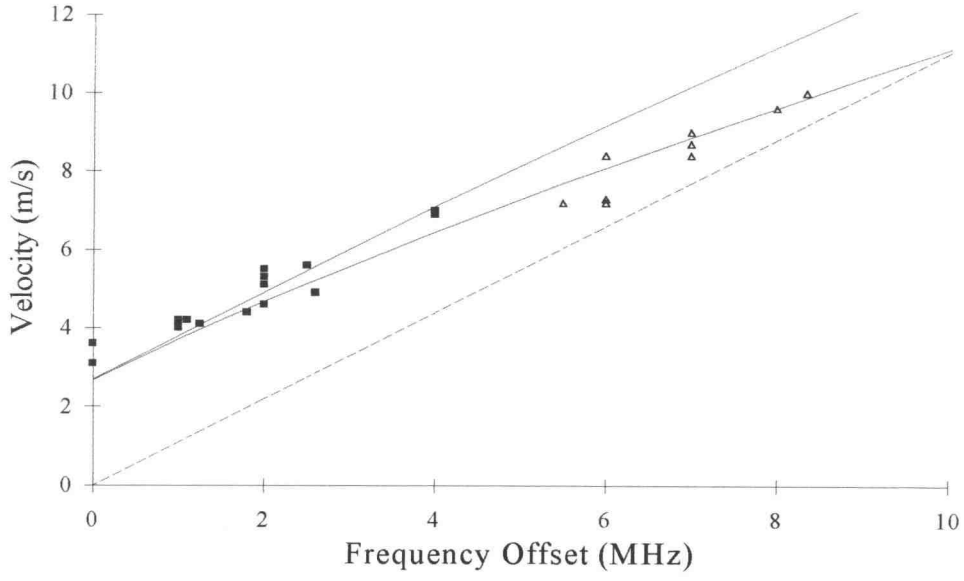

Figure 7.1 Atomic velocity as a function of frequency offset for a funnel loaded using chirped cooling. The dotted line corresponds to the result expected from simple theory. The solid lines takes into account a finite damping time in the funnel and an axial magnetic field. The upper [lower] solid curve corresponds to a nominal detuning of -2Γ [-3Γ].

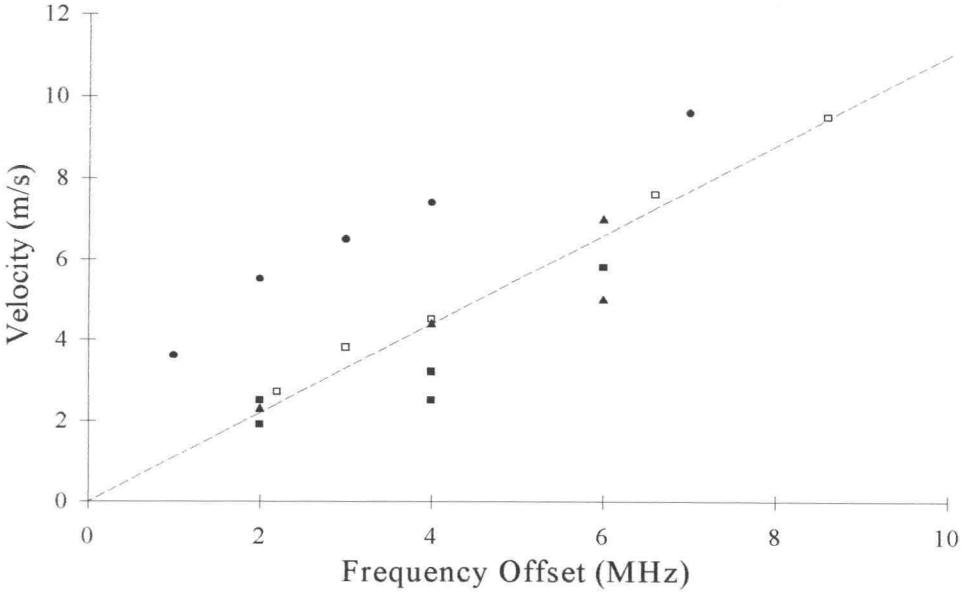

Figure 7.2 Atomic velocity as a function of frequency offset for a funnel loaded using Zeeman-tuned cooling. The dotted line corresponds to the result expected from simple theory. The triangle [square and circle] markers correspond to $+B_{\text{zeeman}}$ [$-B_{\text{zeeman}}$].

sets with slightly different laser beam alignments and background magnetic fields. A major realignment of the trapping lasers occurred between taking the time-of-flight data depicted by the circle markers and the other three data sets. This may account for the difference in the exit velocity characteristics of the circle markers from the other data points. Laser beam alignment can impact the exit velocity characteristics of the funnel since an imbalance of forces can result if the counter-propagating laser beams do not exactly overlap as the atoms leave the trap.

In contrast with the results for the funnel loaded with chirp cooled atoms, the results for the funnel loaded with Zeeman slowed atoms agree more closely with the predictions of simple theory. Since the residual Zeeman magnetic field shifts the zero point of the 2-dimensional magneto-optic trap, it is likely that the atoms experience a different axial magnetic field. This would modify the exit velocity characteristics compared to the funnel loaded using chirped cooling.

During the time-of-flight experiments [Swanson, 1996], the transverse temperature of the beam was estimated from CCD images of atoms fluorescing in the funnel and molasses-probe regions. In the distance between the funnel and the molasses-probe region, the atomic beam will expand in proportion to its transverse velocity. The CCD images provide a way to estimate the width of the atomic beam in the funnel and molasses regions. Using this information, along with the distance traveled and the longitudinal velocity, an estimate of the transverse temperature can be made.

In the horizontal plane, the transverse temperature was estimated from the CCD pictures to be 120^{+60}_{-40} μK. However, it is evident from the CCD image that the molasses-probe region provides horizontal transverse trapping of the atomic beam (i.e. spatial compression of the beam is clearly evident) due to the residual funnel magnetic field. Thus, it is likely that the horizontal transverse temperature estimate obtained by this method is smaller than the actual temperature of atoms leaving the atomic funnel.

The vertical transverse temperature was found to vary moderately from measurement to measurement. The temperature generally did not exceed 600 μK and the minimum temperature, measured at the entrance to the molasses region, was 380^{+80}_{-70} μK.

The molasses-probe laser provides no trapping in the vertical transverse direction. Thus, this temperature is likely more representative of the temperature of atoms leaving the atomic funnel. Theoretically, one expects the vertical and horizontal transverse temperatures to be approximately the same.

Following the molasses-probe region, the horizontal transverse component will be reduced, relative to the vertical component due to transverse cooling of the atomic beam in the molasses region. Recoil heating will result in a larger vertical transverse temperature.

7.3 Surface Ionization Detection: Spatial Characteristics of the Atomic Beam

The surface ionization detector was used to map out the transverse spatial profile of the low-velocity atomic beam. A description of the detector design and the basic theory of operation was provided in Chapter 5. Below, characterization of the detector is provided and methods for signal counting and detection are described. Following this, the theoretical and experimental spatial profiles of the low-velocity atomic beam are presented.

The experimental setup used to characterize the spatial profile of the atomic beam is illustrated in Figure 7.3. The surface ionization detector, located 30 cm from the exit of the atomic funnel, is mounted to a manually controllable translation stage with $\pm$ 0.5 inch travel transverse to the slow atomic beam axis. The front face of the detector consists of a shield with a 0.635 cm (0.25 inch) circular hole in it to allow passage of the atomic beam to the hot wire. The area of the 760 μm wide rhenium ribbon exposed to the beam is 0.0045cm^2. The electrical configuration for operation of the detector was discussed in detail in chapter 5. In the discussion below, the MCP voltage is -1800 V and the hot wire current is 1.25 amps unless otherwise noted.

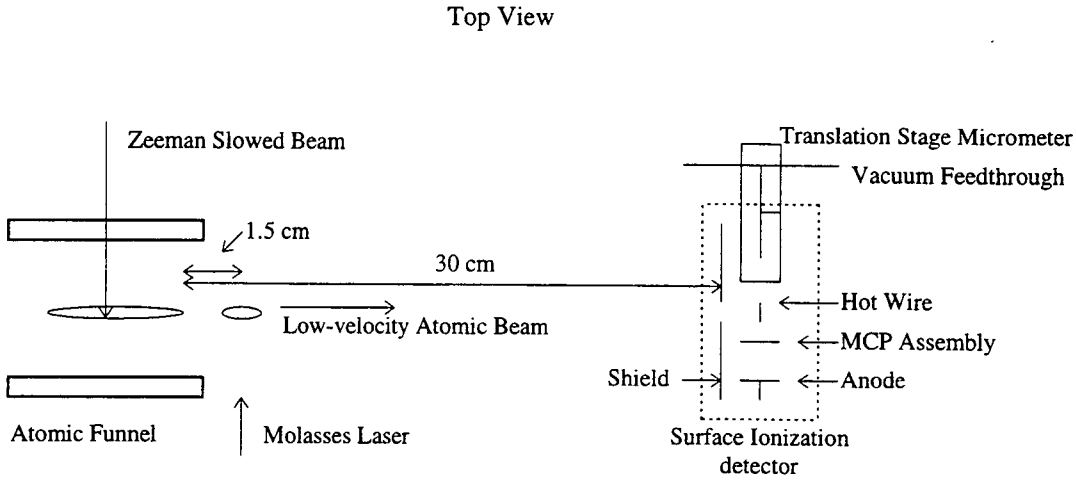

Figure 7.3 Experimental setup for characterizing the spatial profile of the atomic beam.

7.3.1 Detector Pulse Characteristics

Atoms that strike the hot rhenium ribbon are ionized with an efficiency that is dictated by the ribbon temperature. A portion of the ions subsequently emitted from the ionizing surface enter the MCP assembly. Each ion entering the MCP assembly produces a single pulse of electrons. The number of pulses per second is proportional to the number of atoms ionized per second. The size of the pulse is dictated by the MCP voltage. A single pulse from the detector anode is shown in Figure 7.4. The MCP voltage was -1800 V and the anode was terminated using a two parallel 50 Ω resistors to ground. The first 50 Ω resistor connected the anode to ground at the BNC connector feed through on the vacuum system flange. The second 50 Ω resistor, used to terminated the coaxial cable at the input to the oscilloscope, minimized ringing. The typical pulse shown has a FWHM of approximately 2.5 ns and a pulse height of 5 mV. For comparison, the pulse heights for MCP voltages of -1700 V and -1600 V are ~ 4 mV and ~ 3 mV respectively.

The measured pulse height agrees well with the expected signal size. For a MCP gain of 5 x 10^6 and a pulse width of 2.5 ns, the expected amplitude of a single electron

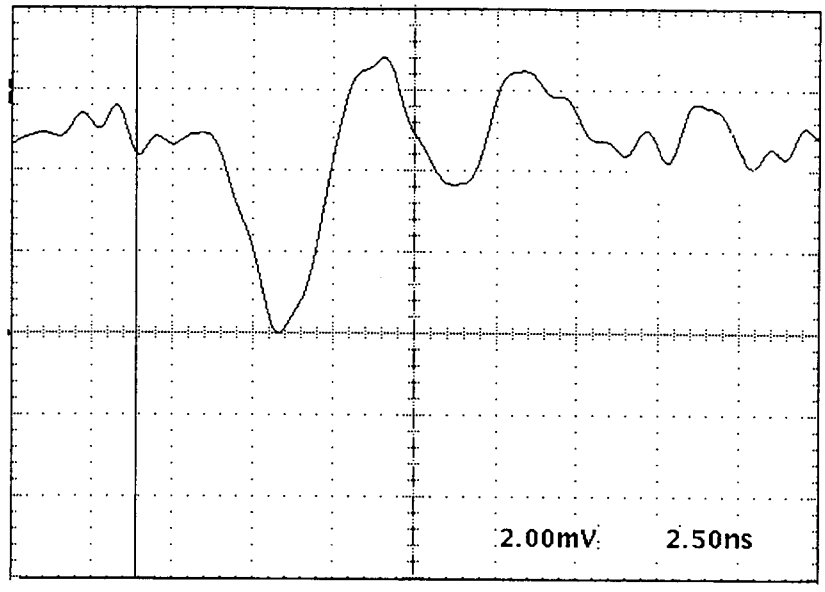

Figure 7.4 A single pulse from the surface ionization detector. The pulse height is dictated by the MCP voltage. The pulse shown corresponds to a MCP voltage of -1800 V.

pulse, estimated from Ohm's law, is ~ 6.5 mV. The ringing present in the signal arises primarily from impedance mismatching and does not preclude accurate detection of the signal.

Two different methods have been used to detect the anode pulses. First, individual pulses were counted using a discriminator and frequency counter. The second method used for signal detection was to monitor the DC current across a 1 MΩ resistor. Both methods are described below.

7.3.2 Pulse counting

Individual pulses from the surface ionization detector were counted using a discriminator in conjunction with a frequency counter. The discriminator converted anode pulses above a specified amplitude into square output pulses of constant width and an amplitude of 2.7 V. An adjustable discriminator level was set to accept the electron

pulses and ignore the smaller amplitude ringing. Because the minimum discriminator level was 5 mV, the output pulses from the detector were pre-amplified using a fast amplifier with a gain of 10. The width of the output pulses from the discriminator was set to 30 ns, the minimum value allowed by the discriminator. The square pulses were input into a frequency counter. The 30 ns discriminator pulse width limits the maximum count rate to 3.3×10^7 counts/s.

The hot wire current was set at 1.125 amps and the accelerator and repelling voltages were each zero. The count rate for the detector was consistent during a given day, but varied a great deal from day to day. Typical count rates for the on-axis detector ranged in value from 150k to 800k counts/s for a trap with the horizontal trapping lasers detuned $\pm$ 8 MHz and a region of downstream molasses. Some of this variation is due to differences in atomic beam alignment from day-to-day. However, it was also found that the background noise signal varied significantly as a function of detector position. These detector irregularities inhibited preliminary attempts to map out the spatial distribution of the atomic beam. The problem was found to be due to an intermittent noise signal being injected onto the detector signal at some off-axis detector positions. The anode signal is carried in a shielded coaxial cable and exits the vacuum chamber through a floating shield vacuum feed through. The noise problem was determined to be due to the shield on the signal line intermittently contacting the vacuum chamber walls. The problem was resolved by hard-wiring the shield to the inside of the vacuum chamber. An additional change was to replace the straight in-line power connector that mates the detector anode to the coaxial cable with a right angle connector. The straight connector was found to provide a torque to the detector anode which moved the anode relative to the MCP assembly for some locations of the detector. In the new configuration, the torque is minimized significantly. Following these modifications, the magnitude of the background noise signal was found to be independent of detector position.

Since the available frequency counter has a digital display, but no analog or digital output, interfacing to a computer was not possible. In addition, the equipment was on short term loan. Thus, an alternative means for signal recording was pursued until a suitable particle counter can be acquired. No further data was taken using the

discriminator and frequency counter following the detector modifications described above.

7.3.3 Monitoring DC current

An alternate method used for signal detection was to monitor the DC current across a 1 MΩ resistor. Calibration of the DC signal was determined by estimating the charge per pulse. The charge contained in a single pulse shown in Figure 7.4 was estimated from Ohm's law to be

$$\frac{Q}{pulse} = \frac{V\,\Delta t}{R} = 5 \times 10^{-13}\ \text{C}. \tag{7.2}$$

The total current for N pulses per second is $(5 \times 10^{-13}\ \text{C})N$. The measured DC signal across a 1 MΩ resistor is therefore given by

$$V_{DC}\ (\text{volts}) = (1\ \text{M}\Omega)(5 \times 10^{-13}\ \text{C})\,N = (5 \times 10^{-7}\ \Omega\text{C})\,N. \tag{7.3}$$

Thus, an easily discernible signal will result for count rates greater than a few thousand counts per second.

With the MCP voltage set at -1800 V and 1.25 amps of current through the hot wire, the typical background noise signal of 18 mV (36k counts/s) was present with no rubidium atoms in the high vacuum chamber. When the gate valve was opened to allow the thermal beam from the hot oven into the chamber the signal increased to 36 mV (62k counts/s) i.e. 18 mV (36k counts/s) above the background noise signal. As the rhenium wire heats up during operation the background noise signal slowly rises, due to an increase in the number of impurities baked out of the detector. After one hour of operation, the background noise signal is typically ~ 80 mV (160k counts/s) with the thermal beam blocked. Unblocking the thermal beam increases the signal to ~100 mV (200k count/s) i.e. 20 mV (40k counts/s) above the background noise signal.

7.3.4 Ionization Detector Efficiency

To determine the optimum operating current, the ionization efficiency of the detector was monitored as a function of hot wire current. Recall from equation 5.5, the ionization efficiency depends upon the temperature of the hot wire. At temperatures above 1200 K, the ionization efficiency is approximately 100%, thus further increases in current will not enhance the number of ionized atoms.

The DC signal from the detector was monitored as a function of hot wire current. The background thermal beam signal and the background noise signal were both recorded as a function of current by monitoring the detector with the thermal beam blocked and unblocked. The results are plotted in Figure 7.5. The background thermal beam signal is shown with the background noise signal subtracted. For hot wire current less that ~ 1.25 amps, increasing the current increases both the background thermal beam signal and the background noise signal. For hot wire current greater than ~1.25 amps, the background noise signal increases dramatically, but no increase in signal from the thermal beam is detected. At the point where thermal beam signal remains constant, the ionization efficiency has reached a maximum. At the normal operating current of 1.25 amps, the ionization efficiency of the hot wire is thus approximately 100%.

Use of the accelerator and repelling grids to increase the detector signal have been ineffective. In the absence of an electric field to accelerate the ions through the accelerator grid, only a fraction of the ions emitted from the ionizing surface will reach the point where they are accelerated toward the MCP assembly. Though this parameter is difficult to access, we will make an estimate to facilitate comparison with the measured data. From geometrical considerations, an estimated 25% of the ions emitted in a symmetric distribution about the hot ribbon will enter the 1 inch diameter MCP assembly Coupled with a MCP detection efficiency of ~ 30% for 2 keV ions[7] , the overall detection efficiency is estimated to be 0.08 = (hot wire efficiency)(MCP efficiency) (geometric factor) = (1)(0.30)(.25).

---

[7] This performance specification is based on microchannel plate product literature provided by Galileo Electro-Optics Corporation.

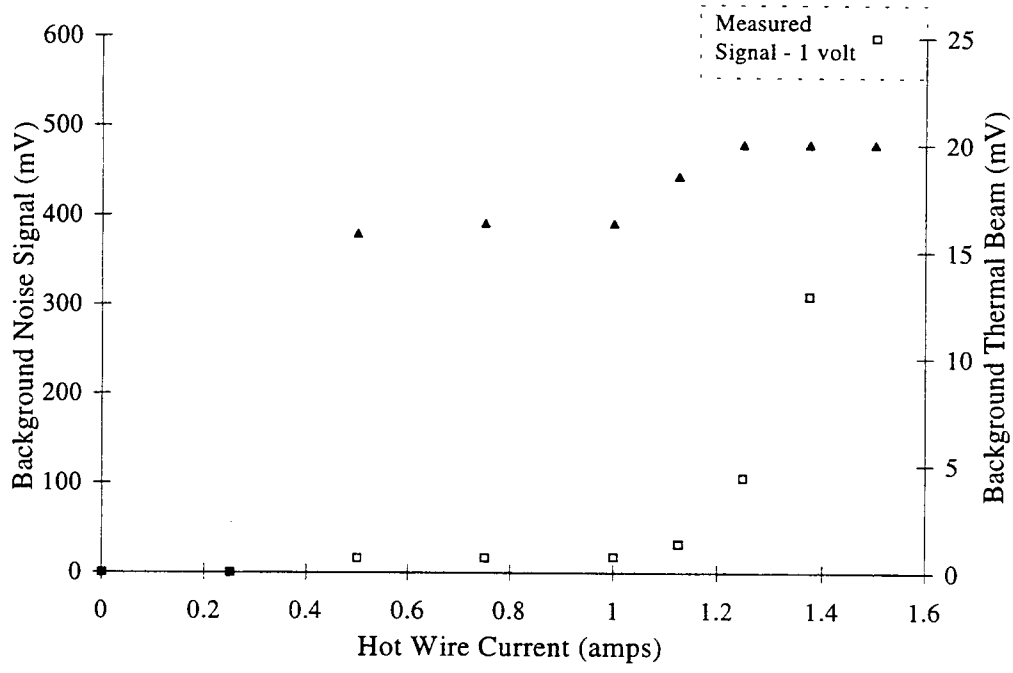

Figure 7.5 Detected DC signal from the surface ionization detector as a function of current through the rhenium ribbon. The square [triangle] markers correspond to the background noise [thermal] signal.

7.3.5 Predicted Spatial Distribution of the Atomic Beam

In the region between the atomic funnel and the detector, the atomic beam will expand due to its finite temperature. Since the horizontal and vertical transverse temperatures may differ, expansion of the beam need not be symmetric in the two dimensions. Transverse velocity damping of the beam is provided in the horizontal direction by the one-dimensional region of molasses downstream from the funnel. In the vertical direction, no velocity damping is provided by the molasses laser. In fact, recoil heating from the molasses laser can increase the vertical transverse temperature.

The spatial extent of the atomic beam at the detector can be estimated from the transverse temperature of the atomic beam in the molasses region. Assuming a

Maxwellian velocity distribution, the number of atoms with transverse velocities between v_T and $v_T + dv_T$ is

$$N(v_T)dv_T = \frac{N_0}{\alpha\sqrt{\pi}} e^{-(v_T/\alpha)^2} dv_T, \tag{7.4}$$

where N_0 is the total number of atoms and α is given by

$$\alpha = \sqrt{2kT / M}\ . \tag{7.5}$$

Figure 7.6 illustrates the predicted horizontal spatial distribution of atoms at the location of the detector for a 10 m/s atomic beam. The horizontal transverse temperature was assumed to be 500 μK. The FWHM of the beam is 14 mm at the detector. The width of the rhenium ribbon and the one inch range of detector travel are indicated for reference. Provided the atomic beam is directed along the center axis, the range in travel of the detector translation stage allows for interception of the majority of the atomic beam. Approximately 4 % of the atomic beam lies outside the detectable region. When stationary and on-axis, the 750 μm wire intercepts approximately 5 % of the atoms in the horizontal spatial distribution.

Figure 7.7 shows the predicted vertical spread of the beam at the detector assuming a 10 m/s velocity beam. The vertical transverse temperature of the beam was assumed to be 1 mK. This value is slightly larger than the ~ 600 μK temperature measured at the entrance to the molasses region to account for an increase in temperature due to recoil heating. The corresponding FWHM of the beam is 21 mm in the vertical direction at the detector. The amount of the beam incident upon the hot wire through the 6.36 mm high opening in the detector shield is indicated for reference. For an atomic beam vertically centered on the opening in the detector shield, ~ 28 % of the vertical beam dimension has access to the hot wire.

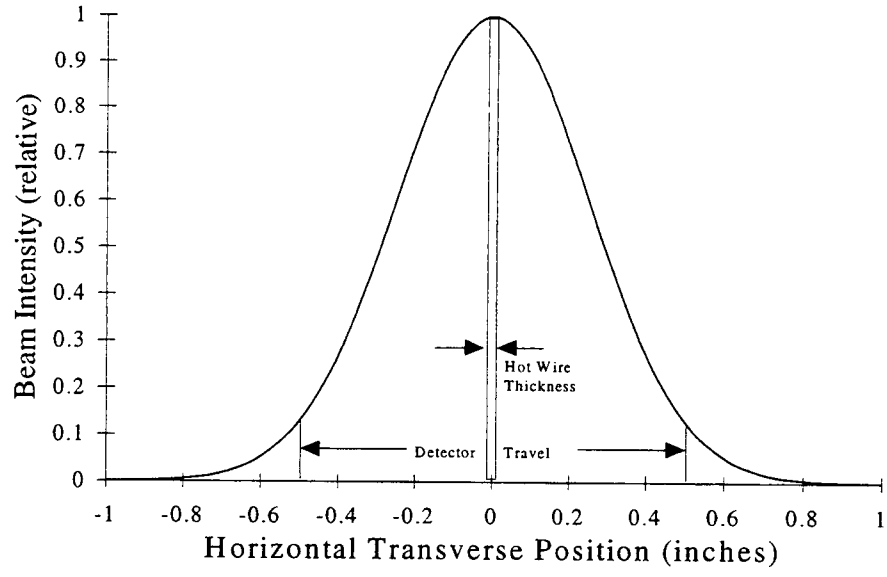

Figure 7.6 Theoretical horizontal distribution of the atomic beam at the surface ionization detector. The distribution shown corresponds to a 10 m/s velocity atomic beam with a horizontal transverse temperature of 500 μK. The range of travel of the detector is indicated for reference.

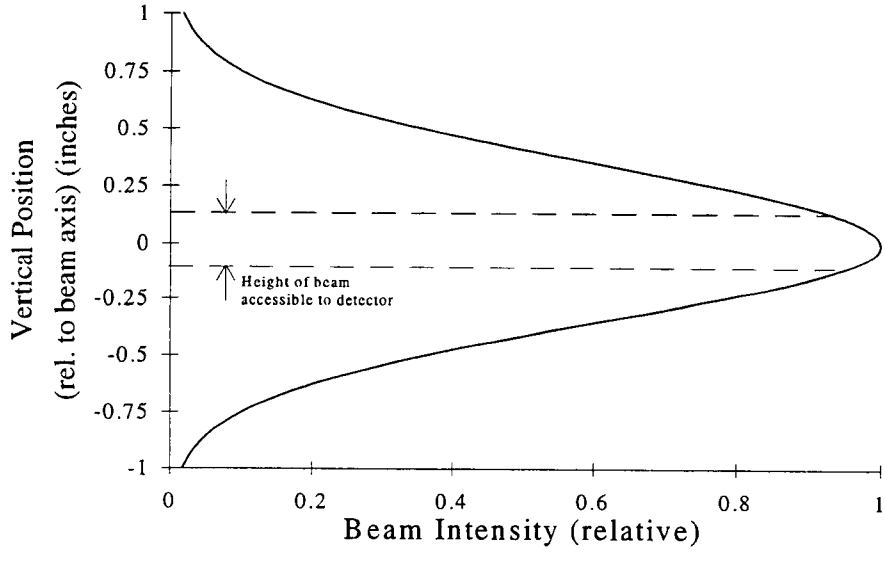

Figure 7.7 Theoretical vertical distribution of the atomic beam at the surface ionization detector. The distribution shown corresponds to a 10 m/s velocity atomic beam with a vertical transverse temperature of 1 mK. The range of the beam incident upon the hot wire through the 6.36 mm high opening in the hot wire detector shield is indicated for reference.

In the region between the atomic funnel and the detector, the atomic beam also falls due to gravity. A 10 m/s atomic beam will fall 4.4 mm in a distance of 30 cm. Since the detector opening is 6.35 mm high (± 3.175 mm from the center line), the center of an atomic beam ejected horizontally from the atomic funnel will be slightly lower than the hot wire in the detection region. As a result, the amount of the vertical beam area that has access to the hot wire is reduced to ~ 25 %.

From the estimates in transverse spread of a 10 m/s velocity atomic beam, we can estimate the flux of atoms incident upon the detector as well as the total flux of atoms detectable in the beam. The flux of atoms exiting the atomic funnel loaded using Zeeman slowing was measured to be 3.4×10^9 atom/s. For a detector efficiency of 8 %, the maximum expected signal for the on-axis detector is 3.4×10^6 atoms/second [(trap flux) (detector efficiency) (horizontal detection range)(vertical detection range)] = [$(3.4 \times 10^9$ atoms/s)(0.08)(0.05)(0.25)]. When using the detector to map out the spatial distribution of the atomic beam, a maximum of 6.5×10^7 atoms/s [$(3.4 \times 10^9$ atoms/s) (0.08)(0.96)(0.25)] lie within the detection range of the surface ionization detector.

An issue which further complicates detection of the low-velocity atomic beam is that deflection of the beam can occur in both the horizontal and vertical directions if an imbalance of forces is present. Misalignment of the trapping lasers at the exit end of the atomic funnel can impart an appreciable horizontal or vertical transverse component of velocity to the exiting beam. The downstream molasses region provides some damping of the transverse velocity. However, lack of confinement in the vertical direction could result in the atomic beam missing the detection region. The CCD camera is used as a diagnostic tool to help optimize alignment of the trapping lasers and minimize deflection.

A large part of the difficulty in aligning the horizontal lasers has been that the opposing beams are not quite counter-propagating. To avoid unwanted feedback to the horizontal lasers, these beams are intentionally slightly misaligned. The recent acquisition of optical isolators for the respective beam paths should simplify alignment of the horizontal beams and help minimize force imbalances at the exit end of the funnel.

A more significant problem arises if the molasses-probe laser is not well aligned. Due to constraints imposed by the system, it is difficult to clearly see the fluorescence

from the exit end of the molasses region on the vertical CCD camera. Thus, misalignment is more difficult to detect. To minimize deflection of the atomic beam careful alignment of the retro-reflected molasses probe laser is required. Because the beam is expanding slightly, perfect overlap between the incident and retro-reflected beams is not possible. To minimize deflection of the exiting atomic beam, the beams are aligned for optimum overlap at the output end of the molasses region. To aid in this process, a razor blade was placed in the incident laser beam path to provide a sharp edge at the exit end of the molasses region. Prior to aligning the molasses laser in this fashion, the measured spatial profile of the beam was skewed relative to the center of the detector, indicating deflection of the atomic beam.

7.3.6 Measured Spatial Distribution of the Atomic Beam

The spatial distribution of the atomic beam was characterized using the surface ionization detector. From the spatial distribution, the horizontal transverse temperature and flux of atoms in the low-velocity atomic beam were estimated. During the experiment, the DC detector signal was monitored as a function of transverse detector position with the atomic funnel operating and a 7 mm wide molasses-probe laser. For each data set, the detector was moved manually via the translation stage in increments of 0.05 inches. The background signal, which drifted up slightly, was subtracted independently from each point.

To estimate the horizontal transverse temperature of the atomic beam, each set of experimental data was fit to the Gaussian curve

$$y(x_T) = a \exp^{\left(-(x_T-b)^2/c^2\right)} \tag{7.6}$$

using the curve fit routine in *KaleidaGraph*[8] . The adjustable parameters are a, b, and c. To use the theoretical fit to estimate the transverse temperature of the atomic beam, equation 7.6 was compared with equation 7.4. The transverse position x_T is related to the transverse velocity v_T by the relationship $v_T = (x_T/x_L)(v_L)$, where x_L is the longitudinal distance to the detector and v_L is the longitudinal velocity. Parameter c is then related to the transverse temperature T and velocity v_L by the expression

$$c = \sqrt{\frac{2kT}{M}}\frac{x_L}{v_L}. \tag{7.7}$$

The longitudinal position x_L is 28.5 cm and the longitudinal velocity v_L is determined from the time-of-flight data. These factors, along with the calculated error in the value of parameter c, allow for the determination of a range of values for the transverse beam temperature.

Figure 7.8 shows the profile of the beam for a frequency offset of the horizontal trapping lasers of ± 7 MHz. The squares correspond to the measured detector signal with the background signal subtracted. The Gaussian curve was fit to the data assuming a 7.7 m/s longitudinal beam velocity. From the theoretical fit., the horizontal transverse temperature of the beam was calculated to be $980^{+130}_{-120}\,\mu$K.

The total flux of detected atoms calculated from the experimental data is 6.5 x10^6 atoms/s. The flux of atoms exiting the funnel while this data was taken was determined from the trap fluorescence signal to be 1.6 x 10^9 atoms/s. Based on the transverse temperature and beam velocity, the expected detector signal is approximately 2.1 x10^7 atoms/s [(trap flux)(detector efficiency)(horizontal detection range)(vertical detection range)] = [(1.6 x 10^9 atom/s)(0.08)(0.93)(0.18)].

Figure 7.9 shows the profile of the beam for a detuning of the horizontal trapping lasers of ± 12 MHz. The squares correspond to the measured detector signal with the background signal subtracted. The curve is the Gaussian fit to the data. For a 13.2 m/s

[8] *KaleidaGraph* is a registered trademark of Abelbeck Software.

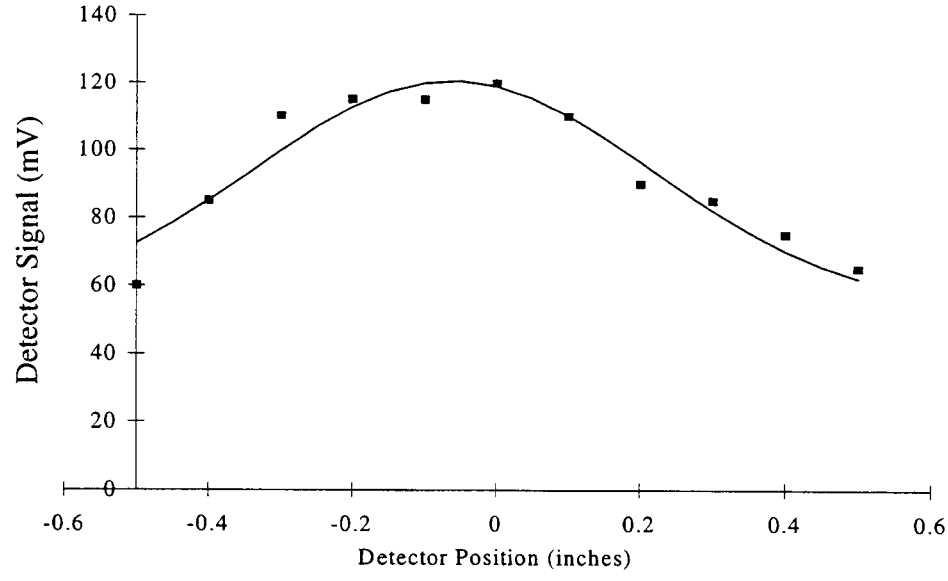

Figure 7.8 Spatial profile of the atomic beam 30 cm from the exit of the funnel for a horizontal trap laser detuning of ± 7 MHz. The squares correspond to the measured data. The curve is the theoretical fit. For a velocity of 7.7 m/s, the calculated transverse beam temperature is 980^{+130}_{-120} μK.

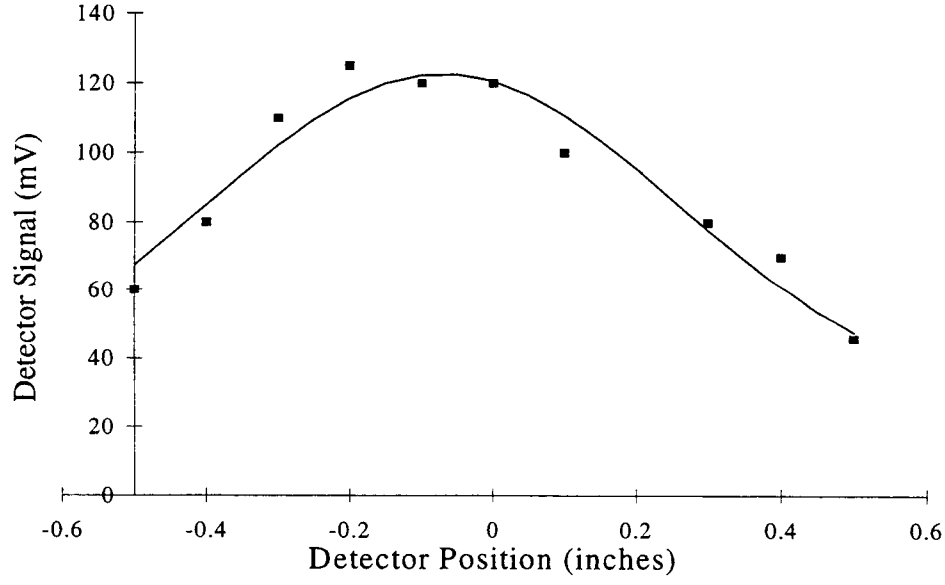

Figure 7.9 Spatial profile of the atomic beam 30 cm from the exit of the funnel for a horizontal trap laser detuning of ± 12 MHz. The squares correspond to the measured data. The curve is the theoretical fit. For a velocity of 13.2 m/s, the calculated transverse beam temperature is $2.2^{+0.3}_{-0.2}$ mK.

beam velocity, the theoretical fit yields a horizontal transverse beam temperature of $2.2^{+0.3}_{-0.2}$ mK. This value, though higher than the temperature for the 7 MHz offset trap, is not unreasonable since the faster velocity beam spends less time in the funnel and molasses region.

The total flux of detected atoms calculated from the experimental data is 6.3 x10^6 atoms/s. At this velocity and temperature, the anticipated number of detected atoms is 3.7 x10^7 atoms/s [(1.6 x 10^9 atom/s)(0.08)(0.86)(0.34)].

From the experimental results, it appears that about 20 to 30% of the low-velocity beam is being detected. This difference is not unreasonable since we were only able to estimate the detection efficiency of the surface ionization detector. However, it is also possible that atoms are missing the detector due to vertical deflection of the atomic beam. If this is the case, more precise alignment of the trapping laser may improve the signal. Minimizing stray magnetic fields will also help.

Since our objective is to use the detector in diffraction and interference experiments, where the flux of atoms is reduced, we would like to maximize the detected signal. External magnetic fields were applied in different orientations to increase the flux of atoms at the detector. A longitudinal magnetic field was used to increase the exit velocity of the atoms leaving the funnel. A slight improvement to the signal resulted due to a decrease in gravitationally induced deflection. However, achievable gains are limited due to the increase in the horizontal transverse temperature of the beam that accompanies the reduction in transit time through the funnel and molasses region.

A vertical transverse magnetic field (i.e., along the axis of the vertical trapping lasers) was applied in order to move the zero point of the magneto-optic trap field up. By raising the beam vertically in the funnel, some compensation can be made for the impact of the gravitational field on the atomic beam trajectory. This technique was unsuccessful, since shifting the vertical location of the trap axis without modifying the alignment of the trapping lasers increased the transverse temperature of the beam. The result was a trap that was visually distended and a decrease in the signal at the surface ionization detector.

To gain further insight into the experimental results, the signal intensity at the on-axis detector was monitored as various laser beams were blocked. In each case, the lasers

not mentioned were not modified from their configuration during normal operation of the trap. Independently blocking the cooling laser, the trap re-pump, or the back horizontal lasers caused the signal at the detector from the low-velocity atomic beam to be zero (the offset voltage due to background rubidium in the chamber remained constant.) Blocking the molasses laser reduced the atomic beam signal by about 70 %, indicating that the confinement provided by the molasses laser significantly enhances the beam like quality of the low-velocity source.

When both vertical beams were simultaneously blocked, the intensity of the signal at the detector did not change. In this configuration fluorescence from the trap is not visible on the CCD camera. Fluorescence from the molasses region can still be observed, however the picture on the CCD camera is dimmer than when the vertical beams are present in the trap. The lack of impact of the vertical lasers could be an indication that very little vertical confinement is being provided. However, measured vertical transverse temperatures in the 600 μK range seems to counter this conclusion, since the measured transverse temperature of the Zeeman slowed beam before trapping was a few Kelvin. It is possible that such a small percentage of the vertical distribution of the beam is being detected that the impact of the vertical lasers is insignificant.

It was discovered that if the vertical lasers and front horizontal laser pair were simultaneously blocked, the signal at the detector increased. Shifting the frequency of the back horizontal lasers over the -8 to -20 MHz frequency detuning range did not noticeably impact the detected signal. The spatial profile, measured with the back horizontal laser pair tuned 13 MHz below resonance, is illustrated in Figure 7.10. The squares correspond to the measured data, and the curve is the theoretical Gaussian fit. The measured spatial distribution is significantly broader than the profile of the trapped beam exiting the funnel. The theoretical fit yields a relationship between transverse temperature and the horizontal velocity of $T = v_L^2\ (2.2\text{x}10^{-5})^{+0.0000018}_{-0.0000013}$. The expected drift velocity imparted to an atom by the back horizontal lasers pair was determined using a simple two-dimensional model of the atomic funnel. In the model, numerical integration

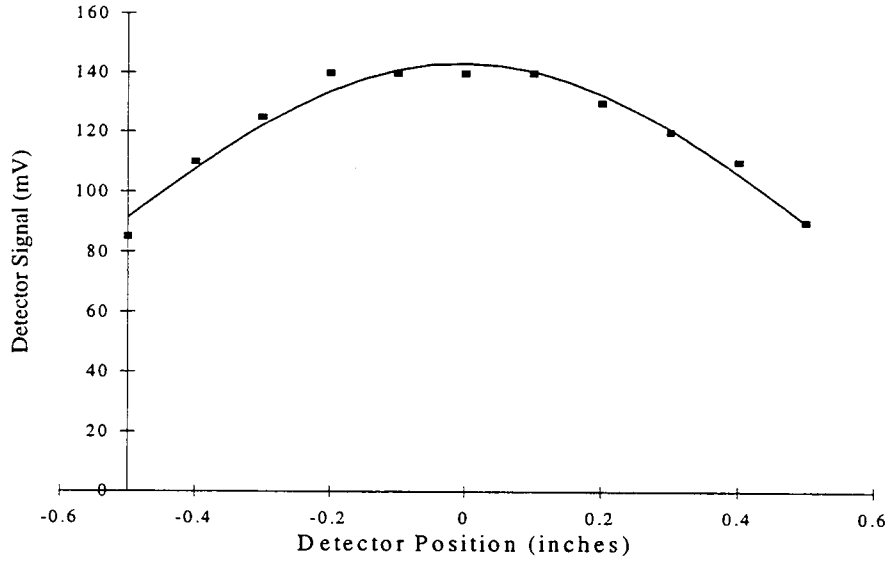

Figure 7.10 Spatial profile of the atomic beam 30 cm from the exit of the funnel with the vertical lasers and front horizontal laser pair blocked. The squares correspond to the measured data and the curve is the theoretical fit. The predicted velocity of the exiting beam is ~15 m/s and the transverse temperature is ~5.0 mK.

of the scattering rate equation (equation 3.6) was used to determine the exit velocity of a 20 m/s atom entering the funnel region. The laser intensity I was 4.5 mW/cm^2 and the detuning of the lasers from resonance was -13 MHz. Substituting the predicted longitudinal velocity of 25 m/s into the relationship above yields a horizontal transverse temperature of the exiting hot beam of approximately $13.8^{+1.1}_{-0.9}$ mK.

For this laser configuration, the detected flux of atoms was 8.4 x10^6 atoms/s, 30% larger than the number measured in the two previous cases in which all the trapping lasers were present. The estimated number of detected atoms is 1.7 x10^7 atoms/s [(1.6 x 10^9 atom/s)(0.08)(0.66)(0.20)]. Due to the absence of the front and vertical trapping lasers, this configuration is less likely than the low-velocity beam exiting the trap to experience deflection from laser misalignment. This could account for the greater number of atoms. It may also be possible that an increased number of the Zeeman slowed atoms participate in this process compared to the number captured and unloaded from the

funnel. It should be noted that the large transverse velocity of this relatively hot flux of atoms makes it less effective as a low-velocity source.

To more efficiently use the detector to optimize system parameters, steps were taken to automate the data acquisition process for mapping out the spatial distribution of the atomic beam. A stepper motor was used to rotate the knob controlling the detector translation stage. As the detector was moved, the DC detector signal was recorded using a computer and a commercially available data acquisition program. However, the maximum rate at which the detector could be moved by the stepper motor was 5 revolutions/minute. Thus, traversing the one inch range of stage travel required 8 minutes. The drift in the lasers during this time was found to be too significant to yield a reasonable atomic beam profile. By using a motor of comparable torque and larger step size and by improving the long term stability of the lasers, this automated process would provide for more efficient data acquisition.

7.4 Demonstration of Magneto-Optical Deflection of a Low-Velocity Beam

Translating the detector to map out the spatial profile proved to be both time consuming and difficult to automate. In order to provide a more rapid means to collect data and optimize system parameters, the detector position was fixed and the low-velocity beam was deflected. Deflection of the beam was accomplished using an applied magnetic field in conjunction with a region of one-dimensional optical molasses. In addition to its use as a tool to examine the beam profile, magneto-optic deflection of a low-velocity atomic beam has many potential commercial applications. Controllable, scanning deflection of a low-velocity atomic beam would provide a valuable atomic beam source for applications similar to existing electron beam devices. Possible applications include atom lithography and atom microscopy. Preliminary results on magneto-optic deflection are provided below.

An atomic beam can be deflected through large angles using magneto-optic forces [Shang, 1991]. Deflection of an atomic beam was demonstrated in our laboratory using an applied magnetic field in conjunction with the one-dimensional region of optical molasses located downstream from the atomic funnel. For $\sigma^+ - \sigma^-$ optical molasses and Doppler cooling, atoms acquire a transverse drift velocity of $v_T = - g_e \mu_B B / (\hbar k) = 0.55B$ (m/s)/G, where g_e is the excited state Lande factor and the direction of B is parallel to the axis of optical molasses [Walhout, 1992]. For polarization gradient cooling, the relationship is $v_T = - g_g \mu_B B / (\hbar k) = 0.36B$ (m/s)/G, where g_g is the ground state Lande factor [Walhout, 1992]. For optical molasses using two beams with orthogonal polarization (lin $\perp$ lin) and polarization gradient cooling, the acquired drift velocity is $v_T = - g_g \mu_B B / (2\hbar k) = 0.18B$ (m/s)/G, where B is applied parallel to the polarization of one of the laser beams [Shang, 1991]. The deflection angle θ is related to the transverse velocity by $\tan\theta = v_T / v_L$. Thus, for a longitudinal velocity v_L of 10 m/s only a few Gauss field is required for large angle deflection.

An externally applied magnetic field was used to horizontally deflect the atomic beam in a region of nominally lin $\perp$ lin optical molasses (imperfect laser polarization results in some circularly polarized light being present as well.) The field was created using the pair of coils added to the chamber to provide a compensation field to counter the residual Zeeman field. (On axis, the generated field is parallel with the axis of the Zeeman solenoid and perpendicular to the axis of the atomic funnel.) The field along the axis of the coils is approximately constant at the center of the atomic funnel, with magnitude of $B_C = 0.93I$ (reference Figure 6.8.) In the molasses region, which is ~ 3.5 cm off-center from the axis of the compensation field coils, the field is reduced slightly in magnitude.

Deflection of the low-velocity atomic beam was demonstrated in both a static and temporally varying magnetic field configuration. In both cases, deflection of the beam in the molasses region was dramatically evident on the vertical CCD camera. For static deflection, a fixed current was passed through the magnetic field coils. To deflect the atomic beam using a temporally varying magnetic field, the current source illustrated in Figure 7.11 was used to modulate the current through the magnetic field coils. A triangle

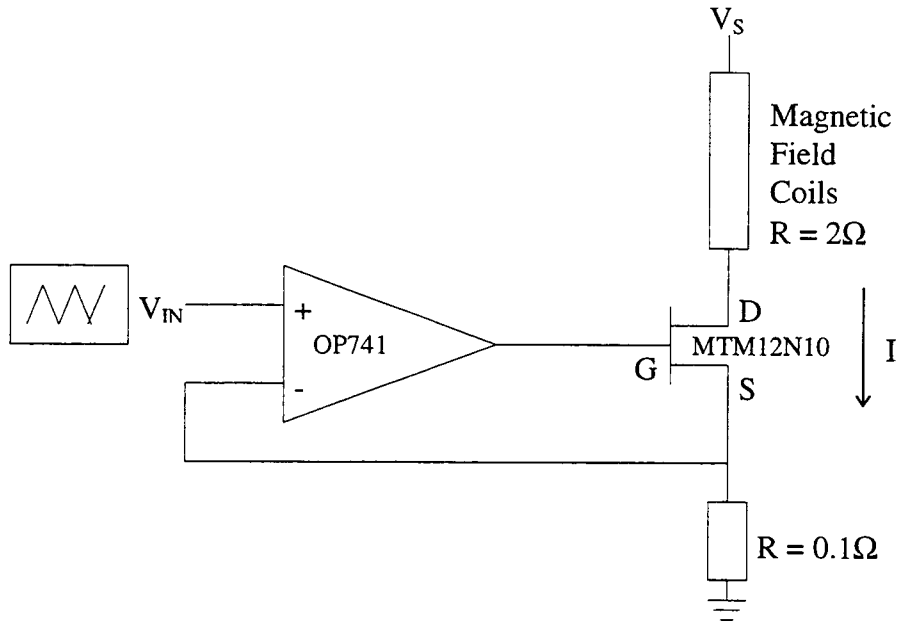

Figure 7.11 Controllable current source for modulating the magnetic field to deflect the low-velocity atomic beam.

wave input applied to the circuit modulated the current through the magnetic field coils, thereby modulating the magnetic field.

For static deflection, a sequence of CCD pictures was taken, corresponding to different fixed values of the applied magnetic field. The frequency offset of the horizontal trapping lasers was 2 MHz, corresponding to a longitudinal velocity of 2.2 m/s. The angular deflection $\theta_{Deflection}$ of the atomic beam in the molasses region was measured as a function of applied magnetic field B_C. The relationship between deflection angle and applied magnetic field was determined empirically to be

$$\theta°_{Deflection} = 3.5° + 5^{+1}_{-1}\,(°/\mathrm{G})\,B_C\,(\mathrm{G}). \qquad (7.8)$$

The 3.5° offset is caused by deflection from the residual Zeeman field and funnel field present in the molasses region. For this measurement, the Zeeman bias magnetic field was zero. A larger bias field results in a larger offset deflection (e.g. the offset deflection

for a 12 amp bias field was measured to be ~ 6°.) The empirical relationship indicates that Zeeman bias fields of zero amps and 12 amps corresponds to residual fields $B_{residual}$ of approximately 0.7 G and 1.2 G respectively. Thus, the empirical relationship can be equivalently stated

$$\theta^{\circ}_{Deflection} = 5^{+1}_{-1}\,(^{\circ}/\mathrm{G})\,B\,(\mathrm{G}), \tag{7.9}$$

where B is the total magnetic field in the molasses region (i.e. $B_C + B_{residual}$).

From the empirical relationship of equation 7.9, the transverse drift velocity v_T as a function of magnetic field can be derived. For small angles the relationship is given by

$$v_T \cong (\theta_{rad})\,v_L = [0.087^{+0.017}_{-0.017}\,B\,(\mathrm{G})]\ 2.2\ \mathrm{m/s}$$

$$= [0.19^{+0.038}_{-0.038}\ (\mathrm{m/s})/(\mathrm{G})]\,B\,(\mathrm{G}). \tag{7.10}$$

This result is in good numerical agreement with the predicted drift velocity for lin ⊥ lin molasses of $v_T = 0.18B$ (m/s)/G. However, the predicted drift velocity is for a magnetic field parallel to the polarization of one of the molasses laser beams. Since the nominal orientation of the applied magnetic field is not is the required direction, there is some uncertainty about the source of the deflection. There may be a sufficient fringing field to create a component of the field in the appropriate direction for deflection by the lin ⊥ lin molasses. Or, since the applied magnetic field is in the appropriate direction for transverse deflection with σ^+ - σ^- optical molasses, the deflection could result from the component of circularly polarized light present in the imperfectly polarized molasses laser beam. For σ^+ - σ^- optical molasses, the predicted drift velocity for polarization gradient cooling is $v_T = 0.36B$ (m/s)/G, larger than that given by equation 7.10. Since the applied magnetic field and longitudinal atomic velocity are not known precisely, the observed deflection could be a result of the σ^+ - σ^- light present in the molasses beam.

Scanning deflection of the atomic beam was monitored as a function of the applied magnetic field using the surface ionization detector. The detector was positioned at the center line of the chamber and the DC detector signal was recorded as a function of the applied magnetic field. Because the electronic circuit only allowed for positive

changes in current, the atomic beam was deflected in one direction, from near the center line (3.5°) to approximately 20°.

Figure 7.12 show the intensity of the on-axis atomic beam as a function of applied magnetic field for traps with horizontal trapping laser offsets of ± 7 MHz and ± 12 MHz and for the configuration with just the back horizontal trapping lasers present. The triangle wave current sweep ranged from zero amps to 3.5 amps. The sweep rate for the data shown was 0.2 Hz, though significantly faster sweep rates are possible. The squares [triangles] {circles} correspond to the measured detector signal for ± 7 MHz [± 12 MHz] {back horizontal lasers} and the curve is the Gaussian fit to the data assuming a symmetric distribution and zero magnetic field at zero current. Because of the 0.7 G magnetic field offset at zero current, the width of the plotted distributions is artificially narrowed. This will result in a reduction in the calculated temperature. The relative signal amplitudes are consistent with the spatial profiles discussed in section 7.3.6. From the theoretical fit, the horizontal transverse temperature of the beam was calculated for each configuration using equation 7.4 and the relationship between transverse velocity

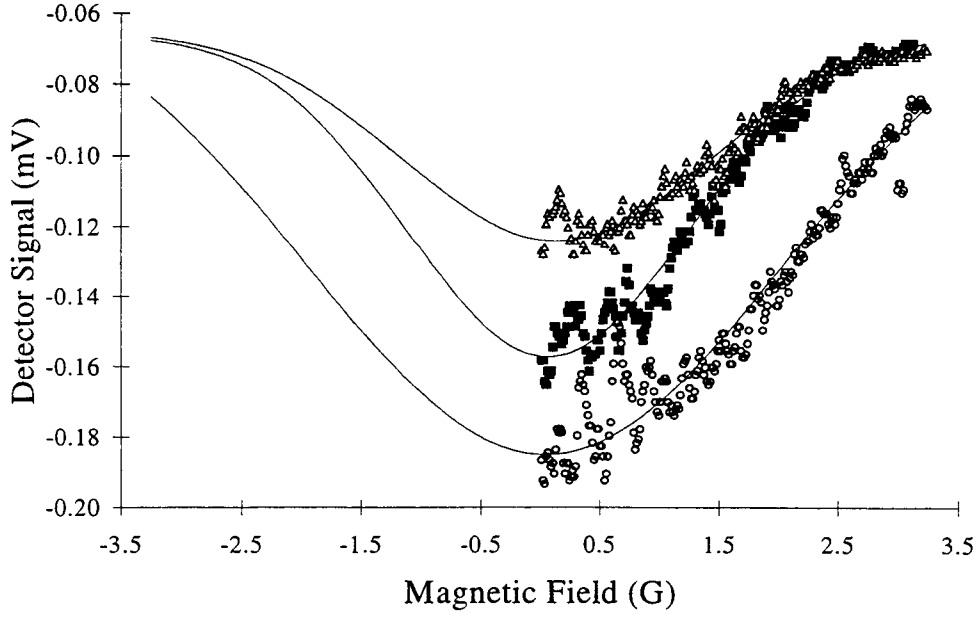

Figure 7.12 Surface ionization signal for an atomic beam deflected using an applied magnetic field. The square [triangle] {circle} data points correspond to ±7 MHz [±12 MHz]{back lasers}and the curves are the theoretical fits.

and magnetic field strength given by equation 7.10. The resulting temperatures of 510^{+14}_{-12} μK, 620^{+20}_{-19} μK, and $3.2^{+0.4}_{-0.4}$ mK respectively for the ± 7 MHz, ± 12 MHz, and 'back horizontal lasers only' configurations are slightly lower, but otherwise consistent with those found for the spatial distributions in section 7.3.6.

Deflection of the low-velocity atomic beam was also demonstrated in a region of nominally σ^+ - σ^- optical molasses using the residual field from both the Zeeman slower and atomic funnel. The frequency offset of the horizontal trapping lasers was 1.5 MHz, corresponding to a longitudinal velocity of approximately 1.6 m/s. The measured deflection was 30° for the zero amp bias field (~ 0.7 Gauss residual field) and 40° for the 12 amp bias field (~1.2 Gauss residual field). Thus, the empirical relationship between deflection angle and magnetic field for σ^+ - σ^- optical molasses is given by

$$\theta^\circ_{Deflection} \cong 38^{+5}_{-5} (^\circ/\mathrm{G})\, B\,(\mathrm{G}). \tag{7.11}$$

The corresponding relationship between velocity v_T and magnetic field B is given by

$$v_T \cong (\theta_{\mathrm{rad}})\, v_L = 1.06^{+0.14}_{-0.14}\, B\,(\mathrm{m/s})/\mathrm{G}. \tag{7.12}$$

The predicted transverse velocity for Doppler cooling and σ^+ - σ^- optical molasses is $v_T = 0.55B$ (m/s)/G. For polarization gradient cooling, the transverse velocity is $v_T = 0.36B$ (m/s)/G. Thus, the measured deflection is significantly larger than anticipated.

In these preliminary demonstrations, it was shown that only a small applied magnetic field is required along with a one-dimensional region of optical molasses to provide controllable, scanning deflection of the low-velocity atomic beam. By adding a second, perpendicular region of optical molasses a two-dimensional deflection system to be developed. Quantitative interpretation of the results was complicated by imperfect laser polarization and the fact that the residual Zeeman field and applied magnetic field deflected the atoms in the atomic funnel as well as in the molasses region. To better characterize magneto-optic deflection of the beam, the applied field should be restricted to the region of optical molasses and the magnitude and direction of the field should be known with greater precision. In addition, better quality laser polarization should be achieved.

7.5 Feasibility Study: Diffraction of the Low-Velocity Atomic Beam by a Transmission Grating.

As a preliminary step, prior to testing the interferometer, a single transmission grating will be placed in the low-velocity atomic beam path in order to observe diffraction. Transmission gratings with 250 nm and 500 nm grating periods have been fabricated for this project [Swanson, 1995]. The gratings were produced in window widths of both 50 μm and 150 μm and window heights of both 0.5 mm and 1.0 mm. Multiple gratings are located on a single chip measuring 12 mm by 7 mm. The chip will be mounted in a holder which is fixed to a movable stage to allow the grating to be moved in and out of the beam path.

To assess the feasibility of using the existing beam for diffraction, three requirements must be considered. First, the diffraction orders must be sufficiently separated at the detector to allow for spatial resolution by the finite width detector wire. Second, the beam must be collimated to an angle less than the diffraction angle so that the divergence of the beam does not wash out the diffraction pattern. The third requirement is that there must be a sufficient beam intensity for detection with the surface ionization detector.

The existing beam has a controllable velocity in the range of 2 to 15 m/s. The de Broglie wavelength, given by $\lambda = h/p$, scales inversely with velocity. Thus, the diffraction angle is maximized by decreasing the beam velocity. Since gravity significantly impacts the trajectory of the beam for velocities less than ~10 m/s, this value will be used for the beam velocity. A 10 m/s rubidium beam has a de Broglie wavelength of 0.5 nm. Using a grating with 250 nm spacing, the diffraction angle for the first order peak will be 2 mrad.

The experimental set-up for observation of diffraction is similar to the illustration shown in Figure 7.3, except a diffraction grating is inserted in the low-velocity beam path in the region between the funnel and the detector. Designating the distance between the atomic funnel and the grating as *L1* and the distance between the grating and the detector as *L2*, the total distance, *L1*+*L2*, is 30 cm for the current location of the surface ionization

detector. The transverse separation d between the zero and first order diffracted beams is related to the diffraction angle and distance $L2$ by the relationship $tan\theta = d/L2$. The maximum practical distance of $L2$ is ~ 20 cm, resulting in a maximum separation of the diffraction orders of ~ 400 μm. The 750 μm wide rhenium ribbon used for preliminary beam characterization is therefore too wide for adequate spatial resolution of the diffracted beam. By turning the ribbon on edge, the width is reduced to 25 μm, which should be sufficiently small to resolve the diffraction orders. An appropriate mount, interchangeable with the existing one, was made for this purpose when the detector was built. Since the same size rhenium ribbon can be used, the detector operating requirements would remain unchanged. It is possible that the ribbon mounted on edge may twist when heated, thereby providing an imprecise front surface area. An alternative option, which would minimize such concerns, is to procure rhenium wire of the desired diameter.[9] The cross sectional area and surface area of the wire will need to be considered in order to appropriately modify the operating hot wire current.

To assure that the diffraction orders do not overlap, the beam must be collimated to an angle less than the 2 mrad diffraction angle. A half angle beam divergence of 0.25 mrad corresponds to a maximum transverse velocity of 2.5 mm/s. Since the recoil velocity of rubidium is 6 mm/s, external collimation is required to achieve this. Sufficient collimation can be achieved by placing a 50 μm slit 10 cm in front of the 50 μm wide grating. (Thus, $L2$ should be less than ~ 15 cm). For $L2$ of 10 cm and a transverse beam temperature of 500 μK, the collimation will decrease the beam intensity by a factor of about 100.

To make an estimate of the beam intensity of the zero and first order diffracted beams, an estimate of the diffraction efficiency of the gratings is required. Similar gratings were used by Keith *et al.* [Keith, 1988] in diffraction of a supersonic sodium beam. In their experiment the zero order beam had 20 % of the incident intensity and the first order beams each had 10 %. For an atomic beam incident on the collimating slit with a flux of 3.4 $x10^9$ atoms/s, the flux of atoms in the zero order beam is approximately

[9] Rhenium wire is available from ESPI in variety of diameters. Their smallest commercially available product is 127μm (0.005") in diameter.

6.8×10^6 atoms/s [(flux of atoms)(reduction by collimation)(transmission through grating)] = [$(3.4 \times 10^9$ atoms/s)(0.01)(.2)]. The intensity in the first order beam is reduced by a factor of two. The maximum detector signal can be estimated from the vertical and horizontal transverse spread of the beam and the detection efficiency of the detector. Assuming a 1.0 mm height grating window and a 25 μm diameter hot wire, the predicted maximum intensity incident upon the detector wire is about 3.8×10^4 atoms/s [(atom flux) (detector efficiency) (horizontal detection range)(vertical detection range)] = [$(6.8 \times 10^6$ atoms/s) (0.08)(0.15)(0.46)]. This size signal corresponds to a 20 mV signal if the DC current across a 1 MΩ resistor is used as the means of detection. A larger resister could be used to increase the voltage. However, at low count rates, detecting the diffracted beam using a suitable particle counter may be more reliable.

Chapter 8: Conclusions and Future Research

A continuous, low-velocity, nearly monochromatic atomic beam was produced using Zeeman-tuned laser cooling and two-dimensional magneto-optic trapping. Rubidium atoms from an effusive oven were slowed and cooled using σ^- Zeeman-tuned slowing. The scattering force from a counter-propagating, frequency-stabilized diode laser was used to decelerate the thermal beam of atoms to a velocity of ~ 20 m/s. A spatially varying magnetic field Zeeman shifted the resonance frequency of the atoms to compensate for the changing Doppler shift, thereby keeping the slowing atoms resonant with the fixed frequency laser. The solenoid for Zeeman-tuned slowing was designed and characterized to provide the appropriate magnetic field profile. An analytical model, developed to theoretically characterize the performance of the Zeeman slower, was found to be in good agreement with the experimental results. The flux of atoms in the 20 m/s slow atomic beam was measured to be 2.7×10^{10} atoms/second. Compared with the previously employed method of chirped cooling, which provided a pulsed slow atomic beam, the beam generated by Zeeman-tuned slowing is continuous.

The slow beam of atoms was loaded into a two-dimensional magneto-optic trap or atomic funnel. In the funnel, atoms are trapped along the funnel axis and experience a molasses-type damping force in all three spatial dimensions. By frequency shifting the laser beams used to make the trap, the atoms are ejected at a controllable velocity. The continuous matter-wave source has a controllable beam velocity in the range of 2 to 15 m/s, and longitudinal and transverse temperatures less than 500 μK. At 10 m/s, the de Broglie wavelength of the beam is 0.5 nm. The flux of atoms exiting the Zeeman-loaded funnel was measured to be 3.4×10^9 atoms/s. This is a factor of 15 greater than previously achieved using chirped cooling.

The spatial profile of the atomic beam was characterized 30 cm from the exit of the atomic funnel using a surface ionization detector. Operation of the surface ionization detector was characterized and methods for signal detection were examined. From the spatial profile of the low-velocity atomic beam, the transverse temperature was found to

be less than 1 mK. The total measured flux of atoms was ~ 6.5 x10^6 atoms/s. Based on the area of intersection between the atomic beam and the detector, and estimates of the detector efficiency, the predicted flux at the detector was ~3 x10^6 atoms/s.

It may be possible to increase the flux of atoms striking the hot wire detector by minimizing deflection of the atomic beam leaving the atomic funnel. To accomplish this, recently acquired optical isolators will be installed in the laser beam paths. This will allow for true retro-reflection of the laser beams, which will minimize the likelihood of unwanted deflection and also simplify alignment of the horizontal trapping lasers,

The low-velocity atomic beam is an ideal source for atom diffraction and interferometry, as well as a variety of applications in the field of atom optics. Preliminary designs have been completed for mounting a single grating in the high vacuum chamber. Next, diffraction from a single grating will be demonstrated as a preliminary step to installing and testing the atom interferometer. The characteristics of the existing beam were examined relative to its use in diffraction by a 250 nm spacing physical grating. For a 10 m/s velocity beam and a 50 μm collimating slit located 10 cm before the grating, the predicted flux of atoms in the zero-order peak was estimated to be 6.8 x10^6 atoms/s at the location of the surface ionization detector. For a 25 μm wide hot wire, the corresponding maximum incident flux is about 3.8 x10^4 atoms/s. Using the existing DC detection method, this corresponds to a 20 mV detected signal. A recently acquired particle counter will provide enhanced signal detection capabilities.

In other experiments in atom optics, an applied magnetic field, along with a one-dimensional region of optical molasses, was used to demonstrate deflection of the low-velocity atomic beam. In these preliminary demonstrations, the applied magnetic field deflected atoms in the atomic funnel as well as in the molasses region. This, coupled with imperfect laser polarization, complicated interpretation of the results. In future experiments, the applied magnetic field will be restricted to the region of optical molasses. In addition, by incorporating a second, perpendicular region of optical molasses, a two-dimensional deflection system will be developed. Controllable, scanning deflection of a low-velocity atomic beam will provide a valuable atomic beam source for applications similar to existing electron beam devices.

Bibliography

Abramowitz, M. and I. A. Stegun (editors), "Handbook of Mathematical Functions," Dover Publications, Inc. (1972).

Adams, C. S., M. Sigel, and J. Mlynek, "Atom Optics", Physics Reports **240,** 143 (1994).

Allman, B.E., A. Cimmino, A. G. Klein, G. I. Opat, H. Kaiser, and S. A. Werner, "Observation of the scalar Aharonov-Bohm effect by neutron interferometry," Phys. Rev. A. **48**, 1799 (1993).

Aminoff, C. G, A. M. Steane, P. Bouyer, P. Desbiolles, J. Dalibard, and C. Cohen-Tannoudji, "Cesium atoms bouncing in a stable gravitational cavity," Phys. Rev. Lett. **71**, 3083 (1993).

Anderson, A., S. Haroche, E. A. Hinds, W. Jhe, D. Meschede, and L. Moi, "Reflection of thermal Cs atoms grazing a polished glass surface," Phys. Rev. A. **34**, 3513 (1986).

Anderson, M. H., J. R. Ensher, M. R. Matthews, C. E. Wieman, and E. A. Cornell, "Observation of Bose-Einstein Condensation in a Dilute Atomic Vapor," Science **269**, 198 (1995).

Aspect, A., J. Dalibard, A. Heidmann, C. Salomon, and C. Cohen-Tannoudji, "Cooling atoms with stimulated emission," Phys. Rev. Lett. **57**, 1688 (1986).

Audretsch, J. and P. Marzlin, "Ramsey fringes in atomic interferometry: measurability of the influence of space-time curvature," Phys. Rev. A. **50**, 2080 (1994).

Bagnato, V. S., C. Salomon, E. Marega Jr., and S. C. Zilio, "Influence of adiabatic following and optical pumping in the production of an intense steady flux of slow atoms," J. Opt. Soc. Am. B. **8**, 497 (1991).

Balykin, V. I., V. S. Letokhov, Y. B. Ovchinnikov, and A. I. Sidorov, "Quantum-state-selective mirror reflection of atoms by laser light", Phys. Rev. Lett. **60**, 2137 (1988).

Balykin, V. I., V. S. Letokhov, and A. I. Sidorov, "Intense stationary flow of cold atoms formed by laser deceleration of atomic beam," Optics Comm. **49**, 248 (1984).

Barrett, T. E., S. W. Dapore-Schwartz, M. D. Ray, and G. P. Lafyatis, "Slowing atoms with σ^- polarized light," Phys. Rev. Lett. **67**, 3483 (1991).

Bauspiess, W., U. Bonse, H. Rauch, and W. Triemer, "Test measurements with a perfect crystal neutron interferometer," Triemer, Z. Physik **271**, 177 (1974).

Berkhout, J. J., O. J. Luiten, I. D. Setija, T. W. Hijmans, T. Mizusake, and J. T. M. Walraven, "Quantum reflection: focusing of hydrogen atoms with a concave mirror," Phys. Rev. Lett. **63**, 1689 (1989).

Beverini, N., S. De Pascalis, E. Maccioni, D. Pereira, F. Strumia, G. Vissani, Y. Z. Wang, and C. Novero, "Evidence for laser cooling in a magnesium atomic beam," Optics Lett. **14**, 350 (1989a).

Beverini, N., F. Giammanco, E. Maccioni, F. Strumia, and G. Vissani, "Measurement of the calcium $^1P_1$-$^1D_2$ transition rate in a laser-cooled atomic beam," J. Opt. Soc. Am. B. **6**, 2188 (1989b).

Bjorkholm, J. E., R. R. Freeman, A. Ashkin and D. B. Pearson, "Observation of focusing of neutral atoms by the dipole forces of resonance-radiation pressure", Phys. Rev. Lett. **41**, 1361 (1978).

Blatt, R., W. Ertmer, and J. L. Hall, "Cooling of an atomic beam with frequency-sweep techniques," Prog. Quantum Electron. **8,** 237 (1984).

Bonse, U. and M. Hart, "An X-ray Interferometer," Appl. Phys. Lett. **6**, 155 (1965).

Bradley, C. C., J. Chen, and R. G. Hulet, "Instrumentation for the stable operation of laser diodes," Rev. Sci. Instrum. **61**, 2097 (1990).

Carnal, O. and J. Mlynek, "Young's double-slit experiment with atoms: A simple interferometer," Phys. Rev. Lett. **66**, 2689 (1991).

Carter, G. M. and D. E. Pritchard, "Recirculating atomic beam oven," Rev. Sci. Instrum. **49**, 120 (1978).

Chang, B. J., R. Alferness, and E. N. Leith, "Space-invariant achromatic grating interferometers: theory," Appl. Opt. **14**, 1592 (1975).

Chapman, M. S., C. R. Ekstrom, T. D. Hammond, R. A. Rubenstein, J. Schmiedmayer, S. Wehinger, and D. E. Pritchard, "Optics and interferometry with Na_2 molecules," Phys. Rev. Lett. **74**, 4783 (1995).

Chinone, N., K. Aiki, and R. Ito, "Stabilization of semiconductor laser outputs by a mirror close to the laser facet," Appl. Phys. Lett. **33**, 990 (1978).

Chow, W. W., J. Gea-Banacloche, L. M. Pedrotti, V. E. Sandars, W. Scleich, and M. O. Scully, "The ring laser gyro," Rev. Mod. Phys. **57**, 61 (1985).

Chu S., L. Hollberg, J. Bjorkholm, A. Cable, and A. Ashkin, "Three-dimensional confinement and cooling of atoms by resonance radiation pressure," Phys. Rev. Lett. **55**, 48 (1985).

Cimmino, A., G. I. Opat, A. G. Klein, H. Kaiser, S. A. Werner, M. Arif, and R. Clothier, "Observation of the topological Aharonov-Casher phase shift by neutron interferometry," Phys. Rev. Lett. **63**, 380 (1989).

Clauser, J. F., "Ultra-high sensitivity accelerometers and gyroscopes using neutral atom matter-wave interferometry," Physica B. **151**, 262 (1988).

Cohen-Tannoudji, C., B. Diu, F. Laloé, "Quantum Mechanics," John Wiley and Sons (1977).

Cohen-Tannoudji, C. N. and W. D. Phillips, "New mechanisms for laser cooling," Physics Today, 33, (Oct. 1990).

Corney, A., "Atomic and Laser Spectroscopy," Oxford University Press (1977).

Dahmani, B., L. Hollberg, and R. Drullinger, "Frequency stabilization of semiconductor lasers by resonant optical feedback," Optics Lett. **12**, 876 (1987).

Dalibard, J. and C. Cohen-Tannoudji, "Laser cooling below the Doppler limit by polarization gradients: simple theoretical models," J. Opt. Soc. B. **6**, 2023 (1989).

Eastham, D. "Atomic Physics of Lasers," Taylor and Francis Inc. (1986).

Ekstrom, C. R., J. Schmiedmayer, M. S. Chapman, T. D. Hammond, and D. E. Pritchard, "Measurement of the electric polarizability of sodium with an atom interferometer," Phys. Rev. A. **51**, 3883 (1995).

Ertmer, W., R. Blatt, J. L. Hall, and M. Zhu, "Laser manipulation of atomic beam velocities: Demonstration of stopped atoms and velocity reversal," Phys. Rev. Lett. **54**, 996 (1985).

Ezekiel, S., "An overview of passive optical "gyros", Proc. SPIE **487**, 13 (1984).

Fabry, C. and A. Perot, Ann. de Chim. et Phys. **12**, 459 (1897).

Fabry, C. and A. Perot, Ann. de Chim. et Phys. **16**, 115 (1899).

Faller, J. E. and I. Marson, "Ballistic methods of measuring g-the direct free-fall and symmetrical rise-and-fall methods compared," Metrologia **25**, 49 (1988).

Figueroa, L., K. Y. Lau, H. W. Yen and A. Yariv., "Studies of (GaAl)As injection lasers operating with an optical fiber resonator", J. Appl . Phys. **51**, 3062 (1980).

Fizeau, H., Ann. de Chim. et Phys. **66**, 429 (1862).

Fleming, M. W. and A. Mooradian, "Spectral characteristics of external-cavity controlled semiconductor lasers," IEEE Journal of Quantum Electronics **QE-17**, 44 (1981a).

Fleming, M. W. and A. Mooradian, "Fundamental line broadening of single-mode (GaAl)As diode lasers," Appl. Phys. Lett. **38**, 511 (1981b).

Frisch, R., "Experimenteller nachweis des Einsteinschen strahlungsruckstobes," Z. Phys. **86**, 42 (1933).

Gaggl, R., L. Windholz, C. Umfer, and C. Neureiter, "Laser cooling of a sodium atomic beam using the Stark effect," Phys. Rev. A. **49**, 1119 (1994).

Gould, P. L., P. D. Lett, P. S. Julienne, W. D. Phillips, H. R. Thorsheim, and J. Weiner, "Observation of associative ionization of ultracold, laser-trapped sodium atoms," Phys. Rev. Lett. **60**, 788 (1988).

Gwinner, G., J. A. Behr, S. B. Cahn, A. Ghosh, L. A. Orozco, G. D. Sprouse, and F. Xu, "Magneto-Optic Trapping of Radioactive ^{79}Rb," Phys. Rev. Lett. **72**, 3795 (1994).

Hänsch, T. W. and A. L. Schawlow, "Cooling of gases by laser radiation," Optics Comm. **13**, 68 (1975).

Hecht, E., "Optics," 2nd edition, Addison-Wesley Publishing Co. (1987).

Hemmerich, A., D.H. McIntyre, D. Schropp, Jr., D. Meschede and T.W. Hansch, "Optically stabilized narrow linewidth semiconductor laser for high resolution spectroscopy," Optics Comm. **75**, 118 (1990).

Henry, C. H., "Theory of the linewidth of semiconductor lasers," IEEE Journal of Quantum Electronics **QE-18**, 259 (1982).

Jackson, J. D., "Classical Electrodynamics," John Wiley and Sons (1975).

Joffe, M. A., W. Ketterle, A. Martin, and D. E. Pritchard, "Transverse cooling and deflection of an atomic beam inside a Zeeman slower," J. Opt. Soc. Am. B **10**, 2257 (1993).

Kasevich, M. and S. Chu, "Atomic interferometery using stimulated Raman transitions," Phys. Rev. Lett. **67**, 181 (1991a).

Kasevich, M. and S. Chu, "Measurement of the gravitational acceleration of an atom with a light-pulse atom interferometer," Appl. Phys. B. **54**, 321 (1992).

Kasevich, M., D. S. Weiss, E. Riis, K. Moler, S. Kasapi, and S. Chu, "Atomic velocity selection using stimulated Raman transitions," Phys. Rev. Lett. **66**, 2297 (1991b).

Keith, D. W., C. R. Ekstrom, Q. A. Turchette, and D. E. Pritchard, "An interferometer for atoms," Phys. Rev. Lett. **66**, 2693 (1991a).

Keith, D. W., M. L. Schattenburg, H. I. Smith, and D. E. Pritchard, "Diffraction of atoms by a transmission grating," Phys. Rev. Lett. **61**, 1580 (1988).

Keith, D. W., R. J. Soave and M. J. Rooks, "Free-standing gratings and lenses for atom optics, J. Vac. Sci. Tech. B., **9**, 2846 (1991b).

Ketterle, W., A. Martin, M. A. Joffe, and D. E. Pritchard, "Slowing and cooling atoms in isotropic laser light," Phys. Rev. Lett. **69**, 2483 (1992).

Lambropoulos, M. and S. E. Moody, "Design of a three-state alkali beam source," Rev. Sci. Instrum. **48**, 131 (1977).

Lawall, J. and M. Prentiss, "Demonstration of a novel atomic beam splitter," Phys. Rev. Lett. **72**, 993 (1994).

Letokhov, V. S. , V. G. Minogin, and B. D. Paulik, "Cooling and trapping of atoms and molecules by a resonant laser field," Optics Comm. **19**, 72 (1976).

Lett, P. D., R. N. Watts, C. I. Westbrook, and W. D. Phillips, "Observation of atoms laser cooled below the Doppler limit," Phys. Rev. Lett. **61**, 169 (1988).

Levenson, M. D. and S. S. Kano, "Introduction to Nonlinear Laser Spectroscopy", Academic Press Inc. (1988).

Lu, Z-T., C. J. Bowers, S. J. Freedman, B. K. Fujikawa, J. L. Mortara, and S-Q. Shang, "Laser Trapping of Short-Lived Radioactive Isotopes," Phys. Rev. Lett **72**, 3791 (1994).

Lummer, O. and E. Gehrcke, Ann. D. Phys. **10**, 457 (1903).

Maki, J.J., N.S. Campbell, C.M. Grande, R.P. Knorpp and D.H. McIntyre, "Stabilized diode-laser system with grating feedback and frequency-offset locking," Optics Comm **102**, 251 (1993).

Martin, P. J., B. G. Oldaker, A. H. Miklich and D. E. Pritchard, "Bragg scattering of atoms from a standing light wave," Phys. Rev. Lett. **60**, 515 (1988).

Marton, L., J. Arol Simpson, and J. A. Suddeth, "Electron Beam Interferometer," Phys. Rev., **90**, 490 (1953).

Mendlowitz, H. and J. A. Simpson, "On the theory of diffraction grating interferometers," J. Opt. Soc. Am. **52**, 520 (1962).

Michelson, A. A., "Interference phenomena in a new form of refractometer," Phil. Mag. **13**, 236 (1882).

Michelson, A. A., "On the application of interference methods to spectroscopic measurements," Phil. Mag. **31**, 338 (1891).

Miniatura, C., J. Robert, S. Le Boieux, J. Reinhardt, and J. Baudon, "A longitudinal Stern-Gerlach atomic interferometer," Appl. Phys. B. **54**, 347 (1992).

Morinaga, M., M. Yasuda, T. Kishimoto, and F. Shimizu, "Holographic manipulation of a cold atomic beam," Phys. Rev. Lett. **77**, 802 (1996).

Nellessen, J., J. Werner and W. Ertmer, "Magneto-optical compression of a monoenergetic sodium atomic beam," Opt. Comm. **78**, 300 (1990).

Oates, C. W., K. R. Vogel, and J. L. Hall, "High precision linewidth measurement of laser-cooled atoms: resolution of the Na $3p^2$ $P_{3/2}$ lifetime discrepancy," Phys. Rev. Lett. **76**, 2866 (1996).

Phillips, W. D. and H. Metcalf, "Laser deceleration of an atomic beam," Phys. Rev. Lett. **48**, 596 (1982).

Phillips, W. D., J. V. Prodan, and H. J. Metcalf, "Laser cooling and electromagnetic trapping of neutral atoms," J. Opt. Soc. Am. B. **2**, 1751 (1985).

Prentiss, M. and A. Cable, "Slowing and cooling an atomic beam using an intense optical standing wave," Phys. Rev. Lett. **62**, 1354 (1989).

Prentiss, M., A. Cable, J. E. Bjorkholm, S. Chu, E. Raab, and D. Pritchard, "Atomic-density-dependent losses in an optical trap," Opt. Lett. **13**, 452 (1988).

Prodan, J. V., W. D. Phillips, and H. Metcalf, "Laser production of a very slow mono-energetic atomic beam," Phys. Rev. Lett. **49**, 1149 (1982).

Raab, E. L., M. Prentiss, A. Cable, S. Chu, and D. E. Pritchard, "Trapping of neutral sodium atoms with radiation pressure," Phys. Rev. Lett. **59**, 2631 (1987).

Ramsey, N. F., "Molecular Beams," Oxford University Press (1956).

Rauch, H., W. Treimar, and U. Bonse, "Test of a single crystal neutron interfometer," Phys. Lett. A. **47**, 369 (1974).

Rieger, V., K. Sengstock, U. Sterr, J. H. Müller, and W. Ertmer, "Atom-interferometric determination of the DC-Stark shift of the Mg-intercombination line," Opt. Comm. **99**, 172 (1993).

Riehle, F., Th. Kisters, A. Witte, J. Helmcke, Ch. J. Bordé, "Optical Ramsey Spectroscopy in a rotating frame: Sagnac effect in a matter-wave interferometer," Phys. Rev. Lett. **67**, 177 (1991).

Riis, E., D. S. Weiss, K. A. Moler, and S. Chu, "Atom funnel for the production of a slow, high-density atomic beam," Phys. Rev. Lett. **64**, 1658 (1990).

Sagnac, G., Compt. Rend. Acad. Sci. **157**, 708 (1913).

Schmidt, O., K. M. Knaak, R. Wynands, D. Meschede, "Cesium saturation spectroscopy revisited: How to reverse peaks and observe narrow resonances", Appl. Phys. B. **59**, 167 (1994).

Schmiedmayer, J., M. S. Chapman, Ekstrom, C. R., T. D. Hammond, S. Wehinger, and D. E. Pritchard, "Index of refraction of various gases for sodium matter waves," Phys. Rev. Lett. **74**, 1043 (1995).

Scoles, G., "Atomic and Molecular Beam Methods," Oxford University Press, New York, (1992).

Shang, S-Q., B. Sheehy, H. Metcalf, P. Van der Straten, and G. Nienhuis, "Velocity-selective resonances in sub-Doppler laser cooling," Phys. Rev. Lett. **67**, 1094 (1991).

Shimizu, F., K. Shimizu, H. Takuma, "Stark phase shift and deflection in the ultracold a atomic interferometer," Jpn. J. Appl. Phys. **31**, L436 (1992).

Silva, N. J., "Laser Cooling and Trapping with Electronically Stabilized Grating-Feedback Diode Lasers," Ph.D. Thesis, Oregon State University (1996).

Smith, P. W. and T. W. Hänsch, "Cross-relaxation effects in the 6328-aa neon-laser line", Phys. Rev. Lett. **26**, 740 (1971).

Steane, A. M., M. Chowdhury, and C. J. Foot, "Radiation force in a magneto-optic trap," J. Opt. Soc. Am. B. **9**, 2142 (1992).

Swanson, T. B., "A Rubidium Atomic Funnel," Ph.D. Thesis, Oregon State University (1995).

Swanson, T. B., N. J. Silva, S. K. Mayer, J. J. Maki, and D. H. McIntyre, "Rubidium atomic funnel," J. Opt. Soc. Am. B. **13**, 1833 (1996).

Ungar, P. J., D. S. Weiss, E. Riis, and S. Chu, "Optical molasses and multilevel atoms: theory," J. Opt. Soc. B. **6**, 2058 (1989).

Walhout, M., J. Dalibard, S. L. Rolston, and W. D. Phillips, "$\sigma_+ - \sigma_-$ Optical molasses in a longitudinal magnetic field," J. Opt. Soc. Am. B. **9**, 1997 (1992).

Walhout, M., H. J. L. Megens, A. Witte, S. L. Rolston, "Magneto-optical trapping of metastable xenon: isotope-shift measurements," Phys. Rev. A. **48**, 879 (1993).

Watts, R. N. and C. E. Wieman, "Manipulating atomic velocities using diode lasers," Opt. Lett. **11**, 291 (1986).

Weast, R.C. editor, "CRC Handbook of Chemistry and Physics," 58th edition, CRC Press, Inc. (1978).

Weiss, D. S., B. C. Young, and S. Chu, "Precision measurements of $\hbar/M_{Cs}$ based on photon recoil using laser-cooled atoms and atomic interferometry," Phys. Rev. Lett. **70**, 2706 (1993).

Weitz, M, B. C. Young, and S. Chu, "Atomic interferometer based on adiabatic population transfer," Phys. Rev. Lett. **73**, 2563 (1994).

Werner, S. A., J. Staudenmann, R. Colella, "Effect of the earth's rotation on the quantum mechanical phase of the neutron", Phys. Rev. Lett. **42**, 1103 (1979).

Wieman, C. and T. W. Hansch, "Doppler-Free Laser Polarization Spectroscopy", Phys. Rev. Lett. **36**, 1170 (1976).

Wieman, C. E. and L. Hollberg, "Using diode lasers for atomic physics," Rev. Sci. Instrum. **62**, 1 (1991).

Wineland, D. and W. Itano, "Laser cooling of atoms" Phys. Rev. A. **20**, 1521 (1979).

Yariv, A., "Optical Electronics", Holt, Rinehart and Winston, Inc. (1985), pg. 221.

Yeh, J. R., B. Hoeling, and R. J. Knize, "Longitudinal and transverse cooling of a cesium atomic beam using the D1 transition with Stark-effect frequency compensation," Phys. Rev. A. **52**, 1388 (1995).

Yu, J., J. Djeman, P. Nosbaum, P. Pillet, "Funnel with orientated Cs atoms," Opt. Comm. **112**, 136 (1994).

Zeeman, P., "On the influence of magnetism on the nature of the light emitted by a substance.", Phil. Mag. **43**, 226, (1897).

Zhu, M., C. W. Oates, and J. L. Hall, "Continuous high-flux monovelocity atomic beam based on a broadband laser-cooling technique," Phys. Rev. Lett. **67**, 46 (1991).

Zhu, M., C. W. Oates, and J. L. Hall, "Improved hyperfine measurements of the Na 5P excited-state through frequency-controlled Dopplerless spectroscopy in a Zeeman magnetooptic laser trap," Opt. Lett. **18**, 1186 (1993).

Appendix

Appendix: Maple Worksheet: Zeeman Shifted Energy Levels of the $5S_{1/2}$ and $5P_{3/2}$ States of Rubidium

A worksheet was developed in *Maple* to compute the Zeeman shift in the energy levels of the $5S_{1/2}$ and $5P_{3/2}$ states of rubidium. The Hamiltonian consists of the hyperfine structure term (equation 2.1) and the Zeeman shift term (equation 2.12). For a magnetic field directed along the z-axis, the total Hamiltonian can be written

$$H = A_J \mathbf{I}\cdot\mathbf{J} + \frac{B_J}{2IJ(2I-1)(2J-1)}\left(3(\mathbf{I}\cdot\mathbf{J})^2 + \frac{3}{2}(\mathbf{I}\cdot\mathbf{J}) - I(I+1)J(J+1)\right)$$

$$+ \mu_B g_J B J_Z - \mu_n g_I B I_Z. \qquad \text{(A.1)}$$

The *Maple* worksheet calculates the eigenvalues of the Hamiltonian in the $|M_J M_I\rangle$ basis using the following operator relationships (note: $\hbar = 1$):

$$J_Z|I\,J\,M_I\,M_J\rangle = M_J|I\,J\,M_I\,M_J\rangle \qquad \text{(A.2)}$$

$$I_Z|I\,J\,M_I\,M_J\rangle = M_I|I\,J\,M_I\,M_J\rangle \qquad \text{(A.3)}$$

$$\mathbf{I}\cdot\mathbf{J} = I_X J_X + I_Y J_Y + I_Z J_Z \qquad \text{(A.4)}$$

$$J_\pm = J_X \pm iJ_Y \qquad \text{(A.5)}$$

$$\mathbf{I}\cdot\mathbf{J} = I_Z J_Z + \frac{1}{2}I_+ J_- + \frac{1}{2}I_- J_+ \qquad \text{(A.6)}$$

$$J_\pm|I\,J\,M_I\,M_J\rangle = \sqrt{J(J+1) - M_J(M_J \pm 1)}\ |I\,J\,M_I\,M_J \pm 1\rangle \qquad \text{(A.7)}$$

$$I_\pm|I\,J\,M_I M_J\rangle = \sqrt{I(I+1) - M_I(M_I \pm 1)}\ |I\,J\,M_I \pm 1\,M_J\rangle \qquad \text{(A.8)}$$

MAPLE WORKSHEET TO CALCULATE ZEEMAN ENERGY SHIFT FOR RUBIDIUM

FILENAME: ZEEMAN

```
> with (linalg):
```

Define the appropriate quantum numbers

Rubidium 85
5P3/2 state: J = 3/2, I = 5/2, S = 1/2, L = 1
5S1/2 state: J = 1/2, I = 5/2, S = 1/2, L = 0
Rubidium 87
5P3/2 state: J = 3/2, I = 3/2, S = 1/2, L = 1
5S1/2 state: J = 1/2, I = 3/2, S = 1/2, L = 0

The calculations that follow are for the 5P3/2 state:

```
> J:=3/2:
> I1:=5/2:
> S:=1/2:
> L:=1:
```

Find the dimension of the matrices (24 x 24 for the 5P3/2 state of rubidium 85).

```
> dim:=(2*J+1)*(2*I1+1):
```

Initialize the matrices to zero.

```
> Jz:=matrix(dim,dim,0):
> Iz:=matrix(dim,dim,0):
> IplusJminus:=matrix(dim,dim,0):
> IminusJplus:=matrix(dim,dim,0):
> IdotJ:=matrix(dim,dim,0):
> IundJ:=matrix(dim,dim,0):
> Ident:=matrix(dim,dim,0):
>
```

Define the identity matrix.

```
> for Q1 from 1 to dim do
>   for Q2 from 1 to dim do
>     if Q1=Q2 then
>       Ident[Q1,Q2]:=1;
>     fi:
>   od;
> od;
```

Define the Kronecker delta function

```
> Delta:=proc(K,K1)
>   if K=K1 then
>     G:=1
>   else
>     G:=0;
>   fi:
> RETURN(G)
> end:
```

Calculate the matrices.

Jz and Iz are diagonal in the Mi, Mj basis (reference equations A.2 and A.3)

```
> i:=0:
> for Mj from -J to J do
>   for Mi from -I1 to I1 do
>     i:=i+1: j:=0:
>     Jz[i,i]:=Mj:
>     Iz[i,i]:=Mi:
>   od:
> od:
```

IplusJminus, and IminusJplus have off diagonal matrix elements (reference equations A.7 and A.8).

```
> i:=0: j:=0:
> for Mj from -J to J do
>   for Mi from -I1 to I1 do
>     j:=j+1: i:=0:
>     for Mj1 from -J to J do
>       for Mi1 from -I1 to I1 do
>         i:=i+1:
>           Iplus:=sqrt(I1*(I1+1)-Mi1*(Mi1+1));
>           Iminus:=sqrt(I1*(I1+1)-Mi1*(Mi1-1));
>           Jplus:=sqrt(J*(J+1)-Mj1*(Mj1+1));
>           Jminus:=sqrt(J*(J+1)-Mj1*(Mj1-1));
>           IplusJminus[j,i]:=Iplus*Jminus*Delta(Mi,Mi1+1)*Delta(Mj,Mj1-1);
>           IminusJplus[j,i]:=Iminus*Jplus*Delta(Mi,Mi1-1)*Delta(Mj,Mj1+1);
>       od:
>     od:
>   od:
> od:
```

Define I(dot)J in terms of Iz, Jz, I+, I-, J+, and J- (reference equation A.6).

```
> IdotJ:=add(multiply(Iz,Jz),1/2*(add(IplusJminus,IminusJplus))):
```

Define the second term of the Hamiltonian in terms of the appropriate operators (reference equation A.1).

```
> term2a:=add(((3/2)*IdotJ),(-I1*(I1+1)*J*(J+1)*Ident)):
> term2b:=add((3*multiply(IdotJ,IdotJ)),(term2a)):
```

Combine the individual matrices to obtain the total Hamiltonian (reference equation A.1).

```
> term1:=add(Aj*IdotJ,g*mu*B*Jz):
> term2:=Bj/(2*I1*(2*I1-1)*J*(2*J-1))*term2b:
> Hhfs:=add(add(term1,-gi*me*mu*B*Iz/Mp),(term2)):
```

Calculate the eigenvalues of the matrix. The results are provided in symbolic form.

```
> Energy:=eigenvals(Hhfs):
```

The energy eigenvalues can be examined by typing
Energy[i]; <CR>
where i = 1 through the number of eigenvalues.

Eigenvalues Energy[1] and Energy[2] are linear functions of B. They correspond to the following eigenvectors:
Energy[1]; F' = 4, MF' = -4, MI = -5/2, MJ = -3/2.
Energy[2]; F' = 4, MF' = 4, MI = 5/2, MJ = 3/2.

For the 5P3/2 state of rubidium 85:
Maple generated 15 eigenvalues rather than the expected 24. Three of the eigenvalues (Energy[8], [9], and [10]) are polynomial expression that Maple could not solve directly. In order to arrive at a result, a common factor of 10^15 was divided out, and then the roots of the polynomial expression were calculated.

For the 5P3/2 state of rubidium 87:
Maple generated 13 eigenvalues rather than the expected 16. One of the eigenvalues (Energy[8]) was a polynomial expression that Maple could not solve directly. In order to arrive at a result, a common factor of 10^15 was divided out, and then the roots of the polynomial expression were calculated.

For the 5S1/2 states or both isotopes, this was not a problem.

```
> Energy[8];
> T1:= (.6384*10^8*B+(-.3015*10^7-.7430*10^5*B-.3169*10^4*B^2)*Z^2+(.4266*10
  ^5+.6001*B)*Z^3+(-.4237*10^9-.5247*10^5*B^2-.5252*10^7*B-.26149*10^1*B^3)
  *Z+.1333*10^6*B^3+.1066*10^8*B^2+.2486*10^4*B^4+.3636*10^3*Z^4-.7134*10
  ^10);
> Solt8:=solve(T1,Z):
```

The four eigenvalues can be examined by typing
Solt8[i]; <CR>
where i = 1 through 4.

```
> Energy[9];
> T2:=(.3636*Z^4+.427*10^2*Z^3+(-.3015*10^4-.3169*10^1*B^2)*Z^2+(-.4237*10^
  6-.4251*10^2*B^2)*Z+.9461*10^4*B^2+.2486*10^1*B^4-.7134*10^7);
> Solt9:=solve(T2,Z):

> Energy[10];
> T3:=(-.6384*10^8*B+(-.4237*10^9-.5247*10^5*B^2+.5251*10^7*B+.2615*10^1*B
  ^3)*Z+(-.3015*10^7+.7430*10^5*B-.3169*10^4*B^2)*Z^2+(.4266*10^5-.6001*B)*Z
  ^3-.1332*10^6*B^3+.1065*10^8*B^2+.2486*10^4*B^4+.3636*10^3*Z^4-.7134*10
  ^10);
> Solt10:=solve(T3,Z):
```

Define the additional parameters.

Rubidium 85
5P3/2 state: gi = .54108, Aj=25.029, Bj = 26.032.
5S1/2 state: gi = .54108, Aj = 1011.9, Bj=0.
Rubidium 87
5P3/2 state: gi = 1.8337, Aj = 84.852, Bj = 12.510.
5S1/2 state: gi = 1.8337, Aj = 3417.3, Bj=0.

g-sub-j

```
> g:=(3*J*(J+1)+S*(S+1)-L*(L+1))/(2*J*(J+1)):
```

g-sub-i

```
> gi:=.54108:
```

mu-sub-b

```
> mu:=1.4:
```

mu-sub-n

```
> mun:=me/Mp*mu:

> Aj:=25.029:
> Bj:=26.032:
> Mp:=1836*me:
> me:=1:
```

Some of the eigenvalues have a very small imaginary component (<10^-7) that I believe originated from the algorithm used to determine the eigenvalues of the matrix. As such, only the real part of the eigenvalue expressions was plotted.

```
> plot({Re(Energy[1]),Re(Energy[2]),Re(Energy[3]),Re(Energy[4]),Re(Energy[5]),
  Re(Energy[6]),Re(Energy[7]),Re(Energy[11]),Re(Energy[12]),Re(Energy[13]),Re
  (Energy[14]),Re(Energy[15]),Re(Solt8[1]),Re(Solt8[2]),Re(Solt8[3]),Re(Solt8[4]),
  Re(Solt9[1]),Re(Solt9[2]),Re(Solt9[3]),Re(Solt9[4]),Re(Solt10[1]),Re(Solt10[2]),R
  e(Solt10[3]),Re(Solt10[4])},B=0..400);
```

>

Zeeman Shifted Energy Levels (in MHz/h)
of the P 3/2 State of Rb 85.

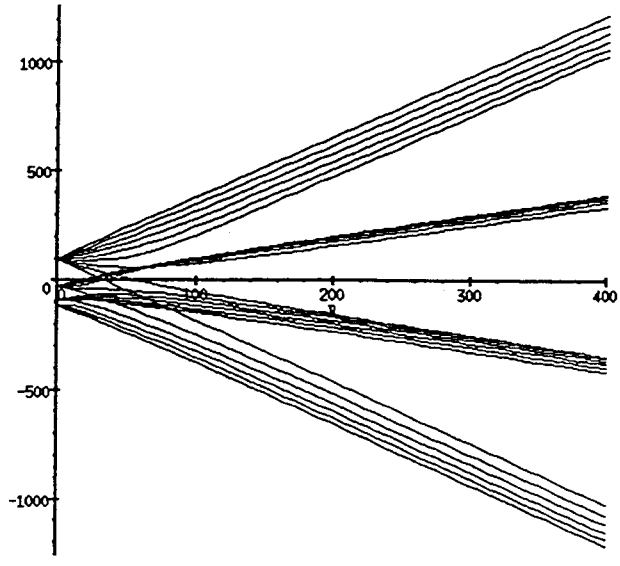

>

Generate numerical data to export to EXCEL

```
> points:=201:
> Bfull:=1005:
> Data1:=matrix(dim,2*points,0):
> B:=0:
> for r from 1 to points do
>   NumEn[1]:=Re(Energy[1]);
>   NumEn[2]:=Re(Energy[2]);
>   NumEn[3]:=Re(Energy[3]);
>   NumEn[4]:=Re(Energy[4]);
>   NumEn[5]:=Re(Energy[5]);
>   NumEn[6]:=Re(Energy[6]);
>   NumEn[7]:=Re(Energy[7]);
>   NumEn[8]:=Re(Energy[11]);
>   NumEn[9]:=Re(Energy[12]);
>   NumEn[10]:=Re(Energy[13]);
>   NumEn[11]:=Re(Energy[14]);
>   NumEn[12]:=Re(Energy[15]);
>   NumEn[13]:=Re(Solt8[1]);
>   NumEn[14]:=Re(Solt8[2]);
>   NumEn[15]:=Re(Solt8[3]);
>   NumEn[16]:=Re(Solt8[4]);
```

```
>   NumEn[17]:=Re(Solt9[1]);
>   NumEn[18]:=Re(Solt9[2]);
>   NumEn[19]:=Re(Solt9[3]);
>   NumEn[20]:=Re(Solt9[4]);
>   NumEn[21]:=Re(Solt10[1]);
>   NumEn[22]:=Re(Solt10[2]);
>   NumEn[23]:=Re(Solt10[3]);
>   NumEn[24]:=Re(Solt10[4]);
>   B:=B+Bfull/points:
>
>   for s from 1 to dim do
>     Data1[s,2*r-1]:=B-Bfull/points;
>     Data1[s,2*r]:=simplify(NumEn[s]);
>   od:
> od:
>
```

Write the numerical data to a file.

```
> readlib(write);
> writeto(datap85R);
> for r from 1 to points do
>   writeln(Data1[1,2*r-1]);
> od:
> for s from 1 to dim do
>   for r from 1 to points do
>     writeln(Data1[s,2*r]);
>   od:
>   writeln();
> od:
> writeto(terminal);
>
```

To examine the result:

```
> plot({'convert(row(Data1,n),list)'$'n'=1..dim},h=0..Bfull,style=point);
```